

School of Chemistry



**PROBING THE BASIS OF CATALYSIS OF
DIHYDROFOLATE REDUCTASE**

A thesis submitted to Cardiff University for the degree of Doctor of
Philosophy by

Aduragbemi S. Adesina

Supervisor: Prof. Rudolf K. Allemann

2018

Declaration

This work has not previously been accepted in substance for any degree and is not being concurrently submitted in candidature for any degree.

Signed..... (Candidate) Date.....

STATEMENT 1

This thesis is being submitted in partial fulfilment of the requirements for the degree of Doctor of Philosophy.

Signed..... (Candidate) Date.....

STATEMENT 2

This thesis is the result of my own independent work/investigation, except where otherwise stated. Other sources are acknowledged by explicit references.

Signed.....(Candidate) Date.....

STATEMENT 3

I hereby give consent for my thesis, if accepted, to be available for photocopying and for interlibrary loan, and for the title and summary to be made available to outside organisations.

Signed..... (Candidate) Date.....

Dedication

To God

To my father, mother, and siblings

To my wife, Adeola

To my son, Gift

Acknowledgement

I want to acknowledge and thank my supervisor, Prof. Rudolf Allemann for the opportunity he gave me to participate in this work and for his constant support, guidance, and patience throughout my Ph.D. programme.

I express my sincere thanks to Dr. Louis Luk for his guidance, suggestions, and advice during my study and for proofreading this thesis, thank you for everything. I would also like to thank Dr. Tsai Yushuan, Dr. Joel Loveridge and Prof. Angela Casini for their help and insightful discussions during my *viva*.

Also, I would like to thank all my colleagues on the DHFR project, especially Dr. Antonio Angelastro and Dr. Alan Scot for proofreading this thesis and, for all the help they offered. I would not forget the help of Dr. Enas Behiry, Dr. Luke Johnson, Sanjay Patel, Ed Kalvaitis, Tom Williams, Rob Hughes, and Christopher Jones. I want to extend my appreciation to all my colleagues in the Allemann group for their support and encouragement. My thanks also go to Dr. Verónica González and Dr. Robert Mart for the help in the laboratory as well as to all academic and technical staff of the School of Chemistry, Cardiff University.

Many thanks to Prof. Vicent Moliner and Dr. Katarzyna Swiderek (Departament de Quimica Fisica I Analitica, Universitat Jaume I, Spain) for theoretical calculations and helpful discussions. I would also like to thank Drs Stephen Lynch, Chris Hodge and Jessica Mabin (School of Physics and Astronomy, Cardiff University) for help and guidance at the start of this project. I have had the pleasure of working with you.

I want to thank the Chemistry Department and the College of Physical Science and Engineering of Cardiff University for funding this Ph.D. project. I would not forget the support of staff and my friends from the Federal University of Technology Akure Nigeria especially Shoetan Ibrahim, Aderibigbe Abiodun, Dr. Ogunjobi Joseph, Dr. Idowu Gideon, Dr. Odukoya Johnson, Dr. Oluwasina Oluwagbenga and Dr. Olasehinde Emmanuel. Thanks to the entire members of the Garden of the Lord Parish, RCCG for their support and prayers. Thanks to Pastor and Pastor

Mrs. Edwin Egede. God bless you for your encouragement. A special thanks to the Durojaiye's family for all the support they offered when the going was tough.

I want to thank my parents -Pastor and Lady Evang. S.K Adesina- and my siblings-Mr &Mrs Olorunfemi, Mr &Mrs Olusola, Mr &Mrs Asifor, Mr &Mrs Olanrewaju Adesina and Mr &Mrs Mayowa Adesina- for their love, prayer, support, and understanding. You mean so much to me.

Special thanks go to my wife Adeola Adesina, who through this journey stood with me and gave me more support than I could ever ask. "Thank you so much. You deserve more than I could say." I will extend this appreciation to my son Gift Adesina, who cheers "daddy" on every day. You bore the stress of the moment.

Finally, I would never have reached this far without the inspiration of God. "Thank you, Jesus, for setting the stage for me.

Abstract

Dihydrofolate reductase (DHFR) is the enzyme that catalyses the reduction of 7,8-dihydrofolate (DHF) to 5,6,7,8-tetrahydrofolate (THF) in the presence of the cofactor reduced nicotinamide adenine dinucleotide phosphate (NADPH). The DHFR catalysed reaction has often been used to study the contribution of protein dynamics to enzyme catalysis. To better understand protein dynamics and to investigate how it relates to electrostatic changes in DHFRs, the dynamics of DHFR from human (HsDHFR), *Escherichia coli* (EcDHFR), the cold-adapted *Moritella profunda* (MpDHFR), the moderately thermophilic *Geobacillus stearothermophilus* (BsDHFR) and the thermophilic enzyme from *Thermatoga maritima* (TmDHFR) are studied using kinetic isotope effects and vibrational Stark effects spectroscopy. Chapter 1 gives a brief introduction to the thesis. In Chapter 2, the purification of HsDHFR was optimised due to the kinetic complexity introduced by the purification strategy. The study showed that using a truncated ligand lessens the complexity that has prevented detailed kinetic characterisation of HsDHFR for three decades. The work presented in Chapter 3 involves optimisation of kinetic conditions to reveal the chemical step of HsDHFR and to study the effects of dynamics on it. The result showed that tunnelling did not contribute to the dynamics of HsDHFR, in contrast to reports for its bacterial homologs. It also showed that protein dynamics are not coupled to the chemical step of the enzyme at its physiological temperature. In Chapter 4, vibrational Stark effect spectroscopy was employed to study ligand interaction in EcDHFR, its conformationally impaired variant EcDHFR-S148P, BsDHFR, MpDHFR and TmDHFR. A site-specific nitrile probe was inserted at a conserved position to monitor electrostatic changes in the enzymes. The results obtained suggest that electrostatics in DHFRs are generally conserved despite exhibiting different dynamic flexibilities. In addition, the preorganisation of cofactor-substrate interaction in the enzyme was found to play a major role in their catalysis. A summary of the work presented in this thesis is provided in Chapter 5 and the materials and methods used in evaluating this work is reported in Chapter 6.

Abbreviations

A	absorption
<i>A</i>	Arrhenius pre-exponential factor
ADB	adenosine-binding domain
ADP	adenosine diphosphate
AIM	Auto-induction media
AMP	ampicillin
APS	ammonium persulfate
βME	β -mercaptoethanol
BsDHFR	dihydrofolate reductase from <i>Geobacillus stearothermophilus</i>
IusConc.	Concentration
CBD	cofactor binding domain
CD	circular dichroism spectroscopy
CV	column volume
D	deuterium
DAD	donor-acceptor distance
DDF	5,10-dideazatetrahydrofolate
DEAE	diethylamino ethyl
dH₂O	deionised water
DHF	7,8-dihydrofolate
DHFR	dihydrofolate reductase
DMF	dimethylformamide
DNA	deoxyribose nucleic acid
dNTP	deoxynucleotide triphosphate
dTMP	deoxythymidine monophosphate
DTT	dithiothreitol
dUMP	deoxyuridine monophosphate
E_a	activation energy
E	enzyme
[E]₀	total enzyme concentration
EDTA	ethylenediaminetetraacetic acid

ES	enzyme-bound substrate complex
FPLC	fast performance liquid chromatography
FRET	Förster/fluorescence resonance energy transfer
FTIR	Fourier transform infrared spectroscopy
Gdn-HCl	guanidine hydrochloride
<i>h</i>	Planck's constant = 6.626176×10^{-34} J s
<i>h̄</i>	Planck's constant divided by 2π , $\hbar = 1.054588664 \times 10^{-34}$ J s
H	hydrogen (protium)
HsDHFR	human dihydrofolate reductase
HPLC	high pressure/performance liquid chromatography
IPTG	isopropyl- β -D-1-thiogalactopyranoside
KIE	kinetic isotope effect
<i>k</i>	rate constant
<i>k_b</i>	Boltzmann constant = $1.3806503 \times 10^{-23}$ J K ⁻¹
<i>k_{cat}</i>	steady-state rate constant or the turnover number
K_M	Michaelis constant
<i>k_{tun}</i>	the rate of tunnelling
K_iP_O₄	potassium phosphate
<i>l</i>	pathlength
LB	Luria-Bertani growth media
LcDHFR	dihydrofolate reductase from <i>Lactobacillus casei</i>
LD	loop domain
<i>m_x</i>	atomic mass
M9	minimal media
MaDHFR	dihydrofolate reductase from <i>Mycobacterium avium</i>
MES	morpholinoethanesulfonic acid
MpDHFR	dihydrofolate reductase from <i>Moritella profunda</i>
MtDHFR	dihydrofolate reductase from <i>Mycobacterium tuberculosis</i>
MmDHFR	dihydrofolate reductase from <i>Mus musculus</i> (mouse)
MyDHFR	dihydrofolate reductase from <i>Moritella yayanosii</i>
MTE	MES Tris ethanolamine sodium chloride

MTX	methotrexate
NAD⁺	oxidised nicotinamide adenine dinucleotide
NADP⁺	oxidised nicotinamide adenine dinucleotide phosphate
NADPD	4R-2H reduced nicotinamide adenine dinucleotide phosphate
NADPH	reduced nicotinamide adenine dinucleotide phosphate
NMR	nuclear magnetic resonance
OD	optical density
P	product
pABG	<i>para</i> -aminobenzoyl glutamate
PAGE	polyacrylamide gel electrophoresis
PCR	polymerase chain reaction
PDB	protein data bank
PYR	Pyrimethamine
Q_t	tunnelling correction
R	Reactant
R	general gas constant
RCF	relative centrifugal force
RNase	Ribonuclease
Rpm	revolutions per minute
S	Substrate
SBD	substrate-binding domain
SDS-PAGE	sodium dodecyl sulfate-polyacrylamide gel electrophoresis
SpDHFR	dihydrofolate reductase from <i>Streptococcus pneumoniae</i>
SvDHFR	dihydrofolate reductase from <i>Shewanella violacea</i>
T	absolute temperature
T	Tritium
TbADH	alcohol dehydrogenase from <i>Thermoanaerobacter brockii</i>
TMP	Trimethoprim
TS	thymidylate synthase
TS	transition state
TST	transition state theory

TEMED	N,N,N',N'-tetramethylenediamine
THF	5,6,7,8-tetrahydrofolate
TM	melting temperature
TmDHFR	dihydrofolate reductase from <i>Thermotoga maritima</i>
TMP	Trimethoprim
TRC	tunnelling ready conformation
Tris	tris(hydroxymethyl)aminomethane
TS	thymidylate synthase
TST	transition state theory
UV/Vis	ultraviolet/visible spectroscopy
ϵ	extinction coefficient
ν	vibrational frequency
v_0	velocity of the reaction
VSE	vibrational Stark effects
V_{\max}	maximal velocity
($V_{\max}/2$)	half maximum velocity
ZPE	zero-point energy
ΔG°	reaction free energy
ΔG^\ddagger	free activation energy of the reaction
ΔH^\ddagger	activation enthalpy
ΔS^\ddagger	activation entropy
λ_B	de Broglie wavelength
σ	standard deviation
σ_M	standard error of the mean
Θ	ellipticity in millideg
Θ_{MRE}	mean residue ellipticity
μ_x	reduced mass
\ddagger	the reactive configuration

Amino Acid	1 letter code	3 letter code
Alanine	A	Ala
Arginine	R	Arg
Asparagine	N	Asn
Aspartic acid	D	Asp
Cysteine	C	Cys
Glutamic acid	E	Glu
Glutamine	Q	Gln
Glycine	G	Gly
Histidine	H	His
Isoleucine	I	Ile
Leucine	L	Leu
Lysine	K	Lys
Methionine	M	Met
Phenylalanine	F	Phe
Proline	P	Pro
Serine	S	Ser
Threonine	T	Thr
Tryptophan	W	Trp
Tyrosine	Y	Tyr
Valine	V	Val

List of figures

Figure 1.1. Reaction pathway of an uncatalysed reaction (black) versus an enzyme-catalysed reaction (red). The tight binding of enzymes to the activated enzyme-substrate complex (ES^\ddagger) reduces the energy required for the reaction compared to the uncatalysed activated substrate (S^\ddagger)	2
Figure 1.2 Timescales of protein motion (blue, above) and experimental and theoretical methods (red, below). Experimental methods like X-ray scattering are shown over the timescale of fluctuation they can detect. Motion on faster timescales averages during the experiments. (Adapted with modification from reference 20)	4
Figure 1.3. Graphical description showing the change in product concentration over the reaction time. The initial burst represents the pre-steady state region (red) that takes place before the reaction reaches equilibrium termed steady state region (blue)	6
Figure 1.4. A schematic diagram of a stopped-flow apparatus indicating the major components: mixer, reaction cell, and detector	6
Figure 1.5. A graphical representation of the Michaelis-Menten plot showing the relation between the reaction velocity (v_0) and substrate concentration [S]. The maximum velocity (V_{max}) and Michaelis constant (K_M) are shown on the graph	8
Figure 1.6. (A) Reaction profiles for hydrogen transfer. The origin of the semi-classical hydrogen isotope effect, arising from differences in the zero-point energy for protium, deuterium and tritium. (B) Illustration of the crossing of the barrier below the transition state, where this occurs in an isotope-dependent manner ($H > D > T$). (Adapted from reference 19,33)	12
Figure 1.7. Arrhenius plot of rates (top panel) and KIEs (bottom panel, green line) of light (L, in blue) and heavy (H, in red) isotopes. In region I, tunnelling is negligible, so $A_l A_h$ is close to unity. Region II is the moderate tunnelling region where only the lighter isotope tunnels and the corresponding $A_l A_h$ is much smaller than unity. Both isotopes tunnelling region III, making the $A_l A_h$ much higher than unity (Adapted from reference 28)	13

Figure 1.8. Potential energy curves for harmonic oscillator approximation (dotted) and anharmonic correction (solid). ⁵⁸	17
Figure 1.9. Representation of the beam paths within Michelson interferometer of Fourier Transform infrared (Adapted with modification from reference 61)	18
Figure 1.10. The reaction catalysed by DHFR showing the transfer of a hydride from C ₄ of the cofactor (NADPH) to the C ₆ of the substrate (DHF) to produce THF and NADP ⁺	23
Figure 1.11. A selection of biological reactions that use different THF derivatives as a cofactor during one-carbon transfer reactions. THF is converted to 5,10-methylene-THF. The 5,10-methylene-THF is then converted to 5-methyl-THF by reduction with NADPH. The methyl group is in turn transferred to homocysteine generating methionine in the presence of cobalamin (Vit B12). The 5,10-methylene-THF is also used in the presence of thymidylate synthase (TS) to methylate the pyrimidine base uracil in deoxyuridine monophosphate (dUMP) to thymine to produce deoxythymidine monophosphate (dTDP) which is essential for DNA synthesis. 5,10-methylene-THF and 5-formyl-THF can be converted into 5,10-methenyl-THF, which is in turn converted to 10- formyl-THF, which acts as a cofactor during purine biosynthesis. (Adapted from reference 84 and 85).	24
Figure 1.12. (A) Cartoon representation of EcDHFR (PDB 1RX2) showing the secondary structural elements; α-helices (red), β -strands (yellow) and connecting loops (green). (B) The structural domain rotated by ~90° and showing the cofactor binding domain (purple), the substrate domain (blue) and the three-active loops: M20 (orange), FG (cyan) and GH (green). The ligands are also shown with colours corresponding to their domains.....	25
Figure 1.13. Structural overlay of (A) EcDHFR in brown (PDB: 1RX2) and BsDHFR in purple (PDB: 1ZDR) indicating the difference in the αE helix. (B) EcDHFR in brown (PDB:1RX2) and TmDHFR in blue and sky blue (1D1G). The domains participating in the dimer interface is shown as red.	26
Figure 1.14. (A) Structural overlay of EcDHFR (brown, PDB: 3QL3) and HsDHFR (cyan, PDB: 4M6K) bound to ligands (FOL and NADP ⁺ in purple). Extension sequence identified in	

phylogenetic analysis as orange in HsDHFR. ⁹⁴ (B) The catalytic rate of HsDHFR and EcDHFR (in parenthesis). Rate constants are written as clockwise (red) and anticlockwise (blue). The lower half of the catalytic cycle represents the major kinetic path of EcDHFR while HsDHFR follows the full cycle. First and second-rate constants are given in the unit of s ⁻¹ and μMs ⁻¹ respectively. (Adapted from reference 95 and 96).	27
Figure 1.15. (A) The catalytic cycle of EcDHFR showing the conformations adopted along with it. Crystal structure of EcDHFR showing (B) the closed conformation (PDB: 1RX2) and the hydrogen bonding interaction with D122 of the FG loop (C) the occluded conformation (PDB: 1RX6) and stabilising interaction with S148 of the GH loop.....	28
Figure 2.1. LC trace of ampicillin hydrolysis by the isolated 28.9 kDa protein (TEM-1 β-lactamase). (Obtained from Dr Luk L. and Williams T.)	36
Figure 2.2. Schematic diagram showing sub-cloning of HsDHFR gene and the step of His-tag coding sequence removal. Blue circle and arc show pET 21(a) and HsDHFR gene, respectively. The brown circle and arc are for pET 28(a) plasmid vector while the orange region of the pET 28(a) plasmid codes for His-tag and thrombin cleavage site.....	37
Figure 2.3. Crystal structure of HsDHFR (light sea green, PDB:4M6K) bound to folate (magenta). Residues interacting with pABG are shown in sea green according to reference 103,144 and 146. NADP ⁺ was omitted for clarity.....	38
Figure 2.4. SDS-PAGE showing the HsDHFR expressions and purification (1: Protein marker in kDa; 2-4: HsDHFR before IPTG; 5-7: HsDHFR after IPTG; 8-10: Selected fractions from Q-sepharose purification; 11: purified HsDHFR (without β-mercaptoethanol); 12-13: cell pellet; 14-15: purified HsDHFR after size exclusion.	39
Figure 2.5. Melting temperature of HsDHFR (10 μM) in phosphate buffer (10 mM) pH 7.0 at 215 nm without ligand (blue), with pABG (red) and folate (orange).....	40
Figure 2.6. ¹ H- ¹⁵ N HSQC overlay of HsDHFR complexed with (A) folate (blue) and pABG:NADP ⁺ (red) and (B) folate:NADP ⁺ (blue) and THF:NADP ⁺ (red).....	41

Figure 2.7. Stopped-flow fluorescence relaxation of folate-bound HsDHFR after pre-equilibration with NADPH and initiation of reaction with DHF showing (A) increasing intensity and (B) wobbly relaxation	43
Figure 2.8. The overlay of TEM-1 β -lactamase (PDB:1ERO, sky blue) and LACTB2 (PDB: 4AD9, brown) Their conserved domains and residues are shown as blue and orange, respectively. The covalently bound boron inhibitor of TEM-1 shown as purple while the two-zinc metals at the active site of LACTB2 are shown as yellow	46
Figure 3.1. Arrhenius plots for hydride (circle) and deuteride (square) transfer plotted on a logarithmic scale against inverse temperature, measured under steady-state conditions at pH 10.0	51
Figure 3.2. (A) Temperature-dependence of substrate KIE measured under steady-state conditions at pH 10.0 and (B) Arrhenius plot of substrate KIE on a logarithmic scale against inverse temperature.....	51
Figure 3.3. Melting temperature of HsDHFR (10 μ M) in different buffers (10 mM) measured at 215 nm: light in phosphate pH 7.0 (blue), boric acid pH 8.0 (red) and boric acid pH 10.0 (orange).....	52
Figure 3.4. Normalised UV/Vis absorbance trace of steady-state kinetics measured over 40 sec with 10 pM enzyme concentration at 10 °C showing three different kinetic rates. NH = NADPH and ND = NADPD (pH 7.0)	53
Figure 3.5. Arrhenius plots for hydride (circle) and deuteride (square) and the corresponding KIEs (square) plotted on a logarithmic scale against inverse temperature, measured under pre-steady-state conditions at pH 8.5	55
Figure 3.6. (A) Temperature-dependence of substrate KIE measured under pre-steady-state conditions at pH 8.5 and (B) Arrhenius plot of substrate KIE plotted on a logarithmic scale against the inverse temperature	55

Figure 3.7. Arrhenius plot of the pre-steady-state hydride transfer rate constant of HsDHFR without methanol (blue) and with 30% methanol cosolvent(red).	56
Figure 3.8. (A) Arrhenius plots of deuteride transfer rate constant in HsDHFR measured at pH 8.0 (blue) and pH 8.5 (red) (B) Arrhenius plots of deuteride transfer rate constant extrapolated at pH 7.0 (orange), pH 8.0 (blue) and pH 8.5 (red). Some points in the linear estimations were removed for clarity.	60
Figure 3.9. Circular dichroism spectra of HsDHFR (10 μ M) at 20 °C in the different buffers (10 mM) reported: light enzyme in phosphate pH 7.0 with folate ligand (cyan), in boric acid pH 8.0 (green), in boric acid with 30% methanol pH 8.0 (dark blue) and in boric acid pH 10.0 (yellow). Heavy enzyme in phosphate pH 7.0 with folate ligand (red),	63
Figure 3.10. (A) Arrhenius plots of the hydride transfer rate constant of light (blue) and heavy HsDHFR (red) at pH 8.5 and (B) The resulting enzyme KIE (k^{LE}/k^{HE})	64
Figure 3.11. Temperature-dependence of enzyme KIE in HsDHFR, k_H (blue) and k_D (red). The k_D values were measured with 30% methanol solvent (square) and without cosolvent (diamond).	64
Figure 4.1. (A) Conformational changes along the catalytic cycle of EcDHFR indicated by blue (open), orange (closed) and red (occluded). Line arrows represent major cycle while the broken arrow represents the step that is rarely observed in vivo. (B) Overlay of the crystal structures of EcDHFR showing the direction of the thiocyanate probe (green spheres) and the configuration of the M20 loop in the open (blue, PDB: 1RA3), closed (orange, PDB: 4P66) and occluded (red, PDB:1RX6). Methotrexate and NADP ⁺ are shown in purple with a mesh surface, while other ligands are removed for clarity.....	72
Figure 4.2. Sequence alignment of different homologues of DHFR. Enzymes and residues mutated are shown in red. The conserved Thr residue (T46 by EcDHFR numbering), labelled in this study are shown as orange in the different enzymes while the equivalent position of the residues mutated are shown in blue.....	74

Figure 4.3. Crystal structures showing mutations introduced into (A) EcDHFR (brown, PDB 1RXA) (B) BsDHFR (purple, PDB 1ZDR) (C) MpDHFR (cyan, PDB 2ZZA) and (D) TmDHFR (blue, PDB 1D1G). The conserved threonine residue changed to cysteine is shown as the yellow spheres while native cysteine residues modified to other amino acid residues are shown as orange spheres.	75
Figure 4.4. Structural overlay of EcDHFR (brown, PDB: 1RX2), MpDHFR (cyan, PDB: 2ZZA), BsDHFR (purple, PDB: 1ZDR) and TmDHFR (blue, PDB: 1D1G) showing the rotamer of the conserved threonine residue	76
Figure 4.5. UV trace for the purification of TmDHFR (A) hydrophobic interaction chromatography eluting over the 60 mL and (B) size exclusion chromatography with exclusion volume between 170 – 200 mL	78
Figure 4.6. (A) Bar charts of the vibrational frequencies of EcDHFR _{cf} T46C-CN and EcDHFR _{cf} S148P/T46C-CN in different complexes. (B) Bar chart comparison between the complexes formed by the enzymes. (C) Calibration of hydrogen bonding interactions of the complexes of EcDHFR _{cf} T46C- ¹³ CN (dark blue triangles) and EcDHFR _{cf} S148P/T46C- ¹³ CN (red diamond). The complexes of the enzymes are represented by 1 = apoenzyme, 2 = E:NADPH, 3 = E:FOL:NADP ⁺ , and 4 = E:THF:NADP ⁺ . Deviation of ~7 cm ⁻¹ from Stark calibration was observed. The Stark model is represented by the open circle connected by the broken line, ⁵¹ indicating the fit for nitrile calibration in different solvents: a = cyclohexane, b = toluene, c = THF, d = chloroform, e = dichloromethane, f = dimethyl sulphoxide, g = acetone and h = dimethylformamide, obtained from reference 193	81
Figure 4.7. (A) Bar charts of the vibrational frequencies of EcDHFR _{cf} T46C-CN, EcDHFR _{cf} S148P/T46C-CN, BsDHFR _{cf} T46C-CN and MpDHFR _{cf} T47C-CN in different complexes. (B) Calibration of hydrogen bonding interactions of the complexes of EcDHFR _{cf} T46C- ¹³ CN (dark blue triangles), EcDHFR _{cf} S148P/T46C- ¹³ CN (red diamond), BsDHFR _{cf} T46C-CN (green square) and MpDHFR _{cf} T47C-CN (orange circle) Deviation from Stark model represented by the open circle connected by a broken line was ~7 cm ⁻¹ . ^{51 193}	84

Figure 4.8. (A) Bar charts of the vibrational frequencies of all the DHFRs studied in their different complexes. (B) Bar chart comparison between the complexes formed by the enzymes. (C) Calibration of hydrogen bonding interactions of the complexes of TmDHFR T47C-CN (black diamond). Deviation from Stark model represented by the open circle connected by a broken line was ~7 cm ⁻¹ . ¹⁹³	88
Figure 4.9. Ligands overlay from the crystal structure of EcDHFR in complex with folate:NADP ⁺ (green, PDB: 1RX2) and MTX:NADP ⁺ (cyan, PDB:4P66) showing the pteridine ring flip of MTX and wider distance from the nitrile probe. The thiocyanate probe from PDB:4P66 is shown as cyan, similar to ligands from the crystal structure.	90
Figure 6.1. Scheme for the post-translational modification of cysteine residues to produce nitrile labelled enzyme.	121

List of tables

Table 2.1. Melting temperature of HsDHFR (10 μ M) in the absence and presence of ligands	40
Table 2.2. The interaction of residues of HsDHFR with folate ligand from crystal structure and solution NMR	42
Table 2.3. Trials of pre-steady-state measurements of HsDHFR (20 μ M) using a stopped-flow apparatus.....	44
Table 3.1. Temperature-dependence of steady-state kinetic parameters of HsDHFR in MTEK buffer pH 10.0	54
Table 3.2. Steady-state kinetic parameters in different buffers at 20 °C.....	57
Table 3.3. Melting temperature determined in different buffers.	57
Table 3.4. Temperature-dependence of pre-steady state kinetic parameters in phosphate-boric-30%methanol buffer pH 8.5	58
Table 3.5. Temperature-dependence of pre-steady-state kinetic parameters in the presence and absence of methanol cosolvent.....	58
Table 3.6. Substrate KIE of DHFR homologs in the presence and absence of methanol cosolvent	59
Table 3.7. Deuteride transfer measured at pH 8.0 and 8.5 in phosphate-boric acid buffer.....	61
Table 3.8. Estimated hydride transfer rate constant in HsDHFR determined from Arrhenius plots at pH 8.5 and 8.0 using substrate KIE of 2.3.....	61
Table 3.9. Steady-state kinetic parameters of light and heavy enzymes in phosphate buffer pH 7.0 and 20 °C	62
Table 3.10. Melting temperature of light and heavy enzymes bound to folic acid	62
Table 3.11. Eyring activation parameters of light and heavy DHFRs under pre-steady-state conditions at pH 7.0 and 25 °C.....	65

Table 3.12. Temperature-dependence of the pre-steady state kinetic parameters light and heavy HsDHFR in phosphate-boric-30% methanol buffer pH 8.5	66
Table 3.13. Pre-steady-state kinetic parameters of light and heavy HsDHFR in phosphate-boric buffer, pH 8.5. Enzyme KIE measured in the absence of cosolvent.	66
Table 3.14. Pre-steady-state kinetic parameters of light and heavy HsDHFR in phosphate-boric-30% methanol buffer pH 8.5. Enzyme KIE measured in the presence of cosolvent.....	66
Table 3.15. Pre-steady-state kinetic parameters of heavy HsDHFR in phosphate-boric-30% methanol buffer pH 8.5. Substrate KIE of heavy HsDHFR.	67
Table 4.1. Summary of ^{13}C NMR shifts, the vibrational frequency at maximum peak, and Full Width at Half Maximum (FWHM) values for the IR spectra in monomeric DHFRs (EcDHFR, EcDHFR S148P, BsDHFR and MpDHFR) determined at 20 °C	86
Table 4.2. Summary of ^{13}C NMR shifts, vibrational frequency at maximum peak, and Full Width at Half Maximum (FWHM) values for the IR spectra in TmDHFR determined at 20 °C.....	88
Table 6.1. E. coli strains used for experiments.....	98
Table 6.2. Components of the SDM reactions.....	104
Table 6.3. Conditions used for the SDM reactions	104
Table 6.4. Primers for Quikchange and overlapping site-directed mutagenesis technique.....	105
Table 6.5. Conditions for gene expression in E. coli.....	107
Table 6.6. Extinction coefficients employed to calculate the concentration of DHFRs measured at 280 nm	119

Table of Contents

Declaration.....	i
Dedication.....	ii
Acknowledgement	iii
Abstract.....	v
Abbreviations	vi
List of figures	xi
List of tables	xviii
Table of Contents	xx
1 . Introduction	1
1.1 Catalytic power of enzymes.....	2
1.2 Investigation of protein dynamics.....	4
1.2.1 Pre-steady-state and steady-state kinetics	5
1.2.2 Kinetic isotope effects (KIEs)	8
1.2.3 Vibrational Stark effect (VSE) spectroscopy	15
1.3 Dihydrofolate reductase (DHFR).....	22
1.3.1 Structural characterisation of DHFRs.....	24
1.3.2 Protein motions in DHFRs	27
1.4 Investigation of protein dynamic effects in DHFRs	29
1.4.1 Kinetic characterisation and flexibility studies	29
1.4.2 KIEs studies.....	31
1.4.3 VSE spectroscopic investigations.....	32

1.4.4	Project Aims	33
2	. Optimised isolation of stable human dihydrofolate reductase for kinetic investigation	32
2.1	Preface	33
2.2	Identification of protein impurity and gene cloning	34
2.3	Optimisation of purification techniques to produce stable HsDHFR	37
2.4	Kinetic investigation of purified HsDHFR	43
2.5	Discussion	45
2.6	Conclusions.....	47
3	. Effects of protein dynamics on the hydride transfer reaction catalysed by human dihydrofolate reductase.....	48
3.1	Preface	49
3.2	Substrate KIE of the reaction catalysed by HsDHFR.....	49
3.2.1	Substrate KIE (KIE_{cat}) measured using steady-state kinetics at high pH.....	50
3.2.2	Substrate KIE (KIE_H) measured using pre-steady state kinetics at cryogenic temperatures.....	54
3.3	Estimation of hydride transfer in HsDHFR	59
3.4	Enzyme KIE measured using pre-steady state kinetics at cryogenic temperatures	61
3.5	Discussion	67
3.6	Conclusions.....	69
4	. Electrostatic changes at the microenvironment of DHFRs investigated by vibrational Stark effects spectroscopy.....	70
4.1	Preface	71
4.2	Labelling of DHFRs for VSE spectroscopy	72
4.2.1	Site-directed mutagenesis	73

4.2.2	Production of DHFRs for nitrile labelling	76
4.2.3	VSE spectroscopic measurements	78
4.3	Electrostatic changes at the microenvironment of DHFRs.....	80
4.3.1	Electrostatic changes in the conformationally impaired EcDHFR variant.....	81
4.3.2	Electrostatics changes at the active site of monomeric DHFRs	83
4.3.3	Different electrostatic trends in monomeric and dimeric DHFRs.....	87
4.4	Discussion	88
4.5	Conclusions.....	92
5	. Summary and future work	94
5.1	Summary and future work	95
6	. Materials and methods.....	97
6.1	Bacterial strains and preparation.....	98
6.1.1	Bacterial strains	98
6.1.2	Competent cells	98
6.1.3	Super-competent cells.....	99
6.2	Growth media and sterile solutions	100
6.2.1	Luria-Burtani (LB) medium	100
6.2.2	LB agar plates.....	100
6.2.3	Auto-induction media (AIM)	100
6.2.4	Minimal (M9) media	101
6.2.5	Sterile solutions	101
6.3	DNA manipulation.....	102
6.3.1	DNA visualization	102

6.3.2	DNA extraction and purification	103
6.3.3	Sub-cloning of gene.....	103
6.3.4	Site-directed mutagenesis (SDM).....	104
6.3.5	Transformation of DNA into competent cells	106
6.4	Gene Expression	106
6.4.1	Production of unlabelled DHFRs	106
6.4.2	Isotopically labelled enzymes.....	107
6.5	Enzyme purification.....	108
6.5.1	Phosphate stock solutions.....	108
6.5.2	Purification buffers	108
6.5.3	Purification methods.....	112
6.6	Ligand synthesis and purification	115
6.6.1	Dihydrofolate (DHF)	115
6.6.2	Synthesis, purification and storage of (R)-[4- ² H]-NADPH.....	116
6.7	SDS-PAGE	116
6.7.1	Resolving buffer	116
6.7.2	Stacking buffer	116
6.7.3	SDS sample loading buffer.....	116
6.7.4	Running buffer stock	116
6.7.5	SDS staining buffer	117
6.7.6	Resolving gel (12%)	117
6.7.7	Stacking gel (5.0%)	117
6.7.8	SDS-PAGE protocol.....	117

6.8 Protein concentration	118
6.8.1 Bicinchoninic acid (BCA) assay	118
6.8.2 UV/Vis spectrophotometer	118
6.9 Protein characterisation.....	119
6.9.1 Assay buffer.....	119
6.9.2 Steady-state.....	119
6.9.3 Michaelis-Menten constant (K_M) measurement	119
6.9.4 Stopped-flow (pre-steady state) measurement	120
6.9.5 CD.....	120
6.10 Thiocyanate Labelling.....	121
6.10.1 Enzyme thiocyanate (SCN) labelling	121
6.10.2 Enzyme ^{13}C -thiocyanate (S^{13}CN) labelling.....	121
6.10.3 Fourier Transform Infrared spectroscopy (FTIR)	122
6.10.4 Nuclear magnetic resonance spectroscopy (NMR)	122
6.10.5 Errors and propagations.....	122
References	124
Appendices	145

1 . Introduction

1.1 Catalytic power of enzymes

Enzymes catalyse chemical reactions at rates of up to 10^{21} relative to uncatalysed reactions. Generally, chemical reactions occur when reacting molecules have sufficient energy to overcome the activation energy barrier.¹ Hence, the height of this barrier and the energy possessed by the reacting molecules dictate the speed of chemical reactions. In the case of enzymes, reducing the height of the energy barrier of reactions is believed to lead to enormous rate enhancement that is essential for cellular functions.¹ Such that, in the absence of enzymes, these barriers are high that some of the chemicals would require several decades to react, especially under the mild conditions of pH, temperature and pressure where enzymes function (Figure 1.1).¹ Therefore, understanding how enzymes achieve this barrier reduction has attracted scientific interest for several decades.

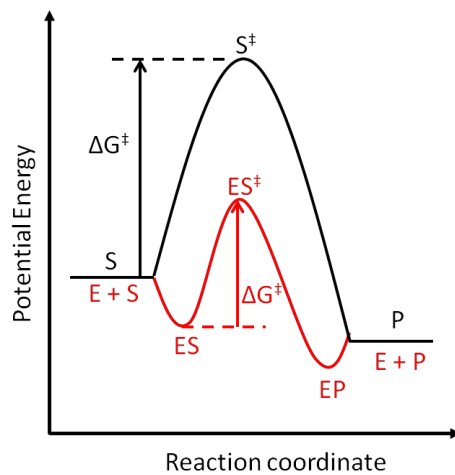


Figure 1.1. Reaction pathway of an uncatalysed reaction (black) versus an enzyme-catalysed reaction (red). The tight binding of enzymes to the activated enzyme-substrate complex (ES^{\ddagger}) reduces the energy required for the reaction compared to the uncatalysed activated substrate (S^{\ddagger})

This quest (that is, the quest to comprehend how enzymes function) has led to several studies and has engineered significant progress in the field of enzymology.²⁻⁷ The history of enzymology probably started in 1849 when Emil Fischer postulated the “lock and key” model

to suggest that enzymes interact with their ligands via rigid contacts.⁸ Almost a decade later, in 1946, Pauling proposed that enzymatic rate enhancements arise from the preferential binding of enzymes to the activated transition-state complex, a proposition that was based on the transition state theory (TST) introduced by Eyring in 1935 (This theory will be described later in this chapter).⁹ However, Koshland was the first to suggest that changes in protein structures may be important for enzyme catalysis when he proposed the “induced fit” model to explain the reorganisation of enzymes active site as a result of ligand binding.¹⁰ Recently, some authors have expanded on Koshland’s proposal to suggest that protein motions are not only crucial for enzyme-ligand interactions but that they also promote the chemical step of enzyme-catalysed reactions.^{11–15} For these models (dynamics-based models), promotion of the chemical step is linked to the compression of the energy barrier and believed to be modulated by the several fluctuations in a protein structure.¹⁶ Hence, they propose that conformational changes in proteins are directly coupled to enzyme’s catalytic mechanism and link the energy involved in breaking and making non-covalent bonds in the enzyme structure to the energy changes that transform reactants into products.^{13,17–19} The implications of the dynamic-based proposals have led to current debates about the basis of enzyme catalysis.

To support their different proposals, several experimental tools are employed to investigate the diverse timescales of protein motions and how each might contribute to enzyme-catalysed reactions (Figure 1.2).²⁰ Some of these techniques include X-ray crystallography, nuclear magnetic resonance (NMR) spectroscopy, kinetic analysis, kinetic isotope effects (KIEs) and in recent times, vibrational Stark effects (VSE) spectroscopy,^{11–15} which provide insights into the mechanism of enzyme catalysis and serve as benchmarks for theoretical calculations into the basis of enzymes’ catalytic power.¹⁶ Overall, they have been applied to enzymes such as dihydrofolate reductase, alcohol dehydrogenase, alanine racemase and others to investigate the role of protein motion in enzyme catalysis.^{14,16,21} Although studies have revealed that protein motions are important for enzyme catalysis,²² their role in the chemical step is not fully understood.

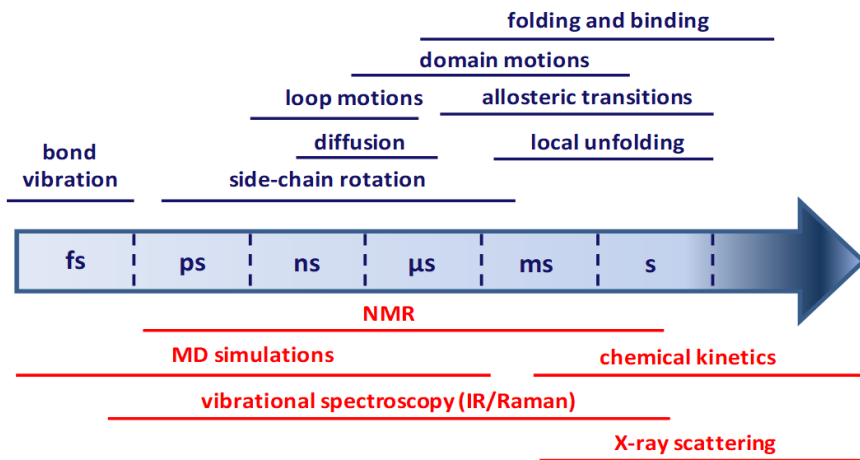


Figure 1.2 Timescales of protein motion (blue, above) and experimental and theoretical methods (red, below). Experimental methods like X-ray scattering are shown over the timescale of fluctuation they can detect. Motion on faster timescales averages during the experiments. (Adapted with modification from reference 20)

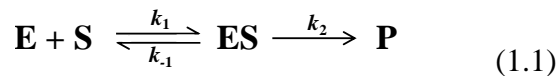
In this thesis, protein dynamics of dihydrofolate reductase (DHFR) - from *Escherichia coli* (EcDHFR), human (HsDHFR), as well as DHFR from psychrophilic *Moritella profunda* (MpDHFR), the moderately thermophilic *Geobacillus stearothermophilus* (BsDHFR) and the hyperthermophilic *Thermatoga maritima* (TmDHFR)- are studied using tools such as KIE measurements and VSE spectroscopy. The investigation of protein dynamics in these enzymes is crucial because they catalyse the same chemical reaction while exhibiting diverse protein motions. This chapter will be discussed according to the following outlines: in the first section, specific tools that are employed to investigate protein dynamics in enzymology will be examined briefly and in the second section, DHFRs and the previous studies on their dynamics will be reviewed.

1.2 Investigation of protein dynamics

The three major tools employed in our study of DHFRs include pre-steady and steady-state kinetics, KIEs and VSE spectroscopy.

1.2.1 Pre-steady-state and steady-state kinetics

Kinetic analysis of enzymatic reactions relies on a simplified scheme that involves the conversion of substrate (S) to product (P) by an enzyme (E) (Eq. 1.1):



The velocity (v) of this reaction correlates with the change in the formation of the product (δP) as a function of time or concentration, which is represented below (Eq. 1.2).

$$v = \frac{\delta[P]}{\delta t} = k_2[ES] \quad (1.2)$$

Note that this mathematical expression can be written as a linear plot of $y = mx$, where y is the dependent variable ($\frac{\delta[P]}{\delta t}$), m is the slope (k_2) and x is the independent variable $[ES]$. This will be a first-order rate equation with a constant slope of (k_2). However, the formation of the enzyme-substrate (ES) complex in enzymatic reactions is not a linear function of the concentration of S, which in turn affects the rate of product formation.

Instead, enzymes exhibit a biphasic time course due to changes in the concentration of the ES complex. In the first instance, a rapid formation of the complex is observed within a short period known as pre-steady-state or burst phase; after which, a steady-state phase is observed when the $[ES]$ complex reaches an equilibrium (Figure 1.3).²³

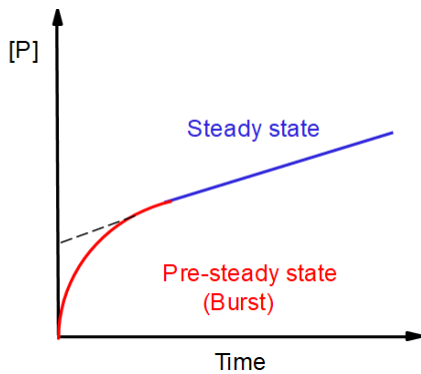


Figure 1.3. Graphical description showing the change in product concentration over the reaction time. The initial burst represents the pre-steady state region (red) that takes place before the reaction reaches equilibrium termed steady state region (blue).

To study the burst phase, one needs instruments that can mix chemical reagents rapidly and measure rate constants of up to a few milliseconds. Examples of such instruments are stopped-flow, quench flow and continuous flow (Figure 1.4).^{23,24} For example, the pre-steady-state kinetics of DHFRs are measured using a stopped-flow apparatus, which allows the rapid conversion of the substrate to the product to be monitored by fluorescence energy transfer. Another requirement for pre-steady-state kinetics is that the concentration of the substrate must be low to measure single-turnover of the product before reaching equilibrium.

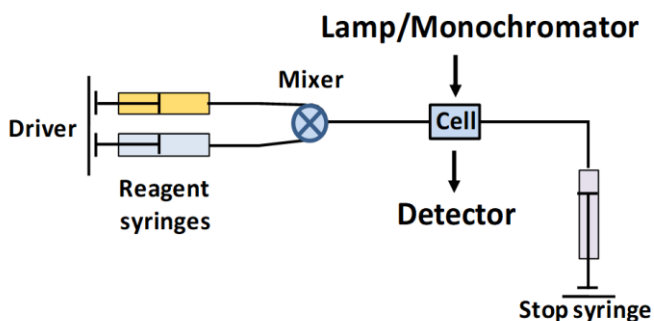


Figure 1.4. A schematic diagram of a stopped-flow apparatus indicating the major components: mixer, reaction cell, and detector.

The linear steady-state phase also called multiple turnover kinetics represents the accumulation of the ES complex due to a slow catalytic step in the reaction. In most biphasic

time course kinetics, the steady-state phase is limited by product release step.²⁴ To determine steady-state kinetics, the concentration of the substrate must be high and saturating, and the corresponding steady-state approximation can be applied. The steady state-approximation is described mathematically by the Michaelis-Menten equation (Eq. 1.3).²⁴

$$v = \frac{[E]_0 k_{cat} [S]}{K_M + [S]} \quad (1.3)$$

where v represents the velocity of the reaction, $[E]_0$ is the total enzyme concentration, $[S]$ is the substrate concentration, k_{cat} is the steady state rate constant, and K_M is the Michaelis constant, which represents the ratio of the rate constants for the dissociation of the ES complex to that of its formation. (Note: the derivation of the Michaelis-Menten equation is given in nearly all biochemistry textbooks, and it is unnecessary to reproduce it here.)

The Michaelis-Menten equation is applicable to most enzymes and is critically important to understand enzyme action in biological systems. At least for simple systems, the Michaelis-Menten equation describes the way that the reaction velocity depends on the substrate concentration. At low substrate concentration, the velocity of the reaction increases linearly with increasing substrate concentration $[S]$. But at high substrate concentration, the velocity of the reaction reaches V_{max} , representing the maximum velocity achieved by the system at saturating substrate concentration. K_M is obtained as the substrate concentration when the reaction velocity is half of V_{max} (Figure 1.5), while k_{cat} equals $V_{max}/[E]_0$. K_M and k_{cat} are intrinsic properties of enzymes under steady-state conditions.

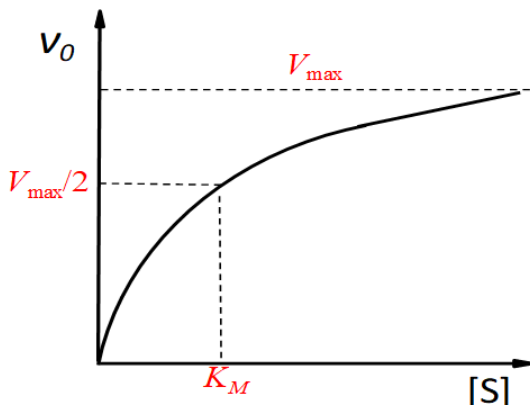


Figure 1.5. A graphical representation of the Michaelis-Menten plot showing the relation between the reaction velocity (v_0) and substrate concentration [S]. The maximum velocity (V_{\max}) and Michaelis constant (K_M) are shown on the graph.

As a result, pre-steady state and steady state rate constants are characteristic of a property of an enzyme and can provide insight into the mechanism and order of events that occur during enzyme catalysis. When these kinetic parameters are altered upon mutagenesis, change in pH, temperatures or solvents, these effects can be related to how the enzyme's reaction is affected. To use this approach to elucidate protein dynamics, amino acid residues implicated in the catalytic mechanism of an enzyme can be mutated to elucidate their function in the enzyme's reaction, observing how pre-steady state rate constants, K_M or k_{cat} are affected. For example, mutation of residues at the centre of the mobile loop of EcDHFR was shown to cause a 500-fold reduction in its pre-steady-state rate constant, which was interpreted to suggest that the loop played a crucial part in the enzyme's catalysis.²⁵ In addition, the pre-steady and steady-state rate constants are also employed to determine the KIEs of enzymatic reactions.

1.2.2 Kinetic isotope effects (KIEs)

KIE has emerged as a tool for probing the basis of enzymatic reactions because experimental findings from the application of KIEs are reproduced by meticulous computations calculations to gain better insight into enzyme catalysis.¹⁶ KIEs are measured by comparing the rate of the reaction of two isotopologues, that is, molecules that differ only in isotopic compositions, which are observed when isotopic substitution of atoms that contribute (directly or indirectly)

to the bonds that are formed or broken during the reaction leading to a change in the reaction rate. Primary (1°) isotope effect is when the atom substituted is directly involved in the reaction, and secondary (2°) if the atom is not directly involved.²⁶ Therefore, KIEs are employed to probe the transition state of chemical reactions.⁷ Popular applications of KIEs to enzymatic reaction is the isotopic substitution of atoms on either on the substrate or enzyme.

1.2.2.1 Substrate KIEs

Substrate KIE ($k_{\text{light}}/k_{\text{heavy}}$) represents the ratio of rate constants when an atom on the substrate is substituted for heavy isotope. Accordingly, quantitative activation parameters of reactions involving the light and heavy isotopes can be deduced from the Arrhenius equation (Eq. 1.4).²⁷

$$k = A e^{\frac{-E_a}{RT}} \quad (1.4)$$

where k is the rate constant, A is the Arrhenius frequency factor or pre-exponential factor, E_a is the activation energy in kJ mol^{-1} , R is the gas constant in $\text{JK}^{-1} \text{mol}^{-1}$ and T is the temperature in Kelvin.

Hence, with KIE ($k_{\text{light}}/k_{\text{heavy}}$), the Arrhenius equation (Eq. 1.4) can be written as:

$$KIE = \frac{k_l}{k_h} = \frac{\frac{A_l e^{\frac{-E_{al}}{RT}}}{A_h e^{\frac{-E_{ah}}{RT}}}}{\frac{A_l}{A_h}} = \frac{A_l}{A_h} e^{\frac{\Delta E_{a(h-l)}}{RT}} \quad (1.5)$$

where k_x is the rate constant, A_x is the Arrhenius pre-exponential factor, and E_{ax} is activation energy for the transfer of isotope x. h and l represent the heavy and light isotopes, respectively. $E_{a(h-l)}$ represents the difference in activation energies for the reaction with heavy and light isotopes.

A linear form of Eq. 1.5 can be obtained by taking the natural logarithm of both sides of the equation. When $\ln(\text{KIE})$ is plotted as a function of $1/T$, a linear plot is obtained. The y-axis intercept represents the logarithm of the ratio of Arrhenius pre-exponential factor for the light and heavy isotopes ($\ln A_l/A_h$) and the slope represents the difference in the activation energy

between the two isotopes $\frac{\Delta E_{\text{a(h-I)}}}{R}$. The temperature-dependence of the slope of KIEs are employed to explain experimental results. Some of the models used to interpret KIEs are briefly outlined below. (For a comprehensive review, readers are referred to references 16,28).

1.2.2.1.1 Semi-classical models

Semi-classical models refer to those models that ignore contributions of quantum mechanical tunnelling, i.e., only consider quantum mechanical effects on vibrational zero-point energy (ZPE). TST assumes that a reaction coordinate may be described by a minimum in free energy that represents the reactant well, and a maximum in free energy called saddle point or transition state, which leads to the product well. In addition, it also infers an equilibrium relationship between the ground state and the transition state.¹⁶ The rate constant (k) described by TST derived from Eyring equation is

$$k = \kappa \frac{k_B T}{h} K^\ddagger \quad (1.6)$$

where K^\ddagger is the equilibrium constant between the transition state and ground state and given as

$e^{\frac{-\Delta G}{RT}}$, κ is the transmission coefficient, T is the absolute temperature, h is the Plank's constant and k_B is the Boltzmann's constant.

According to this model, KIEs result from the difference in vibrational zero-point energy (ZPE = $1/2hv$) of light and heavy isotopes (Figure 1.6A).¹⁹ Because heavier isotopes have lower vibrational ZPEs at ground and transition states, they will require different amounts of activation energies to reach the transition state complex.¹⁹ For example, substituting a hydrogen atom for heavier isotopes is predicted to yield a maximal KIE of 6.9 for k_H/k_D and 15.8 for k_H/k_T .²⁸ This is thought to arise from the vibrational stretching frequencies of C-H, C-D and C-T at 298K being 3000, 2200 and 1800 cm⁻¹, respectively.¹⁹

Deviations from semi-classical behaviour may show up as a nonlinear Arrhenius plot, a low-temperature regime in which the reaction rate is independent of temperature, anomalous

values of Arrhenius pre-exponential factor, an unusual KIE, or a reaction rate that is faster than expected.²⁹ For examples, smaller KIEs can be observed if the primary motion along the reaction coordinate is a bending mode, which has lower ground state-ZPE or if recrossing is significant, in cases of exothermic or endothermic reactions. A typical use of 1° KIEs is to determine the symmetry and structure of the TS.²⁸ An example of a KIE value that is greater than the upper limits of 6.9 predicted by TST has been observed in soybean lipoxygenase (k_H/k_D of ~ 80)³⁰ and in many other enzymes.

1.2.2.1.2 Bell's tunnelling correction

In 1980, Bell introduced a tunnelling correction (Q_t) (Eq. 1.7) to overcome the limitation of TST analysis.³¹

$$k = Q_t A e^{\frac{-Ea}{RT}} \quad (1.7)$$

where Q_t is the tunnelling correction factor defined as the ratio of quantum mechanical to the classical barrier transmission rates, which approaches unity at high temperatures.³¹

Tunnelling occurs when small particles (such as electrons, protons, hydrogen atoms or hydrides) pass through the energy barrier below the saddle point because of their dual wave-particle nature.¹¹ The Bell's tunnelling correction defines the wave property of atoms as a function of mass using de Broglie theory. This phenomenon suggests that the difference in the ZPEs of isotopes could result in a mass-dependent quantum mechanical tunnelling of the atoms through-the-barrier rather than over-the-barrier (Figure 1.6B).^{31,32}

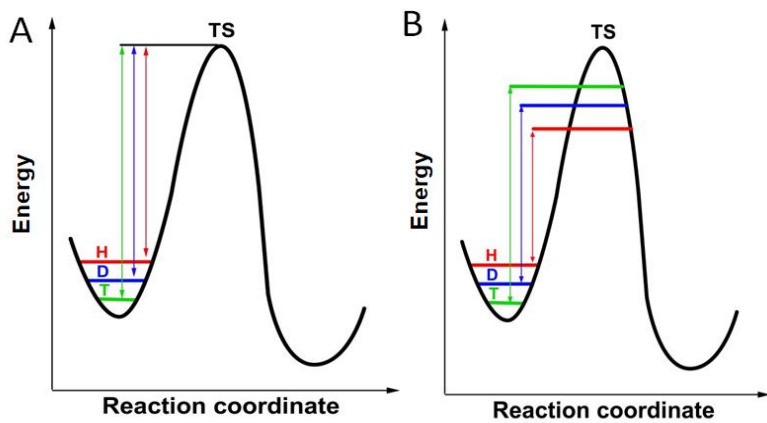


Figure 1.6. (A) Reaction profiles for hydrogen transfer. The origin of the semi-classical hydrogen isotope effect, arising from differences in the zero-point energy for protium, deuterium and tritium. (B) Illustration of the crossing of the barrier below the transition state, where this occurs in an isotope-dependent manner ($H > D > T$). (Adapted from reference 19,33)

In other words, a light isotope has higher zero-point energy and its probability function is less localized in its well (more diffuse wavefunction); thus, it has a higher tunnelling probability.³¹ Such association suggests that different hydrogen isotopes will have varying tunnelling probabilities, which can result in large KIE values.³¹

Using this approach, tunnelling contributions to chemical reactions were categorised based on the temperature-dependence of their rate constants and KIEs as well as the ratio of the Arrhenius pre-factor of the isotopes (A_l/A_h) (Figure 1.7).²⁸ Importantly, Figure 1.7 has been employed to characterise tunnelling in both solution and enzymatic reactions.¹⁶ However, tunnelling correction model is inadequate to explain the origin of temperature-independent KIE when each isotope exhibits temperature-dependent rates.²⁸ Consequently, current propositions are also aimed at revising this limitation.

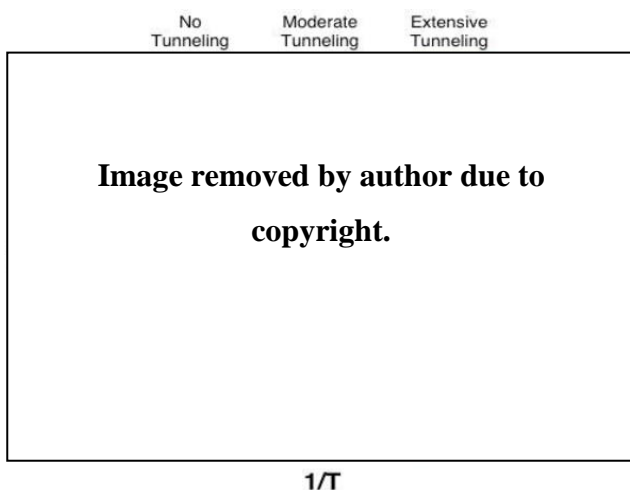


Figure 1.7. Arrhenius plot of rates (top panel) and KIEs (bottom panel, green line) of light (L , in blue) and heavy (H , in red) isotopes. In region I, tunnelling is negligible, so $A_L A_h$ is close to unity. Region II is the moderate tunnelling region where only the lighter isotope tunnels and the corresponding $A_L A_h$ is much smaller than unity. Both isotopes tunnelling region III, making the $A_L A_h$ much higher than unity (Adapted from reference 28).

1.2.2.1.3 Other modern models

Recent models that are employed to interpret the temperature-dependence of substrate KIEs are generally divided on whether protein dynamics contribute to the chemical step or not. Statistical protein motions are those in thermal equilibrium with the surrounding environment and encompass the majority of enzyme motions. On the other hand, non-statistical motions are not in equilibrium with the surrounding thermal environment.³⁴ In the dynamic-based models, non-equilibrium motions modulate the transition state, compress the width of the energy barrier and promote tunnelling.³⁵ These models generally utilise Marcus theory of electron transfer, which links tunnelling probabilities to distance between the donor and acceptor atoms.³⁶ These models are referred to as vibrationally enhanced tunnelling, rate-promoting vibrations, environmentally-coupled tunnelling and other similar propositions.^{30,37,38} For example, Scrutton and co-workers suggest that short-range dynamic motions of protein and solvents are coupled to the reaction coordinate.³⁷ While Schwartz hold a view that networks of long-range motions contribute to the chemical step and promote tunnelling,³⁸ Klinman and Kohen however, suggested that two types of protein motions might

be involved in influencing the chemical step.³⁹ The first which involves large-scale reorganisational motion brings the enzyme into a tunnelling-ready configuration or near-attack configuration. The second is referred to as “passive dynamics” or “gating motions” that actively compress the width of the energy barrier.³⁰

In contrast, other scientists emphasise that since tunnelling is not unique to enzymatic reactions, it is insufficient to account for enzyme’s rate enhancement.⁴⁰ Hence, they utilise modified-transition state theories to account for experimental findings.^{6,40} For instance, the work of Truhlar and co-workers introduced more quantum mechanical corrections such as zero-point energy, tunnelling and recrossing to the TST.⁴¹ Their approach, named ensemble average variational TST and multidimensional tunnelling model (EA-VTST/MT) has been employed to replicate and interpret several experimental observations.^{41,42} They propose that coupling of protein dynamics to the chemical coordinate have negligible effects on enzyme catalysis.⁴¹ Warshel and co-workers also disagree with the importance of protein dynamic effects and are of the opinion that protein motions result from the equilibrium of the potential energy surface.⁴⁰ In addition, the work of Allemand and co-workers investigated the role of electrostatic and dynamic contribution to enzyme catalysis using isotope effects of solvents, substrates and enzyme applied to dihydrofolates from diverse ecological niches as well as to alcohol dehydrogenase.⁷ Their results support that electrostatic preorganisation rather than protein dynamics play a vital role in the chemical transformations of enzyme-catalysed reactions.⁷

1.2.2.2 Enzyme KIEs

Enzyme KIE strategy involves isotopic substitution of non-exchangeable and natural abundance ¹H, ¹²C and ¹⁴N atoms in a “light” enzyme with heavier isotopes, ²H, ¹³C and ¹⁵N, to produce a “heavy” enzyme. According to Born-Oppenheimer approximation, decreased molecular vibrations in the heavy enzyme due to isotopic substitution would not affect the electrostatics of the reaction.⁴³ Hence, enzyme KIE is believed to measure the extent to which slow molecular vibration in the heavy enzyme limits the rate of the reaction. It is taken as the ratio of rate constants of the light to the heavy enzyme ($k^{\text{LE}}/k^{\text{HE}}$).⁴³ Values of enzyme KIEs

greater than unity suggest that protein dynamics are coupled to the kinetic step observed. And enzyme KIE of unity indicates the absence of contributions from non-equilibrium protein fluctuations.⁷ Consequently, enzyme KIE is employed to investigate the role of fast protein vibration in enzyme catalysis. Enzymes such as alcohol dehydrogenase, dihydrofolate reductases, HIV protease, alanine racemase, formate dehydrogenase, and others have all been examined using this approach.^{7,21,44–48}

1.2.3 Vibrational Stark effect (VSE) spectroscopy

Recently, VSE spectroscopy have also been employed to study protein dynamics by connecting conformational changes in enzymes to the electrostatic changes at their active sites.^{49–51} Vibrational Stark effect (VSE) reveal the influence of electric field on the vibrational frequency of a molecular probe. The linear frequency response of this probe to electrostatic perturbation arises from the difference in the dipole moment of the probe at the ground and excited states. Previously, insights into the complex nature of protein electrostatics typically depend on computational models and indirect techniques such as binding studies and pK_a shifts.⁵² But with VSE, electrostatic changes in macromolecules can be elucidated using direct infrared spectroscopic probes.^{53,54} A description of infrared spectroscopy, instrumentation and how they are applied to investigate electrostatic changes in protein are discussed below.

1.2.3.1 Infrared Spectroscopy

Infrared spectroscopy (IR) is an absorption technique that measures the frequency dependent transmittance of quantized infrared radiation through a sample. Each absorbed energy leads to vibrational transitions. The selection rule for infrared absorption is that the vibrational mode must lead to changes in the dipole moment of the molecule with displacement along its vibrational coordinate.⁵⁵ Molecular symmetry operation and point groups are required for understanding absorption of high-symmetry species but in the case of a protein, which has low-symmetry, the dipolar character of the absorbing molecule can be employed to provide qualitative interpretation of the vibrational modes.⁵⁶ The absorption of infrared light by diatomic molecules can be represented by Hooke's law (Eq. 1.8), which relate the vibrational

frequency of a normal mode directly to the force constant of the bond and inversely to the mass of the oscillators.⁵⁷

$$\nu_o = \frac{1}{2\pi} \sqrt{\frac{K}{\mu}} \quad (1.8)$$

where ν_o represents the vibrational frequency, K represents the force constant of the bond and μ is the reduced mass of the diatomic molecule. Hence, the vibrational frequency of molecules will be unique when composed of discrete atoms or different bond hybridizations.⁵⁷ The relative intensity of the absorption peak is proportional to the amount of absorbing species in the molecule according to Beer Lambert's law (Eq. 1.9).

$$I = I_o e^{-\varepsilon cl} \quad (1.9)$$

where I is the transmitted beam intensity, I_o represents the intensity of the incident beam, ε is the molar absorptivity coefficient which is unique for each vibration, c is sample concentration and l is the pathlength of the cell.⁵⁷ This can be rearranged by taking the natural logarithm of the equation to produce a linear relationship between the parameters.

Additionally, Hooke's law describes harmonic oscillations as a continuous diatomic vibration based on the assumption that vibrational energy levels are equally spaced by a factor of $h\nu$. However, interatomic forces are not perfectly harmonic, having both anharmonicities in the normal modes and anharmonic coupling between the modes (Figure 1.8).⁵⁸ Therefore, the Morse potential function described as an anharmonic correction (Eq. 1.10) accounts for quantum mechanical effects observed in vibrational spectroscopy such as coupling of vibrational modes at higher energy levels. These anharmonicities also lead to intramolecular energy redistribution, overtone, and combination mode absorption, vibrational solvatochromism, Fermi resonance, as well as contribute to VSE.⁵⁸

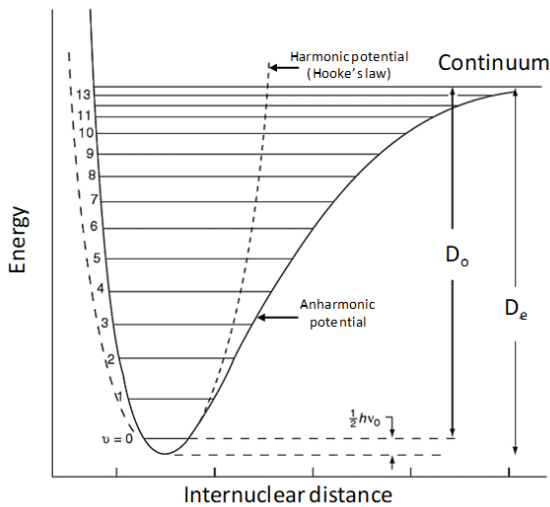


Figure 1.8. Potential energy curves for harmonic oscillator approximation (dotted) and anharmonic correction (solid).⁵⁸

$$V = D_e (1 - e^{-\beta q})^2 \quad (1.10)$$

D_e represents the well depth, β is the width of the potential well (the smaller β is, the larger the well) and q is the displacement of the atoms from equilibrium positions along the vibrational coordinate, which is the midpoint of the parabolic well.

1.2.3.2 Instrumentation

Infrared electromagnetic radiation is divided into three regions: near-infrared, mid-infrared and far-infrared. The region employed in the conventional analysis is the mid-infrared, which spans the frequency of 4000 to 650 cm⁻¹.

The two major spectrometers used to collect infrared spectra are dispersive and Fourier-transform infrared spectrometers (FTIR). In dispersive infrared spectrometer, the beam from the infrared source (often Nernst glower or globar rod) is simultaneously incident on the sample and reference sample to minimize the effects of water vapour and carbon dioxide, both of which absorb strongly in the mid-infrared region.⁵⁹ The beams are collimated by a monochromator and diffraction grating before it is passed to the detector.⁵⁹ However, in

contemporary spectrometers, a Michelson interferometer is utilized to simultaneously scan all the frequency of light projected onto the sample. In this case, the beam enters into the interferometer where a beam splitter divides the beam into two halves; one half is directed towards the moving mirror while the other is incident on a stationary mirror (Figure 1.9). A beam splitter is an optical device that splits an incident light beam into two or more beams that may or may not have the same optical power. In Michelson interferometer, the beams from the different mirrors recombine at the beam splitter before it is directed towards the sample. Due to the moving mirror, the recombined beam results in constructive or destructive interference that creates a path-dependent pattern called an interferogram.⁶⁰ The interferogram is then directed towards the sample and later to the detector. After digitization, the interferogram is sent to a computer that uses Fourier transforms to convert the path-dependent function to the frequency domain (spectrum).⁵⁷ The difference in the intensity of the radiation from the light source and the spectrum obtained after the sample's absorption gives the final spectrum.⁶⁰

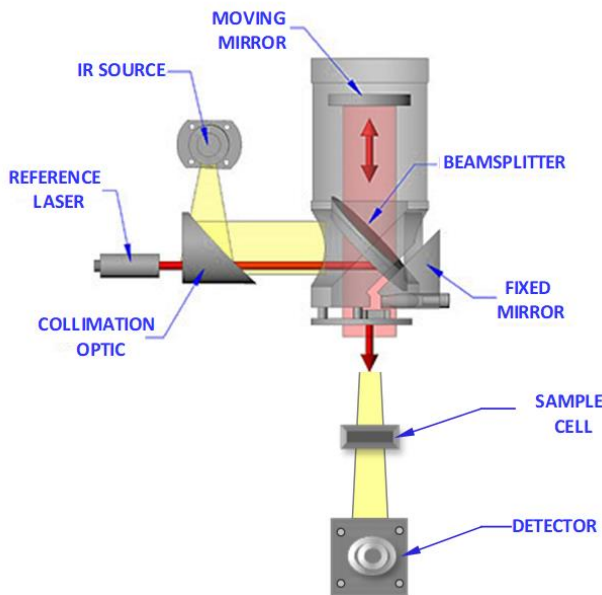


Figure 1.9. Representation of the beam paths within Michelson interferometer of Fourier Transform infrared (Adapted with modification from reference 61)

FTIR spectrometer has three advantages over the dispersive instrument. First, the multiplex (Fellgett) advantage results from the simultaneous measurement of all wavelengths of light in

FTIR instrument whereas dispersive setup records a single wavelength. As a result, FTIR spectrometers collect and average multiple scans in a very short amount of time compared to dispersive instrument.⁶⁰ The second is called throughput (Jacquinot) advantage. This refers to the higher signal-to-noise ratio of FTIR spectrum because the use of slit in dispersive instrument results in low throughput.⁶⁰ Finally, the wavelength (Connes) advantage arise from the use of internal reference (HeNe-helium-neon laser), leading to better wavelength resolution of FTIR.⁶⁰

The advantages of FTIR are associated with the Michelson interferometer, but the use of appropriate detectors for various sample types and applications can also offer significant benefits. The three main types of detectors used in FTIR spectroscopy are thermal, pyroelectric and photon detectors. Thermal detectors follow the temperature-dependent changes in the material that are converted to electrical outputs. This class of detectors are cost-effective, easy to use, and can operate at room temperature but they have lower sensitivity and response time.⁵⁷ Pyroelectric detectors are made from a single crystalline wafer of pyroelectric material. When a field is applied across the crystal, the charges become polarised and the temperature-dependence of their capacitance is thus converted to electrical outputs. An example of this is the deuterated triglycine sulfate (DTGS) used in conventional FTIR instruments. The last class is the photon detectors. These are made from semiconductors that create electrical outputs through changes in the electronic energy distribution of the material. Photon detectors have a fast response time and high sensitivity and are thus the most commonly used commercial detectors. However, they must be kept at cryogenic temperatures to reduce thermal noise.⁵⁷ Mercury cadmium telluride (MCT) represents an example of this type of detector, which is used to study mid- and near IR regions. Different detectors are needed for qualitative and quantitative analysis of infrared absorption. VSE spectroscopy as a quantitative technique requires highly sensitive detectors to accurately determine the vibrational shifts of the infrared probes, which are then correlated with electrostatic changes in macromolecules.

1.2.3.3 Electrostatics interactions and VSE spectroscopy

The role of electrostatic interactions has been recognised in biomolecular processes, in signal transduction, protein folding, enzyme-ligand binding and conformational changes.^{62,63} During enzyme catalysis, enzyme-ligand and enzyme-solvent interactions are reorganised to accommodate and stabilise reaction intermediates, which might involve charge separation, charge transfer, proton exchange, bond polarization or changes in ligand structures. The elucidation of electrostatic forces in proteins and nucleic acids are advanced by the work of Boxer and co-workers.^{52,64–68} Importantly, they noted that the insertion of infrared probes into macromolecules can report local electrostatic changes in them.^{51,69,70}

Charged particles create electric fields in the space surrounding them. Because electric field is vector quantity, the principle of superposition allows for the combination of two or more electric fields. Hence, resultant electrostatic forces observed in protein are a vector sum of the electric field of individual charges.⁷¹

To apply VSE to study electrostatic changes in macromolecules, the infrared probe must be characterised by its sensitivity to electric fields. Two approaches developed by Boxer and co-workers to calibrate the sensitivity of the probe involve direct application of electric field and solvent field to characterise the Stark shifts. In the first strategy called electrochromism, the probe is immobilised between a frozen glass of polymer films before a voltage corresponding to about 1 MV/cm of electric field is applied directly to the capacitor containing the polymer.⁵² Spectral difference between the electric field of the ‘off’ and ‘on’ state relates to the vibrational dipole difference experienced by the probe.⁵²

In the second approach, the probe is dissolved in solvents of different polarities, which exerts an electric field (the solvent reaction field) depending on the size of the probe’s dipole moment. The solvent reaction field results in vibrational frequency shifts (solvatochromism), which can be characterised by dielectric constants or other empirical polarity scales such as E_T (30) and pi scale.⁷²

The sensitivity of infrared probes such as azides, carbon-deuterium bonds, nitriles, carbonyls and phosphates to electric fields have been reported in previous studies.^{49,66,73–75} Once the probe is calibrated, it can be inserted to report local electrostatic changes between two states of a protein as a result of vibrational frequency shift in their infrared absorptions.⁶⁵ The relationship between vibrational frequency shift and the local electric field experienced by the probe in the system can be written as

$$hc\Delta\nu_{obs} = -\Delta\vec{\mu}_{probe} \cdot \Delta\vec{F}_{protein} = -|\Delta\vec{\mu}_{probe}| |\Delta\vec{F}_{protein}| \cos \theta \quad (1.11)$$

where h is Planck's constant; c the speed of light, $\Delta\vec{\mu}_{probe}$ is the difference in dipole moment between the ground and excited states expressed as linear Stark tuning rate ($\text{cm}^{-1}/(\text{MV}/\text{cm})$,

$\Delta\vec{F}_{protein}$ is the local electric field change experienced by the probe in the protein (in MV/cm),

$\Delta\nu_{obs}$ is the vibrational frequency shift (cm^{-1}) and θ is the angle between the vectors defined by

$\Delta\vec{\mu}$ and $\Delta\vec{F}$.⁶⁵ Electric field is a vector quantity; hence, the absolute direction of the probe must be determined by crystal structure or molecular dynamics (MD) simulations.⁷⁶

Nitrile probes are preferred for VSE spectroscopy because they have higher extinction coefficient, absorb in the uncrowded region of macromolecules ($2100 – 2240 \text{ cm}^{-1}$) and can be incorporated readily into proteins by genetic code expansion or via post-translational modification of cysteine side chains.⁵³ However, nitrile probes often deviate from the Stark model when they are involved in direct hydrogen bonding. Hence, a tandem technique, which plots the infrared frequencies and NMR chemical shifts of the probe in different protic and aprotic solvents was introduced to decompose such deviation.⁷⁷ An alternative method developed by Romesberg measures Stark shifts as a function of temperature and their degree of deviation in different solvents.⁷⁸ In both approaches, aprotic solvents give linear plots distinct from when the probe is hydrogen bonded. Recently, Webb and co-workers have shown that nitrile probes can retain electrostatic sensitivity even when they participate in hydrogen bonding.^{79,80}

Since its development, VSE has been applied to investigate electric field changes in enzymes bound to different inhibitors.⁷⁰ It was also used to measure the solvent accessibility of membrane proteins.⁸¹ In one report on ketosteroid isomerase, nitrile probes were employed to report the extremely large electric field imposed on the substrate by the active site of the enzyme.⁸² Comparison between different variants of the enzyme suggests that electric fields at the active site of the enzyme correlated with catalytic rate enhancement.⁸² Another enzyme investigated extensively with this technique is DHFR from *Escherichia coli* (EcDHFR) using nitrile and carbon-deuterium probes.^{49–51}

1.3 Dihydrofolate reductase (DHFR)

DHFR has long been used as a paradigm to investigate the mechanism of enzymatic rate enhancements. DHFR catalyse the transfer of the *pro*-R hydride from the C₄ of NADPH to C₆ of 7,8-dihydrofolate (DHF) and the protonation of N₅ to give 5,6,7,8-tetrahydrofolate (THF) and NADP⁺ (Figure 1.10). Earlier studies have shown that some DHFRs follow a stepwise mechanism where the substrate is protonated before the hydride transfer step, but concerted steps were also observed in other DHFRs.⁸³ This concerted mechanism is native to TmDHFR catalysis at neutral pH but occurs only in EcDHFR when the reaction is carried out at high pH (~pH 9.0).⁸³

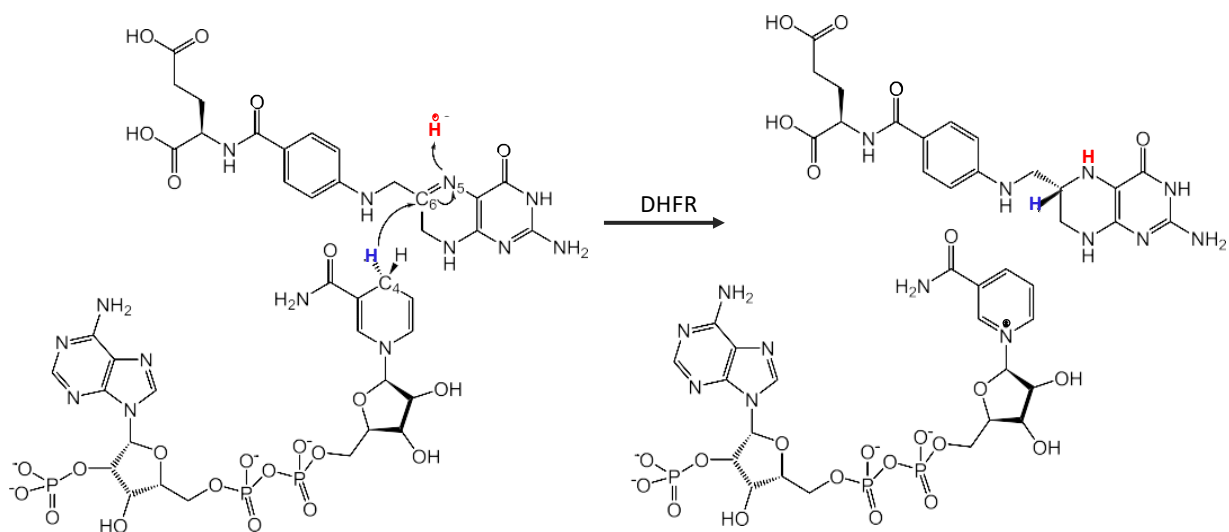


Figure 1.10. The reaction catalysed by DHFR showing the transfer of a hydride from C₄ of the cofactor (NADPH) to the C₆ of the substrate (DHF) to produce THF and NADP⁺.

The product from this reaction (THF) is utilised by the cell as a one-carbon carrier in the cycle that produces DNA nucleoside and other important amino acids such as serine and glycine (Figure 1.11).^{84,85} The dependence of cellular function on THF makes DHFR a potential drug target. Thus, inhibitors of the enzyme such as methotrexate (MTX), trimethoprim and pyrimethamine are used in the treatment of cancer, bacterial infection, malaria and autoimmune diseases.⁸⁶

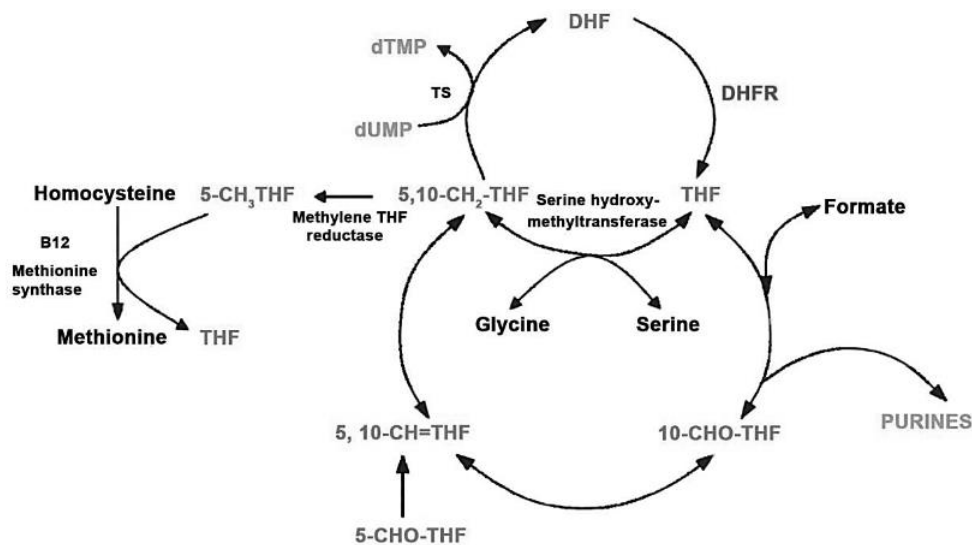


Figure 1.11. A selection of biological reactions that use different THF derivatives as a cofactor during one-carbon transfer reactions. THF is converted to 5,10-methylene-THF. The 5,10- methylene-THF is then converted to 5-methyl-THF by reduction with NADPH. The methyl group is in turn transferred to homocysteine generating methionine in the presence of cobalamin (Vit B12). The 5,10-methylene-THF is also used in the presence of thymidylate synthase (TS) to methylate the pyrimidine base uracil in deoxyuridine monophosphate (dUMP) to thymine to produce deoxythymidine monophosphate (dTMP) which is essential for DNA synthesis. 5,10-methylene-THF and 5-formyl-THF can be converted into 5,10-methenyl-THF, which is in turn converted to 10- formyl-THF, which acts as a cofactor during purine biosynthesis. (Adapted from reference 84 and 85).

The simplicity of the reaction catalysed by DHFRs and their relatively small size (159–170 amino residues) are a few reasons why they are attractive for enzymology studies. Another crucial motive for employing DHFRs is the extensive protein motion observed in EcDHFR.

1.3.1 Structural characterisation of DHFRs

All the chromosomally encoded DHFRs adopt similar secondary and tertiary structural arrangements.⁸⁷ Generally, DHFRs consists of four α -helices, eight β -sheets and three structural subdomains that surround the active site cleft (Figure 1.12A).⁸⁷ The β -sheets are all parallel with the exception of the anti-parallel β H at the C-terminal of the protein. The α -helices are named by their proximity to the β -sheets. Using EcDHFR as a template, their

subdomains can be divided into three: the cofactor binding domain (CBD) (residues 38-88) where the adenosine moiety of NADP(H) binds, the substrate binding domain (SBD) (residues 23-37) where DHF binds to the enzyme and the loop domain (LD).⁸⁸ The loop domain forms approximately 40-50% of the major subdomains and is dominated by a set of three loops on the ligand binding face that surround the active site, the M20 (residue 9-23), FG (residues 116 – 132) and GH (residues 142 – 149) loops (Figure 1.12B).⁸⁹

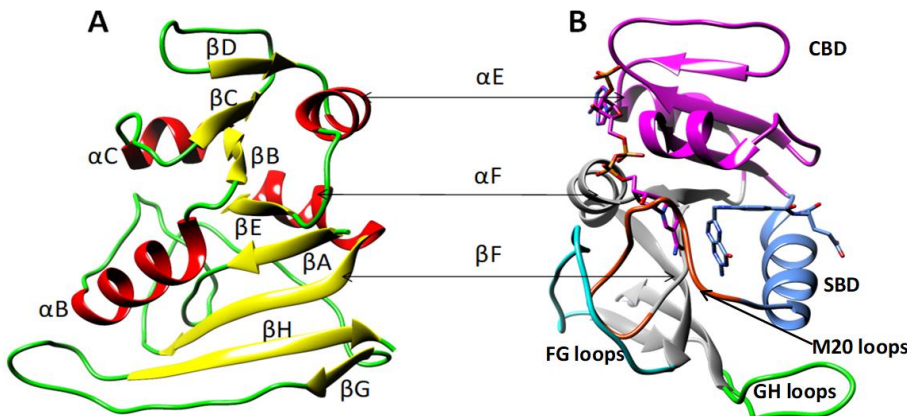


Figure 1.12. (A) Cartoon representation of EcDHFR (PDB 1RX2) showing the secondary structural elements; α -helices (red), β -strands (yellow) and connecting loops (green). (B) The structural domain rotated by $\sim 90^\circ$ and showing the cofactor binding domain (purple), the substrate domain (blue) and the three-active loops: M20 (orange), FG (cyan) and GH (green). The ligands are also shown with colours corresponding to their domains.

This general description fits EcDHFR, but other homologs have slight structural modifications. For example, DHFR obtained from *Geobacillus stearothermophilus* bacterium that thrives at 60°C (BsDHFR) is structurally well-aligned with EcDHFR except at αE (Figure 1.13A). Because this α -helix is in the cofactor binding domain, the affinity of the enzyme for the cofactor is lesser than those of other homologs.⁹⁰ Similarly, DHFR isolated from *Thermatoga maritima* bacterium that survives at 80°C (TmDHFR), forms a quaternary homomeric structure.⁹¹ This enzyme has an extra β -sheet, which participates in the dimer interface along with its loop domain (M20, FG and GH loops). The dimerisation contributed to its thermostability with melting temperature (T_m) of 82°C (Figure 1.13B).^{91,92}

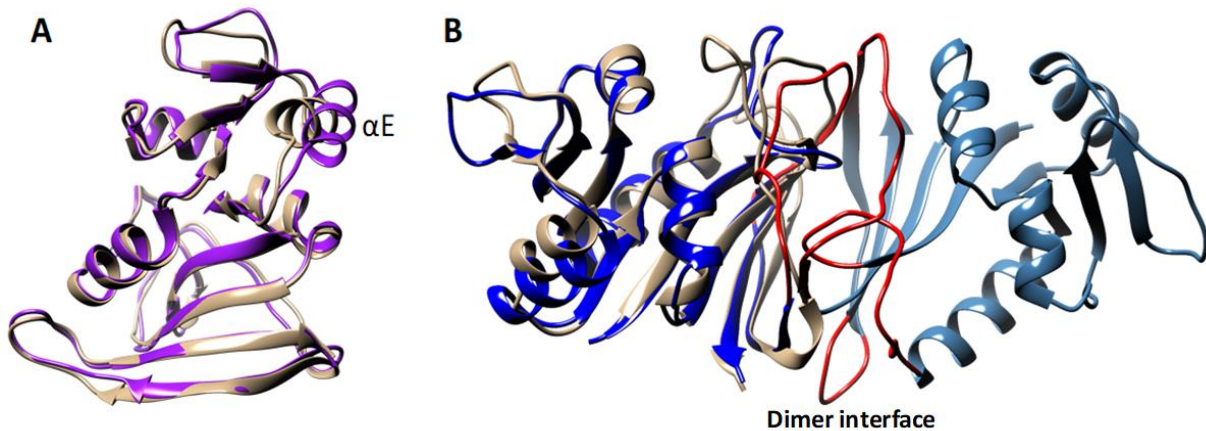


Figure 1.13. Structural overlay of (A) EcDHFR in brown (PDB: 1RX2) and BsDHFR in purple (PDB: 1ZDR) indicating the difference in the α E helix. (B) EcDHFR in brown (PDB: 1RX2) and TmDHFR in blue and sky blue (1D1G). The domains participating in the dimer interface is shown as red.

Besides the extra β -sheet extension of TmDHFR, HsDHFR also has three functional phylogenetic extensions relative to EcDHFR (G51PEKN, L28F and N23PP) (Figure 1.14A).⁹³ These extensions were reported to be common to vertebrate DHFRs⁹³ and are thought to influence their ligand interaction and kinetic character.^{12,94} For example, weak inhibition of HsDHFR by trimethoprim was associated with the extension region, but studies showed that the extensions only alter the affinity of the enzyme for NADP⁺ with no effect on trimethoprim's inhibition.⁹⁴ In addition, this difference is believed to dictate their catalytic cycle (Figure 1.14B).^{95,96}

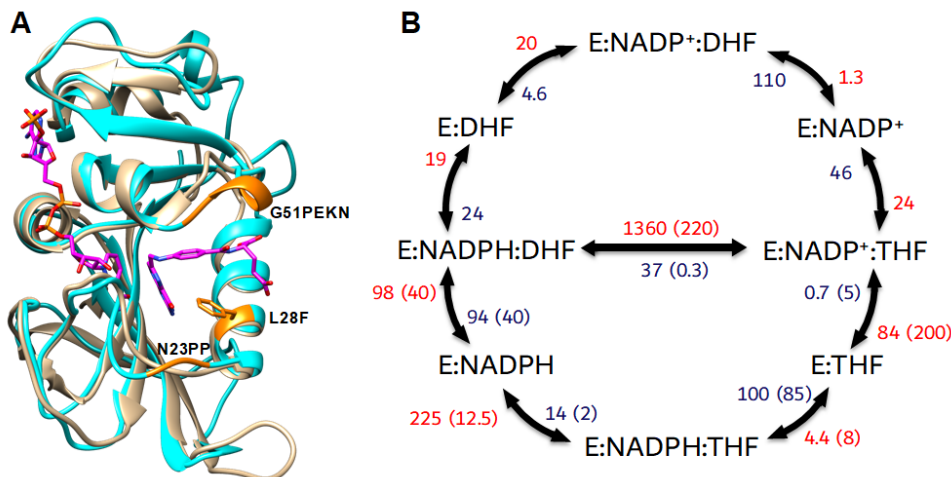


Figure 1.14. (A) Structural overlay of EcDHFR (brown, PDB: 3QL3) and HsDHFR (cyan, PDB: 4M6K) bound to ligands (FOL and NADP⁺ in purple). Extension sequence identified in phylogenetic analysis as orange in HsDHFR.⁹⁴ (B) The catalytic rate of HsDHFR and EcDHFR (in parenthesis). Rate constants are written as clockwise (red) and anticlockwise (blue). The lower half of the catalytic cycle represents the major kinetic path of EcDHFR while HsDHFR follows the full cycle. First and second-rate constants are given in the unit of s^{-1} and $\mu M s^{-1}$ respectively. (Adapted from reference 95 and 96).

In EcDHFR, the turnover rate is limited by the release of THF, but in the case of HsDHFR, both THF and NADP⁺ can be released from the active site leading to complex kinetics.⁹⁷ These sequence extensions also influenced diversity in the flexibility of vertebrate DHFRs in comparison to their bacterial counterparts.⁹⁸

1.3.2 Protein motions in DHFRs

Extensive structural studies of EcDHFR bound to different ligands have identified ligand-dependent conformational changes in the enzyme.⁹⁹ These conformational transitions involve structural and spatial changes in the M20 loop. In the apo form (the unliganded state), the M20 loop of EcDHFR adopts an open conformation where the substrate binding cleft widens and the nicotinamide binding site opens by $\sim 8 \text{ \AA}$.⁹⁹ But in the holoenzyme (enzyme/NADPH) and Michaelis complex (enzyme/NADPH/substrate), the loop assumes a closed conformation where it folds over the active site. A short anti-parallel sheet formed by the central residues of

the loop in this conformation seals the active site and forms hydrogen bonding interactions with Asp122 in the FG loop (Figure 1.15B). In the remaining steps of the catalytic cycle, the M20 loop remains in the occluded conformation after switching upon hydride transfer. To stabilise this state, the M20 loop forms hydrogen bonding interaction with Ser148 of the GH loop. Also, the central region of the M20 loop protrudes into the active site and prohibits the binding of the nicotinamide-ribose moiety (Figure 1.15C).⁹⁹ Although a disordered conformation was noted in their report, this configuration was suggested to be an intermediate between the other conformations.⁹⁹ These loop movements were also observed in subsequent NMR investigation.^{88,100,101}

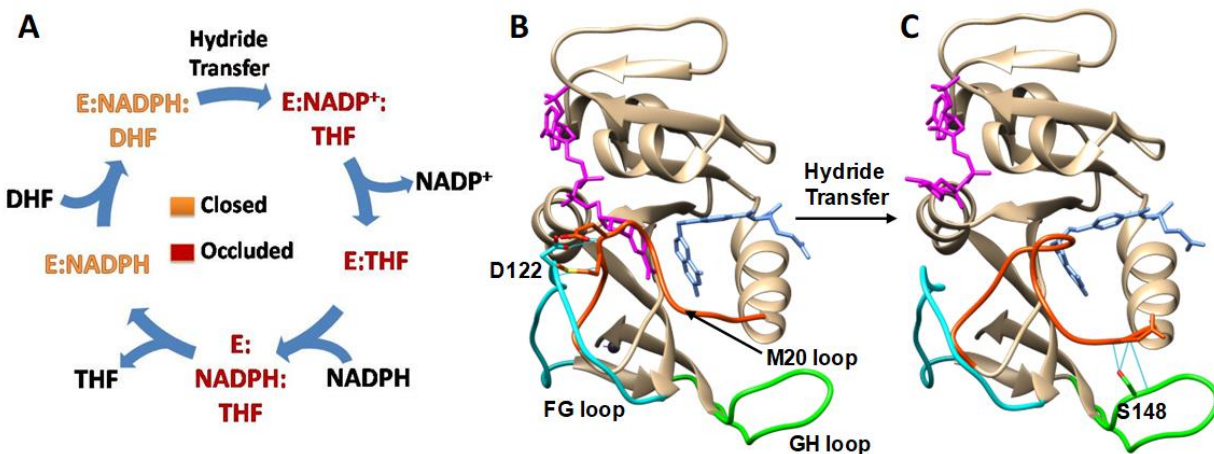


Figure 1.15. (A) The catalytic cycle of EcDHFR showing the conformations adopted along with it. Crystal structure of EcDHFR showing (B) the closed conformation (PDB: 1RX2) and the hydrogen bonding interaction with D122 of the FG loop (C) the occluded conformation (PDB: 1RX6) and stabilising interaction with S148 of the GH loop.

In the same manner, DHFRs from other organisms were studied by X-ray crystallography and NMR techniques.^{92,93,102,103} Both MpDHFR and TmDHFR were reported to also adopt the open conformation.^{92,102,104} Though MpDHFR only assume this conformation when in the apo form,¹⁰⁴ TmDHFR maintains an open conformation throughout its catalytic cycle because its loop domain is locked in the dimer interface.^{92,102} In most DHFRs however, the M20 loop remained closed over the active site in most of their complexes to shield the reactants from the solvent.⁹⁹ The closed conformation is thought to be crucial for DHFR catalysis because it

places an active site Asp/Glu 27-30 (depending on the source organism of the enzyme) at a relative distance where it is believed to coordinate water molecule that protonates the substrate (DHF).^{87,105} This interaction possibly modulate the pK_a of the substrate and facilitates hydride transfer.¹⁰⁵

The resistance of DHFRs to antifolate-inhibitors also propelled scientific investigation of DHFRs. For example, mutation of L22, F31 and F34 in HsDHFR were identified to confer methotrexate resistance to the enzyme.^{106–108} The quest to improve upon current inhibitors contributed to the necessity of understanding the enzymes transition state structure. Although the complex of methotrexate with NADPH is said to mimic the transition state structure, methotrexate binds DHFRs in a different orientation to those observed with 4-oxo-folate derivatives (FOL, DHF and THF).⁸⁷ This is because the pteridine ring of MTX is flipped at C₆-C₉ bond by 180°; thus, place the *pro*-R hydride of the cofactor in proximity to the *si*-face of the inhibitor. Trimethoprim is another inhibitor mentioned earlier that selectively inhibit bacterial DHFRs without adverse effects on humans due to its weak binding to human DHFR.¹⁰⁷ Hence, it is commonly used in the treatment of bacterial infections.⁸⁶

1.4 Investigation of protein dynamic effects in DHFRs

Studies of DHFRs adapted to different temperatures are crucial to understanding how protein dynamics influence their chemical step.^{109–117} A review of selected experimental findings that support and oppose the importance of protein dynamics are presented below.

1.4.1 Kinetic characterisation and flexibility studies

Notably, most investigations are focused on EcDHFR due to the substantial movement in its loop domain during catalysis.^{12,118} To probe the relevance of this motion, site-directed mutagenesis was employed to change residues in the different loops. When residues at the centre of the M20 loop (residue 16-19) were mutated to Gly, hydride transfer rate constant of the variant was reduced by 500-folds relative to the wild-type.¹¹⁹ NMR study of the same variant later showed that cross-peak conformation averaging spotted in the spectra of the wild-type apoenzyme was absent from that of the variant.¹²⁰

Another experiment mutated Gly121 in the FG loop to other amino acid residues to destabilise the closed conformation.¹²¹ NMR studies have previously shown that the Gly121 undergoes large-amplitude motion on the nanoseconds timescale.^{89,121} These mutations were reported to alter hydride transfer rate constant. The authors alleged that long-range motion of the distal residue, which was about 19 Å from the active site, was essential for the chemical step.¹²¹ However, thermal unfolding experiment of G121V variant revealed that the 160-fold reduction in its hydride transfer rate constant was due to a trapped intermediate structure.¹²²

The evolutionary differences in the primary sequence of prokaryotic and eukaryotic DHFRs were also employed to mutate residues in the M20 and GH loops of EcDHFR (N23PP/S148A).²⁵ The low hydride transfer rate constant of this variant was explained to result from a ‘knockout’ of dynamic motions.²⁵ However, the work of Allemann and co-workers on the variant revealed that the observed effect resulted from increased fluctuation at the transition state of the variant despite reduced structural flexibility.^{123,124} This suggests that lack of flexibility on one timescale might not indicate the absence of motion on other timescales. In fact, when a mutation that favoured the adoption of the occluded conformation was introduced into the GH loop of MpDHFR (P150S), hydride transfer rate was not affected.¹¹⁷

Protein dynamics are heterogeneous in both bacterial and vertebrate DHFRs. Other flexibility studies using H-D exchange experiment revealed a faster isotopic exchange of the amide proton of MpDHFR and BsDHFR relative to EcDHFR.^{125,126} Solution NMR report using residue-specific isotopic labelling of Trp and Met showed that TmDHFR has lower dynamic fluctuations along its catalytic cycle compared to the other homologs.¹⁰⁰ The lack of flexibility in the loop domain of TmDHFR, due to their dimer interface association, was thought to impact its low catalytic rate. However, a monomeric version of the enzyme did not show improved catalytic function.⁹²

Vertebrate DHFRs are known to exhibit different dynamic flexibilities compared to their bacterial counterparts.⁹⁹ Backbone and side chain averaging in HsDHFR was reported to have a lower amplitude than that of EcDHFR.¹²⁷ Unlike loop motions in EcDHFR, an aromatic

active site residue in vertebrate DHFRs was reported to change conformations depending on the ligand bound, particularly in HsDHFR and chicken DHFR.¹²⁸ This motion has been implicated in the kinetic complexity of vertebrate DHFRs.¹²⁹

Complexity, as well as protein instability, has particularly discouraged detailed characterisation of HsDHFR's kinetics.¹³⁰ Kinetics of HsDHFR and other vertebrate enzymes showed that their substrate KIEs were lesser than those of their bacterial counterparts.¹²⁹ In addition, apo-HsDHFR could not be isolated without significant aggregation due to structural instability in the absence of a ligand.^{131,132} Consequently, most investigation of protein dynamics and how it influences hydride transfer in DHFRs have focussed on bacterial homologs.

1.4.2 KIEs studies

As earlier mentioned, the effect of protein dynamics on the chemical step of DHFRs can be investigated using the temperature-dependence of KIEs. These results are complicated by inconsistent observations. Studies have shown that many DHFRs exhibited temperature-dependent substrate KIE under pre-steady-state kinetic measurements, which indicate that H-tunnelling contribute to their catalysed reaction.^{133–135} However, different temperature-dependence of substrate KIEs are observed when the pH is changed.^{126,136} For example, substrate KIE in EcDHFR showed a mild temperature-dependence at pH 9.0 but showed biphasic temperature-dependence at pH 9.5. In this case, substrate KIE was temperature-independent above 15 °C, but at lower temperatures, the substrate KIE becomes strongly temperature-dependent.^{113,134}

Because co-solvent changes the physical properties of the reaction by modifying the dielectric constant and viscosity of the medium, their effect on DHFR's catalysis was also examined. Reduction in the dielectric constant will strengthen hydrogen bonding within an enzyme, making it less flexible and increased viscosities would also slow protein motions.^{126,137} Overall, solvent studies of EcDHFR, MpDHFR, BsDHFR and TmDHFR revealed that hydride transfers were insensitive to solvent viscosities but are changed in relation to the dielectric

constant of the solvent mixture.^{39,90,126,137} This indicates that electrostatics rather than protein motion plays a major role in the catalysis of DHFRs.⁷

Nevertheless, these reports could not rule out the importance of fast protein vibrations to DHFR catalysis, which can be elucidated by enzyme KIE measurements. Pre-steady-state kinetics of EcDHFR showed a slight increase in enzyme KIE from 0.93 (10 °C) to 1.18 (40 °C).^{114,138} In other investigations, the cold-adapted MpDHFR⁴⁵ and the moderately thermophilic BsDHFR¹¹⁶ showed enzyme KIEs near unity at their physiological temperatures but exhibit increased enzyme KIEs at non-physiological temperatures.^{45,116} To complement these studies, computational analyses confirmed that when DHFR's performance is hampered by mutations or change in temperature, additional recrossing events on the dividing surface of the energy barrier may occur.^{45,114,123} Based on these observations, the coupling of protein vibrations to hydride transfer appears to happen under unfavourable conditions.^{7,45}

1.4.3 VSE spectroscopic investigations

Apart from KIEs, VSE spectroscopy has also been employed to investigate protein dynamics in enzymes. Carbon-deuterium bond was introduced into EcDHFR by selective deuterium labelling of specific Met residues in the enzyme while the other Met(s) are replaced with Leu.⁴⁹ But the interpretation of the absorption line shapes was non-trivial.⁴⁹ In a different report, non-canonical deuterated tyrosines were incorporated via genetic code expansion at position 100 and 111 to probe electrostatic changes of EcDHFR.⁵⁰ This is because Tyr100 is implicated to form direct contact with the nicotinamide hydride donor and was thought to stabilise the developing charge on the cofactor at the transition state.⁵⁰ The two analyses suggested that the catalytic cycle of EcDHFR is both electrostatically and dynamically heterogeneous.

A recent investigation applied a combined VSE spectroscopy and computational analysis to probe the relationship between protein dynamics and electrostatic changes in EcDHFR.⁵¹ This work employed a site-specific cysteine labelling to insert a nitrile probe at the active site.⁵¹ Experimental infrared spectroscopic characterizations showed that electrostatics at the active site changed dramatically depending on the bound ligand.⁵¹ Further detailed analysis was

obtained with mixed quantum mechanics/molecular mechanics (QM/MM), which identified residues that caused the observed electrostatic change.⁵¹ To this end, the authors suggested that the enzymes motions play a significant role in facilitating hydride transfer.^{15,51}

Previous investigations of dynamics at the microenvironment of DHFRs using VSE spectroscopy were conducted solely with EcDHFR. Therefore, the application of VSE spectroscopy to other homologs of DHFR is important to reveal the link between electrostatic changes and conformational transitions.

1.4.4 Project Aims

The aim of my project is subdivided into the following objectives and analysed in each chapter.

The first is, to optimise the isolation of HsDHFR and reduce purification-associated kinetic complexity. HsDHFR is an enzyme of interest for the study of protein dynamics but the instability of the enzyme under different purification conditions have stalled its characterisation for several decades. To overcome this, binding of folate to the enzyme has been shown to enhance protein stability. However, folate is a substrate for HsDHFR and form inhibitory complex that prevents ideal kinetic investigation. Hence, we explored and reported new strategies to produce a stable enzyme that is viable for kinetic studies.

To determine the effects of protein dynamics on the chemical step of HsDHFR using KIE techniques. Steady and pre-steady-state kinetics of HsDHFR have been reported to be unusual because measured rate constants were isotope insensitive under different conditions. As a result, the chemical step of the enzyme could not be measured reliably. We hereby report techniques to reveal the chemical step of HsDHFR and probe how protein dynamics influenced it.

Lastly, to elucidate the relationship between conformation and electrostatic changes in DHFRs. Previous studies have focussed on EcDHFR; here we investigated electrostatic changes in DHFRs such as EcDHFR, BsDHFR, MpDHFR, and TmDHFR using vibrational Stark effects (VSE) spectroscopy.



2 . Optimised isolation of stable human dihydrofolate reductase for kinetic investigation

2.1 Preface

The reaction catalysed by human DHFR (HsDHFR) has been a target for cancer treatment for several decades. Consequently, the enzyme is often crystallised with different potential lead compounds being tested for inhibition. However, characterisation of HsDHFR is still associated with significant difficulties, especially regarding enzyme purity and stability. First, HsDHFR copurifies with an unidentified 28.9 kDa protein as well as an endogenous ligand (NADPH/NADP⁺) when produced in *E. coli*.¹³⁹ Hence, accurate rate constant could not be measured without subjecting the enzyme to several chromatographic steps. In addition, the apoenzyme is also unstable and often aggregates during purification.^{131,132,139} Last, kinetic analysis of HsDHFR exhibits a complex kinetic time course under both steady and pre-steady state measurements.⁹⁶ Hence, for the last three decades, works on HsDHFR has been stalled because of these challenges.

Previous purification approach to remove bound impurities lead to a poor yield of stable enzyme.¹³⁹ In the proposed method, an extra purification step using High-Performance Liquid Chromatography (HPLC) was introduced to produce an enzyme that is free of protein and ligand impurities.¹³⁹ However, this step involves unfolding the enzyme. Since apo-HsDHFR is unstable, the refolding step leads to 80% loss of enzyme yield, except when refolded in the presence of folate or folate and cofactor.¹³⁹ Even when the two ligands are bound, about 20% of the enzyme still aggregates.

The next challenge is the kinetic study of folate-bound HsDHFR. Because the enzyme is unstable when produced in *E. coli* host,^{130,140,141} the method recommended to overcome this challenge is purification of the enzyme with folate to enhance stability.¹³⁹ The problem with the use of folate in HsDHFR's purification is that both folate, as well as dihydrofolate (DHF), can be reduced by the enzyme and both are bound with similar affinities.⁹⁶ Consequently, kinetic assays of folate-bound HsDHFR can be difficult to isolate when NADPH and DHF are

added to the reaction mixture. This is because simultaneous reduction of both folate and DHF may be observed leading to complex kinetic rates.

Finally, even in the absence of ligand impurities, HsDHFR has been reported to exhibit complex kinetics under steady and pre-steady-state measurements.⁹⁶ Consequently, the absolute rate constant of hydride transfer in the enzyme has not been measured for decades.^{96,129}

To resolve these challenges, an alternative approach to removing the bound 28.9 kDa protein impurity was developed without the loss of protein yield. In addition, a different ligand that is not a substrate for HsDHFR was identified and employed to enhance its stability. This strategy significantly reduced the complexity observed during pre-steady state measurements, which afforded the determination of its hydride transfer rate constant. This chapter will focus on the identification of the protein impurity and the discovery of a new stabilising ligand for HsDHFR while the pre-steady and steady-state measurement of HsDHFR will be discussed later in Chapter 3.

2.2 Identification of protein impurity and gene cloning

Mass spectrometric sequence analysis was employed to elucidate the identity of the tightly bound 28.9 kDa protein impurity. The initial experiment carried out by Dr Luk L. and Williams T. comprises the isolation of the protein by HPLC, treatment of the impurity with trypsin for 2 hrs at 37 °C and analysing the fragments by MS (See Appendix I, Figure A1, A2 and A3,). Trypsin is a protease that cleaves protein/peptide chains mainly at the carboxyl side of the amino acid of lysine or arginine to give unique fragmentation pattern that can be correlated to the parent protein or peptide. The fragments identified here were searched within the protein sequence library and found to align with 80% of TEM-1 β-lactamase as shown below (The signal sequence cleaved *in vivo* is shown in green). In addition, ampicillin was hydrolysed when incubated with the protein and monitored by LC/MS over 24-hours (Figure 2.1)

TEM-1-BLAC	1 MSIQHFRVALIPFFAAFCLPVFAHPETLVVKVDAEDQLGARVGYIELDLN	50
MS-MS FRAG	1 -----HPETLVK-----VGYIELDLN	16
TEM-1-BLAC	51 SGKILESFRPEERFPMMSTFKVLLCGAVLSRIDAGQEQLGRRIHYSQNDL	100
MS-MS FRAG	17 SGKILESFRPEERFPMMSTFKVLLCGAVLSRIDAGQEQLG-RIHYSQNDL	65
TEM-1-BLAC	101 VEYSPVTEKHLTDGMTVRELC SAAITMSDNTAANLLLTTIGGPKE LTAF	150
MS-MS FRAG	66 VEYSPVTEKHLTDGMTVR-----ELTAFL	89
TEM-1-BLAC	151 HNMGDHVTRLDRWEPELNEAIPNDERDTMPAAMATTLRKLLTGELLTLA	200
MS-MS FRAG	90 HNMGDHVT---RWEPELNEAIPNDERDTMPAAMATTLR-LLTGELLTLA	135
TEM-1-BLAC	201 SRQQLIDWMEADKVAGPLRSALPAGWFIADKSGAGERGSRGIIAALGPD	250
MS-MS FRAG	136 SRQQLIDWMEADKVAGPLRSALPAGWFIADKSGAGE---RGIIAALGPD	182
TEM-1-BLAC	251 GKPSRIVVIYTTGSQATMDERNQIAEIGASLIKHW	286
MS-MS FRAG	183 GKPSRIVVIYTTGSQATMDE--RQIAEIGASLIK--	214

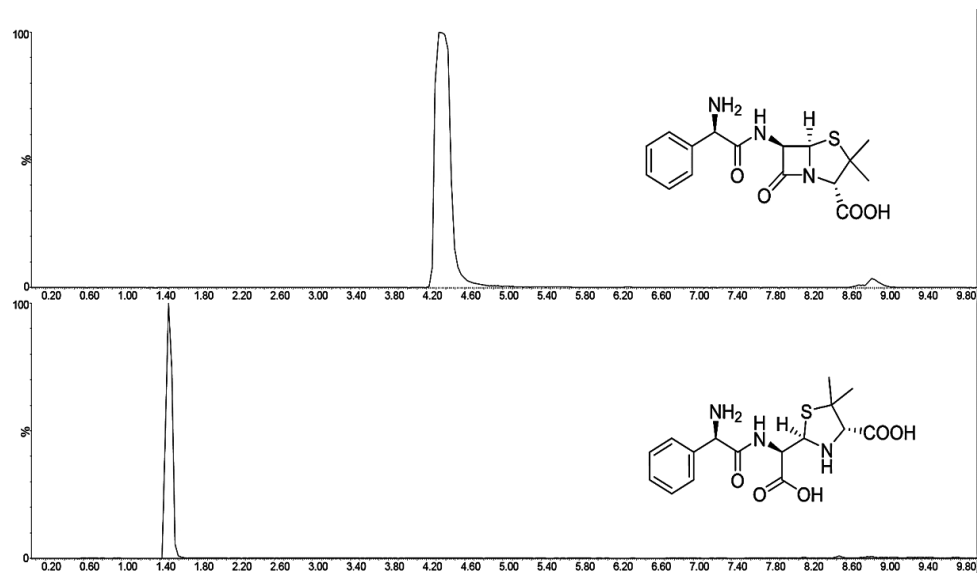


Figure 2.1. LC trace of ampicillin hydrolysis by the isolated 28.9 kDa protein (TEM-1 β -lactamase). (Obtained from Dr Luk L. and Williams T.)

The source of TEM-1 β -lactamase was identified to eliminate the interaction with HsDHFR. It was reasoned that since HsDHFR was produced in a pET-21 plasmid vector, which codes for TEM-1 β -lactamase, the likely origin of TEM-1 β -lactamase would be the plasmid vector (TEM-1 β -lactamase yields resistance to ampicillin antibiotic and helps bacterial cells to retain recombinant plasmids during growth). To remove the strong association of the enzymes, the gene encoding HsDHFR was excised from the pET-21 plasmid vector using restriction enzymes (NdeI and BamHI) that flanked the 5' and 3' ends. This fragment was ligated into pET-28 digested with the same enzymes. As this reading frame gave an unwanted N-terminal His-tag and thrombin cleavage coding sequence, primers were designed to delete them. Figure 2.2 shows the scheme used for the gene cloning. Interestingly, the expression of HsDHFR gene in the kanamycin vector resulted in a protein that is free of the tightly bound β -lactamase.

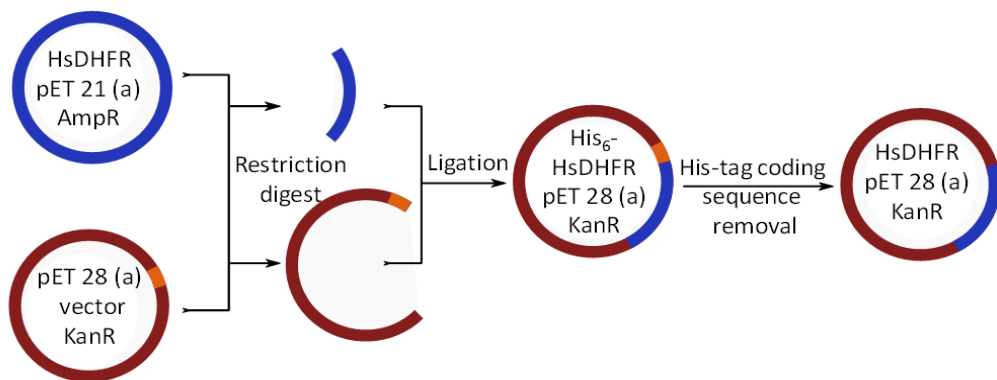


Figure 2.2. Schematic diagram showing sub-cloning of HsDHFR gene and the step of His-tag coding sequence removal. Blue circle and arc show pET 21(a) and HsDHFR gene, respectively. The brown circle and arc are for pET 28(a) plasmid vector while the orange region of the pET 28(a) plasmid codes for His-tag and thrombin cleavage site.

2.3 Optimisation of purification techniques to produce stable HsDHFR

After successfully isolating DHFR from the protein impurity, an alternative ligand was sought for stabilising it. Initial attempts to substitute folate for other ligands failed. Once folate is added to the enzyme at any stage of the purification, it remained tightly bound and cannot be removed without significant loss of protein yield. Hence, antifolate inhibitors were considered as replacements. These are broadly classified into classical (that is, inhibitors that have the glutamate tail) and non-classical (those that lacked the tail).¹⁴² Trimethoprim was preferred as a non-classical inhibitor of DHFRs because of its 10⁵-fold binding selectivity for bacterial than for vertebrate DHFRs.¹⁴³ We, therefore, hypothesise that trimethoprim would adequately stabilise HsDHFR while allowing the exchange for DHF substrate prior to kinetics study. However, substantial aggregation was observed, which is likely a combination of the poor solubility of trimethoprim in aqueous buffers and its lower affinity for HsDHFR.¹⁴³

The second strategy was the use of truncated substrates. Previous crystallographic and NMR studies have identified about 14 amino acid residues that participate in the binding of folate (Figure 2.3 and Table 2.2).^{103,144} Importantly, 65% of these residues are responsible for binding to the *para*-aminobenzoyl glutamate (pABG) moiety of folate. For example, residues

F31 and F34 have been reported to respectively form pi-stacking and van der Waal interaction with the benzoyl group of pABG.¹⁴⁵ We believe these interactions are sufficient to stabilize HsDHFR; hence, pABG was used as ligand during protein purification. The addition of 2 mM pABG into the lysis buffer, followed by the supplement of another 3 mM during size exclusion chromatography, afforded nearly homogeneous complex which is stable at a concentration over 1 mM. Because pABG absorbs at the same wavelength as the enzyme (280 nm), the UV detector of the chromatographic system is often saturated during size exclusion. Thus, SDS-PAGE was employed to identify elution fractions containing the enzyme. Figure 2.4 shows the different stages of the protein production. Further examination employed LC/MS, circular dichroism, NMR spectroscopy and kinetic analysis.

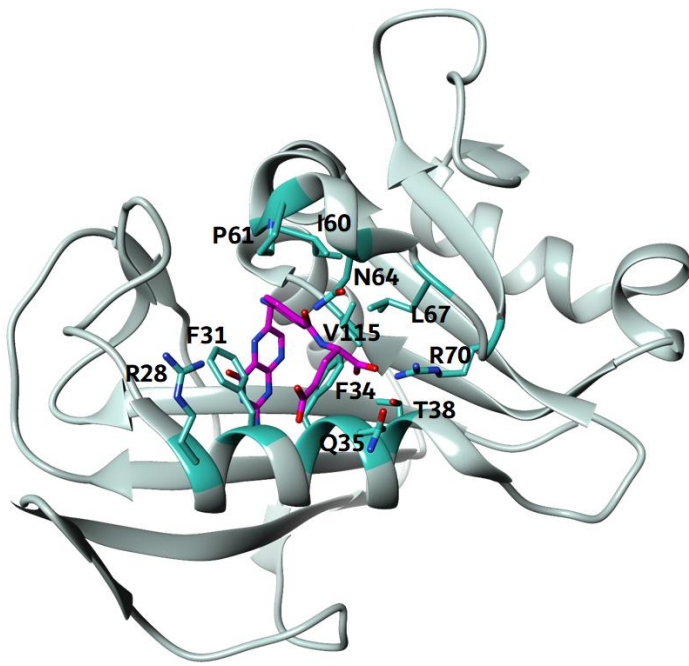


Figure 2.3. Crystal structure of HsDHFR (light sea green, PDB:4M6K) bound to folate (magenta). Residues interacting with pABG are shown in sea green according to reference 103,144 and 146. NADP⁺ was omitted for clarity.

Protein purity was assessed by LC/MS. The mass of 21454.25 ± 1.65 determined by electron spray ionisation-mass spectrometry (ESI-MS) agreed well with the calculated mass of 21452 with intact first methionine. However, a mass of 21323.5 ± 1.53 was also detected by ESI-MS

which was due to the post-translational modification of HsDHFR where the first methionine of the protein sequence has been cleaved. The peak corresponding to this mass indicates that ~40% of HsDHFR has the first methionine cleaved (Appendix I, Figure A4 – A5).

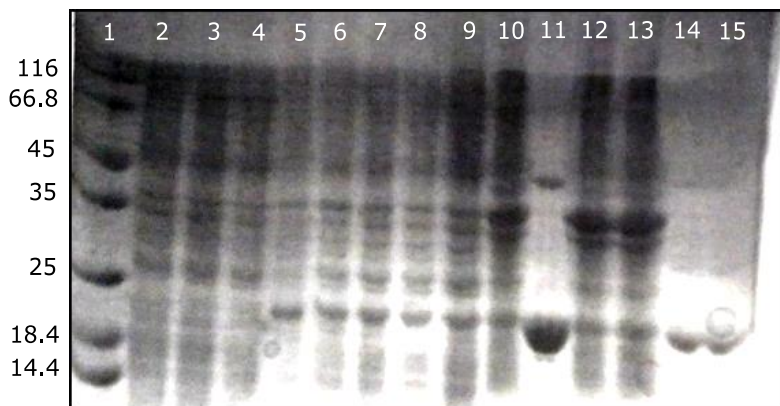


Figure 2.4. SDS-PAGE showing the HsDHFR expressions and purification (1: Protein marker in kDa; 2-4: HsDHFR before IPTG; 5-7: HsDHFR after IPTG; 8-10: Selected fractions from Q-sepharose purification; 11: purified HsDHFR (without β-mercaptoethanol); 12-13: cell pellet; 14-15: purified HsDHFR after size exclusion.

The tolerance of the pABG-bound HsDHFR to ligand exchange was tested and the enzyme-ligand complexes were also investigated by temperature unfolding experiment using circular dichroism. The replacement of pABG with folate produced a more stable enzyme while attempts to displace folate with pABG in folate-bound HsDHFR resulted in instantaneous aggregation. This precipitation signifies that the binding of pABG to HsDHFR is weak, whereas that of folate is strong; thus, causing protein instability on attempts to exchange the strong ligand. The stability of the enzyme-ligand complexes was examined by noting the alterations in the circular dichroism spectra. A change in the secondary structure is reflected as a shift in the spectra from folded to unfolded when the enzyme is heated between 5 and 85 °C. The change in the ellipticity of the backbone structure is plotted against temperature to give the melting curve. The midpoint of the curve taken at a specific wavelength where maximum change in ellipticity is observed, 215 nm in the case of HsDHFR, represents the melting temperature (T_m) (Figure 2.5). The pABG-bound enzyme shows a melting temperature of 40 °C, which is substantially lower than that of the HsDHFR-folate complex (52 °C) (Table 2.1).

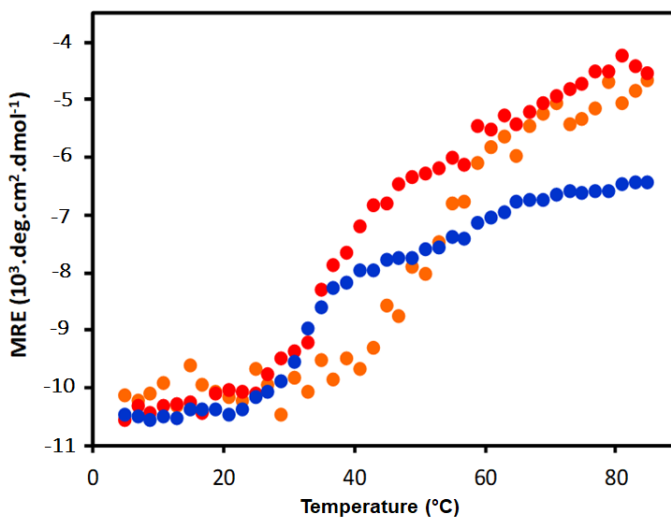


Figure 2.5. Melting temperature of HsDHFR (10 μ M) in phosphate buffer (10 mM) pH 7.0 at 215 nm without ligand (blue), with pABG (red) and folate (orange).

Table 2.1. Melting temperature of HsDHFR (10 μ M) in the absence and presence of ligands

10 mM phosphate buffer	Melting Temperature at 215 nm (T_m) ($^{\circ}$ C)
Enzyme at pH 7.0	37.16 ± 0.10
Enzyme with 100 μ M pABG at pH 7.0	40.49 ± 0.13
Enzyme with 100 μ M folate at pH 7.0	52.46 ± 0.25

The pABG-bound HsDHFR was further examined by ^1H - ^{15}N HSQC NMR spectroscopy. Enzyme complexes with pABG:NADP $^+$, folate:NADP $^+$, DHF:NADP $^+$ and THF:NADP $^+$ were acquired. The spectrum of the enzyme complexed with pABG:NADP $^+$ shows distinct chemical shifts that are different from that of the enzyme:folate:NADP $^+$ complex (Figure 2.6A). This result suggests that a number of residues are exposed to a different chemical environment when pABG is used. In contrast, spectra of the enzyme complexed with either DHF:NADP $^+$ or THF:NADP $^+$ were almost superimposable to that of the folate:NADP $^+$ complex (Figure 2.6B). These complexes respectively are thought to mimic the product and

Michaelis complexes, since HsDHFR can catalyse the reduction of both folate and DHF. This finding agrees with previous works indicating that HsDHFR does not undergo substantial conformational changes after its chemical step.⁹⁸ Overlay of other complexes can be found in Appendix I, Figure A6. We now analysed the kinetic difference between the previous purification strategy where the enzyme is stabilised by binding to folate and our new developed protocol, which employed pABG instead.

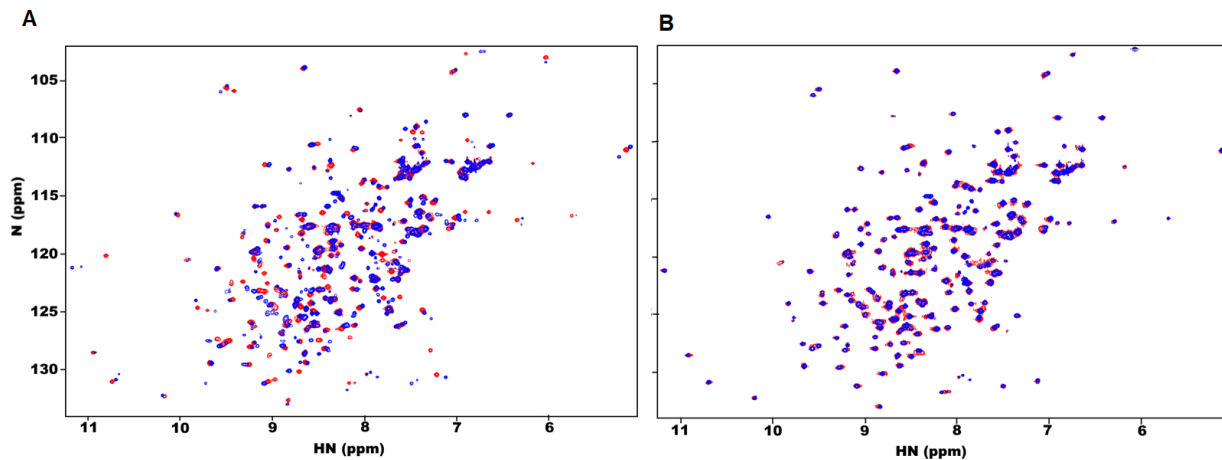


Figure 2.6. ^1H - ^{15}N HSQC overlay of HsDHFR complexed with (A) folate (blue) and pABG:NADP⁺ (red) and (B) folate:NADP⁺ (blue) and THF:NADP⁺ (red).

Table 2.2. The interaction of residues of HsDHFR with folate ligand from crystal structure and solution NMR

Folate component	Residues interacting with ligands PDB: 1DHF ^a	Type of interaction	NMR averaging experiment of hydrophobic and aromatic residues ^b
Pteridine ring	I7	Backbone carbonyl: hypothesized H-bond with N8 DHF, not observed with folate Side chain: Hydrophobic	Significant side chain and or backbone averaging identified
	F31, F34	Van der Waal/hydrophobic	Significant side chain and or backbone averaging identified
	W24, E30	H-bonding network involving structural waters, N3, O4 and 2-amino group	NA
	T136	H-bonding network involving structural waters, N3, O4 and 2-amino group	Significant side chain and or backbone averaging identified
<i>para</i> -aminobenzoic acid	F31, F34, I60, P61, L67	Van der Waal/hydrophobic	Significant side chain and or backbone averaging identified
	N64	H-bond to the carbonyl oxygen of p-ABA	NA
L-glutamic acid	R28	Carbonyl backbone: H-bonding network between H2O and γ -COOH folate	NA
	Q35	In proximity to both α - and γ -COOH folate	NA
	R70	Salt bridge with α -COOH folate	NA
Others	Y33, V50, T38, V115	NA	Significant side chain and or backbone averaging identified
NA= not applicable (a) and (b) are from reference 144 and 103, respectively.			

2.4 Kinetic investigation of purified HsDHFR

Our study revealed that the use of folate ligand during purification contributes to the kinetic complexity of HsDHFR. Folate was initially employed to stabilise the enzyme, prior to the discovery of a suitable substitute. During this period, attempts to measure the kinetics of the folate-bound enzyme were unsuccessful. The kinetic traces, measured with stopped-flow apparatus, were either incomplete, inconsistent or results in low kinetic isotope effects (KIE) (Figure 2.7). A summary of the different attempts is presented in Table 2.3. Notably, the KIE (k_H/k_D) with folate was inverse whereas that of DHF was normal (at pH 10.0). However, when the pABG-purified enzyme was used, consistent kinetic traces and results were measured. In fact, a rate constant measured with NADPD gave $603.67 \pm 60.93 \text{ s}^{-1}$ at 0 °C and pH 7.0, which is similar to the previous report of 600 s^{-1} measured at 6.0 °C and pH 7.65 where isoelectric focusing was employed to remove bound impurities.¹²⁹ Although the kinetics of HsDHFR have been reported to be complex,⁹⁶ the use of folate as ligand during purification significantly enhanced the unusual behaviour.

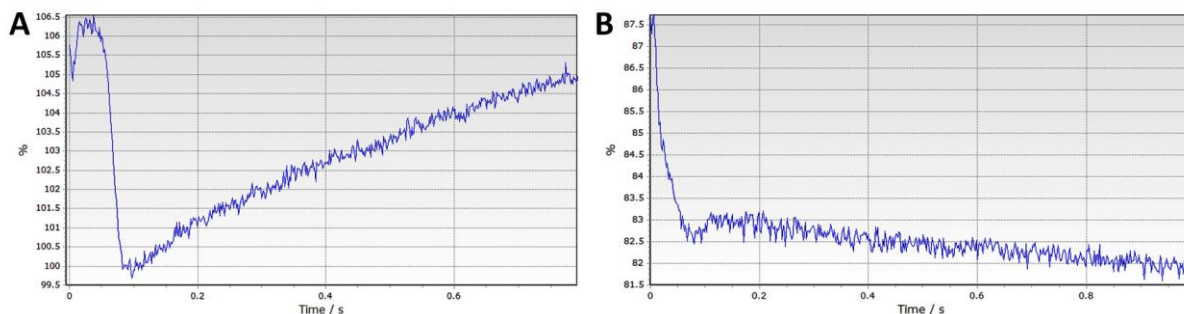


Figure 2.7. Stopped-flow fluorescence relaxation of folate-bound HsDHFR after pre-equilibration with NADPH and initiation of reaction with DHF showing (A) increasing intensity and (B) wobbly relaxation.

In contrast to folate bound HsDHFR, the enzyme complex with endogenous NADPH/NADP⁺, as reported previously,¹³⁹ did not create a problem during kinetic measurements. When expressed in *E. coli*, HsDHFR has been reported to form a tight complex with the cofactors.¹³⁹ Analysis of the complex of the enzyme with folate and with folate:NADP⁺ from ¹H-¹⁵N HSQC NMR spectra indicated that NADPH/NADP⁺ remain partly bound. Using a similar approach, a

truncated version of the cofactor, which comprises of ribose, nicotinamide and adenine diphosphate, were employed to displace the bound cofactor(s). But this attempt was unsuccessful. Interestingly, this limitation did not pose a challenge for kinetic measurements because NADPH is often pre-equilibrated with the enzyme, which should lead to the exchange of NADP⁺ for NADPH.

Table 2.3. Trials of pre-steady-state measurements of HsDHFR (20 μM) using a stopped-flow apparatus.

	Reaction syringe 1 (enzyme)	Reaction syringe 2	pH	F /A bs	k _H	k _D	KIE	Remark
Pre-equilibration with NH/ND								
1	10 μM NH/D	200 μM DHF	9.0	F	32.81 ± 2.97	29.81 ± 2.4	1.07	Low KIE
2	10 μM NH	buffer only	9.0	F	ND	ND	ND	No relaxation.
3	10 μM NH/D	200 μM FOL	9.0	F	583.32 ± 41.7	490.71 ± 1.18	1.18	Not reproducible.
4*	40 μM NH/D	400 μM FOL	9.0	F	523.94 ± 21.7	ND	ND	Not reproducible
pH 10.0 to slow down the transient kinetics ¹⁴⁷								
5	10 μM NH/D	200 μM DHF	10.0	F	15.27 ± 2.85	8.67 ± 1.27	1.76	Low KIE
6	10 μM NH/D	200 μM FOL	10.0	F	80.35 ± 5.38	123 ± 4.23	0.65	Low KIE
Pre-equilibration with FOL/DHF								
7	200 μM FOL	10 μM NH	9.0	F	ND	ND	ND	No relaxation.
8	200 μM FOL	50 μM NH	9.0	F	ND	ND	ND	No relaxation.
9	200 μM FOL	200 μM NH	9.0	F	ND	ND	ND	No relaxation.
10	40 μM FOL	200 μM NH	9.0	F	ND	ND	ND	No relaxation.
11	200 μM DHF	10 μM NH	9.0	F	6.32 ± 3.7	ND	ND	Not consistent

Continued from the previous page								
12	200 μM DHF	50 μM NH	9.0	F	7.95 \pm 1.4	ND	ND	Consistent
* measured with 40 μM enzyme concentration. ND = not determined								

2.5 Discussion

HsDHFR forms both *in vivo* and *in vitro* complexes with many macromolecules, which makes it an enzyme of great interest. For example, HsDHFR binds to its own mRNA, regulating its own translation.¹⁴⁸ It also forms an *in vitro* complex with human thymidylate synthase,¹⁴⁹ with a prediction that the two enzymes might be involved in substrate channelling.¹⁵⁰ HsDHFR also has 92% sequence identity with DHFR-like-1, a second DHFR localized in human mitochondria.¹⁵¹ Hence, HsDHFR might interact with more partners because mitochondria proteins are known to form many complexes.¹⁵²

It is commonly accepted that β -lactamase is responsible for the hydrolysis of β -lactam, but β -lactamases have also been found in eukaryotic cells catalysing seemingly unrelated reactions.^{153,154} One prominent example is human mitochondrial metallo- β -lactamase (LACTB2) which is an endoribonuclease.¹⁵⁵ The crystal structure alignment between the bacterial TEM-1 β -lactamase and LACTB2 reveals conserved domains that form part of the active site (Figure 2.8). One may, therefore, predict that interaction between HsDHFR and TEM-1 β -lactamase signifies that HsDHFR might form other complexes in the cell that are yet to be identified.

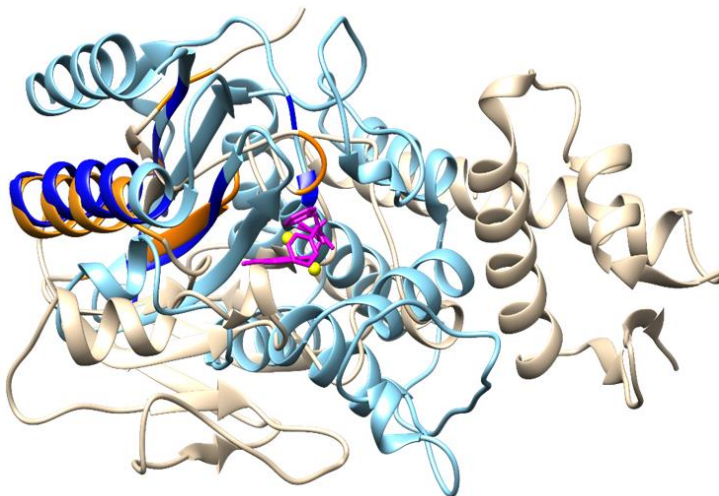


Figure 2.8. The overlay of TEM-1 β -lactamase (PDB:1ERO, sky blue) and LACTB2 (PDB: 4AD9, brown) Their conserved domains and residues are shown as blue and orange, respectively. The covalently bound boron inhibitor of TEM-1 shown as purple while the two-zinc metals at the active site of LACTB2 are shown as yellow

Adding of folate supplement to *E. coli* expression media of HsDHFR was suggested to improve the yield and recovery of a stable recombinant enzyme.¹³⁹ This stability is thought to result from the formation of an *in vivo* ternary complex where both folate and cofactor are bound to the enzyme. However, most bacteria such as *E. coli* which makes folate *de novo* do not use exogenous folate.¹⁵⁶ Instead, they have been shown to uptake and grow on pABG as well as catabolise folate to pABG.¹⁵⁷ Therefore, it is possible that the enhanced expression reported when *E. coli* is grown in folate-rich media result from the uptake of pABG.

Although minimal media expressions were produced with vitamin mix (composed of folate), the different chemical shifts observed in the overlay of the enzyme folate:NADP⁺ and enzyme pABG:NADP⁺ complexes indicate that folate was not endogenously bound. Endogenous folate and NADPH would form an inhibitory enzyme DHF:NADP⁺ complex, which has been reported to trap approximately 90% of HsDHFR under steady-state conditions.⁹⁶ The formation of such a complex would not be exchanged for pABG during purification. Consequently, minor peaks from the complex would have been observed in the ¹H-¹⁵N HSQC NMR spectra of the enzyme pABG:NADP⁺ complex, but these impurities were not noted.

Consequently, this purification strategy would encourage further kinetic and structural investigations of HsDHFR. Blakley and co-workers first reported the challenge with measuring the kinetics of HsDHFR in 1989.¹²⁹ Since then, other experimental attempts to measure the rate constant of the enzyme have failed,^{96,147,158} which has led to the use of computational models as alternatives.^{42,159} We have shown that part of this complexity originates from the use of folate because of its tight interaction.⁹⁶ However, with pABG, the contact was only strong enough to prohibit aggregation while allowing the exchange of tight-binding ligands. Previously, the interaction of pABG with DHFR from *Lactobacillus casei* (LcDHFR) was reported to be 400-fold weaker than that of DHF.¹⁶⁰ Earlier inhibition studies of HsDHFR have focussed on crystallographic evidence,^{93,110,127,146} which usually involves extensive dialysis of inhibitors against the tightly bound folate. Therefore, stabilising the enzyme with pABG, which require less time to exchange for an inhibitor, will encourage more kinetic and inhibition studies.

2.6 Conclusions

Accurate identification of TEM-1 β -lactamase played a central role in developing a high-yielding purification protocol for HsDHFR. Importantly, our result also supports the interactive nature of HsDHFR binding to biomolecules other than its substrates. Instead of folate, a weaker binding ligand pABG was used during purification. This renders the chromatographic procedure from five to only two steps, involving only the use of anion exchange and size exclusion chromatography.¹³⁹ The newly developed purification procedure also enables the facile exchange of different ligands, opening up opportunities to gain valuable structural and kinetic insights of this enzyme. This approach will consequently encourage further studies, which will be useful in the determination of the hydride transfer rate constant and the study of its dynamics.

**3 . Effects of protein dynamics on the hydride transfer
reaction catalysed by human dihydrofolate
reductase**

3.1 Preface

In most bacterial DHFRs, the chemical step can be revealed by measuring the kinetics at high pH under steady-state, or neutral pH under pre-steady-state conditions.^{7,95,161} However, the steady-state kinetics of HsDHFR and other vertebrate DHFRs at elevated pH could not reveal their chemical step.¹²⁹ Other attempts to measure the chemical step by standard stopped-flow techniques were similarly unsuccessful because the rate is faster than the detection limit of the instrument.^{96,129,147,158} Hence, rate constant for the isotope-sensitive step of vertebrate DHFRs could not be determined, a challenge that was suggested to originate from the isomerization of an active site residue in the enzymes.^{103,128,129} Consequently, protein dynamic effects of HsDHFR and other vertebrate homologs could not be studied using conventional approaches that employ substrate and enzyme KIEs.

Although competitive KIE (H/T) method was recently employed to investigate the dynamics of HsDHFR, the approach could not reveal the effect of mass modulation on the hydride transfer rate constant.¹⁵⁸ Based on the success of our purification strategy in the previous chapter and the reduced kinetic complexity from the use of pABG (being a non-substrate ligand), alternative approaches were explored to reveal the hydride transfer step of HsDHFR. Here, the temperature-dependence of the hydride transfer rate constants are measured using steady-state and pre-steady-state kinetics. The method with the most isotope-sensitive rate constant was then employed to determine the hydride transfer rate constant of HsDHFR and later applied to elucidate the contribution of protein dynamics to the chemical step.

3.2 Substrate KIE of the reaction catalysed by HsDHFR

The experiments were optimised for conditions where hydride transfer is significantly rate-limiting based on the sensitivity of the rate constant to isotopic substitution. The rate constants were also measured as a function of temperature for the investigation of protein dynamics. The conditions employed for rate constants are therefore discussed below.

3.2.1 Substrate KIE (KIE_{cat}) measured using steady-state kinetics at high pH

In earlier studies, hydride transfer in bacterial DHFRs was shown to be rate-limiting at pH above 8.4 under steady-state.^{129,95} For example, in EcDHFR, hydride transfer is rate-limiting at pH 9.0 but more limiting at pH 9.5.¹³⁴ But for vertebrate DHFRs, their cross-over pH (that is, the pH where hydride transfer rate become rate limiting) were reported to be higher than those of their bacterial homologs.¹²⁹ Consequently, hydride transfer in HsDHFR under steady-state condition was measured at pH 10.0 with MTEK buffer (50 mM MES, 25 mM Tris, 25 mM ethanolamine and 150 mM KCl)

At 20 °C, the hydride transfer rate constant measured was $1.58 \pm 0.01 \text{ s}^{-1}$, which reduced by two-folds when NADPD was substituted for NADPH ($0.78 \pm 0.04 \text{ s}^{-1}$). This ratio corresponds to a substrate KIE_{cat} (k_{cat}^H/k_{cat}^D) of 2.0. The measurement revealed that hydride transfer rate constant is two-fold faster in HsDHFR than in EcDHFR ($0.72 \pm 0.009 \text{ s}^{-1}$) measured at a lower pH (pH 9.5 and 20 °C).¹³⁴ Further measurement between 5 and 35 °C gave linear Arrhenius plots for both k_{cat}^H and k_{cat}^D (Figure 3.1, Figure 3.2 and Table 3.1). The KIE_{cat} was mildly temperature-dependent and approximately 2.0 (Table 3.1).

Although this KIE_{cat} is lower than the KIE_{cat} expected for DHFRs as proposed in an earlier study,¹²⁹ it is slightly higher than previous reports. Previously, the KIE_{cat} of *Lactobacillus casei* DHFR (LcDHFR) was set as a ‘standard’ for DHFRs.¹²⁹ This is because the KIE_{cat} of LcDHFR did not increase above 3.4 when the pH of the reaction was raised from pH 5.0 to 10.0.¹²⁹ However, the KIE_{cat} measured here for HsDHFR is higher than in the previous report determined under identical conditions of buffer, pH and temperature ($KIE_{cat} = 1.7$).¹²⁹ This discrepancy might result from the 150 mM KCl used in our case instead of 100 mM NaCl employed in the previous study.¹²⁹ Different salt ions and concentrations have been reported to influence the kinetics of DHFRs.⁹⁵ Also, in a previous report, high salt concentration (~800 mM) has been shown to slow the kinetics of mouse DHFR.¹⁶² The KIE_{cat} measured here is also identical to the KIE (H/D) of 2.01 [at 25 °C] calculated for the enzyme using competitive KIE measurement of H/T and D/T at pH 9.0.¹⁵⁸

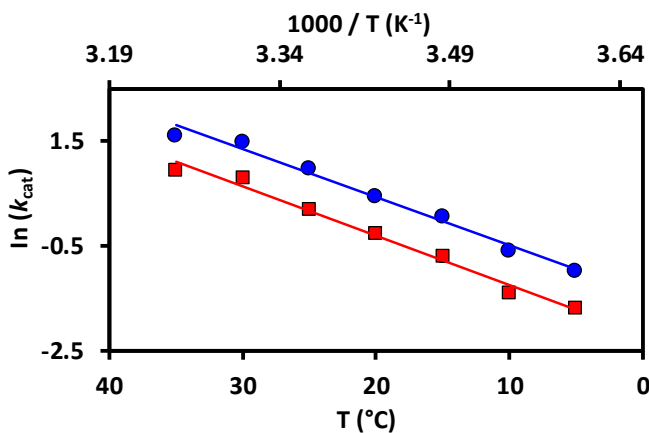


Figure 3.1. Arrhenius plots for hydride (circle) and deuteride (square) transfer plotted on a logarithmic scale against inverse temperature, measured under steady-state conditions at pH 10.0

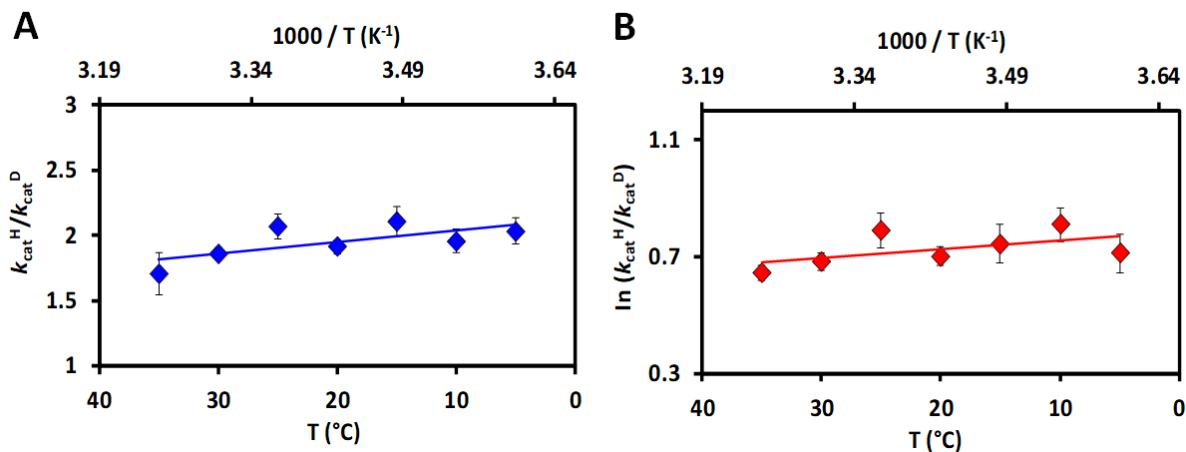


Figure 3.2. (A) Temperature-dependence of substrate KIE measured under steady-state conditions at pH 10.0 and (B) Arrhenius plot of substrate KIE on a logarithmic scale against inverse temperature

Activation energy of the hydride transfer reaction at pH 10.0 was found to be 65.00 ± 3.08 kJ·mol⁻¹, compared to 67.21 ± 3.24 kJ·mol⁻¹ for deuteride transfer (Table 3.1). The corresponding activation energy difference (ΔE_a) is 2.2 ± 5.4 kJ·mol⁻¹ with an Arrhenius prefactor ratio of (A_H/A_D) of 0.83 ± 0.04 (Table 3.1). Typically, lower activation energy was expected for HsDHFR, because the enzyme is known to be extremely fast.⁹⁶ However, changes in pH alter the net charge of an enzyme, which has been reported to affect the mechanism of reaction for EcDHFR.⁸³ EcDHFR has been suggested to switch from a step-wise mechanism at pH 7.0 to a concerted mechanism when the pH is increased to 9.0.⁸³ However, such a pH change did not significantly perturb the activation energy of the reaction.¹²⁴ Furthermore,

effects of pH on the enzyme's structure was also examined using circular dichroism (CD). By employing buffers with different pHs, the effect of pH on the T_m of the enzyme can be investigated. The T_m of HsDHFR measured as changes to the ellipticity of the secondary structure at 215 nm suggests the enzyme stability increases with pH. For example, at pH 7.0 in phosphate buffer, the T_m is 37.0 °C, this increased to 40 °C at pH 8.0 in borate buffer. However, the secondary structure of the enzyme appears not to be fully melted at 85 °C in pH 10.0 borate buffer because the melting curve did not exhibit the characteristic sigmoid curve observed at other pHs (Figure 3.3). The suitability of borate buffer for CD spectra higher pH has been reported due to its buffering capacity at high pH and its low absorption in the region of interest (<210 nm).¹⁶³

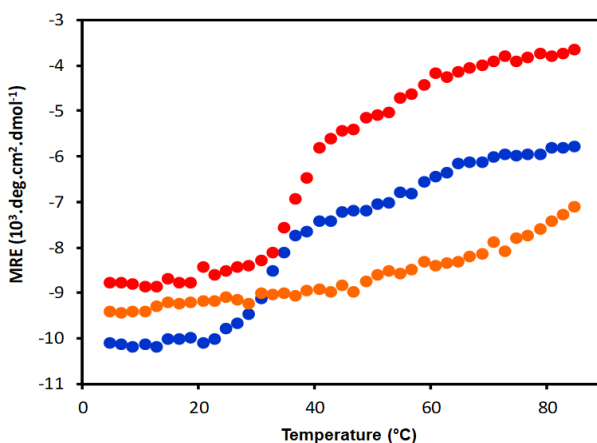


Figure 3.3. Melting temperature of HsDHFR (10 μ M) in different buffers (10 mM) measured at 215 nm: light in phosphate pH 7.0 (blue), boric acid pH 8.0 (red) and boric acid pH 10.0 (orange)

Despite the rate constants measured under our steady-state conditions were more isotope-sensitive, other kinetic steps appear to contribute to the determined rate constants. For example, at 5 °C, two fast rates were observed at the beginning of the UV trace, which lasted for about 120 sec (three kinetic time-course, each lasting 40 sec, see Appendix II, Figure A7). These rates were then followed by a slower rate. Importantly, only the slowest rate gave a linear Arrhenius plot with rate constants measured at higher temperatures. This indicates that other kinetic steps occur at higher temperatures but are too fast to be detected under steady state conditions. The unusual and complex kinetic time-course discovered at lower temperatures was similarly noted at neutral pH and with natural and isotopically labelled cofactors NADP(H/D).

Infact, the use of low enzyme concentration did not alleviate the multiple-time course (Figure 3.4), suggesting the steady-state kinetics is not being observed. Earlier studies have revealed that HsDHFR shows multiple time-course kinetics under different conditions, comprising of a burst, intermediate and a steady-state phase.¹²⁹ According to the study, the steady-state kinetic of HsDHFR exhibits complex behaviour with turnover rate constant k_{cat} of 12 s⁻¹ that has kinetic contributions from the release of both THF and NADP⁺ from the product ternary complex (E:THF:NADP⁺).⁹⁶ Such multiple-time course kinetics suggest other steps contribute to the observed rate constant; hence, pre-steady-state kinetics was attempted as a strategy to lessen the kinetic complexity of the isotope-sensitive step.

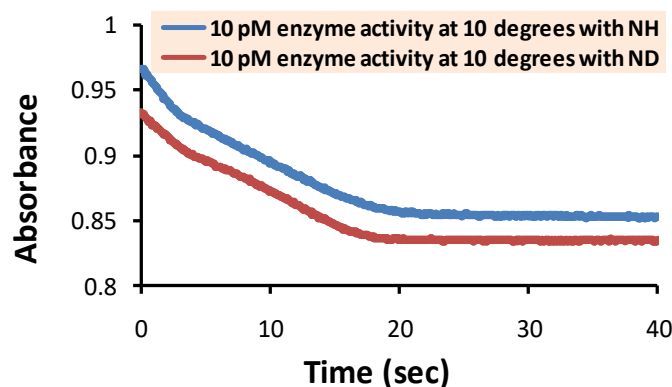


Figure 3.4. Normalised UV/Vis absorbance trace of steady-state kinetics measured over 40 sec with 10 pM enzyme concentration at 10 °C showing three different kinetic rates. NH = NADPH and ND = NADPD (pH 7.0).

Table 3.1. Temperature-dependence of steady-state kinetic parameters of HsDHFR in MTEK buffer pH 10.0

Temperature (°C)	$k_{\text{cat}}^{\text{H}}$ (s ⁻¹)	$k_{\text{cat}}^{\text{D}}$ (s ⁻¹)	$k_{\text{cat}}^{\text{H}}/k_{\text{cat}}^{\text{D}}$
5.0	0.38 ± 0.01	0.19 ± 0.02	2.0 ± 0.21
10.0	0.56 ± 0.04	0.25 ± 0.01	2.2 ± 0.19
15.0	1.06 ± 0.02	0.50 ± 0.06	2.1 ± 0.12
20.0	1.58 ± 0.01	0.78 ± 0.04	2.0 ± 0.06
25.0	2.67 ± 0.13	1.22 ± 0.09	2.2 ± 0.09
30.0	4.42 ± 0.19	2.23 ± 0.04	2.0 ± 0.05
35.0	4.95 ± 0.08	2.60 ± 0.09	1.9 ± 0.04
E_a (kJ·mol ⁻¹)	65.00 ± 3.08	67.21 ± 3.24	A _H /A _D = 0.83 ± 0.04

3.2.2 Substrate KIE (KIE_{H}) measured using pre-steady state kinetics at cryogenic temperatures

Earlier studies have reported that the fast kinetics of HsDHFR can be reduced by lowering the temperatures of the pre-steady-state kinetics is measured.^{96,129} However, rate constant was only measured at a single temperature (6 °C) because higher temperatures resulted in complexity.¹²⁹ To overcome this, a cryo-stopped-flow kinetics approach was developed to measure the temperature-dependence of the reaction at sub-zero temperatures. To prevent the solution from freezing, methanol (30%) was added to the buffer as a cryoprotectant. The reaction was studied at pH of 8.5 to reduce the transient kinetics and afford proper study. The analysis focussed first on obtaining more significant substrate KIE measurements, after which the effect of the cosolvent on the reaction was analysed.

The chemical step measured with NADPH and NADPD at -20 °C were 51.4 ± 2.4 and 20.8 ± 3.5 s⁻¹, respectively, giving a substrate KIE_{H} ($k_{\text{H}}/k_{\text{D}}$) of 2.5 ± 0.10. The slightly higher KIE_{H} measured by this approach (cryo-kinetics) reveals that hydride transfer was more rate-limiting under this condition than the steady-state rate constant determined at pH 10.0. Hydride and deuteride transfer rate constants were measured from -20 to +5 °C (Figure 3.5 and Table 3.4) leading to a temperature-independent KIE_{H} of ~2.3 (Figure 3.6 and Table 3.4). The Arrhenius

plot of KIE_H was linear within the measured temperature range similar to steady-state kinetics. Non-linear Arrhenius plots of substrate KIEs were reported for EcDHFR when studied at extreme conditions of high pH and for TmDHFR at low temperatures.^{134,164} However, the breakpoint of Arrhenius plot of KIE for TmDHFR shifted from 25 °C to lower temperatures when methanol cosolvent was used;³⁹ this suggests the cosolvent influence the observed kinetics.

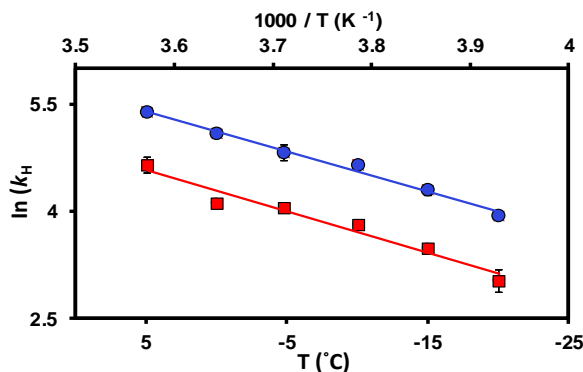


Figure 3.5. Arrhenius plots for hydride (circle) and deuteride (square) and the corresponding KIEs (square) plotted on a logarithmic scale against inverse temperature, measured under pre-steady-state conditions at pH 8.5

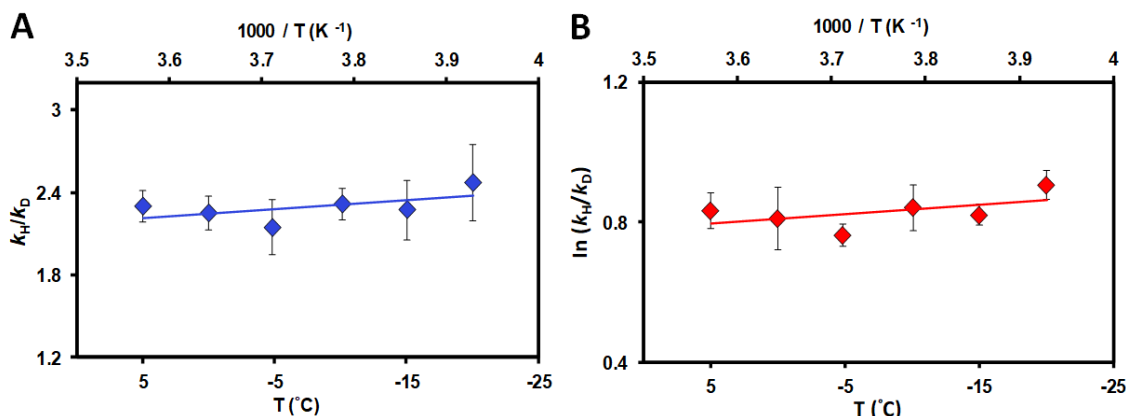


Figure 3.6. (A) Temperature-dependence of substrate KIE measured under pre-steady-state conditions at pH 8.5 and (B) Arrhenius plot of substrate KIE plotted on a logarithmic scale against the inverse temperature

Organic cosolvents often alter the physical properties of aqueous solvent including the dielectric constant and viscosity.¹³⁷ Therefore, the effect of cosolvent (30% methanol) on the reaction was investigated by measuring pre-steady state kinetics in the absence of methanol. The

deuterated cofactor (NADPD) was employed for measurement between 0 to 20 °C to avoid the complexity introduced by high temperatures.^{96,129} The k_D values measured in the presence and absence of methanol at 0 °C were 71.89 ± 3.25 and $97.88 \pm 3.06 \text{ s}^{-1}$, respectively (Table 3.5). On the average, the rate constants reduced by 25% similar to the effect of 33% methanol on the rate constants of bacterial DHFRs, which lead to ~30% reduction.^{39,83,126,137} However, the slope of Arrhenius plots of k_D in the presence and absence of methanol were identical within experimental errors (Figure 3.7). This similarity suggests that the cosolvent did not alter the activation energy of the reaction. The compatibility of methanol as a cosolvent for enzyme kinetics at cryogenic temperatures have been reported for other enzymes. For example, in a previous kinetic study on two thermophilic enzymes determined between +90 and -70 °C, methanol as a cosolvent gave linear Arrhenius plots that were parallel to those measured when cosolvents were not used.¹⁶⁵ Earlier studies have also reported that the $\text{KIE}_H(s)$ of DHFRs are insensitive to methanol cosolvent, between 17 - 33% (Table 3.6).^{39,90,126,137} For example, when EcDHFR was measured in 0% methanol the KIE_H was 2.92 ± 0.10 but only reduced to 2.41 ± 0.08 in the presence of 33% methanol.¹³⁷ On the other hand, KIE_H measured in the presence and absence of 33% methanol for BsDHFR was unaltered (3.44 ± 0.23).⁹⁰ Therefore, the parallel Arrhenius plots (in the presence and absence of methanol) and the insensitivity of KIE_H to cosolvent indicate that the KIE_H measured using cryo-kinetics represents the precise substrate KIE of HsDHFR. The KIE_H measured here is slightly higher than when standard stopped-flow was employed previously at only 6 °C where KIE_H of 2.1 was reported at pH 7.65.¹²⁹

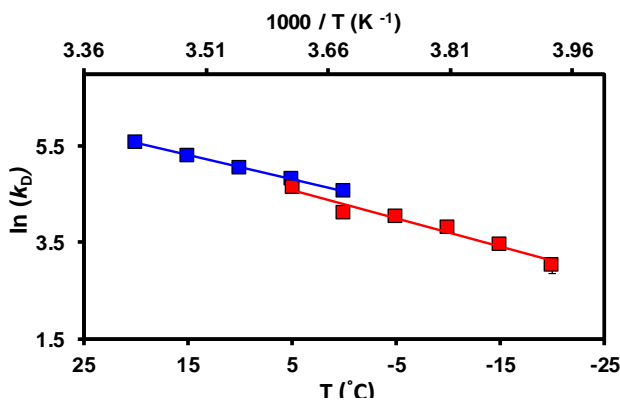


Figure 3.7. Arrhenius plot of the pre-steady-state hydride transfer rate constant of HsDHFR without methanol (blue) and with 30% methanol cosolvent (red).

Although methanol did not alter the kinetics of the reaction, it appears to have a destabilising effect on the enzyme's structure. This influence was noted when the rate constant measured in methanol gradually decrease instead of increasing above 10 °C. Analysis by circular dichroism and steady-state kinetics revealed that the tertiary structure of the enzyme, as well as the turnover rate constant (k_{cat}), were affected by the cosolvent. The k_{cat} dropped four-folds (Table 3.2) while the melting temperature (T_m) of the enzyme was lower by 10 °C when measured in the presence of methanol (Table 3.3). A structurally important water molecule has been previously detected in the enzyme,¹⁶⁶ which may be perturbed by the cosolvent at a higher temperature. However, the Michaelis constants (K_M) measured with and without cosolvent shows that the enzyme-ligand interface was not affected (Table 3.2). The declining rate constant at a higher temperature and structural instability in the presence of cosolvent could arise from conformational perturbation or the onset of a denaturation process.

Table 3.2. Steady-state kinetic parameters in different buffers at 20 °C

Buffer	k_{cat} (s ⁻¹)	K_M DHF (μM)	K_M NADPH (μM)
Phosphate pH 7.0	10.43 ± 0.87	0.14 ± 0.03	3.81 ± 1.33
Phosphate with 30% MeOH pH 7.0	2.82 ± 0.86	0.14 ± 0.06	2.90 ± 0.80
MTEK pH 10.0	1.38 ± 0.68	5.29 ± 1.88	26.01 ± 9.60

Table 3.3. Melting temperature determined in different buffers.

Enzyme and conditions	Melting temperature T_m 215 nm (°C)
10 mM phosphate pH 7.0	37.16 ± 1.04
10 mM Boric acid pH 8.0	40.74 ± 0.20
10 mM Boric acid with 30% MeOH pH 8.0	30.25 ± 0.10

Table 3.4. Temperature-dependence of pre-steady state kinetic parameters in phosphate-boric-30%methanol buffer pH 8.5

Temperature (°C)	k_H (s ⁻¹)	k_D (s ⁻¹)	k_H / k_D
-20.	51.41 ± 2.40	20.79 ± 3.48	2.5 ± 0.10
-15	73.35 ± 3.63	32.29 ± 1.90	2.3 ± 0.09
-10	104.91 ± 3.76	45.27 ± 1.61	2.3 ± 0.05
-5	123.63 ± 3.93	57.60 ± 1.88	2.1 ± 0.09
0	161.66 ± 4.17	71.89 ± 3.25	2.2 ± 0.05
5	217.77 ± 6.70	94.80 ± 6.32	2.3 ± 0.05
E_a (kJ·mol ⁻¹)	32.52 ± 1.54	34.32 ± 1.82	$A_H/A_D = 1.01 \pm 0.06$

Table 3.5. Temperature-dependence of pre-steady-state kinetic parameters in the presence and absence of methanol cosolvent

Temperature (°C)	No solvent	30% methanol
	k_D (s ⁻¹)	k_D (s ⁻¹)
-20	ND	20.79 ± 3.48
-15	ND	32.29 ± 1.90
-10	ND	45.27 ± 1.61
-5	ND	57.60 ± 1.88
0	97.88 ± 3.06	71.89 ± 3.25
5	124.55 ± 1.92	94.80 ± 6.32
10	158.65 ± 6.54	ND
15	202.15 ± 6.54	ND
20	268.29 ± 6.05	ND
E_a (kJ·mol ⁻¹)	33.23 ± 1.00	34.32 ± 1.82
ND = not determined		

Table 3.6. Substrate KIE of DHFR homologs in the presence and absence of methanol cosolvent

Enzyme	k_H/k_D (0% methanol)	k_H/k_D (33% methanol)
EcDHFR ^a	2.92 ± 0.10	2.41 ± 0.08
BsDHFR ^b	3.44 ± 0.23	3.44 ± 0.18
TmDHFR ^c	4.52 ± 0.20	5.02 ± 0.04
MpDHFR ^d	1.91 ± 0.13	1.65 ± 0.10

(a), (b), (c) and (d) are from ref ^{39,90,126,137} respectively.

3.3 Estimation of hydride transfer in HsDHFR

Because hydride transfer reaction in HsDHFR is fast and could not be determined at physiological conditions previously, earlier studies have estimated different rate constants that ranged from 1,360 to 3,000 s⁻¹ at 20 °C pH 7.65.^{96,129} In the first case, a computational model was employed to predict the hydride transfer rate constant,⁹⁶ whereas deuteride transfer rate constant determined by pre-steady-state kinetics was converted to hydride transfer using the substrate KIE of LcDHFR (3.4) in the later.¹²⁹ The use of KIE of 3.4 here appears to be an overestimation since recent kinetic studies have shown that substrate KIEs vary between DHFRs and could take values from 2.0 – 5.0.^{117,133,134} Therefore, hydride transfer rate constant in HsDHFR was estimated using our measured KIE_H of 2.3 determined from cryo-kinetics above (section 3.2.2). Since deuteride transfer reactions are inherently slower than hydride, NADPD was used for the reaction at much higher temperatures at pH 8.5, 8.0 and 7.0. The rate constants at pH 8.5 and 8.0 were determined from 0 – 20 °C (Figure 3.8 and Table 3.7), while pH 7.0 was measured only at 0 °C (because the rate constant at pH 7.0 was extremely fast). At 0 °C the deuteride transfer rate constant at pH 8.5 was 97.88 ± 3.06 s⁻¹, 219.27 ± 9.93 s⁻¹ at pH 8.0 and 603.67 ± 60.39 s⁻¹ at pH 7.0. Using KIE_H of 2.3, hydride transfer at 20 °C and pH 8.0 was $1,093 \pm 31$ s⁻¹, which is very similar to the 1,360 s⁻¹ estimated previously at 20 °C and pH 7.65 by the computational model.⁹⁶ Furthermore, the Arrhenius plots for pH 8.5 and pH 8.0 were extrapolated to higher temperatures, converging at 88.55 °C. The rate obtained at this temperature corresponds to a deuteride transfer rate constant of 3,474.1 s⁻¹ (hydride transfer rate constant of 7,990.5 s⁻¹) (Figure 3.8). A new Arrhenius plot was derived using the rate

constant measured at 0 °C and pH 7.0 and the convergence rate constant (Figure 3.8) (assuming is the pH-independent rate constant of the reaction). From the new Arrhenius plot, hydride transfer rate at pH 7.0 constant after the conversion was determined to be $2,263 \pm 226 \text{ s}^{-1}$ (20 °C) and $3,260 \pm 558 \text{ s}^{-1}$ (37 °C) (

Table 3.8).

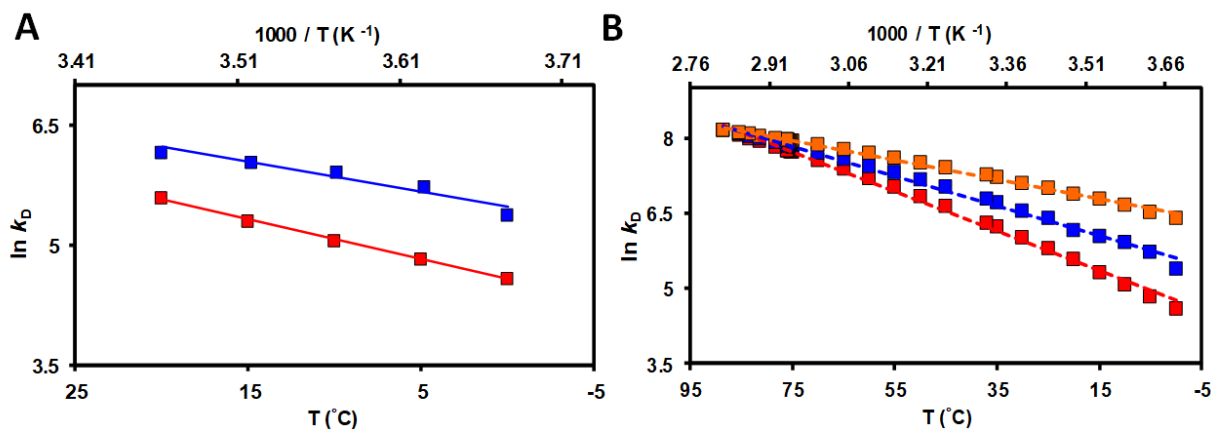


Figure 3.8. (A) Arrhenius plots of deuteride transfer rate constant in HsDHFR measured at pH 8.0 (blue) and pH 8.5 (red) (B) Arrhenius plots of deuteride transfer rate constant extrapolated at pH 7.0 (orange), pH 8.0 (blue) and pH 8.5 (red). Some points in the linear estimations were removed for clarity.

Linear extrapolations of Arrhenius plots have been employed previously to estimate rate constant of hydride transfer in some DHFRs at their physiological conditions. These values were reported as $317.3 \pm 1.6 \text{ s}^{-1}$ for EcDHFR at 37 °C, $255.0 \pm 6.4 \text{ s}^{-1}$ for MpDHFR at 2 °C and $8.2 \pm 0.1 \text{ s}^{-1}$ for TmDHFR at 90 °C.¹²⁶ Hydride transfer rate constant of HsDHFR estimated here shows that the enzyme is ten-fold faster than its mesophilic counterpart (EcDHFR) at their physiological conditions.

Table 3.7. Deuteride transfer measured at pH 8.0 and 8.5 in phosphate-boric acid buffer

Temperature (°C)	pH 8.0 k_D (s ⁻¹)	pH 8.5 k_D (s ⁻¹)
0	219.27 ± 9.93	97.88 ± 3.06
5	309.24 ± 11.92	124.55 ± 1.92
10	374.56 ± 5.25	158.65 ± 6.54
15	422.50 ± 13.56	202.15 ± 6.54
20	475.22 ± 13.59	268.29 ± 6.05
E _a (kJ·mol ⁻¹)	24.7 ± 3.43	33.2 ± 1.00

Table 3.8. Estimated hydride transfer rate constant in HsDHFR determined from Arrhenius plots at pH 8.5 and 8.0 using substrate KIE of 2.3

Temperature (°C)	pH 8.5		pH 8.0		pH 7.0	
	k_D (s ⁻¹)	k_H (s ⁻¹)	k_D (s ⁻¹)	k_H (s ⁻¹)	k_D (s ⁻¹)	k_H (s ⁻¹)
0	97.88 ± 3.06	225.12 ± 7.04	219.27 ± 9.93	504.32 ± 22.84	603.67 ± 60.39	1388.44 ± 138.89
20	268.29 ± 6.05	617.07 ± 13.92	475.22 ± 13.56	1093.01 ± 31.23	983.70 ± 120.78*	2262.51 ± 226.32
37	552.53 ± 13.30*	1270.83 ± 30.59	878.88 ± 27.85*	2021.42 ± 64.89	1417.48 ± 242.78*	3259.50 ± 558.39

*Estimated hydride transfer rate constant from linear extrapolation of Arrhenius plots

3.4 Enzyme KIE measured using pre-steady state kinetics at cryogenic temperatures

Although HsDHFR is structurally rigid, the active site residue Phe31 has been reported to adopt different conformations in the enzyme by rotating its C α –C β bond.¹²⁸ This motion was proposed to regulate solvent accessibility to the active site and substrate binding.^{107,128} It is also said to induce the isomerisation that suppresses the substrate KIE of the enzyme.¹²⁹ Hence, the

role of fast protein vibrations in HsDHFR was investigated by enzyme heavy atom labelling. Light (^{12}C , ^{14}N) and heavy HsDHFR (^{13}C , ^{15}N) were produced, as reported previously.⁴⁴ The heavy enzyme labelling led to a mass increase of 5.1% (Appendix II, Figure A8) but did not alter the kinetics and the tertiary structure of the enzyme as revealed by steady-state kinetics (k_{cat} and K_M) (Table 3.9) and circular dichroism (Table 3.10 and Figure 3.9). Enzyme substituted with heavy atoms that included deuterium isotope (^2H) has been reported previously to cause a minor structural alteration in the thermal unfolding of EcDHFR.¹⁶⁷ However, deuterium labelling was not employed in our case. Notably, the exclusion of deuterium in enzyme labelling has been shown not to alter the effects of mass modulation on studied reaction.¹¹⁶

Table 3.9. Steady-state kinetic parameters of light and heavy enzymes in phosphate buffer pH 7.0 and 20 °C

HsDHFR	$k_{\text{cat}} (\text{s}^{-1})$	$K_M \text{DHF} (\mu\text{M})$	$K_M \text{NADPH} (\mu\text{M})$
Light	10.43 ± 0.87	0.14 ± 0.03	3.81 ± 1.33
Heavy	10.55 ± 0.78	0.10 ± 0.02	3.91 ± 1.19
Enzyme KIE	0.99 ± 0.11	1.40 ± 0.41	0.97 ± 0.45

Table 3.10. Melting temperature of light and heavy enzymes bound to folic acid

Enzyme and conditions	Melting temperature (T_m) _{215 nm} (°C)
Light HsDHFR with folate	54.99 ± 0.20
^{13}C , ^{15}N heavy-HsDHFR with folate	55.05 ± 0.10

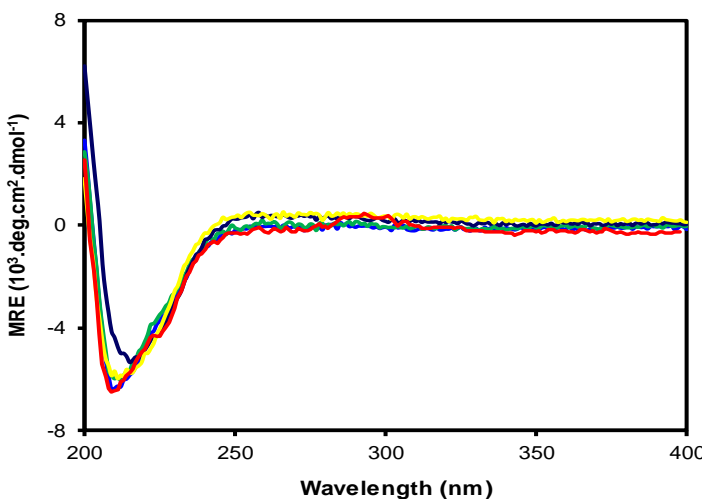


Figure 3.9. Circular dichroism spectra of HsDHFR (10 µM) at 20 °C in the different buffers (10 mM) reported: light enzyme in phosphate pH 7.0 with folate ligand (cyan), in boric acid pH 8.0 (green), in boric acid with 30% methanol pH 8.0 (dark blue) and in boric acid pH 10.0 (yellow). Heavy enzyme in phosphate pH 7.0 with folate ligand (red),

Since cryo-kinetics gave the highest substrate KIE, pre-steady-state kinetics using cryo-stopped flow technique was employed to investigate the effect of protein dynamics on hydride transfer rate. The rates were measured for the light and heavy enzyme between -20 and 0 °C, which showed similar rate constants between 0 and 5 °C. However, the rate constants diverge significantly at lower temperature (< 0 °C), such that enzyme KIE (k_H^{LE} / k_H^{HE}) increased from 1.07 ± 0.05 (5 °C) to 1.72 ± 0.15 (-20 °C) (Figure 3.10 and Table 3.12).

The large enzyme KIE observed at sub-zero temperatures here agrees with previous reports on the effect of non-physiological temperatures on the enzyme KIEs of other homologs.^{45,116} For instance, enzyme KIE of the psychrophilic MpDHFR increased significantly at high, non-physiological temperature (>1.45 above 25 °C),⁴⁵ while that of the moderately thermophilic DHFR from *Geobacillus stearothermophilus* (BsDHFR) increased at low temperature (1.65 at 5 °C).¹¹⁶ But in both enzymes, enzyme KIE was close to unity at their physiological temperatures.^{45,116}

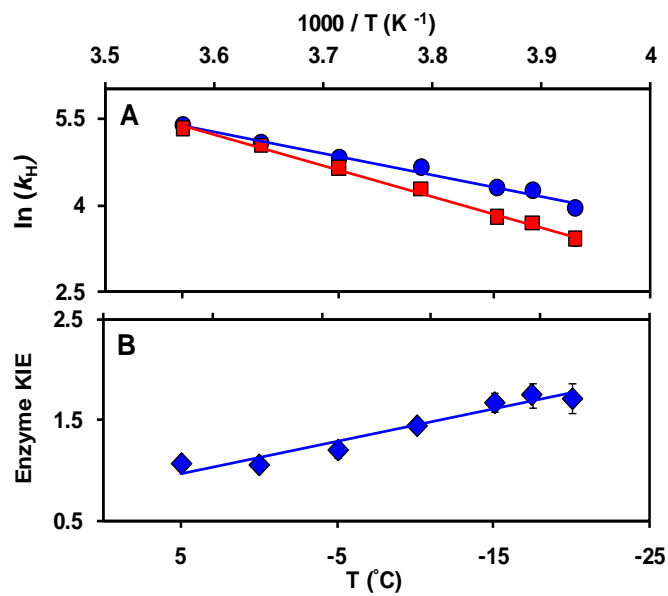


Figure 3.10. (A) Arrhenius plots of the hydride transfer rate constant of light (blue) and heavy HsDHFR (red) at pH 8.5 and (B) The resulting enzyme KIE (k^{LE}/k^{HE})

The enzyme KIEs were also determined with NADPD at -15, 0, 5 and 20 °C and the values were similar to when NADPH was used. The enzyme KIE were determined with 30 % methanol cosolvent (-15 and 5 °C) and in the absence of cosolvent (0 and 20 °C) (Figure 3.11, Table 3.13 and

Table 3.14).

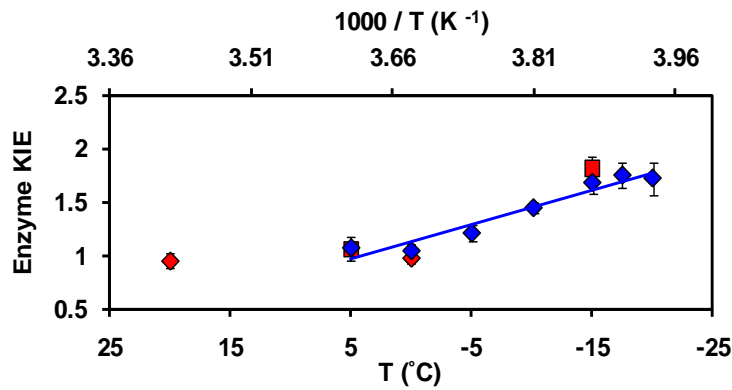


Figure 3.11. Temperature-dependence of enzyme KIE in HsDHFR, k_H (blue) and k_D (red). The k_D values were measured with 30% methanol solvent (square) and without cosolvent (diamond).

In addition, the activation energies of the light and heavy enzymes were strikingly identical despite having different activation enthalpies and entropies. Such entropic-enthalpic compensation has also been observed in heavy enzyme studies of other homologs (Table 3.11). This phenomenon was proposed to originate from the balance of equilibrium conformational sampling and the electrostatic rigidity that enzymes require to form the reaction-ready-configuration.⁴⁵

Table 3.11. Eyring activation parameters of light and heavy DHFRs under pre-steady-state conditions at pH 7.0 and 25 °C

	HsDHFR*		BsDHFR ^a		MpDHFR ^b		EcDHFR ^c		TmDHFR ^d	
	Light	Heavy	Light	Heavy	Light	Heavy	Light	Heavy	Light	Heavy
ΔS^\ddagger (kJ mol ⁻¹ K ⁻¹)	-96 ± 4	-46 ± 4	-112 ± 4	-88 ± 8	-126 ± 4	-163 ± 4	-109 ± 4	-126 ± 8	-96 ± 4	-96 ± 4
ΔH^\ddagger (kJ mol ⁻¹)	28.9 ± 1.7	42.7 ± 1.3	27.2 ± 1.3	28.0 ± 1.3	19.7 ± 0.8	10.0 ± 0.8	28.0 ± 1.3	22.6 ± 2.5	49.0 ± 0.4	49.0 ± 0.4
ΔG^\ddagger (kJ mol ⁻¹)	55.2 ± 1.3	55.2 ± 0.4	61.1 ± 6.7	61.5 ± 7.5	57.7 ± 0.4	58.2 ± 0.4	60.3 ± 6.3	60.3 ± 6.3	77.0 ± 5.4	77.0 ± 8.0
(a) - (d) are from ref ^{45,116,138} * Measured at pH 8.5 and 0 °C										

Substrate KIEs measured for the heavy enzyme at 5 and -15 °C was similar to the light enzyme. (Table 3.15 and Table 3.4). In a previous study, competitive KIE was employed to investigate the effect of protein dynamics on the catalysis of HsDHFR by comparing the substrate KIE (H/T) of light and heavy enzyme.¹⁵⁸ Although this approach has been employed to study protein dynamics of other enzymes,¹⁶⁷ it appears to be unsuitable for revealing the dynamics of HsDHFR. In fact, our finding shows that substrate KIE of the light and heavy HsDHFR measured were identical at 5 and -15 °C, whereas enzyme KIE has increased from 1.07 to 1.68 within the temperature range.

Table 3.12. Temperature-dependence of the pre-steady state kinetic parameters light and heavy HsDHFR in phosphate-boric-30%methanol buffer pH 8.5

Temperature (°C)	Light k_H (s ⁻¹)	Heavy k_H (s ⁻¹)	Enzyme KIE
-20.0	51.41 ± 2.40	29.90 ± 2.44	1.72 ± 0.15
-17.5	70.77 ± 3.83	40.39 ± 1.77	1.75 ± 0.12
-15.0	73.35 ± 3.63	43.75 ± 1.33	1.68 ± 0.09
-10.0	104.91 ± 3.76	74.27 ± 3.95	1.44 ± 0.05
-5.0	123.63 ± 3.93	102.29 ± 8.53	1.21 ± 0.08
0.0	161.66 ± 4.17	154.04 ± 6.32	1.05 ± 0.06
5.0	217.77 ± 6.70	202.99 ± 4.30	1.07 ± 0.05
E_a (kJ·mol ⁻¹)	31.3 ± 1.67	44.8 ± 1.34	

Table 3.13. Pre-steady-state kinetic parameters of light and heavy HsDHFR in phosphate-boric buffer, pH 8.5. Enzyme KIE measured in the absence of cosolvent.

Temperature (°C)	Light k_D (s ⁻¹)	Heavy k_D (s ⁻¹)	Enzyme KIE
0	97.88 ± 3.06	100.76 ± 1.82	0.97 ± 0.04
20	268.29 ± 6.05	282.88 ± 18.00	0.95 ± 0.07
E_a (kJ·mol ⁻¹)	33.5 ± 0.84	34.3 ± 1.84	

Table 3.14. Pre-steady-state kinetic parameters of light and heavy HsDHFR in phosphate-boric-30% methanol buffer pH 8.5. Enzyme KIE measured in the presence of cosolvent.

Temperature (°C)	Light k_D (s ⁻¹)	Heavy k_D (s ⁻¹)	Enzyme KIE
-15	32.29 ± 1.90	17.83 ± 1.57	1.81 ± 0.11
5	94.80 ± 6.32	89.11 ± 8.27	1.06 ± 0.11
E_a (kJ·mol ⁻¹)	33.0 ± 0.75	48.7 ± 2.85	

Table 3.15. Pre-steady-state kinetic parameters of heavy HsDHFR in phosphate-boric-30% methanol buffer pH 8.5. Substrate KIE of heavy HsDHFR.

Temperature (°C)	Heavy k_H (s ⁻¹)	Heavy k_D (s ⁻¹)	k_H/k_D
-15	43.75 ± 1.33	17.83 ± 1.57	2.5 ± 0.09
5	202.99 ± 4.30	89.11 ± 8.27	2.3 ± 0.10
E_a (kJ·mol ⁻¹)	44.0 ± 2.05	48.66 ± 2.84	

3.5 Discussion

Vertebrate DHFRs may have evolved to have a lower substrate KIE. The reason for low substrate KIE observed in most vertebrate DHFRs remain unidentified.¹²⁹ Previously, the study of DHFR's primary sequence has identified that while Phe/Tyr31 is conserved in most vertebrate DHFRs, Leu is conserved in the bacterial homologs.⁹⁴ An experiment designed to change Leu28 in EcDHFR to Phe, alongside other identified functional mutations, led to a reduction in the substrate KIE of the enzyme from 2.7 to 2.1. The rate constant also increased four-fold, from 1100 to 5100 s⁻¹.⁹⁴ However, a report on chicken DHFR, which has low catalytic rate and a Tyr in place of Phe31, showed that the reduced substrate KIE might not be linked to fast hydride transfer rate constant.¹²⁹ In addition, when competitive KIE method was employed to reveal the intrinsic KIE of HsDHFR, a lower intrinsic KIE was calculated (~5.0) compared to that of EcDHFR (~6.0).^{158,168} Furthermore, computational calculations have suggested that lower KIEs in enzymes could result from the smaller distance between the hydride acceptor and donor.⁴⁰

To avoid semantic confusion, protein dynamics is defined here as a time-dependent change in atomic coordinates, which includes both equilibrium and non-equilibrium motions of protein side-chains, loops or domains.¹⁶⁹ Although it is generally recognised that protein dynamics are important for the physical step of ligand association and dissociation and for forming the reaction-ready configuration,⁷ their role in the chemical step is hotly debated.^{11,12,170–172}

Substrate KIE results suggest that tunnelling did not contribute to the chemical step of HsDHFR. Based on previous studies where tunnelling is thought to promote enzyme catalysis, temperature-independent KIEs and Arrhenius prefactor ratios (A_H/A_D) that are close to unity

are interpreted to signify the lack of H-tunnelling contribution.^{30,173} Our study on HsDHFR using steady-state and pre-steady-state kinetics revealed that the substrate KIEs were largely temperature-independent while Arrhenius prefactor ratios from both techniques fell within the semi-classical limits.¹⁷⁴ In addition, changes in conditions such as pH and temperature range were shown to influence the temperature-dependence of KIEs and tunnelling probabilities.¹³⁶ However, the different conditions investigated in this study showed virtually temperature-independent substrate KIEs. Therefore, protein dynamics that are thought to reduce the barrier width and facilitate H-tunnelling may not influence the chemical step of HsDHFR. This finding is in contrast to studies on bacterial DHFRs where H-tunnelling contributed to hydride transfer.^{39,133,134,175}

Dynamic coupling was not observed at the physiological temperature of HsDHFR similar to bacterial DHFRs. While substrate KIE is often related to H-tunnelling probabilities, enzyme KIE is employed to probe the coupling of fast protein vibrations to the chemical step.^{43,174} The heavy atom substitution of HsDHFR revealed large enzyme KIE of 1.72 ± 0.15 at $-20\text{ }^{\circ}\text{C}$ while at $5\text{ }^{\circ}\text{C}$ enzyme KIE was 1.07 ± 0.05 . Similarly, the psychrophilic MpDHFR showed enzyme KIE of approximately unity at temperatures closer to its physiological temperature ($2\text{ }^{\circ}\text{C}$) but increased significantly to 1.45 at $25\text{ }^{\circ}\text{C}$.¹¹⁶ Enzyme KIE of BsDHFR was also high (1.65) when measured at $5\text{ }^{\circ}\text{C}$ but unity at $45\text{ }^{\circ}\text{C}$.⁴⁵ These results show that dynamic coupling in DHFRs are minimal at their physiological temperatures. Although a mild increase in enzyme KIE of EcDHFR was reported at $40\text{ }^{\circ}\text{C}$,¹³⁸ orthogonal isotopic labelling of the mobile M20 loop of the enzyme showed that this dynamics is not linked to the motion of the loop.¹¹⁴ Hence, protein or residue motions did not couple to the chemical step of HsDHFR under physiological conditions.

An enzyme KIE that is greater than unity was proposed to signify increased recrossing events at the dividing surface of the enzyme's chemical coordinate.^{45,116,123} Notably, various biophysical factors have been shown to induce recrossing events in DHFRs.^{45,116,123} Equilibrium protein reorganizational motions and non-equilibrium dynamic coupling should be minimised at lower temperatures.⁴⁵ However, studies have shown that the disruption of equilibrium motions at low temperatures increases internal friction along the reaction coordinate of enzymes, which prevents them from forming the optimal electrostatic

environment that is crucial for stabilizing the transition state.^{44,45} Consequently, non-equilibrium motions that couple to the chemical coordinate is increased.^{45,116} The low activation entropy of heavy HsDHFR (Table 3.11) indicates diminished flexibility that results in the large enzyme KIE measured at sub-zero temperatures. Together with our previous works, this result indicates that protein dynamics are negligible when enzymes are at their physiological conditions but appears to drive hydride transfer reactions under conditions that the host organisms are not normally exposed to.^{45,116}

3.6 Conclusions

In this work, the extremely fast and nearly undetectable chemical reaction catalysed by HsDHFR was measured using high pH and sub-zero temperatures. The substrate KIE measured by pre-steady-state was employed to estimate the hydride transfer rate of the enzyme close to the physiological conditions, 35 °C at pH 7.0 (This can be estimated for other temperatures). In addition, the substrate KIEs determined by steady and pre-steady-state kinetics were largely temperature-independent in both measurements, which signify that the contribution of quantum mechanical tunnelling to the observed chemical step was negligible.¹³⁴ When enzyme KIE was investigated, fast protein vibrations did not contribute to the chemical step above 0 °C but only at lower temperatures (< 0 °C). This result clearly shows that dynamic coupling is likely an unfavourable factor in the catalysis of DHFRs since enzyme isotopic substitution caused no measurable effect under (nearly) physiological conditions in HsDHFR and in other studied bacterial DHFRs.^{7,45,114,116,123,138} This observation is different from that of purine nucleoside phosphorylases (PNP) where dynamic coupling was thought to be beneficial.^{176,177} Hence, the alleged importance of protein dynamics to enzyme catalysis remain disputable as a generalised model. In the next chapter, we will explore how conformational changes and ligand interactions alter electrostatic changes at the microenvironment of bacterial DHFRs.

**4 . Electrostatic changes at the microenvironment of
DHFRs investigated by vibrational Stark effects
spectroscopy**

4.1 Preface

Electrostatic forces have long been recognised as fundamental to protein functions.^{3,62,178} Because partial charges have long-range effects and are widely distributed throughout a protein, the study of protein electrostatics can be complicated.¹⁷⁹ In addition, protein electrostatics often change during ligand interaction and catalysis, which may be accompanied by motional reorganisation.^{3,53} Although it is generally accepted that protein motions and electrostatic changes are linked,⁶³ it is not clear how ligand's electric field and electrostatic changes in enzymes due to evolution can influence protein motion.

Electrostatic changes that accompany the ligand-dependent motions of EcDHFR has been implicated in facilitating its hydride transfer.⁵¹ EcDHFR adopts three major conformations- open, closed and occluded- during its catalytic steps.⁹⁹ These conformations refer to the configuration that is assumed by its active site loop (M20 loop).⁹⁹ In a recent investigation of electrostatic changes in the enzyme, vibrational Stark effect (VSE) spectroscopy and computational analysis were employed to determine the total electric field projected toward its donor-acceptor axis.⁵¹ According to the study, this electric field is a resultant of the individual electric fields that originate from the ligands and several amino acid residues in the enzyme.^{15,51} One-third of this total electric field was said to be from the protein.⁵¹ But because some of the identified residues have been implicated previously in a ‘network of coupled motion’,¹¹⁸ it was concluded that conformational changes drive the enzyme’s chemical step.⁵¹ On the other hand, the M20 loop of DHFRs from several other species adopts the closed conformation as their sole configuration,^{93,99,104,180,181} which is important for modulating the pK_a of the substrate.¹⁰⁵ Hence, it is not clear how homologs that lack the conformational dynamics reported for EcDHFR would alter the electrostatics of their active site.

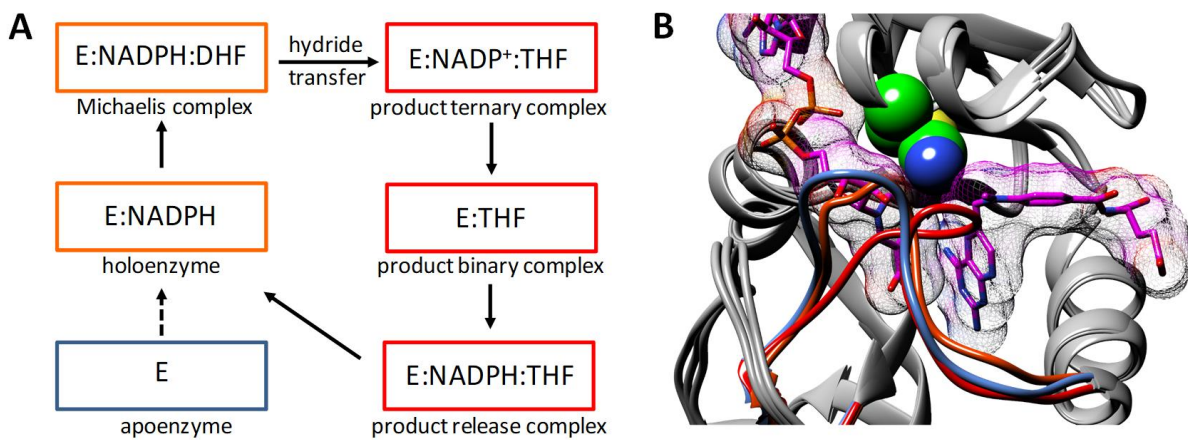


Figure 4.1. (A) Conformational changes along the catalytic cycle of EcDHFR indicated by blue (open), orange (closed) and red (occluded). Line arrows represent major cycle while the broken arrow represents the step that is rarely observed in vivo. (B) Overlay of the crystal structures of EcDHFR showing the direction of the thiocyanate probe (green spheres) and the configuration of the M20 loop in the open (blue, PDB: 1RA3), closed (orange, PDB: 4P66) and occluded (red, PDB:1RX6). Methotrexate and NADP⁺ are shown in purple with a mesh surface, while other ligands are removed for clarity.

To characterise the dynamics of DHFRs, and how it influences electrostatic changes at their active site, VSE spectroscopy was employed to study electrostatics of monomeric DHFRs (EcDHFR, EcDHFR S148P-a conformationally impaired variant, BsDHFR and MpDHFR) and the dimeric TmDHFR. The complexes studied include the apoenzyme and holoenzyme (enzyme bound to NADPH) as well as enzyme complex with folate:NADP⁺ and THF:NADP⁺, which are thought to mimic the Michaelis and the product complex, respectively. Other enzyme complexes examined include NADP⁺ and MTX:NADPH. The methods employed to generate the labelled enzymes and measure the VSE spectroscopy for all the enzymes are first discussed before the electrostatic implication of the results obtained are outlined in the later section.

4.2 Labelling of DHFRs for VSE spectroscopy

To study these enzymes by VSE spectroscopy via nitrile probes, there are three stages to this. First is that native cysteine residues in the enzymes must be mutated, and a cysteine residue inserted at desired positions by site-directed mutagenesis.¹⁸² Other approaches to achieve selective labelling of protein with nitriles are discussed elsewhere.⁵³ Next, would be the

production of high enzyme concentration to measure highly resolved infrared peaks and the last steps of the experiment comprised of nitrile labelling, FTIR and ^{13}C -NMR measurements as well as data processing.

4.2.1 Site-directed mutagenesis

DHFRs from different species have a varying number of native cysteine residues. For instance, EcDHFR has two native cysteine residues (C85 and C152), BsDHFR and MpDHFR have only one (C73 and C105, respectively) while TmDHFR has no cysteine residue. Cysteine-free EcDHFR (C85A/C152S) (EcDHFR_{cf}) has been studied previously in our group and elsewhere, where they showed that the variant has identical kinetic and structural characteristic with wild-type EcDHFR (The cf subscript indicate cysteine-free).^{183,184} Similarly, cysteine-free MpDHFR has been studied previously where Cys105 of the enzyme was mutagenised to Ala, Val, Ser, and Phe.¹⁸⁵ The C105F variant has similar kinetics with the wild-type enzyme. The presence of Phe at the equivalent position in EcDHFR was reasoned to justify the wild-type character of the variant since MpDHFR and EcDHFR have high sequence identity (53%).¹⁸⁵ However, cysteine-free BsDHFR has not been generated previously. Sequence alignment with other homologs was therefore conducted. The result shows that other DHFRs have Ala or Val at the equivalent position where BsDHFR has a Cys (Figure 4.2). Computational analysis of the two possible variants was undertaken using a web-based server reported in previous studies (<http://www-cryst.bioc.cam.ac.uk/~sdm/sdm.php>).¹⁸⁶ The software used (Site Directed Mutator) is a statistical potential energy function that uses environment-specific amino-acid substitution frequencies within homologous protein families to calculate a stability score, which is analogous to the free energy difference between the wild-type and mutant protein.¹⁸⁶ The analysis predicted that C73V mutagenesis has minimal impact on the enzymes hydrophobic packing. Hence, BsDHFR C73V variant was created by site-directed mutagenesis.

MaDHFR	MTRAE VGLVWAQSTSGVIGRGGDIPWS-V PEDLTRFKEVTMG-----HTVIMGRRTWE	52
MtDHFR	----MVGLIWAQATSGVIGRGGDIPWR-L PEDQAHFREITMG-----HTIVMGRRTWD	48
LcDHFR	----TAFLWAQDRDGLIGRDGHLWPWH-L PDDLHYFRAQTVG-----KIMVVGRRTYE	47
MpDHFR	---MIVSMIAALANNRVIGLDNKMPWH-L PAELQLFKRATLG-----KPIVMGRNTFE	49
MyDHFR	-----MIAALANNRVIGLDNKMPWH-L PAELQLFKRATLG-----KPIVMGRNTFE	45
EcDHFR	----MISLIAALAVDRVIGMENAMPWN-L PADLAWFKRNTLD-----KPVIMGRHTWE	48
SvDHFR	---MKIAMIAAMANNRVIGKDQNQMPWH-L PEDLKHFKAMTLG-----KPIVMGRKTYYD	49
BsDHFR	----MISHIVAMDENRVIGKDNRLPWH-L PADLAYFKRVTMG-----HAIVMGRKTFE	48
BaDHFR	---MIVSFMVAMDENRVIGKDNNLPWR-L PSELQYVKRTTMG-----HPLIMGRKNYE	49
SpDHFR	-MTRKIVAIWAQDEEGVIGKDNRLPWH-L PAELQHFRETTLN-----HAILMGRTFD	51
hDHFR	--VGSLNCIVAVSQNMGIGKNGDLWPPLRNEFRYFQRMTTSSVEGKQNLVIMGKKTWF	58
mmDHFR	-MVRPLNCIVAVSQNMGIGKNGDLWPPLRNEFKYFQRMTTSSVEGKQNLVIMGKKTWF	59
MaDHFR	SLPAKVRPLPGRNCCCCSRPDFVAEGARVAG-SLEAALEYA--G-----SDPAPWVIGGA	105
MtDHFR	SLPAKVRPLPGRNVLSRQADFMASGAEVVG-SLEEAALT-----SPETWVIGGG	97
LcDHFR	SFPK--RPLPERTNVVLTHQEDYQAQGAVVH-DVAAVFAYAKQH---PDQELVIAGGA	100
MpDHFR	SIG--RPLPGRNLNIVLSRQTDYQPEGVTVVA-TLEDAVVAAGD-----VEELMIIGGA	99
MyDHFR	SIG--RPLPGRNLNIVLSRQTDYQPEGVTVVA-TLEDAVVAAGD-----VEELMIIGGA	95
EcDHFR	SIG--RPLPGRKNIILSSQPG-TDDRTWTWK-SVDEAIAACGD-----VPEIMVIGGG	97
SvDHFR	SIG--RALPGRNLNIVISRQEGLSIPGVTCVT-SFEMAVEAAGE-----CEELVVVIGGG	99
BsDHFR	AIG--RPLPGRDNCCCCTGNGRSFRPEGCLVLH-SLEEVKQWIASR-----ADEVFIIGGA	99
BaDHFR	AIG--RPLPGRNIIIVTRNEGYHVEGCEVAH-SVEEVFELCKN-----EEEIFIFGGA	99
SpDHFR	GMGR--RLLPQRRETLLTRNPEEKIDGAVTFQ-DVQSVDWYQAO-----EKNLYILGGK	103
hDHFR	SIPEKNRPLKGGRINLVLSSRELKEPPQGAHFLSRLSLDDALKLT EQPELANKVDMVWIVGGS	118
mmDHFR	SIPEKNRPLKDRINIVLSRELKEPPRGAHFLAKSLSLDDALRLIEQPELASKVDMVWIVGGS	119
MaDHFR	QIYLLALPHAT--RCEVTEIEIDLRRDDD DALAPALDDSWVGETG---EWLASRSGLRY	159
MtDHFR	QVYALALPYAT--RCEVTEVDIGLPLPREGDALAPVLDETWRGETG---EWRFSSRSGLRY	151
LcDHFR	QIFTAFKDDDVD--TLLVTRILAGSFEGD-TKMIPLNWDDFTKVSSR---TVEDTNPAITH	153
MpDHFR	TIYNQCLAAAD--RLYLTHIELTTEGDTWFPDYEQYNWQEIEHES---YAADDKNPPhNY	153
MyDHFR	TIYNQYLAAD--RLYLTHIELTIEGD-TWFPDYEQYHWQEIEHES---YAADDKNPPhDY	149
EcDHFR	RVYEQFLPKAQ--KLYLTHIDAEVEGD-THFPDYEPDDWESVFSEF---HDADAQNSHSY	151
SvDHFR	QLYASILSKAD--KLYLTEINLDVAGD-TFFPQWDDGSWERISQEM--LVNGAG--LEY	151
BsDHFR	ELFRATMPIVD--RLYVTKIFASFPGD-TFYPPISDDEWEIVSYTP---GGKDEKNPYEH	153
BaDHFR	QIYDLFLPYVD--KLYITKIHAFEGD-TFFPEMDMTNWKEVFVEK---GLTDEKNPYTY	153
SpDHFR	QIFQAFPEPYLD--EVIVTHI HARVEGD-TYFPFEEFDLSLFETVSSKF--YAKDEKNPYDF	158
hDHFR	SVYKEAMNHPGHLKLFVTRIMQDFESD-TFFPEIDLEKYKLLPEYPGVLSDVQEEKGIKY	177
mmDHFR	SVYQEAMNQPGHLRLFVTRIMQE FESD-TFFPEIDLGKYKLLPEYPGVLSVQEEKGIKY	178
MaDHFR	RFHSYRRD--- 167	
MtDHFR	RLYSYHRS--- 159	
LcDHFR	TYEVWQKKA-- 162	
MpDHFR	RFSLLERVK-- 162	
MyDHFR	RFSLLERVK-- 158	
EcDHFR	CFEILER--- 159	
SvDHFR	SFINLVK--- 158	
BsDHFR	AFIIYERKKAK 164	
BaDHFR	YYHVYEKQQ-- 162	
SpDHFR	TIQYRKKEV-- 168	
hDHFR	KFEVYERND-- 186	
mmDHFR	KFEVYERKD-- 187	

Figure 4.2. Sequence alignment of different homologues of DHFR. Enzymes and residues mutated are shown in red. The conserved Thr residue (T46 by EcDHFR numbering), labelled in this study are shown as orange in the different enzymes while the equivalent position of the residues mutated are shown in blue.

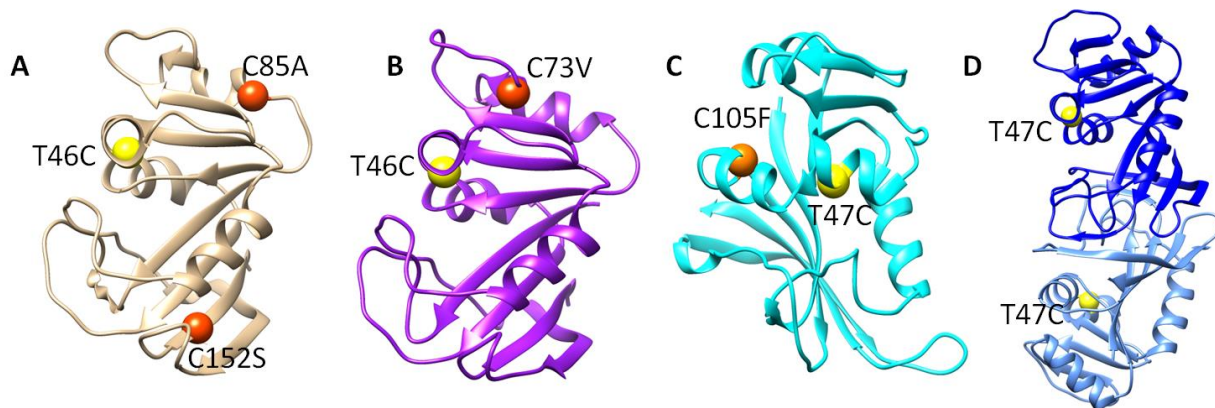


Figure 4.3. Crystal structures showing mutations introduced into (A) EcDHFR (brown, PDB 1RXA) (B) BsDHFR (purple, PDB 1ZDR) (C) MpDHFR (cyan, PDB 2ZZA) and (D) TmDHFR (blue, PDB 1D1G). The conserved threonine residue changed to cysteine is shown as the yellow spheres while native cysteine residues modified to other amino acid residues are shown as orange spheres.

Once the native cysteine residues have been removed, a cysteine residue was inserted at equivalent positions in all the enzymes. Earlier, the crystal structure of EcDHFR revealed that a nitrile probe inserted at position 46 was $\sim 5 \text{ \AA}$ from the donor-acceptor axis and did not perturb its steady and pre-steady-state kinetics.⁵¹ Interestingly, the sequence analysis *vide supra* (Figure 4.2) shows that position 46 (EcDHFR numbering) is conserved in most DHFRs. In addition, the crystal structure overlay of the DHFRs studied in this report reveals that the orientation of this residue in the active site is also conserved (Figure 4.4). Therefore, positions equivalent to Thr 46 of EcDHFR were mutated to cysteine in BsDHFR, MpDHFR and TmDHFR. The mutation is to ensure that the nitrile probe in the enzymes reports on identical events. Also, the nitrile probe in the other homologs might adopt the same orientation as γ -C-CN of EcDHFR_{cf} T46C-CN shown in Figure 4.1.⁵¹

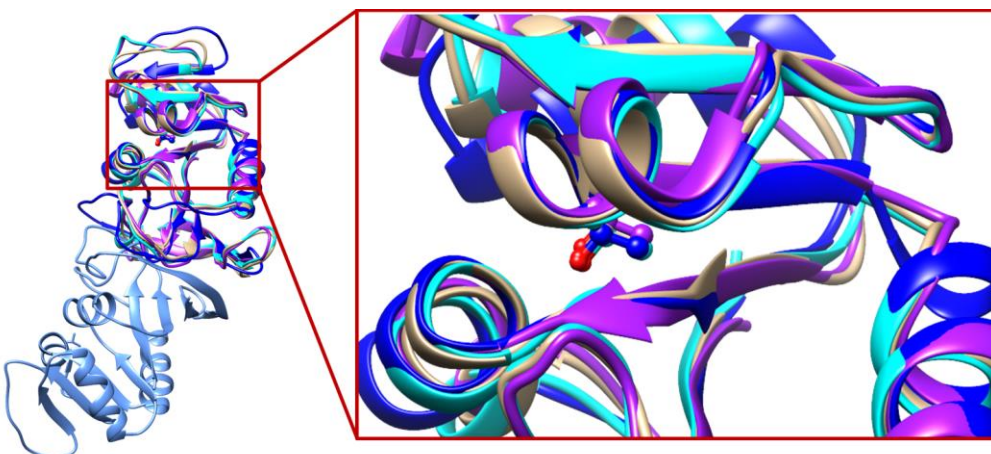


Figure 4.4. Structural overlay of EcDHFR (brown, PDB: 1RX2), MpDHFR (cyan, PDB: 2ZZA), BsDHFR (purple, PDB: 1ZDR) and TmDHFR (blue, PDB: 1D1G) showing the rotamer of the conserved threonine residue

Because the different homologs have different dynamics, we introduced a mutation into EcDHFR to understand how conformational changes influence electrostatic changes at its active site. The formation of the occluded conformation of EcDHFR has been shown to depend on hydrogen bonding between the mobile M20 loop and Ser148 of the GH loop.⁹⁹ The disruption of this interaction when Ser148 is mutated to other residues like Pro or Ala have been reported to impair the enzymes' ability to adopt the occluded conformation.¹¹⁷ A previous study has shown that the mutation of Ser148 to Pro in EcDHFR disrupts the enzyme-product interaction without a significant effect on the hydride transfer rate constant.¹¹⁷ Furthermore, both MpDHFR and BsDHFR have Pro at positions that are equivalent to Ser148 in EcDHFR. Hence, S148P mutation was introduced into EcDHFR_{cf} T46C variant to produce EcDHFR_{cf} S148P/T46C).

4.2.2 Production of DHFRs for nitrile labelling

After successful mutagenesis, the enzymes must be produced at high concentration to study their Stark shift. Currently, one of the constraints of studying protein by FTIR spectroscopy is low sensitivity.⁵⁶ Although nitrile probes have higher extinction coefficients and increased absorption compared to other probes,⁵⁴ high enzyme concentration is still required for the optimum dynamic range. Alternatively, the path length of the sample cell can be increased for enhanced absorption

but this would also raise the intensity of water absorption in the background spectrum, leading to suppression of relevant peaks.⁵⁶ High protein concentrations were achieved with the monomeric DHFRs without significant aggregation but the dimeric TmDHFR could not be obtained at desired concentrations because of inadequate purification procedure and protein instability.⁹¹

To resolve the limitation of TmDHFR's concentration, the purification process was optimised for increased protein yield and stability. Earlier protocols for producing TmDHFR involves the use of cation exchange chromatography¹³³ or repeated use of size exclusion chromatography. In the first case, the binding of the enzyme to this resin was not reproducible. In the second case, the clarified crude lysate (after *E. coli* proteins are precipitated by heating at 78 °C¹³³) is usually above the sample size that is recommended for size exclusion and highly viscous for a concentration step. Hence, these methods were unsuitable for producing TmDHFR on the scale required for FTIR measurement. In addition, TmDHFR often aggregates at high concentration due to its low net charge.⁹¹

A new protocol was developed using hydrophobic interaction chromatography (HIC) as the first purification step. Selective screening of binding and elution buffer was carried out because of the relative hydrophobicity of the enzyme and instability in at neutral pH (Appendix III, Table A3). Dam and co-workers previously recommended lower pH buffer for producing stable TmDHFR.⁹¹ Hence, low pH buffers and buffers known to increase protein hydrophobicity were prepared (based on Hoffmeister series) and employed to stabilise TmDHFR in the first step.^{187,188} In the second step of the purification, equimolar concentration of glutamate and arginine were added to the buffer as reported in a protein solubility optimisation protocol.¹⁸⁹ These additives led to significant structural stability of TmDHFR at high concentration. We also noted that the enzyme was more stable when concentrated at room temperature than when concentrated in the cold. Figure 4.5 shows the UV trace of the two purification steps.

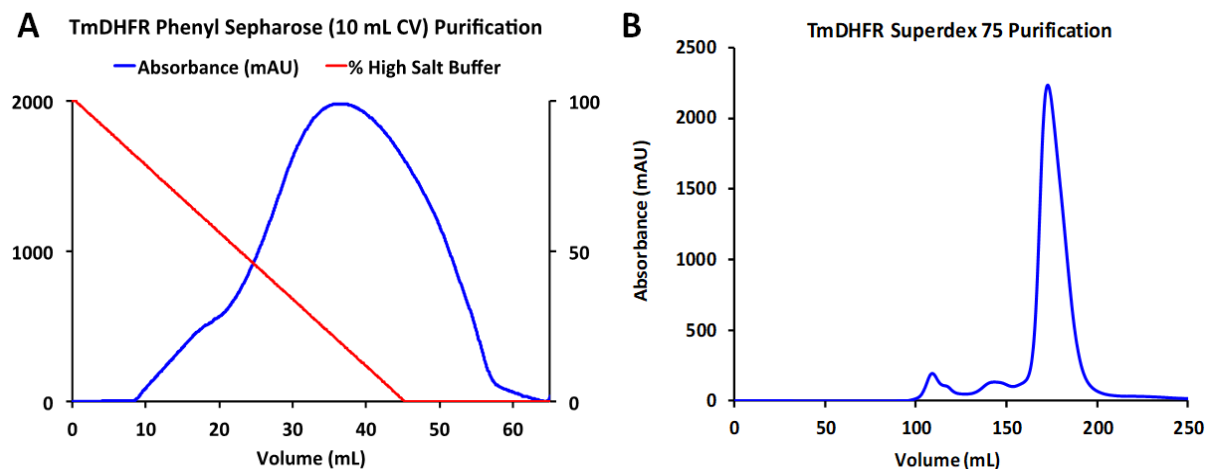


Figure 4.5. UV trace for the purification of TmDHFR (A) hydrophobic interaction chromatography eluting over the 60 mL and (B) size exclusion chromatography with exclusion volume between 170 – 200 mL

4.2.3 VSE spectroscopic measurements

VSE spectroscopy directly relates electric field changes at the active site of an enzyme to the shifts in their vibrational frequencies by using a specific infrared probe. After the high production of all the enzymes, side-chain labelling with Ellman reagent was carried out, followed by several washes with KCN or K¹³CN to produce the nitrile-labelled enzymes for FTIR and ¹³C-NMR, respectively (See Materials and Methods, Section 6.10).¹⁹⁰ Initial optimisation of labelling conditions and FTIR measurement was carried out using glutathione, a well-known tripeptide containing N-terminal glutamate coupled via gamma carboxyl side chain to cysteine and glycine (Appendix III, Table A2 and Figure A9 – A11). Labelling of the enzymes was confirmed by LC/MS (See Appendix III, Figure A12 – A22).

The FTIR absorptions were analysed according to previous reports on VSE spectroscopy.^{51,191,192} A high-resolution FTIR equipped with a Mercury-Cadmium-Telluride (MCT) detector was employed to measure the Stark shifts. Approximately 2.0 – 4.0 mM of the enzymes were employed to measure the vibrational frequency of the probe in the apoenzyme, holoenzyme (E:NADPH), Michaelis complex (E:folate:NADP⁺) and the product ternary complex (E:THF:NADP⁺). Unlike DHF, folate cannot be further oxidized in solution. Thus, the abortive

E:folate:NADP⁺ complex is an excellent mimic of the Michaelis complex (E:DHF:NADPH) and its stability makes it well suited for the study.^{99,120} Ten-fold excess of the ligands were equilibrated with the enzymes to form the complexes. The samples were purged under a streams of nitrogen gas prior to measurement and the temperature of the sample was kept at 20 °C by connecting the liquid cell to a thermocycler (water bath). The spectra were composed of 2000 scans at 1 cm⁻¹ spectra resolution. The peak of the absorption was obtained as the average of second derivative processing as well as first derivative processing and Gaussian fit of the background-subtracted spectra (See Appendix III, Figure A23 and A24). Origin 9.0 of OriginLab software was employed for the data analysis. Uncertainty in absorption energy is reported as the standard deviation of at least two independent measurements.

Direct hydrogen bonding to the probe has been reported to deviate VSE from the Stark model.¹⁹³ Hence, a tandem of IR-NMR calibration curve was developed to correct the hydrogen bond induced deviation.¹⁹³ Consequently, ¹³C-CN labelled enzymes were also produced and the chemical shifts of the ¹³C probe were determined in the same complex used for FTIR measurements. Deviations of the vibrational frequencies from the linear Stark model were elucidated using the reported IR-NMR cross peak analysis,¹⁹³ which revealed that hydrogen bonding was formed with the nitrile probe in all the complex formed by all the DHFR studied with a deviation of ~7 cm⁻¹. This result suggests that correction of the vibrational frequency is unnecessary in our case.¹⁹³

The difference in the vibrational frequency of the nitrile probe in two states (complexes) of the enzyme was converted directly to the local electric field change in the enzymes (Eq 4.1).⁵¹

$$hc\Delta\nu_{obs} = \Delta\vec{\mu}_{probe} \cdot \Delta\vec{F}_{protein} \quad (4.1)$$

where h is Planck's constant; c the speed of light, $\Delta\vec{\mu}_{probe}$ is the difference in dipole moment between the ground and excited states expressed as linear Stark tuning rate (cm⁻¹/(MV/cm)), $\Delta\vec{F}_{protein}$ is the local electric field change experienced by the probe in the protein (in MV/cm), and $\Delta\nu_{obs}$ is the vibrational frequency shift (cm⁻¹).⁵¹ Equation 4.1 has been applied to EcDHFR

based on the convention that the angle between $\Delta\vec{\mu}_{\text{probe}}$ and $\Delta\vec{F}_{\text{protein}}$ are 180° according to reference 51,70. Previously, the Stark tuning rate for nitrile probes ($\Delta\vec{\mu}_{\text{CN}}$) has been determined in different environments and given as $\sim 0.7 \text{ cm}^{-1}/(\text{MV/cm})$.¹⁹⁴ However, the absolute direction of the probe must be determined by either crystallography or computational simulation.¹⁹⁴ The direction of the probe is not a challenge here because it has been confirmed in EcDHFR_{cf} T46C-CN by X-ray crystallography.⁵¹ And it is likely that the nitrile probe in the other homologs will have the same direction with the probe of EcDHFR_{cf} T46C-CN, *vide supra*.

Results from VSE spectroscopy are also studied by computational simulation to predict the energy associated with the vibrational transitions of the probe.¹⁹⁵ Preliminary theoretical calculations by our Spanish collaborators (Prof. Vicent Moliner and Dr. Katazyna Swiderek of Departament de Quimica Fisica I Analitica, Universitat Jaume I, Spain) suggests that hydrogen bonding difference in the complexes of EcDHFR_{cf} T46C-CN contributed significantly to the Stark shifts observed. Although there appear to be some differences in the hydrogen bonding microenvironment of the probe in different complexes, the full-width at half maximum (FWHM) of the absorption peaks were identical for all the complexes formed by EcDHFR but vary from complex to complex in the other homologs.

4.3 Electrostatic changes at the microenvironment of DHFRs

To understand quantitative electrostatic changes at the microenvironment of DHFRs, the difference between the electric field at the active site of EcDHFR_{cf} T46C-CN were first compared to its conformationally-impaired variant EcDHFR_{cf} S148P/T46C-CN. This relationship was then extended to electrostatic changes in the monomeric DHFRs before the rigid dimeric TmDHFR was considered in the last section. The purpose of this study is to understand how DHFRs with diverse conformational dynamics regulate electrostatics at their active site.

4.3.1 Electrostatic changes in the conformationally impaired EcDHFR variant

Earlier report has shown that when Ser148 of EcDHFR is replaced with a Pro, ability of the enzyme to adopt occluded conformation become impaired.¹¹⁷ In IR spectroscopy, this amino acid replacement leads to a redshift of -1.82 cm^{-1} in the apoenzyme (Figure 4.6 and Table 4.1). Using equation 4.1, this shift corresponds to -2.6 MV/cm difference in electric field between the enzymes.

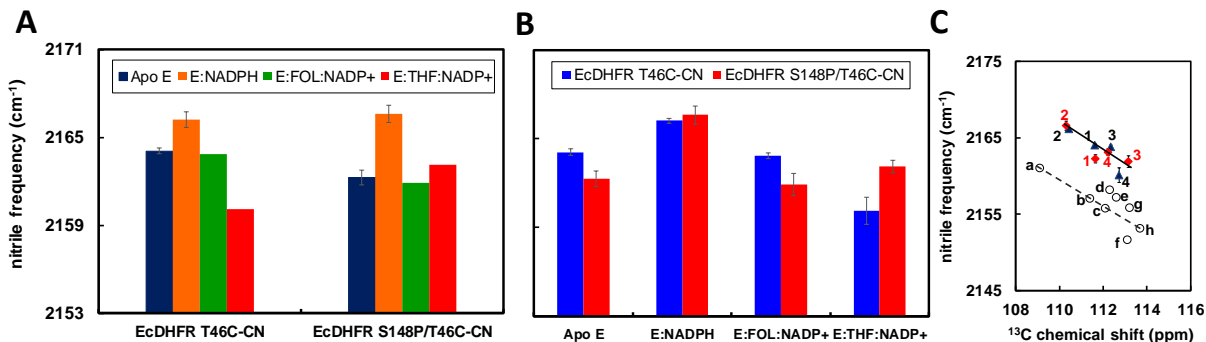


Figure 4.6. (A) Bar charts of the vibrational frequencies of EcDHFR_{cf} T46C-CN and EcDHFR_{cf} S148P/T46C-CN in different complexes. (B) Bar chart comparison between the complexes formed by the enzymes. (C) Calibration of hydrogen bonding interactions of the complexes of EcDHFR_{cf} T46C-¹³CN (dark blue triangles) and EcDHFR_{cf} S148P/T46C-¹³CN (red diamond). The complexes of the enzymes are represented by 1 = apoenzyme, 2 = E:NADPH, 3 = E:FOL:NADP⁺, and 4 = E:THF:NADP⁺. Deviation of $\sim 7\text{ cm}^{-1}$ from Stark calibration was observed. The Stark model is represented by the open circle connected by the broken line,⁵¹ indicating the fit for nitrile calibration in different solvents: a = cyclohexane, b = toluene, c = THF, d = chloroform, e = dichloromethane, f = dimethyl sulphoxide, g = acetone and h = dimethylformamide, obtained from reference 193

The staggering difference in the electrostatic at the active site of the enzymes in their unliganded state indicates differences in the enzyme's ground state structures. Previous NMR spectroscopic studies reported three conformers in the apoenzyme of EcDHFR, one of which resembles the occluded conformer.¹⁹⁶ But molecular dynamics simulation revealed the existence of multiple conformers (up to six metastable states) in EcDHFR when no ligand is bound.¹⁹⁷ Hence, it is possible that the S148P mutation shifted the populations in the enzyme towards other possible conformers.

Notably, the most significant difference between the enzymes is when their Michaelis and product complexes are compared. For EcDHFR_{cf} T46C-CN, a redshift of -3.7 cm⁻¹ (-5.3 MV/cm) was observed when the ligand was changed from the substrate (folate/NADP⁺) to the product (THF/NADP⁺) complex. In contrast, for the conformationally impaired variant, such ligand variation led to a blueshift of 1.2 cm⁻¹ (1.7 MV/cm). This shift was more significant in the EcDHFR_{cf} T46C-CN, which undergoes a conformational change alongside the ligand change. But, more importantly, the conformationally impaired variant experienced a reverse electric field compared to EcDHFR_{cf} T46C-CN, which signify the lack of the occluded conformations in the variant. These results show that electrostatic changes occurred in both enzymes despite their conformational difference. Hence, electrostatic changes at the microenvironment of EcDHFR is not only linked to conformational changes.

Electrostatic changes in the enzymes are therefore induced by the ligand difference, which will only occur after the conversion of substrate to product. EcDHFR adopts the closed conformation in the Michaelis complex, but a minor (4%) population of the enzyme also form the occluded conformation.¹⁰⁹ The formation of product (THF and NADP⁺) in the active site of EcDHFR cause a steric clash between the products as a result of the 1.8 Å overlap between C₄ of the cofactor and C₇ of the puckered THF.⁹⁹ This clash necessitates the reorganisation of the active site to accommodate the ligands.¹⁹⁸ If S148 is present in the enzyme, active site reorganisation in EcDHFR can lead to the formation of the occluded conformation.¹¹⁷ Consequently, the initial 4% population will increase significantly due to the stability of the alternative conformation. An NMR study has shown that the transition of EcDHFR from the closed to the occluded conformations is 10-fold slower than the rate constant of hydride transfer and thus, could not be linked to its chemistry.¹⁰⁹

The transition of EcDHFR to the occluded conformation, however, has been associated with the rate of substrate turnover (k_{cat}) and the prevention of product inhibition.¹²⁰ The conformationally impaired variant, with an electrostatic change of 1.7 MV/cm, only reorganizes its active site to accommodate the nicotinamide moiety of NADP⁺. Crystal structure of the occluded conformation revealed that Met16 and Glu17 of the M20 loop are projected into the active site and sterically block the binding of the nicotinamide moiety of NADP⁺.⁹⁹ Interestingly, enzymes

that lack the occluded conformation show sensitivity to NADP⁺ inhibition.^{98,117,139} For instance, both EcDHFR S148P and MpDHFR were reported to be inhibited by NADP⁺.¹¹⁷ Similarly, human DHFR and a variant of EcDHFR (EcDHFR-N23PP/S148A) were ten times more sensitive to inhibition by NADP⁺ than EcDHFR.⁹⁸ The half-maximal inhibitory concentration (IC₅₀) for HsDHFR was 620 μM while EcDHFR was 5 mM.⁹⁸ These enzymes (that is, HsDHFR and EcDHFR-N23PP/S148A) also bind tightly to endogenous NADP⁺ when expressed in *E. coli*.¹³⁹ Therefore, the binding of the nicotinamide moiety of NADP⁺ within the active site might be linked to this inhibition and explains the small vibrational shift observed in the variant.

4.3.2 Electrostatics changes at the active site of monomeric DHFRs

The distinct position of charges and polar residues in enzymes, even when at some distance from the active site, are thought to be aligned to maximize the interaction of enzymes with their ligands.¹⁹⁹ These charges are shown to reduce the configurational space of bound substrates.^{200,201} However, an adaptation of enzymes to different environments can modify their enzyme-ligand interactions.²⁰² Hence, electrostatic changes at the microenvironment of the mesophilic EcDHFR and EcDHFR S148P, the psychrophilic MpDHFR and the moderately thermophilic BsDHFR were explored along conformationally relevant steps.

In our study of these enzymes, the nitrile probe was found to experience an intense electric field in the holoenzymes leading to high-frequency absorptions of 2166.2 ± 0.15 , 2166.6 ± 0.6 , 2166.1 ± 0.4 , 2162.7 ± 0.4 cm⁻¹ for EcDHFR, EcDHFR S148P variant, BsDHFR and MpDHFR, respectively (Figure 4.7 and Table 4.1). Moderately high vibrational frequencies were also observed when the enzymes are bound to NADP⁺ but the binding of NADPH gave the highest frequency in all the homologs. The cofactor binding domain was shown to have a lower occupancy when NADP⁺ binds to EcDHFR than when NADPH is bound.⁹⁹

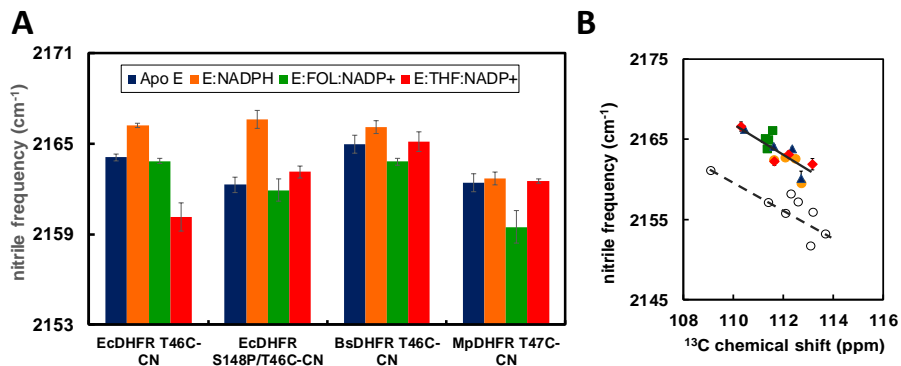


Figure 4.7. (A) Bar charts of the vibrational frequencies of EcDHFR_{cf} T46C-CN, EcDHFR_{cf} S148P/T46C-CN, BsDHFR_{cf} T46C-CN and MpDHFR_{cf} T47C-CN in different complexes. (B) Calibration of hydrogen bonding interactions of the complexes of EcDHFR_{cf} T46C- ^{13}CN (dark blue triangles), EcDHFR_{cf} S148P/T46C- ^{13}CN (red diamond), BsDHFR_{cf} T46C-CN (green square) and MpDHFR_{cf} T47C-CN (orange circle) Deviation from Stark model represented by the open circle connected by a broken line was $\sim 7 \text{ cm}^{-1}$.^{51 193}

The high-frequency absorptions in the holoenzymes also resulted in blueshifts, during the transition of apoenzymes to holoenzymes. These shifts were more significant in EcDHFR and EcDHFR S148P leading to 2.45 and 4.07 cm^{-1} shifts, respectively (equivalent to 3.5 and 5.81 MV/cm) (Figure 4.7 and Table 4.1). However, the blueshifts were less significant in BsDHFR and MpDHFR. The result may be caused by the low affinity of BsDHFR for NADPH (K_M of $\sim 100 \mu\text{M}$) and the structural instability of MpDHFR at the experimental temperature (20 °C).^{90,203} Overall, the enzymes appear to experience similar electrostatic trends when NADPH is bound (Figure 4.6).

When folate binds to the holoenzyme (that is, forming the Michaelis complex), the resultant electric field experienced by the probe in this complex is a reverse of the high-frequency absorption observed in the holoenzymes. In other words, the progression of the enzymes from holoenzymes to the Michaelis complexes resulted in redshifts of similar magnitudes to the blueshifts experienced in the apo-to-holoenzyme transition. The observation was similar in the complex of EcDHFR with either folate:NADP⁺ or folate:NADPH.⁵¹ Since both the holoenzyme and the Michaelis complex adopt the closed conformation, the redshift during this transition

indicate that the binding of folate offsets the initial electric field projected unto the probe by the cofactor

The transition of EcDHFR from the Michaelis (folate:NADP⁺) to the product ternary complex (THF:NADP⁺) has been the major focus of several studies because of the enzyme chemistry and the conformational change that accompanies it.^{12,51,100,117,126} Our study shows that this transition resulted in a redshift of ~4 cm⁻¹ (equivalent to -5.3 MV/cm) in EcDHFR. However, for EcDHFR S148P, BsDHFR and MpDHFR the transition caused blueshifts of 1.2, 1.3 and 3.0 cm⁻¹ (that is, 1.7, 1.8 and 4.3 MV/cm), respectively (Figure 4.7 and Table 4.1).

The fact that EcDHFR S148P, BsDHFR and MpDHFR experienced blueshifts indicate their lack of the occluded conformation as discussed earlier when electrostatic changes in EcDHFR and EcDHFR S148P were compared (Section 4.3.1). These blueshifts were minimal in all the enzymes except in MpDHFR, which was attributed to the unfavourable temperature used. When the experiment was conducted at a lower temperature (5 °C) for MpDHFR, the blueshift dropped significantly to 0.4 cm⁻¹ (Table 4.1). This result shows that the relatively large electrostatic change between the Michaelis and the product complex of EcDHFR arises from the exclusion of the nicotinamide moiety from its binding cleft and the protrusion of the M20 loop into the active site in the occluded conformation.⁹⁹ In all the enzymes, only EcDHFR exhibited a redshift during this transition. Hence, the occluded conformation could be regarded as a binary complex with regards to the active site probe since only the substrate binding cleft is occupied in this conformation.

In all the monomeric enzymes, the electric field of the cofactor and the substrate counteracts in their ternary complexes. That is, the high-frequency absorption experienced by the probe in the holoenzyme is red-shifted and becomes identical to that of the apoenzyme when folate, DHF or THF binds to the substrate binding domain. To understand if this redshift relates to the interaction between the ligands, both EcDHFR and MpDHFR were complexed with MTX:NADPH. In both enzymes, the high-frequency absorptions of the holoenzymes were not reduced in the MTX:NADPH complex (Table 4.1). Instead, the frequencies were identical to that of the holoenzyme. However, the enzymes' complexes with MTX:NADPH have distinctly narrow linewidth (FWHM = 8 cm⁻¹) compared to other complexes. The lineshape might indicate

a less polar microenvironment due to the stronger interaction of the inhibitor with DHFRs.^{49,99} Earlier study that employed deuterated Tyr100 to study electrostatic changes in EcDHFR reported similarity between the electrostatic experienced by the C-D probe in the holoenzyme and the enzyme complex with MTX:NADPH.⁵⁰

Table 4.1. Summary of ^{13}C NMR shifts, the vibrational frequency at maximum peak, and Full Width at Half Maximum (FWHM) values for the IR spectra in monomeric DHFRs (EcDHFR, EcDHFR S148P, BsDHFR and MpDHFR) determined at 20 °C

DHFR	Complex	Vibrational frequency (cm^{-1})	FWHM (cm^{-1})	Chemical shifts (ppm)
$\text{EcDHFR}_{\text{cf}} \text{T46C-CN}$	E	2164.1 ± 0.22	13.5	111.6
	E:NADPH	2166.2 ± 0.15	13.5	110.5
	E:FOL:NADP ⁺	2163.9 ± 0.18	13.2	112.4
	E:THF:NADP ⁺	2160.1 ± 0.93	14.3	112.72
	E:NADP ⁺	2164.6 ± 0.24	13.3	ND
	E:MTX:NADPH	2167.2 ± 0.13	8.4	ND
$\text{EcDHFR}_{\text{cf}} \text{S148P/T46C-CN}$	E	2162.3 ± 0.52	13.1	116.3
	E:NADPH	2166.6 ± 0.60	14.5	110.5
	E:FOL:NADP ⁺	2161.9 ± 0.74	12.11	112.4
	E:THF:NADP ⁺	2163.1 ± 0.41	14.5	112.7
	E:NADP ⁺	2165.2 ± 1.04	14.0	ND
$\text{BsDHFR}_{\text{cf}} \text{T46C-CN}$	E	2165.0 ± 0.61	15.9	111.4
	E:NADPH	2166.1 ± 0.43	16.6	111.6
	E:FOL:NADP ⁺	2163.8 ± 0.23	17.2	111.4
	E:THF:NADP ⁺	2165.1 ± 0.66	14.4	111.3
	E:NADP ⁺	2165.5 ± 0.19	16.2	ND
$\text{MpDHFR}_{\text{cf}} \text{T47C-CN}$	E	2162.4 ± 0.61	13.2	111.7
	E:NADPH	2162.7 ± 0.43	11.5	112.1
	E:FOL:NADP ⁺	2159.5 ± 1.01	12.8	112.7
	E:THF:NADP ⁺	2162.5 ± 0.14	9.9	112.5

Continued from previous page				
	E:MTX:NADPH	2167.4 ± 0.54	8.9	ND
MpDHFR _{cf} T47C-CN at (5 C)	E:FOL:NADP ⁺	2162.4	13.1	ND
	E:THF:NADP ⁺	2162.8	11.9	ND
FOL = folate, ND = not determined				

4.3.3 Different electrostatic trends in monomeric and dimeric DHFRs

Monomeric DHFRs and TmDHFR exhibit different flexibilities, hydride transfer mechanism and transition state dynamics.^{7,45,91,102} In addition, TmDHFR is currently the only chromosomal DHFR that is known to forms a homodimer and highly thermostable with melting temperature (T_m) of ~82 °C.⁹¹ In this study, notable differences between the monomeric DHFRs and the dimeric TmDHFR were observed.

First, from the apoenzyme of TmDHFR to the subsequent complexes formed, the enzyme's probe experienced redshift. (Figure 4.8A). Consequently, the apoenzyme of TmDHFR has the highest vibrational frequency unlike in monomeric DHFRs where the probe experienced the strongest electric field in the holoenzyme. The transition from apoenzyme to holoenzyme in TmDHFR was identical within error. However, equivalent transitions in the monomeric homologs were blueshifts. The binding of folate to the holoenzyme (to form the Michaelis complex) followed a similar redshift with the monomeric homologs, with a frequency shift of -1 cm⁻¹ (equivalent to -1.43 MV/cm). This redshift supports our hypothesis that the ligands' electric fields are counterbalanced in the Michaelis complex. However, the Michaelis to product ternary complex transition in TmDHFR exhibited a redshift of -1.2 cm⁻¹, equivalent to 1.71 MV/cm. In the monomeric enzymes, only EcDHFR exhibited a redshift during this transition. It is possible that TmDHFR has a different mechanism to prevent the inhibition of the NADP⁺ through selective electrostatic interaction with the product complex. These results show that electrostatic changes in TmDHFR follow a different trend to that of monomeric DHFRs.

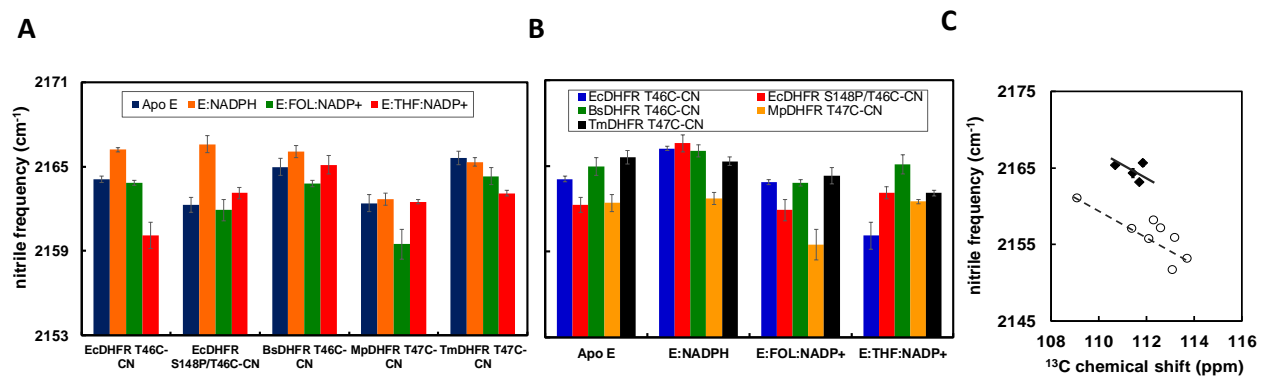


Figure 4.8. (A) Bar charts of the vibrational frequencies of all the DHFRs studied in their different complexes. (B) Bar chart comparison between the complexes formed by the enzymes. (C) Calibration of hydrogen bonding interactions of the complexes of TmDHFR T47C-CN (black diamond). Deviation from Stark model represented by the open circle connected by a broken line was $\sim 7 \text{ cm}^{-1}$.¹⁹³

Table 4.2. Summary of ¹³C NMR shifts, vibrational frequency at maximum peak, and Full Width at Half Maximum (FWHM) values for the IR spectra in TmDHFR determined at 20 °C

DHFR	Complex	Vibrational frequency (cm⁻¹)	FWHM (cm⁻¹)	Chemical shifts (ppm)
TmDHFR T47C-CN	E	2165.6 ± 0.47	11.2	111.9
	E:NADPH	2165.3 ± 0.30	12.9	110.7
	E:FOL:NADP ⁺	2164.3 ± 0.59	15.6	111.4
	E:THF:NADP ⁺	2163.1 ± 0.19	13.0	111.7
	E:NADP ⁺	2165.6 ± 0.44	14.0	ND
FOL is folate, ND = not determined				

4.4 Discussion

All the DHFRs studied here experienced electrostatic changes at their microenvironment when bound to different ligands. The trend of electrostatic changes in EcDHFR S148P was identical to that experienced by BsDHFR and MpDHFR. This result suggests that the interactions of the enzymes with their ligands are conserved. This electrostatic trend was slightly different in EcDHFR due to conformational changes and in TmDHFR because of its structural rigidity.

The structural difference between TmDHFR and the monomeric enzymes studied could account for the different electrostatic trends. Monomeric DHFRs exhibit induced-fit ligand binding while TmDHFR rigidity can be described by the Fischer's lock-and-key model.⁹¹ Consequently, the crystal structure of TmDHFR has a root-means-square-deviation (R.M.S.D) of only 0.5 Å between the unliganded and liganded states.⁹¹ However, movement of the M20 loop in EcDHFR transverse a distance of about 10 Å among other subdomain motions.⁹⁹ In the same way, MpDHFR and BsDHFR exhibit significant flexibilities.^{125,126}

TmDHFR is not only structurally diverse from the monomeric homologs, but its catalytic mechanism also reflects that it has a different electrostatic trend. Monomeric DHFRs form closed conformation to exclude solvent from their active site,⁹⁹ but in TmDHFR the major catalytic loops (M20, FG and GH loops) participates in the dimer interface, which keeps its active site accessible to solvent in all complexes.^{91,102} Because the M20 loop of TmDHFR adopts the open conformation and unable to stabilise the protonated form of DHF (H_3F^+), hydride transfer occurs in the enzyme via a concerted mechanism.⁸³ In contrast, catalysis in EcDHFR under the same condition occurs via a stepwise mechanism, with protonation before hydride transfer.⁸³ Furthermore, enzyme KIE of TmDHFR is temperature-independent over 60 °C,⁷ whereas that of monomeric DHFRs showed significant sensitivity to temperature change, which results in enzyme KIE of above unity at non-physiological temperatures (similar temperature sensitivity was observed in HsDHFR reported previously in chapter 3).^{7,45} This result shows that monomeric DHFRs experienced frictions along their reaction coordinate at lower temperatures but such friction does not occur in TmDHFR.

The high-frequency absorption of the nitrile probe when the enzymes are bound to NADPH might indicate a higher energy structure of the enzymes or might be due to the electric field of the cofactor. The progression of most DHFRs through their catalytic cycle occurs via intermediate interaction with the cofactors by interacting cooperatively with either their substrate or product after the cofactors are bound.^{95,129,160,204} Crystal structures showed that when the cofactor binds to EcDHFR, the substrate binding cleft (involving the B and C helices) is opened by 0.7 Å in comparison to the Michaelis complex.⁹⁹ In addition, a higher energy conformational

sampling has also been observed in the holoenzyme of EcDHFR, which is thought to increase fluctuations in the substrate binding domain.²⁰⁵

The counteraction of this electric field in the ternary complexes of the enzyme might result from the positioning of the cofactor and substrate (or product). The significantly different electrostatics observed in the occluded conformation of EcDHFR can be linked to the exclusion of the nicotinamide ribose moiety from its active site. But for other monomeric DHFRs, their ternary complexes (that is both Michaelis and product complexes) have highly similar electrostatics.

In contrast, the high-absorption frequency observed in holoenzyme was not counterbalanced in the MTX:NAPDH, which can be related to the orientation of MTX when bound to DHFRs. Previously, crystal structure has shown that the pteridine ring of MTX in DHFRs is flipped by 180° around the C₆–C₉ bond, relative to folate (Figure 4.9), which is different from that of the 4-oxo-folates (folate, DHF, THF).⁹⁹ Also, the pyrazine ring of the 4-oxo-folates binds deeper in the active site of DHFRs in comparison to MTX, which creates a vacancy at the active site where the C₆ of folate normally resides.²⁰⁴ Since the electric field of the ligands are aligned in the ternary complex (being vector quantities), the structural difference in the binding of MTX and the vacancy of the C₆ could alter the superposition of the electric fields such that the resultant electric field of the MTX:NADPH complex results in high-frequency vibrations.

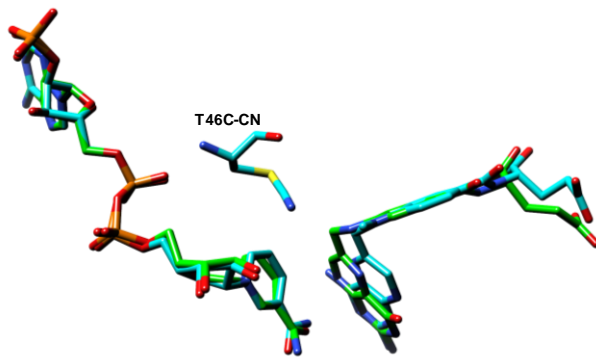


Figure 4.9. Ligands overlay from the crystal structure of EcDHFR in complex with folate:NADP⁺ (green, PDB: 1RX2) and MTX:NADP⁺ (cyan, PDB: 4P66) showing the pteridine ring flip of MTX and wider distance from the nitrile probe. The thiocyanate probe from PDB:4P66 is shown as cyan, similar to ligands from the crystal structure.

The difference in the electrostatics of ternary complex with MTX and the 4-oxo-folates suggests that MTX does not represent the transition state structure of DHFRs.⁹⁹ Previously, VSE study using a C-D probe of [D4] Tyr100-EcDHFR revealed a unique microenvironment in the Michaelis complex (enzyme:folate:NADP⁺) that was not observed in the enzyme:MTX:NADPH complex.⁵⁰ The electrostatics of EcDHFR when complex with MTX/NADPH and folate/NADP⁺ were also found to be different when studied by the C-D bond probe of *d*₃Met20.⁴⁹ Although MTX is usually employed to mimic the transition state of DHFRs, our result shows that the electrostatics of the enzymes when bound to MTX:NADPH did not reflect that of the transition state of DHFRs (at least for EcDHFR and MpDHFR studied).

The transition state of DHFRs should properly align the cofactor and the substrate for catalysis. In earlier studies, geometric and angular orientation, as well as the proximity of reacting ligands, were suggested to be important for enzyme-catalysed reactions.²⁰⁶ This alignment of ligands might explain the difference in the reaction rates of diverse substrates. This observation is consistent with the report that photoactivation is required for a hydride transfer from NADPH to MTX to produce 5,8-dihydro-MTX.²⁰⁷ Since folate is structurally identical to MTX, the difference in their catalysis may be due to their alignment in the active site with respect to the cofactor. Substrate orientation has also been found to be important for catalysis in other enzymes. One example is xanthine oxidase where the substrate can adopt two configurations.²⁰⁸ Only one of the two orientations was found to be favourable for catalysis and produces 98% of the product mixture.²⁰⁸

One may, therefore, predict that the alignment of the cofactor and the substrate in DHFRs caused counterbalancing of the electric field in the ternary complexes and might play a role in their catalysis. Studies have shown that the p*K*_a of protonated DHF (H₃F⁺) in EcDHFR changes from 2.6 in solution to 4.0 in the binary complex and 6.5 in the Michaelis complex.²⁰⁹ Molecular dynamics simulation also showed that the p*K*_a of the substrate in the Michaelis complex is significantly influenced by first, the proximity of the nicotinamide and pterin rings and second, the parallel orientation between the rings.¹⁰⁵ In fact, the previous electrostatic investigation of EcDHFR using nitrile label showed that two-thirds of the total electric field calculated at the active site of EcDHFR arose from the cofactor-substrate positioning.⁵¹ Although the study

inaccurately concluded that conformational changes “facilitate hydride transfer” in EcDHFR despite showing that amino acid residues contributed only one-third of the total electric field.⁵¹ Our results from other DHFRs that lack such flexibility supports that ligand alignment might have a greater effect on their catalysis. Overall, these studies agree with our hypothesis that the positioning of the cofactor and the substrate in DHFRs is important for modulating the pK_a of the substrate and aiding the chemical step.

Since electrostatics in the DHFRs studied here exhibit similar trends as they transit from one catalytic step to another despite having different flexibilities, their ability to catalyse identical reactions signify that electrostatics preorganisation at their active site dictate their catalytic rate. Homologs of other enzymes have also been found to possess identical electric fields at their active site.²¹⁰ A study on lysozymes from bacteriophage, egg white and human found that the three homologs have similar charge distribution and electrostatic components at their active site, which was said to account for a rate enhancement of >37 kJ/mol.²¹⁰ The total electric field calculated for the cofactor-substrate positioning and amino-acid residues in EcDHFR might result from preorganisation of the enzyme active site.

4.5 Conclusions

Electrostatic changes in DHFRs from organisms adapted to different temperatures were studied. A comparison between the monomeric DHFRs (EcDHFR, its conformationally impaired variant-EcDHFR S148P, BsDHFR and MpDHFR) show that the large electrostatic changes in EcDHFR between the Michaelis and the product complex correlated with its conformational transition. However, the close-to-occluded transition relates to a product-induced active site reorganisation and is not linked to the chemical step since other homologs experience similar active site reorganisation to a lesser degree.

Our investigation revealed that electrostatic trends in the enzymes are generally identical with the highest-frequency absorption observed in their holoenzymes. This high-frequency absorption was different in TmDHFR, where it occurred in both the apo and holoenzymes. The interaction of the enzymes with their ligands follows a similar pattern.

The high-frequency absorption of the holoenzyme is balanced out when the ligand bound to the substrate binding domain is correctly oriented and aligned with the cofactor. Since this cofactor-substrate positioning has been shown to influence the substrate pK_a , we hypothesise that the ligand-ligand interaction achievable through electrostatic preorganisation of the enzyme's active site, have the greater influence on catalysis. Atomic-level details from computational calculations will be pursued to test the importance of the cofactor-substrate interaction and how they relate to catalysis in these enzymes. Our experimental data show that DHFRs have conserved active site electrostatic interactions despite having different dynamic flexibilities.

5 . Summary and future work

5.1 Summary and future work

The importance of an optimised purification technique for studying enzyme kinetics was revealed in our investigation on HsDHFR. The truncated substrate (pABG) was shown to lessen the kinetic complexity observed when folate is used for stabilising the enzyme during purification. Also, the tight binding 28.9 kDa protein impurity observed during HsDHFR purification was sequenced and identified as β -lactamase. Because β -lactamase is produced to select the gene for expression in *E. coli*, the protein was removed by producing HsDHFR in a *Kan-R* vector. This optimisation afforded the purification of HsDHFR in two-steps rather than the five-step recommended in the previous report.¹³⁹ Further study would involve understanding the interaction between HsDHFR and TEM-1 β -lactamase by co-crystallising the enzymes, especially with the aim of developing an inhibitor for either HsDHFR or TEM-1 β -lactamase since both enzymes are known therapeutic targets.

The chemical step of HsDHFR was also studied by both steady and pre-steady-state kinetics. The cryo-kinetic approach developed for reducing the transient kinetics of the enzyme allowed us to determine the temperature-dependence of the chemical step with a substrate KIE of ~2.3. In addition, we estimated hydride transfer in the enzyme under physiological condition and finally, the contribution of protein dynamics to the chemical step of the enzyme was elucidated by temperature-dependence of the substrate and enzyme KIEs. In this report, H-tunnelling contribution was not observed in the chemical step of HsDHFR even at non-physiological and sub-zero temperatures. However, dynamic coupling due to recrossing events at the dividing surface of the reaction predominate only at non-physiological temperature. Our result suggests that the quantitative description of enzyme catalysis require the inclusion of other quantum mechanical factors to provide a comprehensive explanation to experimental observations. Our findings from HsDHFR and other DHFRs clearly showed that the couplings of non-equilibrium protein dynamics to the chemical coordinate of these enzymes are minimized at their respective physiological temperatures. It would be interesting to investigate how mutation of the active site residue Phe31 to other residues will influence the dynamics of HsDHFR.

The investigation of the electrostatic at the microenvironment of EcDHFR, EcDHFR S148P BsDHFR and MpDHFR showed that the interaction of the enzymes with their ligands follow a conserved electrostatic trend. Except for the dimeric TmDHFR, which appears to follow the trend only partly. This is because, in most DHFRs, the formation of the closed DHFR–substrate complex excludes solvent molecules from the active site and allows the formation of a geometric and electrostatic environment conducive to hydride transfer. But in TmDHFR, such conformational sampling is prevented by the enzyme's dimeric structure, which compromises the electrostatic preorganization.¹¹⁵ The fact that enzymes from different environmental niches and with different flexibilities display the same electrostatic behaviour in their cofactor–substrate interactions strongly suggest that electrostatic preorganisation of the active site that maximises the interaction of the ligands is crucial for catalysis. There are still many questions that our VSE study could not answer. Some of which are: how do the enzymes differentiate their substrate and products if the ternary complexes of DHFRs are similar electrostatically? How did the mutations introduced altered the electrostatics of the native enzymes? Are these vibrational shifts due to electrostatic changes or artefacts of experimental conditions such as temperature, pH and buffer system? Therefore, we hope to answer some of these questions in further investigations.

Overall, our study revealed that unlike dynamic effects which vary between DHFRs, electrostatics of the enzymes, especially in reactive complexes appears to be conserved. However, the enzymes have diverse electrostatics in their product complexes, suggesting that product release were tuned to the different species. Our results indicate electrostatic preorganisation in the reactive complex is crucial to enzyme catalysis.

6 . Materials and methods

6.1 Bacterial strains and preparation

6.1.1 Bacterial strains

The different *Escherichia coli* strains employed in these experiments are listed below (Table 6.1).

Table 6.1. E. coli strains used for experiments

Strains	Use
XL1 Blue	Plasmid amplification
BL21(DE3)	Gene expression of DHFR from <i>Homo sapiens</i> (HsDHFR), <i>Bacillus stearothermophilus</i> (BsDHFR) and <i>Moritella profunda</i> (MpDHFR)
BL21- Star (DE3)	Gene expression of DHFR from <i>Escherichia coli</i> (EcDHFR)
BL21-CodonPlus (DE3)-RP	Gene expression of DHFR <i>Thermatoga maritima</i> (TmDHFR)

6.1.2 Competent cells

6.1.2.1 Calcium chloride buffer I

Calcium chloride (1.11g) was dissolved in 80 mL of deionised water. The total volume was taken to 100 mL. The solution was sterilized in an autoclave.

6.1.2.2 Calcium chloride buffer II

Calcium chloride (1.11g) and glycerol (15% v/v) were dissolved in 80 mL of deionised water. The total volume was taken to 100 mL before sterilization by autoclave.

6.1.2.3 Competent cell preparation

50 µL of the desired strain (Table 6.1) were incubated in 20 mL of non-selective LB media overnight in a shaker at 37 °C. In the case of XL1-blue, tetracycline (50 mg/L) was added to the pre-culture and chloramphenicol (34 mg/L) for BL21-CodonPlus (DE3)-RP cell. 1 mL of the overnight culture was used to inoculate 100 mL of non-selective LB media (with 50 mg/L of tetracycline and 34 mg/L of chloramphenicol for XL1-Blue and BL21-CodonPlus (DE3)-RP cells respectively). The optical density of the cell was monitored to 0.89 at 600 nm. The cells were then placed on ice for 15 min before harvesting by centrifugation at 4000 rpm and the supernatant discarded. The cells were re-suspended in 60 mL of calcium chloride buffer I, incubated on ice for a further 15 min before repeating the centrifugation step. The cells were finally re-suspended in 6 mL of calcium chloride buffer II, divided into 50-100 µL aliquots and flash frozen in liquid nitrogen. The cells were then stored in -80 °C freezers.

6.1.3 Super-competent cells

6.1.3.1 Rubidium chloride buffer I

Potassium acetate (0.294 g), rubidium chloride (1.21 g), calcium chloride (1.11 g), manganese chloride (0.692 g) and glycerol (15% v/v) were dissolved in 80 mL deionised water. The pH was adjusted to 5.8 using dilute acetic acid and the volume was taken to 100 mL with deionised water. A 0.2 µm syringe filter was used to sterilize the solution and then stored at 4 °C.

6.1.3.2 Rubidium chloride buffer II

3-(N-Morpholino) propanesulfonic acid (0.209 g), rubidium chloride (1.21 g), calcium chloride (0.832 g) and glycerol (15% v/v) were dissolved in 80 mL deionised water. The pH was adjusted to 6.5 using sodium hydroxide and the volume was taken to 100 mL with deionised water. A 0.2 µm syringe filter was used to sterilize the solution and then stored at 4 °C.

6.1.3.3 Super-competent cell preparation

Super-competent cells were prepared in the same manner as with competent cells but with calcium chloride buffer I and II replaced with rubidium chloride buffer I and II

6.2 Growth media and sterile solutions

6.2.1 Luria-Burtani (LB) medium

Tryptone (10.0 g) yeast extract (5.0 g) and NaCl (10.0 g) were dissolved in 0.8 L of deionised water and the final volume taken to 1 L. The solution was sterilized in an autoclave at 121 °C and stored at 4 °C. The required antibiotic was added before use.

6.2.2 LB agar plates

Tryptone (10.0 g) yeast extract (5.0 g), NaCl (10.0 g) and agar (15.0 g) were dissolved in 0.8 L of deionised water and the final volume taken to 1 L. The solution was sterilized in an autoclave at 121 °C. The required antibiotic was added once the solution was cool enough to hold by hand and the LB agar poured into Petri dishes under sterile conditions. The agar was allowed to solidify in the Petri dishes and the plates stored at 4 °C.

6.2.3 Auto-induction media (AIM)

6.2.3.1 AIM premix I

Glucose (5.0 g), lactose (100 g) and NH₄Cl (26.7 g) were premixed. 3.5 g of the premix were added directly to the media.

6.2.3.2 AIM premix II

KH₂PO₄ (68 g), Na₂HPO₄ (71 g) and glycerol 50% (v/v) were dissolved in 0.3 L deionised water and the final volume made up to 1 L before sterilization by autoclave.

6.2.3.3 Trace Element

EDTA (5mg) was dissolved in 0.8 L of deionised water and the pH adjusted to 7.5. FeCl₃.6H₂O (0.83 g), ZnCl₂ (84 mg), CuCl₂.2H₂O (13 mg), CoCl₂.6H₂O (10 mg), H₃BO₃ (10 mg) and MnCl₂.4H₂O (1.6 mg) were added and the final volume adjusted to 1 L with deionised water. The solution was sterilized in an autoclave at 121 °C and stored at 4 °C.

6.2.3.4 Preparation of AIM

Tryptone (5.0 g), yeast extract (2.5 g), NaCl (5.0 g) and MgCl₂ (0.5 g) were added into a 2L conical flask and made up to 0.5 L using deionised water. The solution was sterilized by

autoclave at 121 °C and allowed to cool to room temperature. AIM premix I (3.5 g) was weighed into sterile tube and added directly to the media. AIM premix II (10 mL) and trace element (500 µL) were added to the solution. The required antibiotic was added prior to use.

6.2.4 Minimal (M9) media

6.2.4.1 Preparation of M9 media

Na₂HPO₄ (6.76 g), KH₂PO₄ (3.0 g) and NaCl (0.5 g) were added to 1 L of deionised water and sterilized by autoclave. After the solution is cooled, glucose (4.0 g), NH₄Cl (1.0 g), 1 M MgSO₄ (2 mL), 1 M CaCl₂ (100 L) and trace element (1 mL) were added to the sterile M9 salt solution. The required antibiotic was added under sterile condition immediately before use.

6.2.4.2 Preparation of isotopically labelled media

Na₂HPO₄ (6.76 g), KH₂PO₄ (3.0 g) and NaCl (0.5 g), 1 M MgSO₄ (2 mL), 1 M CaCl₂ (100 L) and trace element (1 mL) were added 0.9 L of deionised water. [¹⁵N, 98%] NH₄Cl (1.0 g) and [¹³C₆, 99%] glucose (4.0 g) were added and the volume taken to 1 L with deionised water. The media was sterilized by passing through a sterile 0.2 µm filter and stored at 4 °C. The required antibiotic was added under sterile condition immediately before use.

6.2.5 Sterile solutions

6.2.5.1 Ampicillin stock solution

Ampicillin (400 mg) was dissolved in 4 mL deionised water to give a concentration of 100 mg/mL. The solution was filtered with a sterile 0.2 µm syringe filter, aliquoted and stored at -20 °C.

6.2.5.2 Kanamycin solution

Kanamycin (200 mg) was dissolved in 4 mL deionised water to give a concentration of 50 mg/mL. The solution was filtered with a sterile 0.2 µm syringe filter, aliquoted and stored at -20 °C.

6.2.5.3 Chloramphenicol solution

Chloramphenicol (340 mg) was dissolved in 10 mL ethanol to give a concentration of 34 mg/mL. The solution was filtered with a sterile 0.2 µm syringe filter, aliquoted and stored at -20 °C.

6.2.5.4 Isopropyl-β-D-1-thiogalactopyranoside (IPTG) solution

Isopropyl-β-D-1-thiogalactopyranoside (IPTG) (360 mg) was dissolved in 3 mL deionised water to give a concentration of 120 mg/mL. The solution was filtered with a sterile 0.2 µm syringe filter, aliquoted and stored at -20 °C.

6.2.5.5 50% (v/v) glycerol solution

100 mL of glycerol was added to 100 mL deionised water to give 50% (v/v) solution of glycerol. The solution was sterilized in an autoclave at 121 °C for 20 minutes and stored at 4 °C.

6.3 DNA manipulation

6.3.1 DNA visualization

6.3.1.1 TAE buffer stock solution

Tris base (242 g), glacial acetic acid (57.1 mL) and 100 mL EDTA (0.5 M, pH 8.0) were dissolved in 900 mL deionised water. The volume was taken to 1 L with deionised water. Immediately prior to use, the solution was diluted in a 1:49 ratio with deionised water.

6.3.1.2 Agarose gel electrophoresis

Agarose gels were prepared in a 1% agarose (w/v) ratio using dilute TAE buffer. The solution was preheated in a microwave for 2 min before pouring into a mould to set. 2 µL DNA green buffer (FastDigest buffer from ThermoFisher Scientific) was added to the DNA sample which was then loaded onto the gel. The run programme was set at a current of 80 mA for 1 hr before being placed in a dilute ethidium bromide solution for 10 minutes whilst shaking. The DNA bands were visualized using a Syngene GeneFlash UV light box (Syngene, Cambridge, UK) and compared to a molecular weight standard run on the same gel.

6.3.2 DNA extraction and purification

6.3.2.1 DNA miniprep

A single colony from an agar plate, or a spike from a glycerol stock, harbouring the required transformed plasmid was used to inoculate 10 mL of LB medium (with the appropriate antibiotic selection marker) and incubated overnight on a shaker at 37 °C. Cells were then harvested by centrifugation at 4000 rpm for 15 minutes. The QIAprep spin miniprep kit (QIAGEN, Crawley, UK) was used with EconoSpin All-in-1 mini spin columns (Epoch Biolabs, Inc, TX, USA) to purify the plasmid following the manufacturer's protocol.

6.3.2.2 Agarose gel DNA purification

The required samples are subjected to agarose gel electrophoresis and the DNA visualized by staining with DNA Safe Stain from New England Biolab. The DNA bands were then visualized on a DNA lab view equipped with blue-led light and the appropriate DNA bands cut from the agarose gel using a razor blade. DNA was extracted from the agarose gel using QIAquick gel extraction kit (QIAGEN, Crawley, UK) with EconoSpin All-in-1 mini spin columns (Epoch Biolabs, Inc, TX, USA) following the manufacturer's protocol.

6.3.3 Sub-cloning of gene

6.3.3.1 Restriction digest of DNA

Restriction enzymes NdeI/BamHI were employed to excise human DHFR (HsDHFR) gene from a pET21 (a) and similar treatment of the acceptor plasmid, pET(28a). The restriction digest was performed sequentially; first, NdeI was added to the required plasmid and incubated for 4 hours at 37 °C. NdeI was afterwards heat deactivated at 60 °C for 20 minutes before the addition of the BamHI which was activated for a further 4 hours at 37 °C. Restriction enzymes were removed via agarose gel purification.

6.3.3.2 Ligation of DNA into expression vector

Following successful restriction digest and agarose gel purification of HsDHFR gene and pET 28(a) plasmid. The gene and the plasmid were ligated to form a new expression vector construct. Plasmid and gene in a 1:5 ratio were incubated with 2 µL T4 DNA ligase buffer and

sterile deionised water (sterilized by passing through a 22 µm syringe filter) in a volume of 20 µL. 1 µL T4 DNA ligase was added and the ligation reaction incubated at 16 °C overnight. The reaction was immediately transformed into super-competent cells. The hexa-his tag region in the pET28 (a) was subsequently removed by overlapping primer site-directed mutagenesis method.

6.3.4 Site-directed mutagenesis (SDM)

Site-directed mutagenesis was used to delete, insert or alter DNA bases at specific location in a gene. Primer designs were based on established technique and a published strategy to aid exponential amplification of the desired plasmid sequence. For both type of primer design method, similar components (Table 6.2) and conditions

Table 6.2. Components of the SDM reactions

Components	Volume (µL)
dNTPs (40 mM total, 10 mM each NTP)	0.5
Forward primer (62.5 ng/µL)	1
Reverse primer (62.5 ng/µL)	1
Template plasmid (5-15 ng/µL)	1
pfU polymerase buffer + MgCl ₂	2.5
Sterile dH ₂ O	Make up to 25 µL
pfU polymerase (1 unit/ µL)	0.5

Table 6.3. Conditions used for the SDM reactions

Step	Temperature (°C)	Time (min)
Initial denaturation	96	3
Denaturation*	96	1
Annealing	60	1
Elongation	72	2 per kilo bp
Final Elongation	72	30

*The denaturation, annealing and elongation step was cycled 16 times

6.3.4.1 Primer design

Quick-change require the design of complementary primers following specific primer parameters published in the manufacturer's manual. Specific primers (Table 6.4) are designed using this kit. Primers were designed with the appropriate mutation on each primer; however, each primer is also designed to overlap with the template.²¹¹ The overlapping region of the primer should have a melting temperature (T_m) of about 5 - 10 °C above the T_m of the complementary region between the primers. This method was used to design primers for deleting the hexa-histidine tag region of the HsDHFR gene ligated into pET 28(a). The yield from the SDM is exponential, hence could be successfully transformed into calcium competent cells.

Table 6.4. Primers for Quikchange and overlapping site-directed mutagenesis technique

Primer	Sequence
HsDHFR-Del1	5' AGCCATCATAGCCATATGGTGGGTTCGCTGAATTGTATCGTC 3', 5' CATATGGCTATGATGGCTGCTGCCGATGGTATATCTCCTTC 3'
HsDHFR-Del2	5' GAGATATAACCATGGTGGGTTCGCTGAATTGTATCGTCGCCGTTTC 3' 5' CAGCGAACCCACCATGGTATATCTCCTTCTTAAAGTTAAACAAAAA TTATTCTAGAGG 3'
EcDHFR-T46C ^b	5' GTGATTATGGGCCGCCATT <u>GCTGGGA</u> ATCAATCGGTC 3' 5' GACCGATTGATTCCC <u>CAGCA</u> ATGGCGGCCATAATCAC 3'
EcDHFR-S148P ^a	5' CAGAACCTCACAGCTATTCTTGAGATTCTGG 3' 5' CTGTGAGGGTTCTGCGCATCAGCATCGTG 3'
BsDHFR-C73V ^a	5' GAAGGC <u>GTC</u> CTGGTACTGCATAGCCTGGAAGAAGTG 3' 5' GTACCAGG <u>ACGC</u> CTTCCGGACGAAAGCTACGGTTC 3'
BsDHFR-T46C ^a	5' CGTAAAT <u>GCTT</u> GAAGCGATGGCGTCCGCT 3' 5' CGCTCAA <u>AGCA</u> TTACGACCCATTACAATGGCATGACC 3'
MpDHFR-TAATAA ^a	5' CGTGTAA <u>ATAATA</u> AGGATCCGAATTGAGCTCCGTCGACAAGC 3' 5' CGGAT <u>CCTTATT</u> TTAACACGTTCCAGCAGCGAGAAGCGGTAATTG 3'
MpDHFR-C105F ^a	5' CTATAACCA <u>ATT</u> CTGGCAGCTGCGGACCGCCTGTACC 3' 5' CTGCCAG <u>AAATT</u> GGTTAGATGGTGCACCGCCGATAATCATC 3'

Continued from previous page	
MpDHFR-T47C ^a	5' CGCAACT <u>G</u> CTTCGAAAGCATTGGTCGTCGCCG 3' 5' GCTTCGAAG <u>C</u> AGTTGCGACCCATCACAAATCGGTTGCCA 3'
TmDHFR-T47C ^b	5'CGTTGTGATGGGAAGAAC <u>T</u> GCTTCGAGGAAATAGGAAGACC 3' 5'GGTCTTCCTATTCCCTGAAG <u>C</u> AGATTCTCCCATCACAAACG 3'
^a Overlap SDM protocol employed and ^b Standard Quikchange mutagenesis protocols	

6.3.5 Transformation of DNA into competent cells

The appropriate competent cells and plasmid DNA were thawed slowly on ice. 2 µL plasmid DNA solutions (5 – 10 µL in the case of SDM and ligation reactions) was mixed gently with the competent cells. The DNA/cell mixture was incubated on ice for at least 20 minutes, heat shocked at 42 °C for 45 seconds and returned to ice for at least 2 minutes. Non-selective LB medium (1 mL) was added to the DNA/cell mixture and incubated on a shaker at 37 °C for 1 hr. Cells were harvested by centrifugation on bench top centrifuge (Eppendorf centrifuge 5415R) for 1 minute at 13,000 rpm and the supernatant solution discarded. The cell pellet was re-suspended in 100 µL LB medium, plated on agar plates containing the appropriate antibiotic selection and incubated at 37 °C overnight in an oven.

6.4 Gene Expression

6.4.1 Production of unlabelled DHFRs

6.4.1.1 IPTG induction

E. coli cells containing a plasmid harbouring the target gene (picked directly from a plate or from glycerol stocks stored in the -80 °C freezer) were incubated overnight in antibiotic selective LB medium (10 – 100 mL) at 37 °C overnight in a shaker. This overnight culture was used to inoculate LB medium with the appropriate antibiotic (1 mL of culture per 100 mL of LB medium). The cultures were incubated at 37 °C until optical density of the medium reached 0.6 at 600 nm. IPTG (0.5 – 1.0 mM) was added to the LB medium and incubated for the

required time and temperature (Table 6.5). The induced cells were harvested via centrifugation at 4000 rpm for 20 min.

6.4.1.2 Auto-induction

Cell culture preparation where similar to when IPTG is used for induction except the overnight culture are inoculated in AIM medium with the appropriate antibiotic (1 mL of culture per 100 mL of AIM medium). After overnight growth the large-scale expression are carried out until OD₆₀₀ is between 0.6 – 0.8. The shaker is then adjusted to the appropriate temperature and left for the required time. The induced cells were harvested via centrifugation at 4000 rpm for 20 minutes.

Table 6.5. Conditions for gene expression in E. coli

DHFR	E. coli expression strain	Media for expression	Induction temperature (°C)	Time (hr)
HsDHFR	BL21 (DE3)	IPTG (1.0 mM)	25	O/N
EcDHFR	BL21 (DE3)	Auto-induction	25	O/N
		IPTG (0.5 mM)	37	
TmDHFR	BL21-CodonPlus (DE3)-RP	IPTG (0.5 mM)	22	O/N
MpDHFR	BL21 (DE3)	IPTG (0.5 mM)	16	O/N
BsDHFR	BL21–Star TM (DE3)	Auto-induction	25	O/N

6.4.2 Isotopically labelled enzymes

Cells containing a plasmid harbouring the target gene (picked directly from a plate or from glycerol stocks stored in the -80 °C freezer) were incubated overnight in antibiotic selective M9 medium (10 – 100 mL) at 37 °C overnight in a shaker. This overnight culture was used to inoculate M9 medium with the appropriate antibiotic (10 mL of culture per 100 mL of medium). The cultures were incubated at 37 °C until OD₆₀₀ equal 0.8 – 0.9. IPTG (0.5 – 1.0 mM) was added to the M9 medium and incubated for the required time and temperature. The induced cells were harvested via centrifugation at 4000 rpm for 20 minutes. The isotopically

labelled enzyme was produced with a similar protocol in M9 medium supplemented with heavy isotopes of glucose and NH₄Cl.

6.5 Enzyme purification

6.5.1 Phosphate stock solutions

6.5.1.1 1 M KH₂PO₄

KH₂PO₄ (68.1 g) was added to 450 mL of deionised water. The volume was made up to 500 mL and the solution stored at 4 °C.

6.5.1.2 1 M K₂HPO₄

K₂HPO₄ (87.1 g) was added to 450 mL of deionised water. The volume was made up to 500 mL and the solution stored at 4 °C.

6.5.2 Purification buffers

6.5.2.1 Purification buffer A (Anion-exchange HsDHFR)

Tris base (6.1 g) and ethylene diamine tetraacetate (EDTA, 1.86 g) were added to 900 mL of deionised water. The pH was adjusted to 8.5 using 6 M HCl and the total volume taken to 1 L with deionised water. The solution was filtered and degassed via vacuum pump (Vacuubrand GmbH + CO KG, MD4C, Werthein, Germany). β-mercaptoethanol (βME, 350 µL) was added to the solution to give a final concentration of 50 mM Tris, 5 mM EDTA and 5 mM βME. The solution was stored at room temperature.

6.5.2.2 Purification buffer B (Anion-exchange HsDHFR)

Tris base (6.1 g), NaCl (58.44 g) and EDTA (1.86 g) were added to 900 mL of deionised water. The pH was adjusted to 8.5 using 6 M HCl and the total volume taken to 1 L with deionised water. The solution was filtered and degassed via vacuum pump (Vacuubrand GmbH + CO KG, MD4C, Werthein, Germany). βME (350 µL) was added to the solution to give a final concentration of 50 mM Tris, 1 M NaCl, 5 mM EDTA and 5 mM βME. The solution was stored at room temperature.

6.5.2.3 Purification buffer C (Size exclusion HsDHFR)

Tris base (6.1 g), KCl (7.44 g), paraaminobenzoyl glutamate (pABG, 0.399 g) and EDTA (1.86 g) were added to 950 mL of deionised water. The pH was adjusted to 8.0 using 6 M HCl and the total volume taken to 1 L with deionised water. The solution was filtered and degassed via vacuum pump (Vacuubrand GmbH + CO KG, MD4C, Werthein, Germany). βME (350 µL) was added to the solution to give a final concentration of 50 mM Tris, 100 mM KCl, 1.5 mM pABG, 5 mM EDTA and 5 mM βME. The solution was stored at room temperature.

6.5.2.4 Purification buffer D (Anion-exchange EcDHFR)

1 M KH₂PO₄ (19.5 mL), 1 M K₂HPO₄ (30.5 mL), NaCl (0.58 g) and EDTA (1.86 g) were added to 850 mL of deionised water. The pH was adjusted to 7.0 using 1 M NaOH and the total volume taken to 1 L with deionised water. The solution was filtered and degassed via vacuum pump (Vacuubrand GmbH + CO KG, MD4C, Werthein, Germany). βME (350 µL) was added to the solution to give a final concentration of 50 mM potassium phosphate, 10 mM NaCl, 5 mM EDTA and 5 mM βME. The solution was stored at room temperature.

6.5.2.5 Purification buffer E (Anion-exchange EcDHFR)

1 M KH₂PO₄ (19.5 mL), 1 M K₂HPO₄ (30.5 mL), NaCl (58.44 g) and EDTA (1.86 g) were added to 850 mL of deionised water. The pH was adjusted to 7.0 using 1 M NaOH and the total volume taken to 1 L with deionised water. The solution was filtered and degassed via vacuum pump (Vacuubrand GmbH + CO KG, MD4C, Werthein, Germany). βME (350 µL) was added to the solution to give a final concentration of 50 mM potassium phosphate, 1 M NaCl, 5 mM EDTA and 5 mM βME. The solution was stored at room temperature.

6.5.2.6 Purification buffer F (Size exclusion and IR buffer EcDHFR and BsDHFR)

1 M KH₂PO₄ (19.5 mL), 1 M K₂HPO₄ (30.5 mL), NaCl (1.17 g) and EDTA (1.86 g) were added to 850 mL of deionised water. The pH was adjusted to 7.4 using 1 M NaOH and the total volume taken to 1 L with deionised water to give a final concentration of 50 mM potassium phosphate pH 7.4, 20 mM NaCl and 1 mM EDTA. The solution was filtered, degassed via vacuum pump (Vacuubrand GmbH + CO KG, MD4C, Werthein, Germany) and stored at room temperature.

6.5.2.7 Purification buffer G (Hydrophobic interaction TmDHFR)

Sodium acetate (6.1 g), Na₂SO₄ (58.44 g) and EDTA (1.86 g) were added to 850 mL of deionised water. The pH was adjusted to 5.0 using glacial acetic acid and the total volume taken to 1 L with deionised water. The solution was filtered and degassed via vacuum pump (Vacuubrand GmbH + CO KG, MD4C, Wertheim, Germany). βME (350 µL) was added to the solution to give a final concentration of 50 mM Na acetate, 1 M Na₂SO₄ pH 5.0, 5 mM EDTA and 5 mM βME. The solution was stored at room temperature.

6.5.2.8 Purification buffer H (Hydrophobic interaction TmDHFR)

Bis-tris propane (6.1 g) and ethylene diamine tetraacetate (EDTA, 1.86 g) were added to 950 mL of deionised water. The pH was adjusted to 6.0 using 1 M HCl and the total volume taken to 1 L with deionised water. The solution was filtered and degassed via vacuum pump (Vacuubrand GmbH + CO KG, MD4C, Wertheim, Germany). β-mercaptopropanoic acid (βME, 350 µL) was added to the solution to give a final concentration of 20 mM Bis-tris pH 6.0, 5 mM EDTA and 5 mM βME. The solution was stored at room temperature.

6.5.2.9 Purification buffer I (Size exclusion and IR buffer TmDHFR)

1 M KH₂PO₄ (58.5 mL), 1 M K₂HPO₄ (91.5 mL), NaCl (1.17 g) and EDTA (1.86 g) were added to 800 mL of deionised water. The pH was adjusted to 7.4 using 1 M NaOH and the total volume taken to 1 L with deionised water to give a final concentration of 150 mM potassium phosphate pH 7.4, 20 mM NaCl and 1 mM EDTA. The solution was filtered, degassed via vacuum pump (Vacuubrand GmbH + CO KG, MD4C, Wertheim, Germany) and stored at room temperature.

6.5.2.10 Purification buffer J (Anion-exchange MpDHFR)

1 M KH₂PO₄ (7.8 mL), 1 M K₂HPO₄ (12.2 mL) and EDTA (1.86 g) were added to 850 mL of deionised water. The pH was adjusted to 7.0 using 1 M NaOH and the total volume taken to 1 L with deionised water. The solution was filtered and degassed via vacuum pump (Vacuubrand GmbH + CO KG, MD4C, Wertheim, Germany). βME (350 µL) was added to the solution to give a final concentration of 20 mM potassium phosphate pH 7.0, 5 mM EDTA and 5 mM βME. The solution was stored at room temperature.

6.5.2.11 Purification buffer K (Anion-exchange MpDHFR)

1 M KH₂PO₄ (7.8 mL), 1 M K₂HPO₄ (12.2 mL), NaCl (58.44 g) and EDTA (1.86 g) were added to 850 mL of deionised water. The pH was adjusted to 7.0 using 1 M NaOH and the total volume taken to 1 L with deionised water. The solution was filtered and degassed via vacuum pump (Vacuubrand GmbH + CO KG, MD4C, Werthein, Germany). βME (350 μL) was added to the solution to give a final concentration of 20 mM potassium phosphate pH 7.0, 1 M NaCl, 5 mM EDTA and 5 mM βME. The solution was stored at room temperature.

6.5.2.12 Purification buffer L (Size exclusion and IR buffer MpDHFR)

1 M KH₂PO₄ (7.8 mL), 1 M K₂HPO₄ (12.2 mL), NaCl (1.17 g) and EDTA (1.86 g) were added to 850 mL of deionised water. The pH was adjusted to 7.4 using 1 M NaOH and the total volume taken to 1 L with deionised water to give a final concentration of 20 mM potassium phosphate, 20 mM NaCl and 1 mM EDTA. The solution was filtered, degassed via vacuum pump (Vacuubrand GmbH + CO KG, MD4C, Werthein, Germany) and stored at room temperature.

6.5.2.13 Purification buffer M (Anion-exchange BsDHFR)

Tris base (6.1 g) and ethylene diamine tetraacetate (EDTA, 1.86 g) were added to 900 mL of deionised water. The pH was adjusted to 9.0 using 6 M HCl and the total volume taken to 1 L with deionised water. The solution was filtered and degassed via vacuum pump (Vacuubrand GmbH + CO KG, MD4C, Werthein, Germany). β-mercaptoproethanol (βME, 350 μL) was added to the solution to give a final concentration of 50 mM Tris pH 9.0, 5 mM EDTA and 5 mM βME. The solution was stored at room temperature.

6.5.2.14 Purification buffer N (Anion-exchange BsDHFR)

Tris base (6.1 g), NaCl (58.44 g) and EDTA (1.86 g) were added to 900 mL of deionised water. The pH was adjusted to 9.0 using 6 M HCl and the total volume taken to 1 L with deionised water. The solution was filtered and degassed via a vacuum pump (Vacuubrand GmbH + CO KG, MD4C, Werthein, Germany). βME (350 μL) was added to the solution to give a final concentration of 50 mM Tris pH 9.0, 1 M NaCl, 5 mM EDTA and 5 mM βME. The solution was stored at room temperature.

6.5.2.15 Purification buffer O (Anion-exchange NADPD)

Tris base (1.21 g) was dissolved in 400 mL of deionised water and the pH was adjusted to 9.0 and the total volume taken 500 mL with deionised water to give a final concentration of 20 mM Tris. The buffer was filtered and degassed on a vacuum pump (Vacuubrand GmbH + CO KG, MD4C, Weitheim, Germany) and stored at room temperature.

6.5.2.16 Purification buffer P (Anion-exchange NADPD)

Tris base (1.21 g) and NaCl (29.22 g) were dissolved in 400 mL of deionised water and the pH was adjusted to 9.0 and the total volume taken 500 mL with deionised water to give final concentration of 20 mM Tris and 1 M NaCl. The buffer was filtered and degassed on a vacuum pump (Vacuubrand GmbH + CO KG, MD4C, Weitheim, Germany) and stored at room temperature.

6.5.3 Purification methods

6.5.3.1 Purification method for HsDHFR

Frozen pellets of harvested HsDHFR cell expression (Section 6.4) were resuspended in pH adjusted purification buffer A (Section 6.5.2.1) with 2 mM pABG and 0.1 mM PMSF protease inhibitor (Melford).¹³⁹ The suspension was lysed by sonication (pulse rate: 5 seconds, on cycle and 10 seconds, off cycle) for 15 minutes. The solution was clarified by centrifugation at 4 °C, 18,000 rpm for 30 minutes. The supernatant was passed through a 22 µm syringe filter before applying to a Q-sepharose column (~70 mL CV) pre-equilibrated with buffer A. The flow-through was collected and the column washed with 2 CV of buffer A until baseline absorbance was reached. A salt gradient was applied in two stages from 0.0 – 0.5 M NaCl (50% purification buffer B, section 6.5.2.2) over 2 CV followed by 0.5 – 1.0 M NaCl (100% buffer L) over 1 CV. Fractions were collected (12 mL) and the absorbance monitored at 280 nm. All fractions were analysed by SDS-PAGE and DHFR activity assay.

The fractions containing the target protein were concentrated to ~10 mL on 10,000 Da membrane using Amicon ultrafiltration device. The concentrated sample was applied to a Superdex75 (26/260) column pre-equilibrated with buffer C (Section 6.5.2.3). The fractions

collected (10 mL) were analysed by SDS-PAGE and activity assay of DHFR to identify the fractions containing HsDHFR due to high absorptivity of pABG at 280 nm. Protein concentration was determined by Bicinchoninic acid assay method (Section 6.8.1).

6.5.3.2 Purification method for EcDHFR

Frozen pellets of harvested EcDHFR cell expression (Section 6.4) were resuspended in buffer D (Section 6.5.2.4). The suspension was lysed by sonication (pulse rate: 5 seconds, on cycle and 10 seconds, off cycle) for 15 minutes. The solution was clarified by centrifugation at 4 °C, 18,000 rpm for 30 minutes. The supernatant was passed through a 22 µm syringe filter before applying to a Q-sepharose column (\sim 70 mL CV) pre-equilibrated with buffer D. The flow-through was collected and the column washed with 2 CV of buffer D until baseline absorbance was reached. A salt step of 0.2 M (20% purification buffer E, section 6.5.2.5) over 2.5 CV followed by 2 stages of salt gradient from 0.2 M – 0.5 M NaCl (50% purification buffer E) over 2 CV then 0.5 – 1.0 M NaCl (100% buffer E) over 1 CV. Fractions were collected (12 mL) and the absorbance monitored at 280 nm. All fractions were analysed by SDS-PAGE and DHFR activity assay.

The fractions containing the target protein were concentrated to \sim 10 mL on 10,000 Da membrane using Amicon ultrafiltration device. The concentrated sample was applied to a Superdex75 (26/260) (\sim 320 mL) column pre-equilibrated with buffer F for FTIR experimental samples (Section 6.5.2.6) . Fractions of 10 mL were collected over 1.5 CV and analysed by both SDS-PAGE and activity assay of DHFR to identify the fractions containing EcDHFR.

6.5.3.3 Purification method for TmDHFR

Frozen pellets of harvested TmDHFR cell expression (Section 6.4) were resuspended in buffer G (Section 6.5.2.7). DNase solution (1 µg/mL) and RNase (1 µg/mL) were added to the lysis buffer. The suspension was lysed by sonication (pulse rate: 5 seconds, on cycle and 10 seconds, off cycle) for 15 minutes. The solution was heated at 37 °C for 30 minutes and heat shocked at 75 °C for 30 minutes on a water bath to precipitate *E. coli* proteins. The suspension was then clarified by centrifugation at 4 °C, 18,000 rpm for 30 minutes. The supernatant was passed

through a 22 µm syringe filter before applying to a phenyl Sepharose column (~15 mL CV) pre-equilibrated with buffer G. The flow-through was collected and the column washed with 8 CV of binding buffer G before elution with 6 CV of buffer H (section 6.5.2.8) applied 1 CV at a time. Fractions were collected (20 mL) before being analysed by SDS-PAGE and DHFR activity assay.

The fractions containing the target protein were concentrated to ~10 mL on 10,000 Da membrane using Amicon ultrafiltration device at room temperature. The concentrated sample was applied to a Superdex75 (26/260) (~320 mL) column pre-equilibrated with buffer I (Section 6.5.2.9). Fractions of 10 mL were collected over 1.5 CV and analysed by both SDS-PAGE and activity assay of DHFR to identify the fractions containing TmDHFR.

6.5.3.4 Purification method for MpDHFR

Frozen pellets of harvested MpDHFR cell expression (Section 6.4) were resuspended in buffer J (Section 6.5.2.10). The suspension was lysed by sonication (pulse rate: 5 seconds, on cycle and 10 seconds, off cycle) for 15 minutes. The solution was clarified by centrifugation at 4 °C, 18,000 rpm for 30 minutes. The supernatant was passed through a 22 µm syringe filter before applying to a Q-sepharose column (~70 mL CV) pre-equilibrated with buffer J. The flow-through was collected and the column washed with 2 CV of buffer J until baseline absorbance was reached. Salt gradient were applied in two stages from 0.0 M – 0.5 M NaCl (50% purification buffer K, section 6.5.2.11) over 4 CV then 0.5 – 1.0 M NaCl (100% buffer K) over 1 CV. Fractions were collected (12 mL) and the absorbance monitored at 280 nm. All fractions were analysed by SDS-PAGE and DHFR activity assay.

The fractions containing the target protein were concentrated to ~10 mL on 10,000 Da membrane using Amicon ultrafiltration device. The concentrated sample was applied to a Superdex75 (26/260) (~320 mL) column pre-equilibrated with buffer L (Section 6.5.2.12). Fractions of 10 mL were collected over 1.5 CV and analysed by both SDS-PAGE and activity assay of DHFR to identify the fractions containing MpDHFR.

6.5.3.5 Purification method for BsDHFR

Frozen pellets of harvested BsDHFR cell expression (Section 6.4) were resuspended in buffer M (Section 6.5.2.13). The suspension was lysed by sonication (pulse rate: 5 seconds, on cycle and 10 seconds, off cycle) for 15 minutes. The solution was heat shocked at 55 °C for 30 minutes on a water bath to precipitate *E. coli* proteins. The solution was clarified by centrifugation at 4 °C, 18,000 rpm for 30 minutes. The supernatant was passed through a 22 µm syringe filter before applying to a DEAE column (\sim 50 mL CV) pre-equilibrated with buffer M.

The flow-through was collected and the column washed with 2 CV of buffer M until baseline absorbance was reached. Salt gradient were applied in two stages from 0.0 M – 0.5 M NaCl (50% purification buffer N, section 6.5.2.14) over 4 CV then 0.5 – 1.0 M NaCl (100% buffer N) over 1 CV. Fractions were collected (12 mL) and the absorbance monitored at 280 nm. All fractions were analysed by SDS-PAGE and DHFR activity assay.

The fractions containing the target protein were concentrated to \sim 10 mL on 10,000 Da membrane using Amicon ultrafiltration device. The concentrated sample was applied to a Superdex75 (26/260) (\sim 320 mL) column pre-equilibrated with buffer F (Section 6.5.2.6). Fractions of 10 mL were collected over 1.5 CV and analysed by both SDS-PAGE and activity assay of DHFR to identify the fractions containing BsDHFR.

6.6 Ligand synthesis and purification

6.6.1 Dihydrofolate (DHF)

Folic acid (400 mg) was dissolved in a minimal volume of 5 M NaOH and added to 80 mL of 10% L-ascorbic acid solution (pH 6.0). The pH of the solution was readjusted to 6.0 if a change in pH occurred due to the mixture. The mixture was stirred under N₂ and sodium dithionite (4.4 g) added. The reaction was cooled on ice for 5 minutes and the pH slowly lowered to 2.8 by the addition of 1 M HCl. The mixture was centrifuged at 4, 4000 rpm for 10 minutes. The above step was repeated by dissolving the pellet in 80 mL of 10% L-ascorbic acid. After which the pellet was re-suspended in acetone (20 mL), purged with N₂ and re-centrifuged. The washing

step and centrifugation was repeated once more with acetone and then with diethyl ether. The product was dried with N₂ and stored at -20 °C in a N₂ purged, foil wrapped container.

6.6.2 Synthesis, purification and storage of (R)-[4-²H]-NADPH

Thermoanaerobacter brockii ADH (1 mg) and NADP⁺ (7 mg) were dissolved in purification buffer O (2 mL, section 6.5.2.15) and d8-2H-isopropanol (0.2 mL) was added. The reaction mixture was incubated at 40 for 10 minutes and loaded onto a SAX10 (4X250 mm) anion exchange column equilibrated with purification buffer M. Salt (NaCl) gradient was applied from 0.0 -1.0 M (100% purification buffer P, section 6.5.2.16) over 30 mins. Absorbance at 260 and 340 nm were monitored, and fractions collected when absorbance at 340 nm increased. DHFR assay method was used to ascertain the eluted NADPD. The fractions containing the heavy cofactor were pooled, aliquoted, lyophilized and stored at -80 °C.

6.7 SDS-PAGE

6.7.1 Resolving buffer

Tris base (27.23 g) was dissolved in 80 mL of deionised water and the pH adjusted to 8.8. The final volume was taken to 150 mL.

6.7.2 Stacking buffer

Tris base (6.0 g) was dissolved in 80 mL of deionised water and the pH adjusted to 6.8. The final volume was taken to 150 mL.

6.7.3 SDS sample loading buffer

Tris base (6.0 g) was dissolved in 80 mL of deionised water and the pH adjusted to 6.8. The final volume was taken to 150 mL.

6.7.4 Running buffer stock

Tris base (30.3 g), glycine (144.0 g) and SDS (10.0 g) were dissolved in 900 mL of deionised water. The final volume was taken to 1 L with deionised water. Buffer was diluted 1: 9 with deionised water prior to use.

6.7.5 SDS staining buffer

Coomassie Blue G250 (110 mg) was dissolved in ethanol (10 mL) and the volume taken to 900 mL with deionised water. The solution was acidified with concentrated HCl (4 mL) and the final volume was taken to 1 L with deionised water.

6.7.6 Resolving gel (12%)

30% acrylamide/bis-acrylamide (4 mL), resolving buffer (2.5 mL, section 6.6.1), 10% (w/v) SDS (100 µL) and deionised water (3.4 mL) were mixed together. Immediately prior to pouring, freshly made 10% ammonium persulfate (APS, 100 µL) and N,N,N',N'-tetramethylenediamine (TEMED, 20 µL) were added and the solution gently mixed to initiate polymerisation.

6.7.7 Stacking gel (5.0%)

30% acrylamide/bis-acrylamide (0.83 mL), resolving buffer (1.25 mL, section 6.6.1), 10% (w/v) SDS (50 µL) and deionised water (2.85 mL) were mixed together. Immediately prior to pouring, freshly made 10% ammonium persulfate (APS, 50 µL) and N,N,N',N'-tetramethylenediamine (TEMED, 10 µL) were added and the solution gently mixed to initiate polymerisation.

6.7.8 SDS-PAGE protocol

The resolving gel was prepared (Section 6.6.6) and poured into an SDS-PAGE mould up to 90% and allowed to polymerise. Stacking gel was also prepared (section 6.6.7) and poured. A comb was inserted to create loading wells. Fraction samples (10 µL) were incubated with sample loading buffer (Section 6.6.3) for 10 minutes at 85 and loaded onto the gel. Running buffer (section 6.6.4) was added and gel allowed to run at 160V for 50 minutes. The gel was washed twice with water after heating in the microwave for 1 minute. Preheated SDS staining buffer (section 6.6.5) was then applied to the gel and the protein bands were visualized using a Syngene Gene Flash UV light box (Syngene, Cambridge, UK). The bands were compared to a protein standard run on the same gel.

6.8 Protein concentration

6.8.1 Bicinchoninic acid (BCA) assay

BCA assay is used to determine the total level of protein in a solution. In this assay, two molecules of bicinchoninic acid chelate a single Cu⁺ ion, forming a purple water-soluble complex that strongly absorbs light at 562 nm. Unlike Bradford assay, the protein backbone contributes to absorption intensity alongside cysteine, tryptophan and tyrosine residues. The reactions are measured using plate reader.

6.8.2 UV/Vis spectrophotometer

Filtered and degassed potassium phosphate (50 mM, pH 7.0) was used. The Beer-Lambert law was used to calculate the concentration (mg mL⁻¹) of all the protein solution using Shimadzu UV/Vis spectrophotometer:

$$A = \varepsilon \cdot c \cdot l \quad (6.1)$$

where A = absorbance at the given wavelength, ε = the extinction coefficient, c = concentration of the sample and l = the pathlength of the cuvette (cm). Average extinction coefficients for proteins at 210, 215 and 220 nm ($\varepsilon = 20, 15, 11 \text{ mL mg}^{-1} \text{ cm}^{-1}$ respectively) were used. The concentration in mg mL was divided by the molecular weight of the protein (~18,000 g mol⁻¹), to give a molar concentration)

The absorbance of the protein samples was also determined at 280 nm and used in combination with the previously calculated enzyme concentration to determine the extinction coefficient of the enzyme at 280 nm using the Beer-Lambert equation.

$$\varepsilon = \frac{A}{c \cdot l} \quad (6.2)$$

Due to the higher extinction coefficient of enzymes at 210, 215 and 220 nm, the calculated extinction coefficient of the enzyme was used to determine the enzyme concentration at 280 nm using Shimadzu UV/Vis spectrophotometer.

Table 6.6. Extinction coefficients employed to calculate the concentration of DHFRs measured at 280 nm

Enzymes	Approximate extinction coefficient at 280 nm
EcDHFR	31,117
TmDHFR	30,008
MpDHFR	26,032
BsDHFR	24,095

6.9 Protein characterisation

6.9.1 Assay buffer

1 M K₂HPO₄ (12.3 mL), 1 M KH₂PO₄ (7.7 mL), NaCl (1.17 g) were added to 150 mL deionised water. The pH was adjusted to 7.0 and the total volume taken to 200 mL to give a final concentration of 50 mM potassium phosphate pH 7.0 and 100 mM NaCl. The solution was filtered and degassed via vacuum pump (Vacuubrand GmbH + CO KG, MD4C, Wertheim, Germany). The solution was stored at room temperature.

6.9.2 Steady-state

Steady state turnover numbers (k_{cat}) were measured under saturating conditions by monitoring the linear decrease in the absorbance of the reduced cofactor NADPH at 340 nm with time *via* UV spectroscopy. For all the steady state kinetics reported in this work, 8-50 nM DHFR was incubated with NADPH/NADPD (100 μM) in the appropriate assay buffer for 60 seconds at the experimental temperature, to avoid hysteresis, prior to the addition of DHF (100 μM) to initiate the reaction.

6.9.3 Michaelis-Menten constant (K_M) measurement

Michaelis constants were measured following the same method as k_{cat} (Section 6.9.2), except that an enzyme concentration of 10-20 nM was used. The concentration of NADPH was varied from 0.1 to 200 μM, and of the concentration of DHF was varied from 0.1 to 100 μM. When

the concentration of one substrate was varied, that of the other was maintained at 100 μM . Each data point is the result of three independent measurements. The Michaelis-Menten equation was fit to the change in initial rate with concentration using SigmaPlot 10.

6.9.4 Stopped-flow (pre-steady state) measurement

Pre-steady state kinetic experiments were performed on Hi-Tech TgK stopped-flow spectrophotometer. Hydride transfer rate constants were measured following the fluorescence resonance energy transfer from the protein to the reduced cofactor NADPH. The reaction mixture was excited at 292 nm and the emission was measured using an output filter with a cut-off at 400 nm. DHFR (20-40 μM syringe concentration) was incubated with NADPH or NADPD (10-20 μM) at the experimental temperature for at least 3 minutes to avoid hysteresis. Then the reaction was started by rapidly mixing with an equal volume of dihydrofolate (200-400 μM).

6.9.5 CD

All circular dichroism spectroscopy was carried out using a ChirascanTM spectrometer (Applied Photophysics Limited, UK).

5 mM potassium phosphate buffer (pH 7) was used to record the thermal melting temperature of the various enzymes used. The buffer was sterilised with a 0.2 μm syringe filter and degassed *via* vacuum pump. A blank run was always taken of the buffer alone before starting the experiment.

The signal obtained from CD experiments was converted into mean residue ellipticity (Θ_{MRE}) using:

$$\Theta_{\text{MRE}} = \Theta / 10.\text{n.c.l} \quad (6.3)$$

where: Θ = CD signal in millideg, n = number of backbone peptide bonds (*i.e.* number of amino acid residues - 1), c = molar concentration of sample, and l = pathlength of cuvette used in cm. Typically a 1 mm pathlength cuvette was used to monitor the CD spectrum of DHFR from 190-400 nm using $\sim 10 \mu\text{M}$ enzyme.

6.10 Thiocyanate Labelling

6.10.1 Enzyme thiocyanate (SCN) labelling

Each enzyme containing a single cysteine residue was labelled using NTCB 1.1 molar equivalence and the release of 2-nitro-5-thiobenzoate (TNB) anion at spectrophotometer absorbance at 412 nm. However, in the second step 12 mM KCN was used to wash the enzyme three times with concentration step after each wash. Excess labelling reagent and TNB anions were removed by passing the labelled enzyme through Sephadex G-25 column pre-equilibrated with appropriate purification buffer (purification buffer F, I and L for EcDHFR/BsDHFR, TmDHFR and MpDHFR, respectively). Thiocyanate labelled enzyme were concentrated to 1.5 – 4 mM for FTIR measurements. Enzyme labelling was confirmed by ESI-MS due to a mass increase of 25 Da (See Appendix III, Figure A12 – A22).

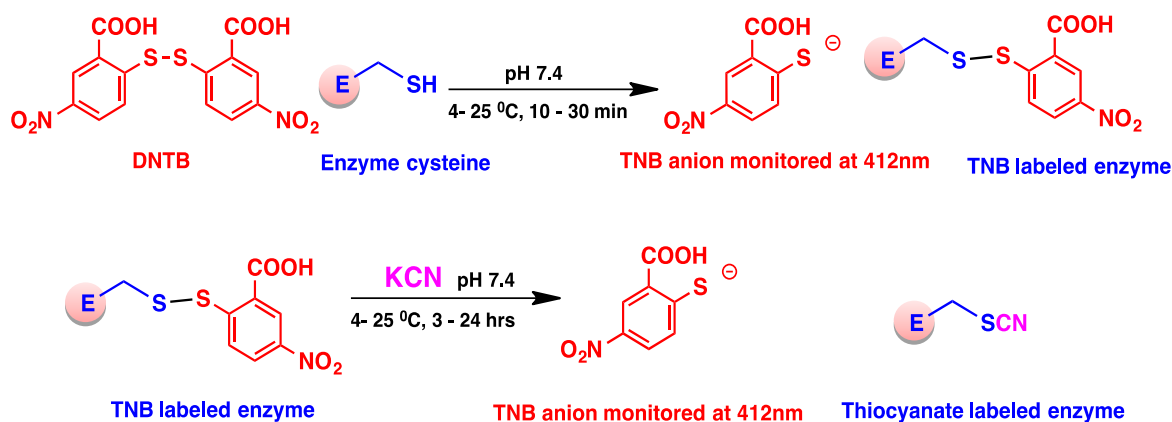


Figure 6.1. Scheme for the post-translational modification of cysteine residues to produce nitrile labelled enzyme.

6.10.2 Enzyme ^{13}C -thiocyanate (S^{13}CN) labelling

The ^{13}C -thiocyanate labelling was carried out in similar manner to the natural abundance thiocyanate labelling. However, 5, 5'-dithiobis-2-nitrobenzoic acid (DNTB) was used and K^{13}CN was finally used to cleave the mixed disulphide to give ^{13}C -labelled thiocyanate.

6.10.3 Fourier Transform Infrared spectroscopy (FTIR)

Approximately 2.0 – 4.0 mM of the enzymes (EcDHFR_{cf} T46C-CN, EcDHFR_{cf} S148P/T46C-CN, BsDHFR_{cf} T46C-CN, MpDHFR_{cf} T47C-CN, TmDHFR T47C-CN) were employed to measure the vibrational frequency of the probe in the apoenzyme, holoenzyme (E:NADPH), Michaelis complex mimic (E:folate:NADP⁺) and the product ternary complex (E:THF:NADP⁺) similar to previous studies.^{99,120} Ten-fold excess of the ligands were equilibrated with the enzymes to form the complexes. The samples were purged under nitrogen prior to measurements and the temperature of the samples were kept constant at 20 °C by connecting the liquid cell to a thermocycler (water bath). Each spectrum was composed of 2000 scans at 1 cm⁻¹ spectra resolution and the peak of the absorption was obtained as the average of second derivative processing, first derivative processing and Gaussian fit of the background-subtracted spectra using Origin 9.0, OriginLab software (See Appendix III, Figure A23 - A24). Uncertainty in absorption energy is reported as the standard deviation of at least two independent measurements.

6.10.4 Nuclear magnetic resonance spectroscopy (NMR)

The NMR spectroscopy samples were prepared according to previous report with 2.0 mM of labelled protein, 10 mM ligands with 2.5 mM of 3-(trimethylsilyl)-1-propanesulfonic acid sodium salt as external standard. Each sample was purged with nitrogen and protected from light before measurement on a Varian INOVA-600 NMR.

6.10.5 Errors and propagations

The errors in this work are reported as the standard error of the mean (σ_M) as in Equation 6.4 which is defined as the standard deviation (Equation 6.5) of the values in the sample divided by the square root of the sample size.

$$\sigma_M = \frac{\sigma}{\sqrt{n}} \quad (6.4)$$

Where X is each value measured in the sample, M is the mean of the sample and n is the sample size

$$\sigma = \sqrt{\frac{\sum (X - M)^2}{(n-1)^2}} \quad (6.5)$$

6.10.5.1 Propagations of errors

In this thesis the effect of the uncertainty of values directly measured experimentally (X or Y) on the uncertainty of a function based up on them (Z) was calculated using Equations 6.6-9. The equation used is dependent on the treatment of X and Y in order to obtain the value of Z.

If $Z = X + Y$ or $Z = X - Y$ then

$$\Delta Z = \sqrt{(\Delta X^2 + \Delta Y^2)} \quad (6.6)$$

If $Z = X * Y$ or $Z = X/Y$ then

$$\Delta Z = Z \sqrt{\left(\frac{\Delta X}{X}\right)^2 + \left(\frac{\Delta Y}{Y}\right)^2} \quad (6.7)$$

If $Y = \ln X$ then

$$\Delta Y = \frac{\Delta X}{X} \quad (6.8)$$

$Y = e^X$ then

$$\Delta Y = \Delta X * e^X \quad (6.9)$$

where X and Y are independently measured values, ΔX and ΔY are their errors or uncertainty, and Z is the calculated value and ΔZ is its propagated error.

References

1. Quinn, D. M. & Sikorski, R. S. Enzymatic Rate Enhancements. Wiley, John Wiley & Sons, Ltd. *eLS* 1–7 (2014).
2. Kazemi, M., Himo, F. & Åqvist, J. Enzyme catalysis by entropy without Circe effect. *Proc. Natl. Acad. Sci.* **113**, 2406–2411 (2016).
3. Fried, S. D. & Boxer, S. G. Electric Fields and Enzyme Catalysis. *Annu. Rev. Biochem.* **86**, 387–415 (2017).
4. Garcia-Viloca, M., Gao, J., Karplus, M. & Truhlar, D. G. How Enzymes Work: Analysis by Modern Rate Theory and Computer Simulations. *Science (80)*. **303**, 186–195 (2004).
5. Wolfenden, R. Transition state analogues for enzyme catalysis. *Nature* **223**, 704–705 (1969).
6. Kamerlin, S. C. L. & Warshel, A. At the dawn of the 21st century: Is dynamics the missing link for understanding enzyme catalysis. *Proteins Struct. Funct. Bioinforma.* **78**, 1339–1375 (2010).
7. Luk, L. Y. P., Loveridge, E. J. & Allemand, R. K. Protein motions and dynamic effects in enzyme catalysis. *Phys. Chem. Chem. Phys.* **17**, 30817–30827 (2015).
8. Lichtenthaler, F. W. 100 Years Schlussel-Schloss-Prinzip: What Made Emil Fischer Use this Analogy? *Angew. Chemie Int. Ed. English* **33**, 2364–2374 (1995).
9. Pauling, L. Molecular Architecture and Biological Reactions. *Chem. Eng. News* **24**, 1375–1377 (1946).
10. Koshland, D. E. The Key-Lock Theory and the Induced Fit Theory. *Angew. Chemie Int. Ed.* **33**, 2375–2378 (1995).
11. Klinman, J. P. & Kohen, A. Hydrogen tunneling links protein dynamics to enzyme catalysis. *Annu. Rev. Biochem.* **82**, 471–96 (2013).
12. Francis, K., Stojković, V. & Kohen, A. Preservation of protein dynamics in

- dihydrofolate reductase evolution. *J. Biol. Chem.* **288**, 35961–35968 (2013).
13. Sutcliffe, M. J. & Scrutton, N. S. A new conceptual framework for enzyme catalysis: Hydrogen tunneling coupled to enzyme dynamics in flavoprotein and quinoprotein enzymes. *Eur. J. Biochem.* **269**, 3096–3102 (2002).
 14. Hammes-Schiffer, S. & Benkovic, S. J. Relating protein motion to catalysis. *Annu. Rev. Biochem.* **75**, 519–541 (2006).
 15. Hanoian, P., Liu, C. T., Hammes-Schiffer, S. & Benkovic, S. Perspectives on electrostatics and conformational motions in enzyme catalysis. *Acc. Chem. Res.* **48**, 482–489 (2015).
 16. Pu, J., Gao, J. & Truhlar, D. G. Multidimensional tunneling, recrossing, and the transmission coefficient for enzymatic reactions. *Chem. Rev.* **106**, 3140–3169 (2006).
 17. Singh, P., Abeysinghe, T. & Kohen, A. Linking Protein Motion to Enzyme Catalysis. *4*, 1192–1209 (2011).
 18. Hammes, G. G., Benkovic, S. J. & Hammes-Schiffer, S. Flexibility, diversity, and cooperativity: Pillars of enzyme catalysis. *Biochemistry* **50**, 10422–10430 (2011).
 19. Kohen, A. Kinetic Isotope Effects as Probes for Hydrogen Tunneling in Enzyme Catalysis. *Prog. React. Kinet. Mech.* **28**, 119–156 (2003).
 20. Fenwick, R. B., Esteban-Martín, S. & Salvatella, X. Understanding biomolecular motion, recognition, and allostery by use of conformational ensembles. *Eur. Biophys. J.* **40**, 1339–1355 (2011).
 21. Toney, M. D., Castro, J. N. & Addington, T. A. Heavy-Enzyme Kinetic Isotope Effects on Proton Transfer in Alanine Racemase. *J. Am. Chem. Soc.* **135**, 2509–2511 (2013).
 22. Gutteridge, A. & Thornton, J. Conformational change in substrate binding, catalysis and product release: An open and shut case? *FEBS Letters* **567**, 67–73 (2004).
 23. Joel Loveridge, E., Allemand, R. K., Loveridge, E. J. & Allemand, R. K. Chapter 8. Direct Methods for the Analysis of Quantum-Mechanical Tunnelling: Dihydrofolate Reductase. in *Quantum Tunnelling in Enzyme-Catalysed Reactions* 179–198 (2009).

24. Sassa, A., Beard, W. A., Shock, D. D. & Wilson, S. H. Steady-state, Pre-steady-state, and Single-turnover Kinetic Measurement for DNA Glycosylase Activity. *J. Vis. Exp.* 1–9 (2013).
25. Bhabha, G. *et al.* A Dynamic Knockout Reveals That Conformational Fluctuations Influence the Chemical Step of Enzyme Catalysis. *Science (80)*. **332**, 234–238 (2011).
26. Northrop, D. B. The Expression of Kinetic Isotope Effects during the Time Course of Enzyme-Catalyzed Reactions. **193**, 177–193 (1989).
27. Meek, S. J., Pitman, C. L. & Miller, A. J. M. Deducing Reaction Mechanism: A Guide for Students, Researchers, and Instructors. *J. Chem. Educ.* **93**, 275–286 (2016).
28. Roston, D., Islam, Z. & Kohen, A. Isotope effects as probes for enzyme catalyzed hydrogen-transfer reactions. *Molecules* **18**, 5543–5567 (2013).
29. McMahon, R. J. Chemistry: Chemical reactions involving quantum tunneling. *Science* **299**, 833–834 (2003).
30. Kohen, A. & Klinman, J. P. Enzyme catalysis: Beyond Classical paradigms. *Acc. Chem. Res.* **31**, 397–404 (1998).
31. Sutcliffe, M. J. & Scrutton, N. S. Enzymology takes a quantum leap forward. *Philos. Trans. R. Soc. A Math. Phys. Eng. Sci.* **358**, 367–386 (2000).
32. Bell, R. P. & Le Roy, R. J. The Tunnel Effect in Chemistry. *Phys. Today* **35**, 85–86 (2008).
33. Klinman, J. P. The role of tunneling in enzyme catalysis of C–H activation. *Biochim. Biophys. Acta - Bioenerg.* **1757**, 981–987 (2006).
34. Olsson, M. H. M., Parson, W. W. & Warshel, A. Dynamical contributions to enzyme catalysis: Critical tests of a popular hypothesis. *Chemical Reviews* **106**, 1737–1756 (2006).
35. Roston, D., Cheatum, C. M. & Kohen, A. Hydrogen Donor – Acceptor Fluctuations from Kinetic Isotope Effects: A Phenomenological Model. *Biochemistry* **51**, 6860–6870 (2012).

36. Roston, D., Islam, Z. & Kohen, A. Kinetic isotope effects as a probe of hydrogen transfers to and from common enzymatic cofactors. *Archives of Biochemistry and Biophysics* **544**, 96–104 (2014).
37. Pudney, C. R. *et al.* Fast protein motions are coupled to enzyme H-transfer reactions. *J. Am. Chem. Soc.* **135**, 2512–2517 (2013).
38. Masterson, J. E. & Schwartz, S. D. Evolution alters the enzymatic reaction coordinate of dihydrofolate reductase. *J. Phys. Chem. B* **119**, 989–996 (2015).
39. Loveridge, E. J., Evans, R. M. & Allemand, R. K. Solvent Effects on Environmentally Coupled Hydrogen Tunnelling During Catalysis by Dihydrofolate Reductase from *Thermotoga maritima*. *Chem. - A Eur. J.* **14**, 10782–10788 (2008).
40. Warshel, A. & Bora, R. P. Perspective: Defining and quantifying the role of dynamics in enzyme catalysis. *J. Chem. Phys.* **144**, 180-901 (2016).
41. Masgrau, L. & Truhlar, D. G. *The importance of ensemble averaging in enzyme kinetics. Accounts of Chemical Research* **48**, 431–438 (2015).
42. Zinovjev, K. & Tuñón, I. Quantifying the limits of transition state theory in enzymatic catalysis. *Proc. Natl. Acad. Sci.* **114**, 12390–12395 (2017).
43. Katarzyna, S., Javier, R.-P. J., Vicent, M. & Inaki, T. Heavy enzymes-experimental and computational insights in enzyme dynamics. *Curr. Opin. Chem. Biol.* **21**, 11–18 (2014).
44. Behiry, E. M. *et al.* Isotope Substitution of Promiscuous Alcohol Dehydrogenase Reveals the Origin of Substrate Preference in the Transition State. *Angew. Chemie - Int. Ed.* **57**, 3128–3131 (2018).
45. Ruiz-Pernía, J. J. *et al.* Minimization of dynamic effects in the evolution of dihydrofolate reductase. *Chem. Sci.* **7**, 3248–3255 (2016).
46. Kipp, D. R., Silva, R. G. & Schramm, V. L. Mass-dependent bond vibrational dynamics influence catalysis by HIV-1 protease. *J. Am. Chem. Soc.* **133**, 19358–19361 (2011).
47. Ranasinghe, C. *et al.* Protein Mass Effects on Formate Dehydrogenase. *J. Am. Chem. Soc.* **139**, 17405–17413 (2017).

48. Kholodar, S. A., Ghosh, A. K. & Kohen, A. Measurement of isotope effects. in *Methods of enzymology* **596**, 43–77 (Elsevier Inc., 2017).
49. Thielges, M., Case, D. A. & Romesberg, F. E. Carbon– Deuterium Bonds as Probes of Dihydrofolate Reductase. *J. Am. Chem. Soc.* **130**, 6597–6603 (2008).
50. Groff, D., Thielges, M. C., Cellitti, S., Schultz, P. G. & Romesberg, F. E. Efforts toward the direct experimental characterization of enzyme microenvironments: tyrosine100 in dihydrofolate reductase. *Angew. Chemie Int. Ed.* **48**, 3478–3481 (2009).
51. Liu, C. T. *et al.* Probing the electrostatics of active site microenvironments along the catalytic cycle for escherichia coli dihydrofolate reductase. *J. Am. Chem. Soc.* **136**, 10349–10360 (2014).
52. Bublitz, G. U. & Boxer, S. G. Stark spectroscopy: applications in chemistry, biology, and materials science. *Annu. Rev. Phys. Chem.* **48**, 213–242 (1997).
53. Adhikary, R., Zimmermann, J. & Romesberg, F. E. Transparent Window Vibrational Probes for the Characterization of Proteins With High Structural and Temporal Resolution. *Chem. Rev.* **117**, 1927–1969 (2017).
54. Silverman, L. N., Pitzer, M. E., Ankomah, P. O., Boxer, S. G. & Fenlon, E. E. Vibrational stark effect probes for nucleic acids. *J. Phys. Chem. B* **111**, 11611–11613 (2007).
55. Günzler, H. & Williams, A. *Handbook of Analytical Techniques. Handbook of Analytical Techniques* **1–2**, (2008).
56. Fabian, H. & Mäntele, W. Infrared Spectroscopy of Proteins Biochemical Applications Infrared Spectroscopy of Proteins. *Handb. Vib. Spectrosc.* (2006).
57. Stuart, B. *Infrared Spectroscopy: Fundamentals and Applications*. Wiley (John Wiley & Sons, Ltd, 2004).
58. Coleman, W. F. & Lim, K. F. The effect of anharmonicity on diatomic vibration: A spreadsheet simulation. *J. Chem. Educ.* **82**, 126-133 (2005).
59. Theophanides, T. Introduction to Infrared Spectroscopy. *Infrared Spectrosc. - Mater.*

- Sci. Eng. Technol.* 1–10 (2012).
60. Werner, H. & Gronholz, J. Understanding FT-IR Data Processing. Part 1: Data Acquisition and Fourier Transformation. *Comput. Appl. Lab.* **2**, 216–220 (1984).
 61. Gemini Spectra Sciences. FTIR Gas Analysis. Available at: <http://www.gascell.com/htmls/direct3a.htm>.
 62. Neves-Petersen, M. T. & Petersen, S. B. Protein electrostatics: A review of the equations and methods used to model electrostatic equations in biomolecules - Applications in biotechnology. *Biotechnol. Annu. Rev.* **9**, 315–395 (2003).
 63. Simonson, T. Electrostatics and dynamics of proteins. *Reports Prog. Phys.* **66**, 737–787 (2003).
 64. Bublitz, G. U., Ortiz, R., Marder, S. R. & Boxer, S. G. Stark spectroscopy of donor/acceptor substituted polyenes. *J. Am. Chem. Soc.* **119**, 3365–3376 (1997).
 65. Park, E. S., Andrews, S. S., Hu, R. B. & Boxer, S. G. Vibrational Stark Spectroscopy in Proteins: A Probe and Calibration for Electrostatic Fields. *J. Phys. Chem. B* **103**, 9813–9817 (1999).
 66. Waegele, M. M., Culik, R. M. & Gai, F. Site-specific spectroscopic reporters of the local electric field, hydration, structure, and dynamics of biomolecules. *J. Phys. Chem. Lett.* **2**, 2598–2609 (2011).
 67. Błasiak, B., Ritchie, A. W., Webb, L. J. & Cho, M. Vibrational solvatochromism of nitrile infrared probes: beyond the vibrational Stark dipole approach. *Phys. Chem. Chem. Phys.* **18**, 18094–18111 (2016).
 68. Boxer, S. G. Stark realities. *J. Phys. Chem. B* **113**, 2972–2983 (2009).
 69. Stafford, A. J., Walker, D. M. & Webb, L. J. Electrostatic effects of mutations of Ras glutamine 61 measured using vibrational spectroscopy of a thiocyanate probe. *Biochemistry* **51**, 2757–2767 (2012).
 70. Webb, L. J. & Boxer, S. G. Electrostatic Fields Near the Active Site of Human Aldose Reductase : 1. New Inhibitors and Vibrational Stark Effect Measurements. *Biochemistry*

- 47, 1588–1598 (2008).
71. Andrews, S. S. & Boxer, S. G. Vibrational Stark effects of nitriles II. Physical origins of Stark effects from experiment and perturbation models. *J. Phys. Chem. A* **106**, 469–477 (2002).
72. Levinson, N. M., Fried, S. D. & Boxer, S. G. Solvent-induced infrared frequency shifts in aromatic nitriles are quantitatively described by the vibrational stark effect. *J. Phys. Chem. B* **116**, 10470–10476 (2012).
73. Bazewicz, C. G., Liskov, M. T., Hines, K. J. & Brewer, S. H. Sensitive, site-specific, and stable vibrational probe of local protein environments: 4-azidomethyl-1-phenylalanine. *J. Phys. Chem. B* **117**, 8987–8993 (2013).
74. Levinson, N. M., Bolte, E. E., Miller, C. S., Corcelli, S. A. & Boxer, S. G. Phosphate vibrations probe local electric fields and hydration in Biomolecules. *J. Am. Chem. Soc.* **133**, 13236–13239 (2011).
75. Dalosto, S. D., Vanderkooi, J. M. & Sharp, K. a. Vibrational Stark Effects on Carbonyl, Nitrile, and Nitrosyl Compounds Including Heme Ligands, CO, CN, and NO, Studied with Density Functional Theory. *J. Phys. Chem. B* **108**, 6450–6457 (2004).
76. Schkolnik, G. Vibrational Stark Spectroscopy as a Tool for Probing Electrostatics at Protein Surfaces and Self Assembled Monolayers. MSc Dissertation, p116 (Technischen Universität Berlin, 2012).
77. Fried, S. D., Bagchi, S. & Boxer, S. G. Measuring electrostatic fields in both hydrogen-bonding and non-hydrogen-bonding environments using carbonyl vibrational probes. *J. Am. Chem. Soc.* **135**, 11181–92 (2013).
78. Adhikary, R., Zimmermann, J., Dawson, P. E. & Romesberg, F. E. Temperature Dependence of CN and SCN IR Absorptions Facilitates Their Interpretation and Use as Probes of Proteins. *Anal. Chem.* **87**, 11561–11567 (2015).
79. Slocum, J. D., First, J. T. & Webb, L. J. Orthogonal Electric Field Measurements near the Green Fluorescent Protein Fluorophore through Stark Effect Spectroscopy and pKaShifts Provide a Unique Benchmark for Electrostatics Models. *J. Phys. Chem. B*

- 121**, 6799–6812 (2017).
80. Slocum, J. D. & Webb, L. J. Nitrile Probes of Electric Field Agree with Independently Measured Fields in Green Fluorescent Protein even in the Presence of Hydrogen Bonding. *J. Am. Chem. Soc.* **138**, 6561–6570 (2016).
81. Stafford, A. J., Ensign, D. L. & Webb, L. J. Vibrational stark effect spectroscopy at the interface of Ras and Rap1A bound to the Ras binding domain of RalGDS reveals an electrostatic mechanism for protein-protein interaction. *J. Phys. Chem. B* **114**, 15331–15344 (2010).
82. Fried, S. D., Bagchi, S. & Boxer, S. G. Extreme electric fields power catalysis in the active site of ketosteroid isomerase. *Biophysics (Oxf)*. **346**, 1510–1513 (2014).
83. Loveridge, E. J., Behiry, E. M., Swanwick, R. S. & Allemand, R. K. Different Reaction Mechanisms for Mesophilic and Thermophilic Dihydrofolate Reductases. *J. Am. Chem. Soc.* **131**, 6926–6927 (2009).
84. Anderson, D. D., Quintero, C. M. & Stover, P. J. Identification of a de novo thymidylate biosynthesis pathway in mammalian mitochondria. *Proc. Natl. Acad. Sci. U. S. A.* **108**, 15163–8 (2011).
85. Sirawaraporn, W. Dihydrofolate reductase and antifolate resistance in malaria. *Drug Resist. Updat.* **1**, 397–406 (1998).
86. Schweitzer, B. I., Dicker, A. P. & Bertino, J. R. Dihydrofolate reductase as a therapeutic target. *FASEB J.* **4**, 2441–2452 (1990).
87. Polshakov, V. I. Dihydrofolate reductase: Structural aspects of mechanisms of enzyme catalysis and inhibition. *Russ. Chem. Bull.* **50**, 1733–1751 (2001).
88. Osborne, M. J., Venkitakrishnan, R. P., Dyson, H. J. & Wright, P. E. Diagnostic chemical shift markers for loop conformation and substrate and cofactor binding in dihydrofolate reductase complexes. *Protein Sci.* **12**, 2230–2238 (2003).
89. Schnell, J. R., Dyson, H. J. & Wright, P. E. Structure, Dynamics, and Catalytic Function of Dihydrofolate Reductase. *Annu. Rev. Biophys. Biomol. Struct.* **33**, 119–140 (2004).

90. Guo, J., Luk, L. Y. P., Loveridge, E. J. & Allemann, R. K. Thermal adaptation of dihydrofolate reductase from the moderate thermophile *Geobacillus stearothermophilus*. *Biochemistry* **53**, 2855–63 (2014).
91. Dams, T. *et al.* The crystal structure of dihydrofolate reductase from *Thermotoga maritima*: molecular features of thermostability. *J. Mol. Biol.* **297**, 659–672 (2000).
92. Guo, J., Loveridge, E. J., Luk, L. Y. P. & Allemann, R. K. Effect of Dimerization on Dihydrofolate Reductase Catalysis. *Biochemistry* **52**, 3881–3887 (2013).
93. Davies, J. F. *et al.* Crystal Structures of Recombinant Human Dihydrofolate Reductase Complexed with Folate and 5-Deazafolate. *Biochemistry* **29**, 9467–9479 (1990).
94. Liu, C. T. *et al.* Functional significance of evolving protein sequence in dihydrofolate reductase from bacteria to humans. *Proc. Natl. Acad. Sci. U. S. A.* **110**, 10159–64 (2013).
95. Fierke, C. A., Johnson, K. A. & Benkovic, S. J. Construction and evaluation of the kinetic scheme associated with dihydrofolate reductase from *Escherichia coli*. *Biochemistry* **26**, 4085–4092 (1987).
96. Appleman, J. R. *et al.* Unusual transient- and steady-state kinetic behavior is predicted by the kinetic scheme operational for recombinant human dihydrofolate reductase. *J. Biol. Chem.* **265**, 2740–2748 (1990).
97. Oyen, D., Fenwick, R. B., Stanfield, R. L., Dyson, H. J. & Wright, P. E. Cofactor-Mediated Conformational Dynamics Promote Product Release From *Escherichia coli* Dihydrofolate Reductase via an Allosteric Pathway. *J. Am. Chem. Soc.* **137**, 9459–9468 (2015).
98. Bhabha, G. *et al.* Divergent evolution of protein conformational dynamics in dihydrofolate reductase. *Nat. Struct. Mol. Biol.* **20**, 1243–1249 (2013).
99. Sawaya, M. R. & Kraut, J. Loop and subdomain movements in the mechanism of *Escherichia coli* dihydrofolate reductase: Crystallographic evidence. *Biochemistry* **36**, 586–603 (1997).
100. Hughes, R. L., Johnson, L. A., Behiry, E. M., Loveridge, E. J. & Allemann, R. K. A

- rapid analysis of variations in conformational behavior during dihydrofolate reductase catalysis. *Biochemistry* **56**, 2126–2133 (2017).
101. Osborne, M. J., Schnell, J., Benkovic, S. J., Dyson, H. J. & Wright, P. E. Backbone dynamics in dihydrofolate reductase complexes: Role of loop flexibility in the catalytic mechanism. *Biochemistry* **40**, 9846–9859 (2001).
 102. Loveridge, E. J., Rodriguez, R. J., Swanwick, R. S. & Allemand, R. K. Effect of Dimerization on the Stability and Catalytic Activity of Dihydrofolate Reductase from the Hyperthermophile *Thermotoga maritima*. *Biochemistry* **48**, 5922–5933 (2009).
 103. Tuttle, L. M., Dyson, H. J. & Wright, P. E. Side chain conformational averaging in human dihydrofolate reductase. *Biochemistry* **53**, 1134–1145 (2014).
 104. Hay, S. *et al.* Are the catalytic properties of enzymes from piezophilic organisms pressure adapted? *ChemBioChem* **10**, 2348–2353 (2009).
 105. Khavrutskii, I. V., Price, D. J., Lee, J. & Brooks, C. L. Conformational change of the methionine 20 loop of *Escherichia coli* dihydrofolate reductase modulates pKa of the bound dihydrofolate. *Protein Sci.* **16**, 1087–1100 (2007).
 106. Ercikan-Abali, E. A. *et al.* Variants of Human Dihydrofolate at Leucine-22: Effect on Catalytic Properties Reductase with Substitutions and Inhibitor Binding mc. *Mol. Pharmacol.* **49**, 430–437 (1996).
 107. Prendergast, N. J., Appleman, J. R., Delcamp, T. J., Blakley, R. L. & Freisheim, J. H. Effects of Conversion of Phenylalanine-31 to Leucine on the Function of Human Dihydrofolate Reductase. *Biochemistry* **28**, 4645–4650 (1989).
 108. Nakano, T., Spencer, H. T., Appleman, J. R. & Blakley, R. L. Critical role of phenylalanine 34 of human dihydrofolate reductase in substrate and inhibitor binding and in catalysis. *Biochemistry* **33**, 9945–52 (1994).
 109. McElheny, D., Schnell, J. R., Lansing, J. C., Dyson, H. J. & Wright, P. E. Defining the role of active-site loop fluctuations in dihydrofolate reductase catalysis. *Proc. Natl. Acad. Sci. U. S. A.* **102**, 5032–5037 (2005).

110. Pitts, C., Bowen, D. & Southerland, W. M. Interaction energy analysis of nonclassical antifolates with human dihydrofolate reductase. *J. Mol. Model.* **6**, 467–476 (2000).
111. Lam, T. *et al.* Structure-based design of new dihydrofolate reductase antibacterial agents: 7-(benzimidazol-1-yl)-2,4-diaminoquinazolines. *J. Med. Chem.* **57**, 651–668 (2014).
112. Lamb, K. M., G-Dayanandan, N., Wright, D. L. & Anderson, A. C. Elucidating features that drive the design of selective antifolates using crystal structures of human dihydrofolate reductase. *Biochemistry* **52**, 7318–7326 (2013).
113. Pu, J., Ma, S., Gao, J. & Truhlar, D. G. Small temperature dependence of the kinetic isotope effect for the hydride transfer reaction catalyzed by *Escherichia coli* dihydrofolate reductase. *J. Phys. Chem. B* **109**, 8551–8556 (2005).
114. Luk, L. Y. P. *et al.* Chemical Ligation and Isotope Labeling to Locate Dynamic Effects during Catalysis by Dihydrofolate Reductase. *Angew. Chemie - Int. Ed.* **54**, 9016–9020 (2015).
115. Luk, L. Y. P., Loveridge, E. J. & Allemand, R. K. Different Dynamical Effects in Mesophilic and Hyperthermophilic Dihydrofolate Reductases. *J. Am. Chem. Soc.* **136**, 6862–6865 (2014).
116. Luk, L. Y. P. *et al.* Protein Isotope Effects in Dihydrofolate Reductase from *Geobacillus stearothermophilus* Show Entropic–Enthalpic Compensatory Effects on the Rate Constant. *J. Am. Chem. Soc.* **136**, 17317–17323 (2014).
117. Behiry, E. M., Luk, L. Y. P., Matthews, S. M., Loveridge, E. J. & Allemand, R. K. Role of the occluded conformation in bacterial dihydrofolate reductases. *Biochemistry* **53**, 4761–4768 (2014).
118. Agarwal, P. K., Billeter, S. R., Rajagopalan, P. T. R., Benkovic, S. J. & Hammes-Schiffer, S. Network of coupled promoting motions in enzyme catalysis. *Proc. Natl. Acad. Sci. U. S. A.* **99**, 2794–2799 (2002).
119. Li, L., Falzone, C. J., Benkovic, S. J. & Wright, P. E. Functional Role of a Mobile Loop of *Escherichia coli* Dihydrofolate Reductase in Transition-State Stabilization.

- Biochemistry* **31**, 7826–7833 (1992).
120. Falzone, C. J., Benkovic, S. J. & Wright, P. E. Dynamics of a Flexible Loop in Dihydrofolate Reductase from *Escherichia coli* and Its Implication for Catalysis. *Biochemistry* **33**, 439–442 (1994).
121. Cameron, C. E. & Benkovic, S. J. Evidence for a functional role of the dynamics of glycine-121 of *Escherichia coli* dihydrofolate reductase obtained from kinetic analysis of a site-directed mutant. *Biochemistry* **36**, 15792–15800 (1997).
122. Swanwick, R. S., Shrimpton, P. J. & Allemann, R. K. Pivotal Role of Gly 121 in Dihydrofolate Reductase from *Escherichia coli*: The Altered Structure of a Mutant Enzyme May Form the Basis of Its Diminished Catalytic Performance †. *Biochemistry* **43**, 4119–4127 (2004).
123. Ruiz-Pernia, J. J. *et al.* Increased Dynamic Effects in a Catalytically Compromised Variant of *Escherichia coli* Dihydrofolate Reductase. *J. Am. Chem. Soc.* **135**, 18689–18696 (2013).
124. Loveridge, E. J., Behiry, E. M., Guo, J. & Allemann, R. K. Evidence that a ‘dynamic knockout’ in *Escherichia coli* dihydrofolate reductase does not affect the chemical step of catalysis. *Nat. Chem.* **4**, 292–297 (2012).
125. Oyeyemi, O. A. *et al.* Comparative Hydrogen-Deuterium Exchange for a Mesophilic vs Thermophilic Dihydrofolate Reductase at 25 °C: Identification of a Single Active Site Region with Enhanced Flexibility in the Mesophilic Protein. *Biochemistry* **50**, 8251–8260 (2011).
126. Loveridge, E. J. *et al.* The role of large-scale motions in catalysis by dihydrofolate reductase. *J. Am. Chem. Soc.* **133**, 20561–20570 (2011).
127. Cody, V., Pace, J. & Nowak, J. Structural analysis of human dihydrofolate reductase as a binary complex with the potent and selective inhibitor 2,4-diamino-6-{2'-O-(3-carboxypropyl)oxydibenz[b,f]-azepin-5-yl}methylpteridine reveals an unusual binding mode. *Acta Crystallogr. D. Biol. Crystallogr.* **67**, 875–80 (2011).
128. Shrimpton, P., Mullaney, A. & Allemann, R. K. Functional role for Tyr 31 in the

- catalytic cycle of chicken dihydrofolate reductase. *Proteins Struct. Funct. Genet.* **51**, 216–223 (2003).
129. Beard, W. A., Appleman, J. R., Delcamp, T. J., Freisheim, J. H. & Blakley, R. L. Hydride transfer by dihydrofolate reductase. Causes and consequences of the wide range of rates exhibited by bacterial and vertebrate enzymes. *J. Biol. Chem.* **264**, 9391–9399 (1989).
130. Noé, V., MacKenzie, S. & Ciudad, C. J. An intron is required for dihydrofolate reductase protein stability. *J. Biol. Chem.* **278**, 38292–38300 (2003).
131. Sompornpisut, P., Wijitkosoom, A., Parasuk, V. & Sirawaraporn, W. Molecular dynamics simulation of the human apo-dihydrofolate reductase: An investigation of an unstable enzyme. *Mol. Simul.* **29**, 111–121 (2003).
132. Ainavarapu, S. R. K., Li, L., Badilla, C. L. & Fernandez, J. M. Ligand binding modulates the mechanical stability of dihydrofolate reductase. *Biophys. J.* **89**, 3337–3344 (2005).
133. Maglia, G., Javed, M. H. & Allemand, R. K. Hydride transfer during catalysis by dihydrofolate reductase from *Thermotoga maritima*. *Biochem. J.* **374**, 529–535 (2003).
134. Swanwick, R. S., Maglia, G., Tey, L. & Allemand, R. K. Coupling of protein motions and hydrogen transfer during catalysis by *Escherichia coli* dihydrofolate reductase. *Biochem. J.* **394**, 259–265 (2006).
135. Hata, K. *et al.* High pressure nmr study of dihydrofolate reductase from a deep-sea bacterium *Moritella profunda*. *Cell. Mol. Biol. (Noisy-le-grand)*. **50**, 311–6 (2004).
136. Loveridge, E. J. & Allemand, R. K. Effect of pH on Hydride Transfer by *Escherichia coli* Dihydrofolate Reductase. *ChemBioChem* **12**, 1258–1262 (2011).
137. Loveridge, E. J., Tey, L.-H. & Allemand, R. K. Solvent Effects on Catalysis by *Escherichia coli* Dihydrofolate Reductase. *J. Am. Chem. Soc.* **132**, 1137–1143 (2010).
138. Luk, L. Y. P. *et al.* Unraveling the role of protein dynamics in dihydrofolate reductase catalysis. *Proc. Natl. Acad. Sci. U. S. A.* **110**, 16344–16349 (2013).

139. Bhabha, G., Tuttle, L., Martinez-Yamout, M. A. & Wright, P. E. Identification of endogenous ligands bound to bacterially expressed human and *E. coli* dihydrofolate reductase by 2D NMR. *FEBS Lett.* **585**, 3528–3532 (2011).
140. Appleman, J. R., Prendergast, N., Delcamp, T. J., Freisheim, J. H. & Blakley, R. L. Kinetics of the formation and isomerization of methotrexate complexes of recombinant human dihydrofolate reductase. *J. Biol. Chem.* **263**, 10304–10313 (1988).
141. Chazarra, S. *et al.* Purification and kinetic properties of human recombinant dihydrofolate reductase produced in *bombyx mori* chrysalides. *Appl. Biochem. Biotechnol.* **162**, 1834–1846 (2010).
142. Rosowsky, A., Wright, J. E., Vaidya, C. M. & Forsch, R. A. The effect of side-chain, para-aminobenzoyl region, and B-ring modifications on dihydrofolate reductase binding, influx via the reduced folate carrier, and cytotoxicity of the potent nonpolyglutamatable antifolate N(α)-(4-amino-4-deoxypteroyl)-N(δ)-hemiph. *Pharmacol. Ther.* **85**, 191–205 (2000).
143. Roberts, V. A., Dauber-Osguthorpe, P., Ostguthorpe, D. J., Levin, E. & Hagler, A. T. A Comparison of the Binding of the Ligand Trimethoprim to Bacterial and Vertebrate Dihydrofolate Reductases. *Isr. J. Chem.* **27**, 198–210 (1986).
144. Fossati, E. Directed evolution of human dihydrofolate reductase: towards a better understanding of binding at the active site. (Université de Montréal, 2008).
145. Schweitzers, B. *et al.* Probing the role of two hydrophobic active site residues in the human dihydrofolate reductase by site-directed mutagenesis. *J. Biol. Chem.* **34**, 20786–20795 (1989).
146. Bhosle, A. & Chandra, N. Structural analysis of dihydrofolate reductases enables rationalization of antifolate binding affinities and suggests repurposing possibilities. *FEBS J.* **283**, 1139–1167 (2016).
147. Appleman, J. R. *et al.* Atypical transient state kinetics of recombinant human dihydrofolate reductase produced by hysteretic behavior. Comparison with dihydrofolate reductases from other sources. *J. Biol. Chem.* **264**, 2625–2633 (1989).

148. Ercikan-Abali, E. A. *et al.* Translational upregulation of dihydrofolate reductase by methotrexate is an intrinsic mechanism of resistance. *Cancer Res.* **65**, 777–777 (2005).
149. Antosiewicz, A. *et al.* Human dihydrofolate reductase and thymidylate synthase form a complex in vitro and co-localize in normal and cancer cells. *J. Biomol. Struct. Dyn.* **35**, 1474–1490 (2017).
150. Wang, N. & McCammon, J. A. Substrate channeling between the human dihydrofolate reductase and thymidylate synthase. *Protein Sci.* **25**, 79–86 (2016).
151. McEntee, G. *et al.* The former annotated human pseudogene dihydrofolate reductase-like 1 (DHFRL1) is expressed and functional. *Proc. Natl. Acad. Sci. U. S. A.* **108**, 15157–62 (2011).
152. Scheweppe, D. K. *et al.* Mitochondrial protein interactome elucidated by chemical cross-linking mass spectrometry. *Proc. Natl. Acad. Sci. U. S. A.* **114**, 1732–1737 (2017).
153. Garau, G. *et al.* Update of the standard numbering scheme for class B β -lactamases. *Antimicrobial Agents and Chemotherapy* **48**, 2347–2349 (2004).
154. Philippon, A., Dusart, J., Joris, B. & Frère, J. The diversity, structure and regulation of beta-lactamases. *Cell. Mol. Life Sci.* **54**, 341–346 (1998).
155. Levy, S. *et al.* Identification of LACTB2, a metallo- β -lactamase protein, as a human mitochondrial endoribonuclease. *Nucleic Acids Res.* **44**, 1813–1832 (2016).
156. Suh, J. R., Herbig, A. K. & Stover, P. J. New perspectives on folate catabolism. *Annu. Rev. Nutr.* **21**, 255–282 (2001).
157. Carter, E. L. *et al.* Escherichia coli abg genes enable uptake and cleavage of the folate catabolite p-aminobenzoyl-glutamate. *J. Bacteriol.* **189**, 3329–3334 (2007).
158. Francis, K., Sapienza, P. J., Lee, A. L. & Kohen, A. The Effect of Protein Mass Modulation on Human Dihydrofolate Reductase. *Biochemistry* **55**, 1100–1106 (2016).
159. Happel, J. New Treatment of Enzyme Kinetics Applied to Human Dihydrofolate Reductase. *Society* 5209–5212 (2000).
160. Birdsall, B., Burgen, A. S. V. & Roberts, G. C. K. Effects of coenzyme analogs on the

- binding of p-aminobenzoyl-L-glutamate and 2,4-diaminopyrimidine to *Lactobacillus casei* dihydrofolate reductase. *Biochemistry* **19**, 3732–3737 (1980).
161. Gawlita, E., Caldwell, W. S., O’Leary, M. H., Paneth, P. & Anderson, V. E. Kinetic isotope effects on substrate association: reactions of phosphoenolpyruvate with phosphoenolpyruvate carboxylase and pyruvate kinase. *Biochemistry* **34**, 2577–83 (1995).
162. Thillet, J., Adams, J. A. & Benkovic, S. J. The Kinetic Mechanism of Wild-Type and Mutant Mouse Dihydrofolate Reductases. *Biochemistry* **29**, 5195–5202 (1990).
163. Kelly, S. M., Jess, T. J. & Price, N. C. How to study proteins by circular dichroism. *Biochim. Biophys. Acta - Proteins Proteomics* **1751**, 119–139 (2005).
164. Maglia, G. & Allemand, R. K. Evidence for Environmentally Coupled Hydrogen Tunneling during Dihydrofolate Reductase Catalysis. *J. Am. Chem. Soc.* **125**, 13372–13373 (2003).
165. More, N., Daniel, R. M. & Petach, H. H. The effect of low temperatures on enzyme activity. *Biochem. J.* **305 Pt 1**, 17–20 (1995).
166. Meiering, E. M. & Wagner, G. Detection of Long-Lived Bound Water-Molecules in Complexes of Human Dihydrofolate-Reductase with Methotrexate and Nadph. *J. Mol. Biol.* **247**, 294–308 (1995).
167. Wang, Z., Singh, P., Czekster, C. M., Kohen, A. & Schramm, V. L. Protein Mass-Modulated Effects in the Catalytic Mechanism of Dihydrofolate Reductase: Beyond Promoting Vibrations. *J. Am. Chem. Soc.* **136**, 8333–8341 (2014).
168. Liu, C. T. *et al.* Escherichia coli dihydrofolate reductase catalyzed proton and hydride transfers: temporal order and the roles of Asp27 and Tyr100. *Proc. Natl. Acad. Sci. USA* **111**, 18231–6 (2014).
169. Henzler-Wildman, K. & Kern, D. Dynamic personalities of proteins. *Nature* **450**, 964–972 (2007).
170. Stojković, V., Perissinotti, L. L., Willmer, D., Benkovic, S. J. & Kohen, A. Effects of the

- donor acceptor distance and dynamics on hydride tunneling in the dihydrofolate reductase catalyzed reaction. *J Am Chem Soc.* **134**, 1738–1745 (2012).
171. Kohen, A. Role of dynamics in enzyme catalysis: Substantial versus semantic controversies. *Acc. Chem. Res.* **48**, 466–473 (2015).
172. Stojkovic, V. Contribution of active site dynamics to enzyme catalysis : study on a series of mutants of dihydrofolate reductase. (2012).
173. Liu, H. & Warshel, A. Origin of the temperature dependence of isotope effects in enzymatic reactions: The case of dihydrofolate reductase. *J. Phys. Chem. B* **111**, 7852–7861 (2007).
174. Kohen, A. Kinetic isotope effects as probes for hydrogen tunneling, coupled motion and dynamics contributions to enzyme catalysis. *Prog. React. Kinet. Mech.* **28**, 119–156 (2003).
175. Pang, J., Pu, J., Gao, J., Truhlar, D. G. & Allemand, R. K. Hydride Transfer Reaction Catalyzed by Hyperthermophilic Dihydrofolate Reductase Is Dominated by Quantum Mechanical Tunneling and Is Promoted by Both Inter- and Intramonomeric Correlated Motions. *J. Am. Chem. Soc.* **128**, 8015–8023 (2006).
176. Silva, R. G., Murkin, A. S. & Schramm, V. L. Femtosecond dynamics coupled to chemical barrier crossing in a Born-Oppenheimer enzyme. *Proc. Natl. Acad. Sci. U. S. A.* **108**, 18661–5 (2011).
177. Suarez, J. & Schramm, V. L. Isotope-specific and amino acid-specific heavy atom substitutions alter barrier crossing in human purine nucleoside phosphorylase. *Proc. Natl. Acad. Sci.* **112**, 11247–11251 (2015).
178. Warshel, A. and & Papazyan, A. Electrostatic effects in macromolecules: fundamental concepts and practical modeling. *Curr. Opin. Struct. Biol.* **8**, 211–217 (1998).
179. Warshel, A., Sharma, P. K., Kato, M. & Parson, W. W. Modeling electrostatic effects in proteins. *Biochim. Biophys. Acta - Proteins Proteomics* **1764**, 1647–1676 (2006).
180. Bennett, B. C., Xu, H., Simmerman, R. F., Lee, R. E. & Dealwis, C. G. Crystal structure

- of the anthrax drug target, *Bacillus anthracis* dihydrofolate reductase. *J. Med. Chem.* **50**, 4374–4381 (2007).
181. Hecht, D., Tran, J. & Fogel, G. B. Structural-based analysis of dihydrofolate reductase evolution. *Mol. Phylogenet. Evol.* **61**, 212–230 (2011).
182. Fafarman, A. T., Webb, L. J., Chuang, J. I. & Boxer, S. G. Site Specific Conversion of Cysteine Thiols into Thiocyanate Creates an IR Probe for Electric Fields in Proteins. *J. Am. Chem. Soc.* **128**, 13356–13357 (2008).
183. Swanwick, R. S., Daines, A. M., Tey, L.-H., Flitsch, S. L. & Allemand, R. K. Increased Thermal Stability of Site-Selectively Glycosylated Dihydrofolate Reductase. *ChemBioChem* **6**, 1338–1340 (2005).
184. Iwakura, M., Jones, B. E., Luo, J. & Matthews, C. R. A Strategy for Testing the Suitability of Cysteine Replacements in Dihydrofolate Reductase from *Escherichia coli*. *J. Biochem* **117**, 480–488 (1995).
185. Evans, R. M. Hydride transfer reactions in dihydrofolate reductase from *Moritella profunda*. (Cardiff University, 2010).
186. Worth, C. L., Preissner, R. & Blundell, T. L. SDM--a server for predicting effects of mutations on protein stability and malfunction. *Nucleic Acids Res.* **39**, W215–W222 (2011).
187. Gagnon, P., Mayes, T. & Danielsson, Å. An adaptation of hydrophobic interaction chromatography for estimation of protein solubility optima. *J. Pharm. Biomed. Anal.* **16**, 587–592 (1997).
188. Sedláček, E., Stagg, L. & Wittung-Stafshede, P. Effect of Hofmeister ions on protein thermal stability: Roles of ion hydration and peptide groups? *Arch. Biochem. Biophys.* **479**, 69–73 (2008).
189. Golovanov, A. P. *et al.* A Simple Method for Improving Protein Solubility and Long-Term Stability. *J. Am. Chem. Soc.* **126**, 8933–8939 (2004).
190. Getahun, Z. *et al.* Using nitrile-derivatized amino acids as infrared probes of local

- environment. *J. Am. Chem. Soc.* **125**, 405–411 (2003).
191. Maddams, W. F. & Southon, M. J. III. The effect of band width and band shape on resolution enhancement by derivative spectroscopy. *Spectrochim. Acta Part A Mol. Spectrosc.* **38**, 459–466 (1982).
192. Andrews, S. S. The Measurement and Physics of Vibrational Stark effects. (Stannford University, 2001).
193. Fafarman, A. T., Sigala, P. A., Herschlag, D. & Boxer, S. G. Decomposition of vibrational shifts of nitriles into electrostatic and hydrogen-bonding effects. *J. Am. Chem. Soc.* **132**, 12811–12813 (2010).
194. Fafarman, A. T. *et al.* Quantitative, directional measurement of electric field heterogeneity in the active site of ketosteroid isomerase. *Proc. Natl. Acad. Sci. U. S. A.* **109**, 299–308 (2012).
195. Brewer, S. H. & Franzen, S. A quantitative theory and computational approach for the vibrational Stark effect. *J. Chem. Phys.* **119**, 851–858 (2003).
196. Venkitakrishnan, R. P. *et al.* Conformational changes in the active site loops of dihydrofolate reductase during the catalytic cycle. *Biochemistry* **43**, 16046–16055 (2004).
197. Nishimura, M., Saito, H., Kawaguchi, K. & Nagao, H. Conformational stability of Met20 loop of DHFR: A molecular dynamics study. in *AIP Conference Proceedings* **1518**, 654–657 (2013).
198. Weikl, T. R. & Boehr, D. D. Conformational selection and induced changes along the catalytic cycle of Escherichia coli dihydrofolate reductase. *Proteins Struct. Funct. Bioinforma.* **80**, 2369–2383 (2012).
199. Morgenstern, A., Jaszai, M., Eberhart, M. E. & Alexandrova, A. N. Quantified electrostatic preorganization in enzymes using the geometry of the electron charge density. *Chem. Sci.* **8**, 5010–5018 (2017).
200. Head-Gordon, T. & Brooks, C. L. The role of electrostatics in the binding of small

- ligands to enzymes. *J. Phys. Chem.* **3**, 3342–3349 (1987).
201. Villa, J. *et al.* How important are entropic contributions to enzyme catalysis? *Proc. Natl. Acad. Sci.* **97**, 11899–11904 (2000).
202. Fields, P. A. Review: Protein function at thermal extremes: Balancing stability and flexibility. *Comp. Biochem. and Phys.* **129**, 417–431 (2001).
203. Xu, Y., Feller, G., Gerday, C. & Glansdorff, N. Moritella Cold-Active Dihydrofolate Reductase: Are There Natural Limits to Optimization of Catalytic Efficiency at Low Temperature Moritella Cold-Active Dihydrofolate Reductase : Are There Natural Limits to Optimization of Catalytic Efficiency at Low T. *J. Bacteriol.* **185**, 5519–5526 (2003).
204. Bystroff, C. & Kraut, J. Crystal Structure of Unliganded Escherichia coli Dihydrofolate Reductase. Ligand-Induced Conformational Changes and Cooperativity in Binding. *Biochemistry* **30**, 2227–2239 (1991).
205. Boehr, D. D., McElheny, D., Dyson, H. J. & Wright, P. E. The dynamic energy landscape of dihydrofolate reductase catalysis. *Science* **313**, 1638–1642 (2006).
206. Storm, D. R. & Koshland, D. E. A source for the special catalytic power of enzymes: orbital steering. *Proc. Natl. Acad. Sci. U. S. A.* **66**, 445–52 (1970).
207. Chen, Y. Q., Gulotta, M., Cheung, H. T. & Callender, R. Light activates reduction of methotrexate by NADPH in the ternary complex with Escherichia coli dihydrofolate reductase. *Photochem. Photobiol.* **69**, 77–85 (1999).
208. Cao, H., Pauff, J. M. & Hille, R. Substrate Orientation and Catalytic Specificity in the Action of Xanthine Oxidase. *J. Biol. Chem.* **285**, 28044–28053 (2010).
209. Chen, Y. Q., Kraut, J. & Callender, R. pH-dependent conformational changes in Escherichia coli dihydrofolate reductase revealed by raman difference spectroscopy. *Biophys. J.* **72**, 936–941 (1997).
210. Sun, D., Liao, D. & Remington, S. Electrostatic Fields In The Active-Sites Of Lysozymes. *Proc. Natl. Acad. Sci. U. S. A.* **86**, 5361–5365 (1989).
211. Liu, H. & Naismith, J. H. An efficient one-step site-directed deletion, insertion, single

and multiple-site plasmid mutagenesis protocol. *BMC Biotechnol.* **8**, 91–99 (2008).

Appendices

Appendix I

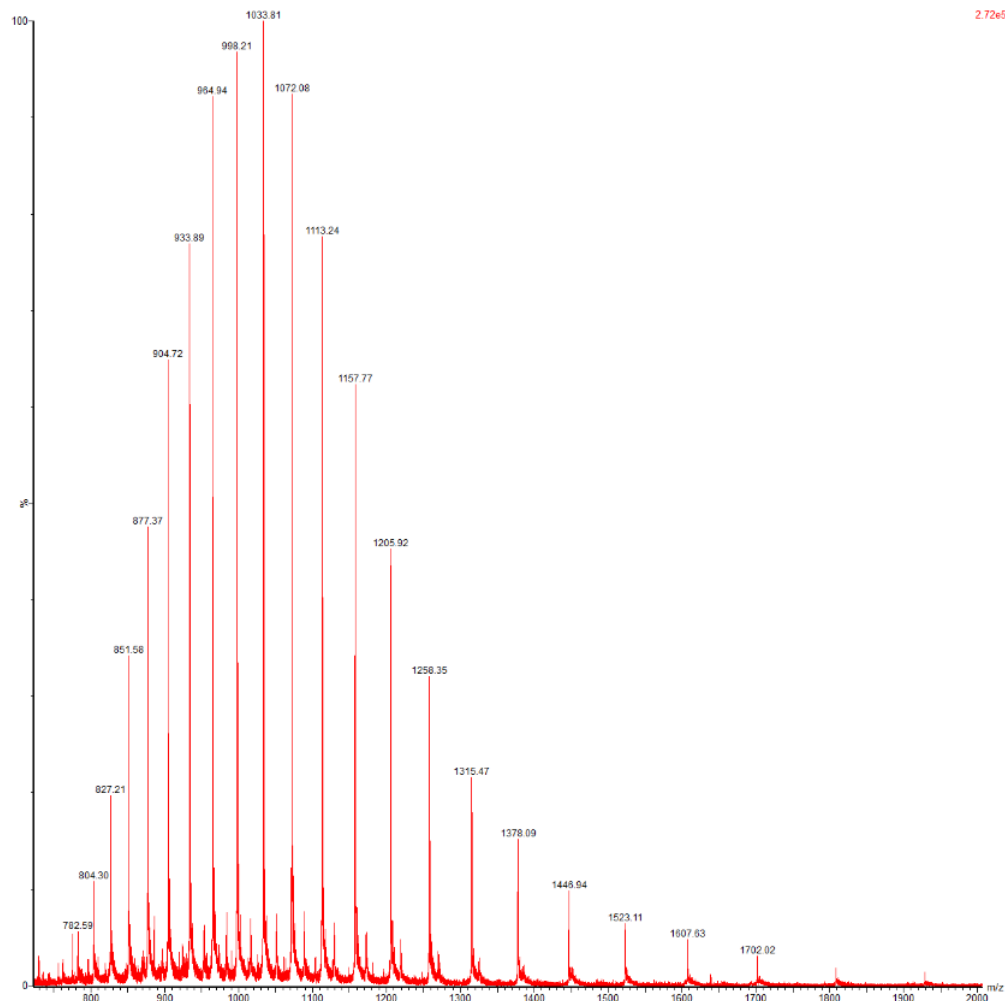


Figure A1: Charge state envelope of TEM-1 β -lactamase

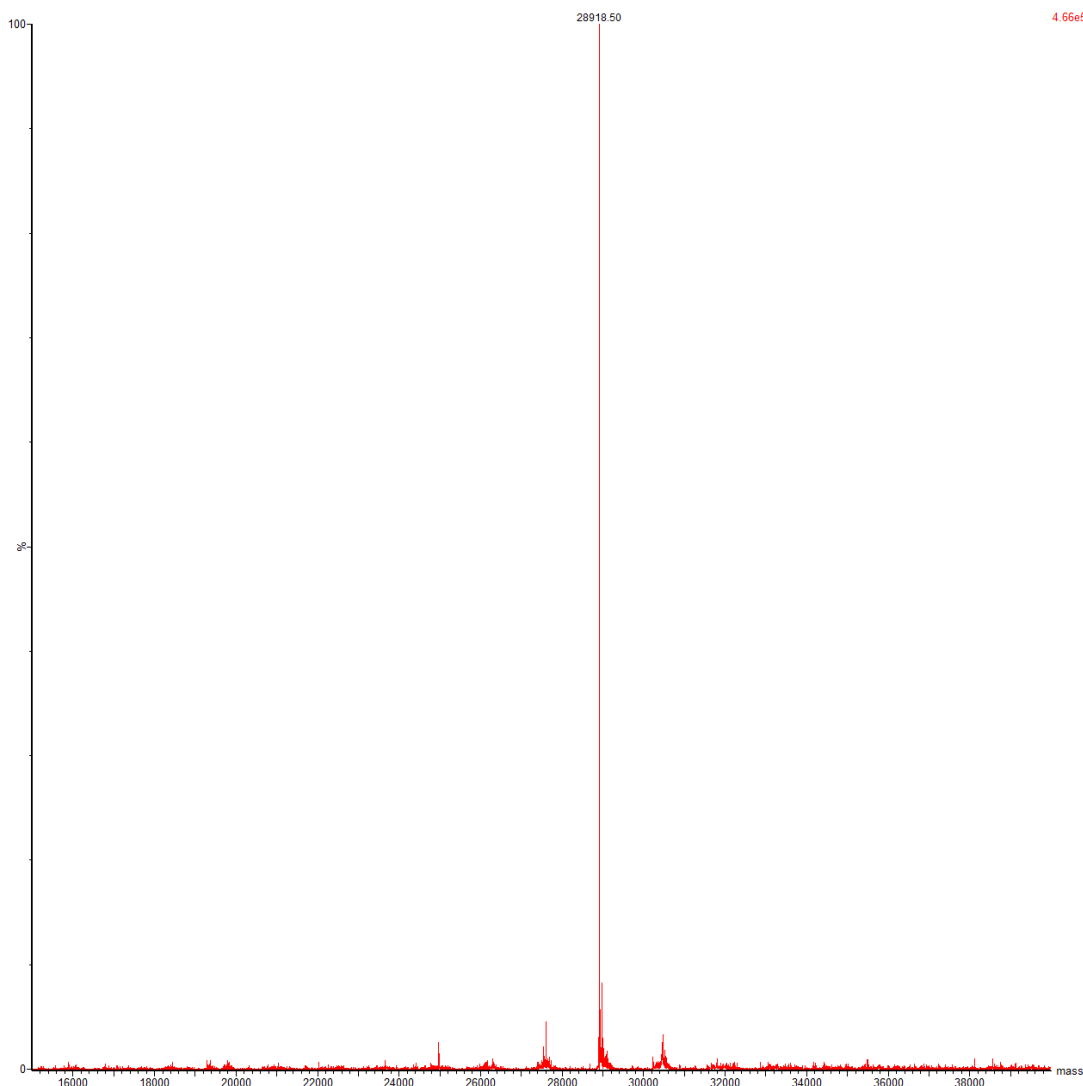


Figure A2: A deconvoluted mass of TEM-1 β -lactamase

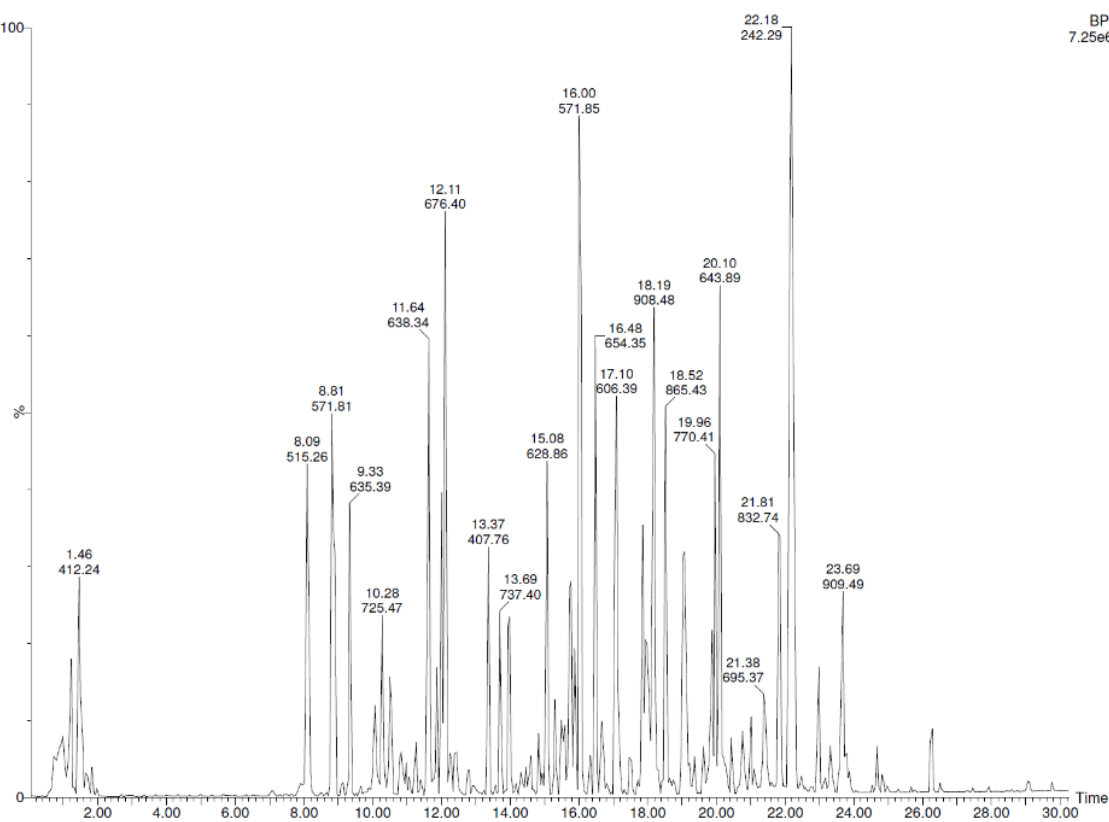


Figure A3: LC-MS chromatogram of trypsinated TEM-1 β -lactamase

Table A1 showing sequence coverage of TEM-1 β -lactamase

No.	Retention time (min)	m/z	Charge	Mass	Peptide sequence	N-C termina l protein sequenc e order
1*	N/A	N/A	N/A	2604.31	ELCSAAITMSDNTAANLLLTTIGGPK	N/A
2	13.98	674.66	+3	2020.97	IHYSQNDLVEYSPVTEK	7
3	14.60	892.45	+2	1782.88	IVVIYTTGSQATMDER	18
4	15.06	870.93	+2	1739.84	ELTAFLHNMGDHVTR	9
5	15.92	856.40	+2	1710.78	WEPELNEAIPNDER	10
6	15.49	690.34	+2	1378.66	DTTMPAAAMATTR	11
7	17.86	688.83	+2	1375.64	QQLIDWMEADK	13
8	12.11	676.38	+2	1350.76	GIIAALGPDGKPSR	17
9	16.48	654.35	+2	1306.68	VGYIELDLNSGK	2
10	20.10	643.83	+2	1285.76	LLTGELLTLASR	12
11	19.07	638.34	+2	1274.67	SALPAGWFIADK	15
12	11.64	638.34	+2	1274.66	ILESFRPEER	3
13	15.85	571.85	+2	1141.67	QIAEIGASLIK	19
14	8.86	543.79	+2	1085.55	IDAGQEIGASLIK	6
15	8.09	515.29	+2	1029.60	VLLCGAVLSR	5

16	8.51	515.2 6	+2	1028.5 1	HLTDGMTVR	8
17	15.88	988.4 6	+1	987.46	FPMMSTFK	4
18 *	N/A	N/A	N/A	973.45	DAEDQLGAR	N/A
19	2.72	412.2 4	+2	822.46	HPETLVK	1
20	10.08	725.4 7	+1	724.46	VAGPLLR	14
21	1.05	576.2 8	+1	575.27	SGAGER	16
*Peptide not detected. Result obtained by Dr Louis Luk and Thomas Williams						

28.9 kDa Protein sequence identified

HPETLVKVGYIELDLSGKILESFRPEERFPMMSTFKVLLCGAVLSRIDAGQEQLGRIHYSQN
 DLVEYSPVTEKHLTDGMTVRELTAFLHNMGDHVTRWEPELNEAIPNDERDTTMPAAMATTRL
 LTGEELLTLASRQQLIDWMEADKVAGPLRSALPAGWFIADKSGAGERGIIAALGPDGKPSRIV
 VIYTTGSQATMDERQIAEIGASLIK

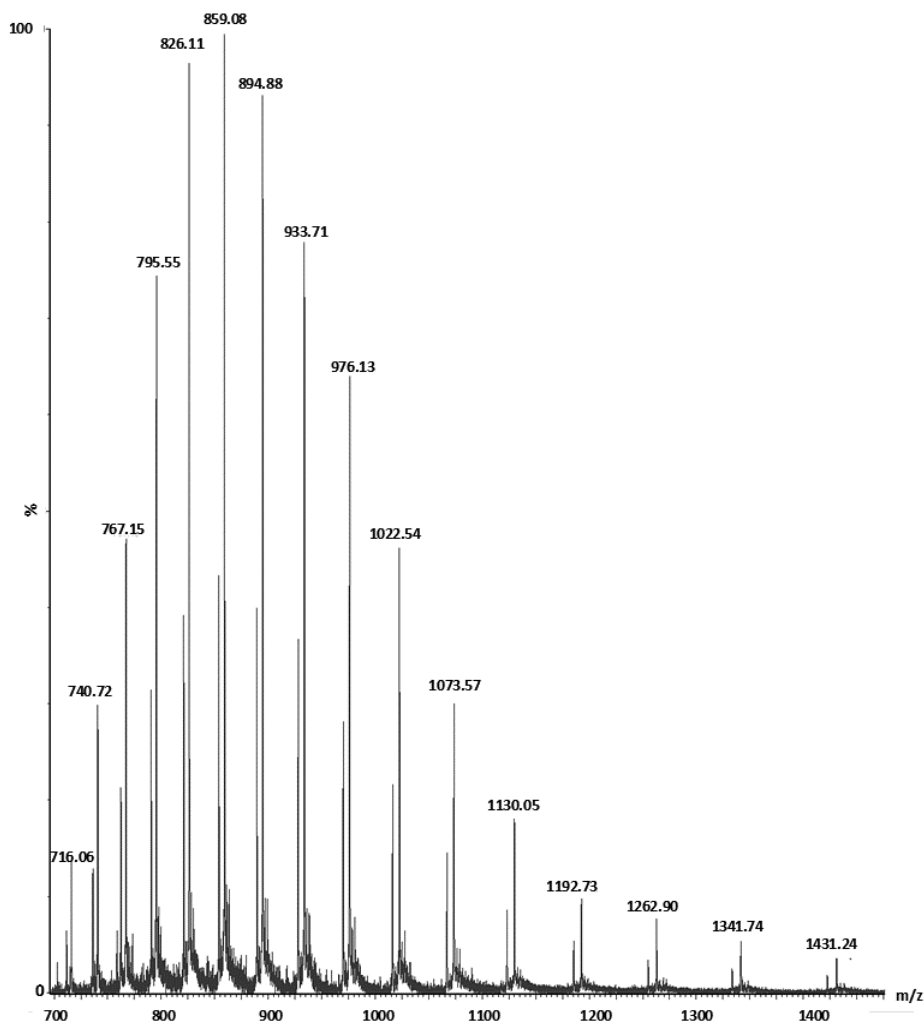


Figure A4: Charge state envelope of HsDHFR

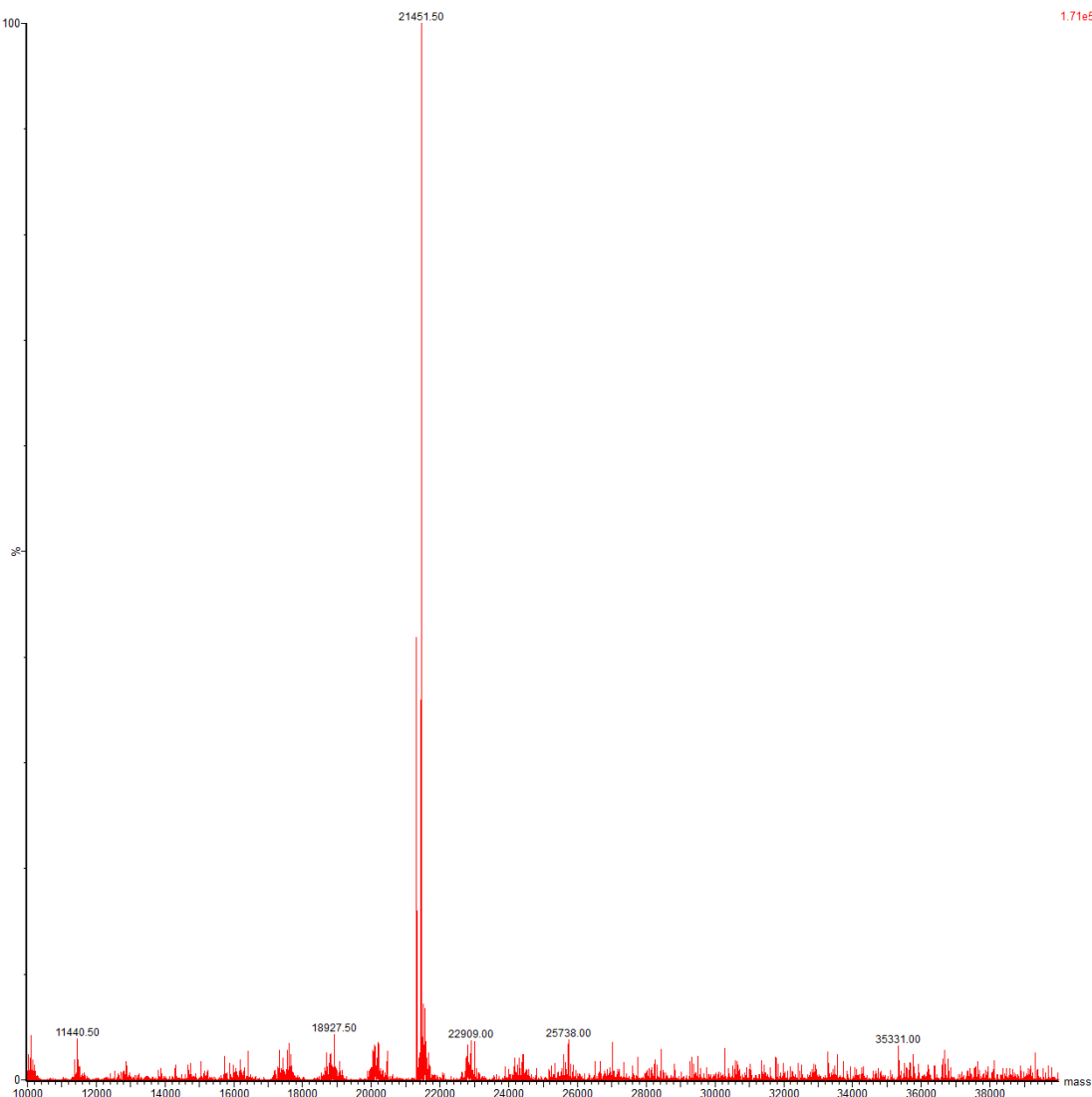


Figure A5: Deconvoluted mass of HsDHFR showing a mass of 21451.5 kDa

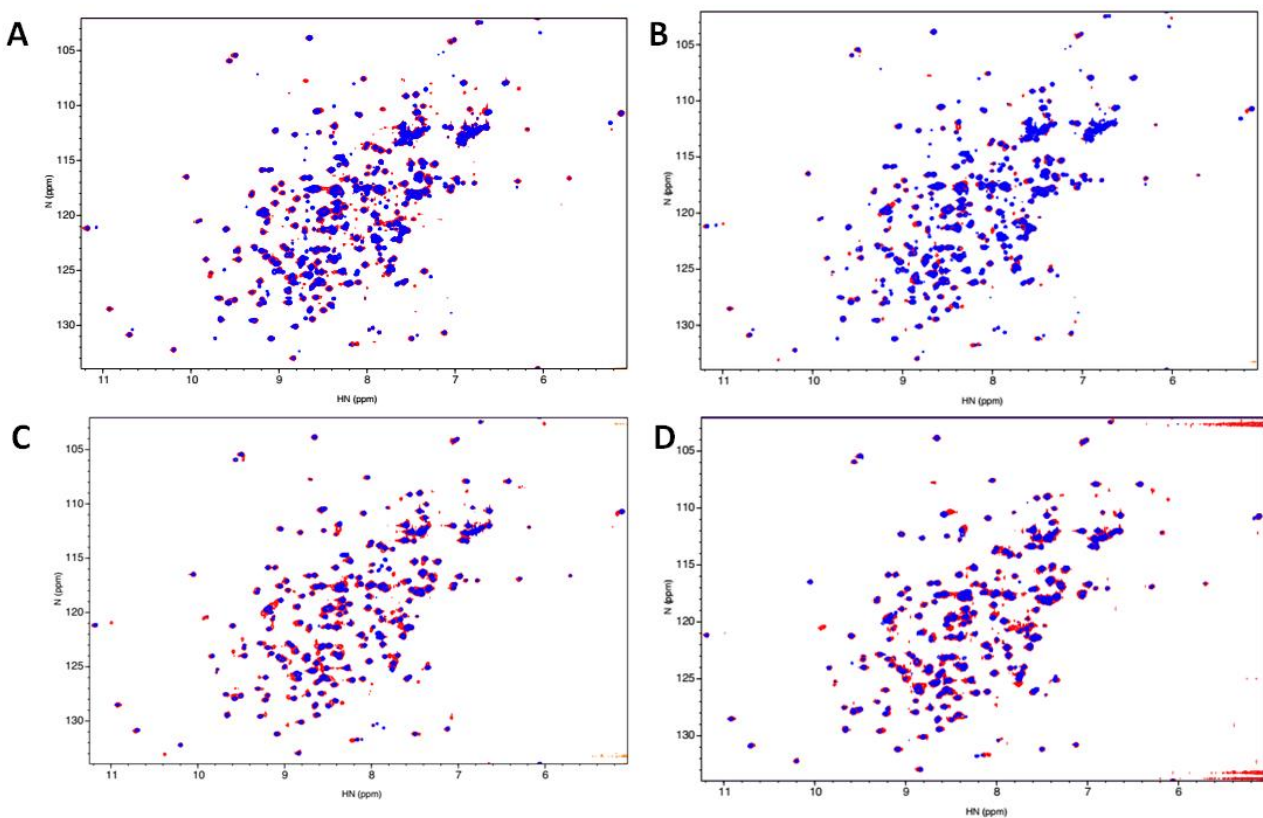


Figure A6: ^1H - ^{15}N HSQC overlay of HsDHFR complexed with (A) folate (blue) and folate:NADP⁺ (red); (B) folate + (blue) and DHF:NADP⁺ (red). (C) folate:NADP⁺ (blue) and DHF:NADP⁺ (red) and (D) DHF:NADP⁺ (blue) and THF:NADP⁺ (red)

Appendix II

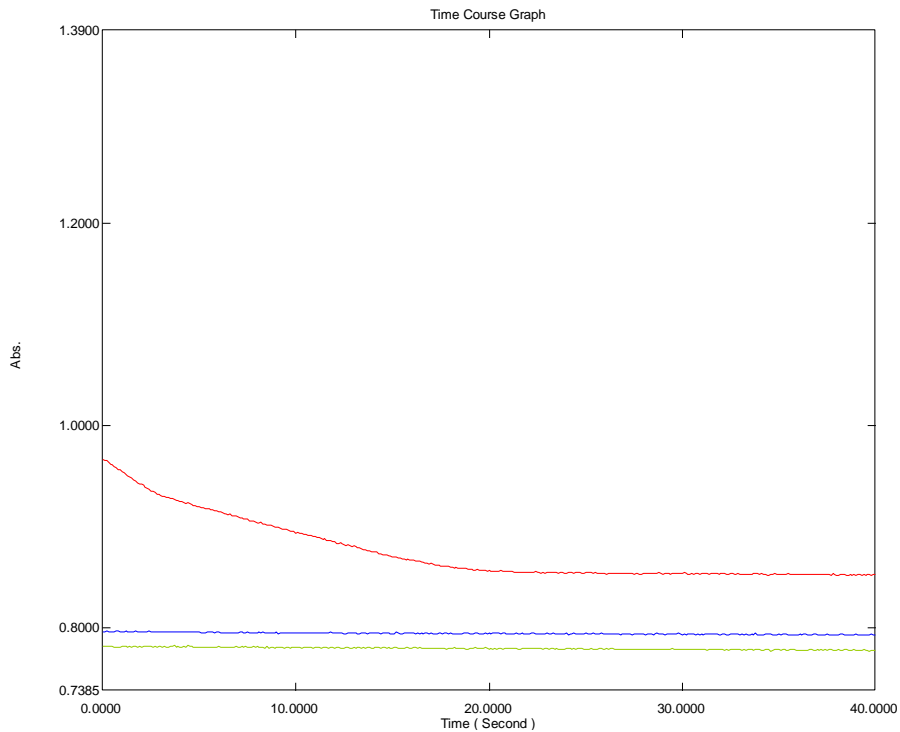


Figure A7: UV-Vis trace of unusual time course observed at pH 10.0 and 5 °C, starting at below 1.0 A.U (red trace) to 0.8 A.U (blue trace). Steady state kinetics at higher temperatures all have a trace less than 0.8 A.U (green trace).

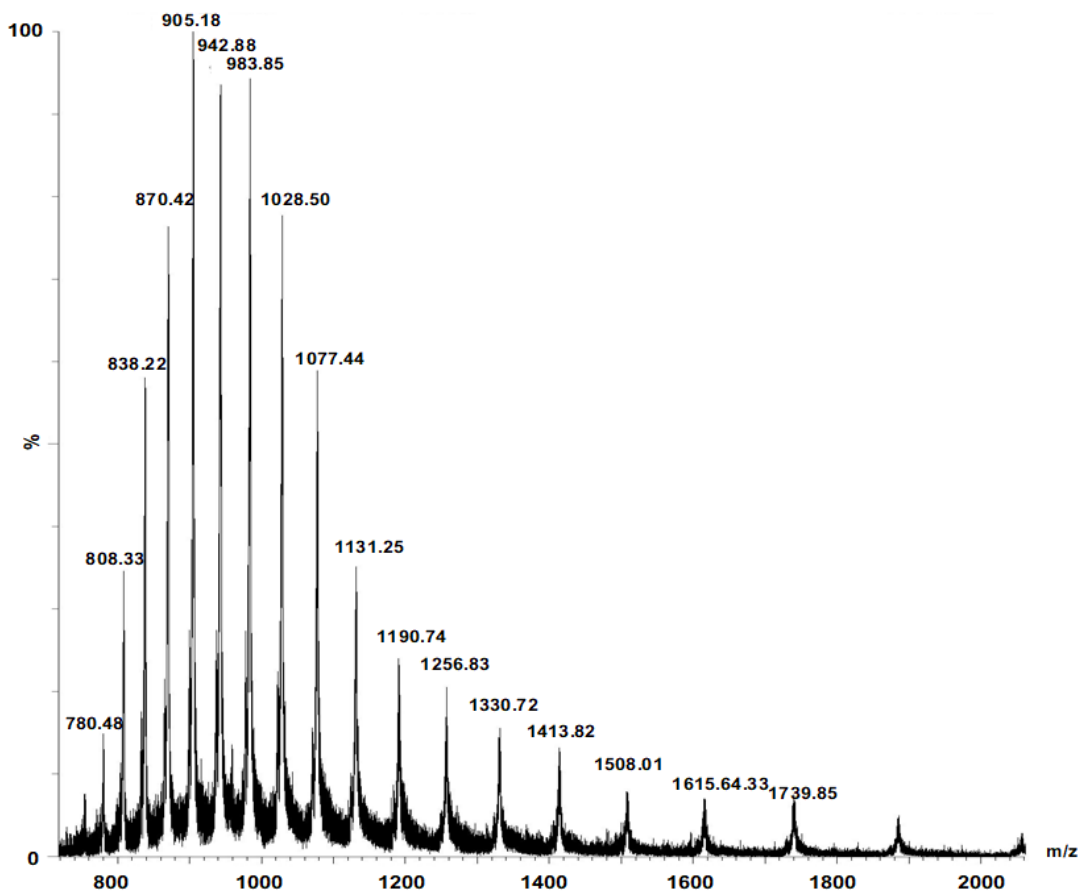


Figure A8: Mass spectra of ^{13}C , ^{15}N -HsDHFR showing a mass increase of 5.1 % (22605.5 kDa)

Appendix III

Labelling Optimisation

Glutathione (GSH), a tripeptide containing N-terminal glutamate coupled via gamma carboxyl side chain to cysteine and glycine, was employed for optimisation of labelling and FTIR measurement. Reduced glutathione (GSH) was dissolved in 50 mM Tris buffer pH 7.4, 1 mM EDTA to a final concentration and reacted with 1.1 molar equivalence of Ellman reagent dissolved in 50 mL of 50 mM Tris buffer with pH readjusted to 7.4. The formation of glutathione-thionitrobenzoate mixed disulphide (GSTNB) was monitored by LC-MS and the second step of the reaction, which involves a nucleophilic attack on the disulphide bond by cyanide, was examined at different conditions, Table A2. The reaction only proceeds to completeness within 1 hr at 30 °C when 3.0 molar equivalence of KCN was used. The reaction was acidified with 0.1 M HCl to about pH 2.0 (by pH paper test) under the fume hood and the 2-nitro-5-thiobenzoate (TNB) anion was extracted with ethyl acetate (3 x 50mL). Then, the aqueous layer containing thiocyanate labelled glutathione (GSCN) was lyophilised and purified by HPLC using Supercosil PLC-18 column, 25 cm x 21.2 mm. 12 µm. Isocratic method was used with 5% acetonitrile and 95% ddH₂O pH 6.0. Purified GSCN was lyophilised and kept at -20 °C. Labelling was confirmed by ESI-MS.

Table A2: Optimisation of glutathione labelling reaction

Molar ratio KCN:glutathione-TNB	Temp. (°C)	Labelled % glutathione (1 hr)	Labelled % glutathione (24 hrs)
1:1	18	10	15
1:1	25	25	40
2:1	25	50	75
3:1	30	99	nd
nd means not determined			

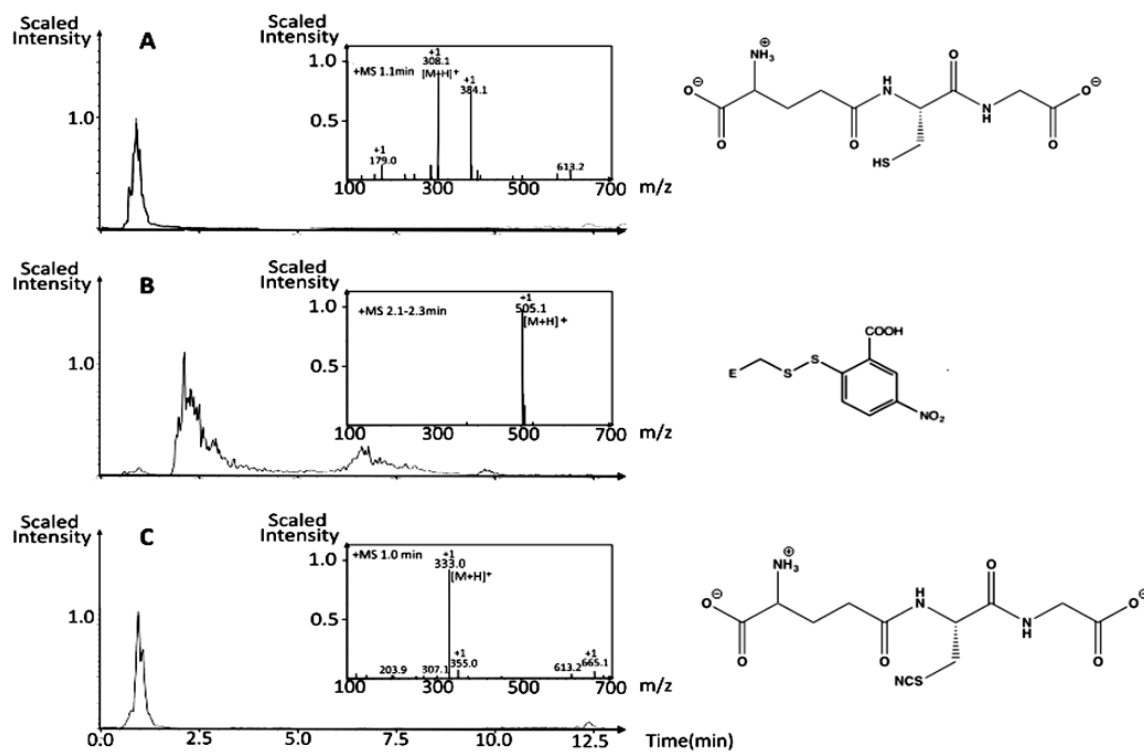


Figure A9. (A) LC and MS of glutathione (M_w : 307.3 Da) (B) LC and MS of glutathione-thionitrobenzoate mixed disulphide GSTNB (M_w : 504.7 Da) (C) LC and MS of glutathione thiocyanate, GSCN (M_w : 332.3 Da). Each inset shows the mass spectra corresponding to the chromatogram.

FTIR Sampling technique optimisation

Concentration requirement for measurement were determined using different sample cells and optimising conditions such as resolution, number of background and samples scans afforded vibrational spectra of low concentrated sample to be obtained.

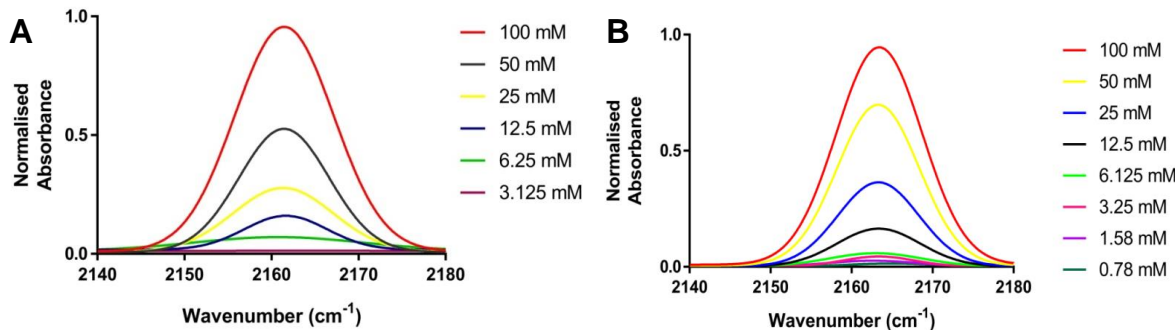


Figure A10: ATR cells with 0.7-micron pathlength (B) Transmission cell with 45-micron pathlength

Effect of temperature on nitrile peak

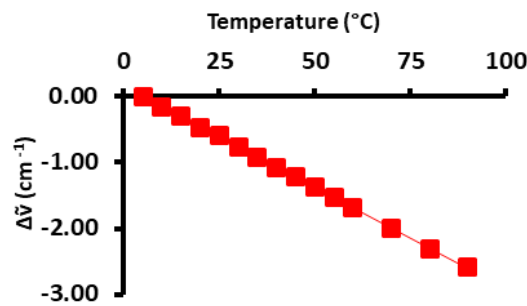


Figure A11: Temperature dependence of maximum absorption peak of thiocyanate in nitrile labelled glutathione.

Optimisation of purification for TmDHFR

Analysis of residues in TmDHFR revealed significant hydrophobic residue. 37.5 % of residues in TmDHFR are hydrophobic: Ala: 3 %, Ile: 4.8 %, Leu: 8.9%, Phe: 9.5 % and Val: 11.3 %.

Table A3: Hydrophobic interaction chromatography condition optimisation for Phenyl sepharose resin

Binding Buffer	Elution Buffer	Remark
50 mM Tris 1 M NaCl, pH 7.0	50 mM Tris, pH 7.0	No binding
50 mM Tris 3 M NaCl, pH 7.0	50 mM Tris, pH 7.0	Binds too tightly
50 mM Tris 1 M $(\text{NH}_4)_2\text{SO}_4$, pH 7.0	-	Salting out effect
50 mM Tris 1 M Na_2SO_4 , pH 7.0	50 mM Tris, pH 7.0	Precipitates during concentration step before SEC
50 mM Na acetate 1 M $(\text{NH}_4)_2\text{SO}_4$, pH 5.0	50 mM Na acetate, pH 5.0	Low overall yield, poor elution
50 mM Na acetate 1 M Na_2SO_4 , pH 5.0	50 mM Na acetate, pH 6.0, 10% acetonitrile	Low overall yield, poor elution
50 mM Na acetate 1 M Na_2SO_4 , pH 5.0	20 mM Bis Tris, pH 6.0	Higher overall yield and stable to concentration

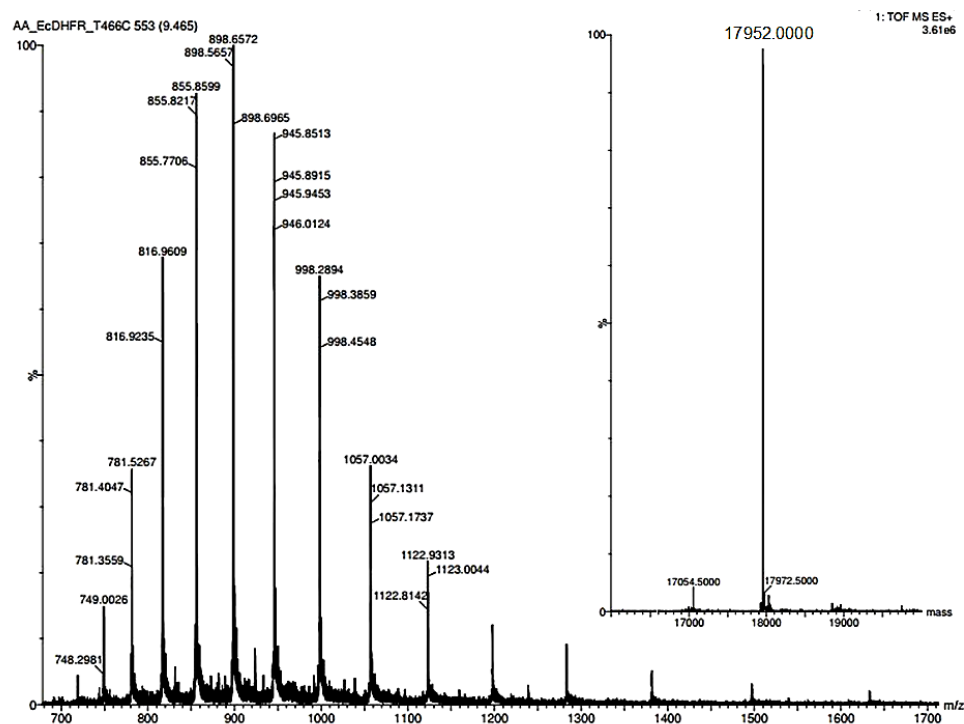
MS of labelled DHFRs variants**EcDHFR**

Figure A12: Charge envelope and deconvoluted mass spectra of EcDHFR_{cf} T46C with mass of 17952.0 Da.

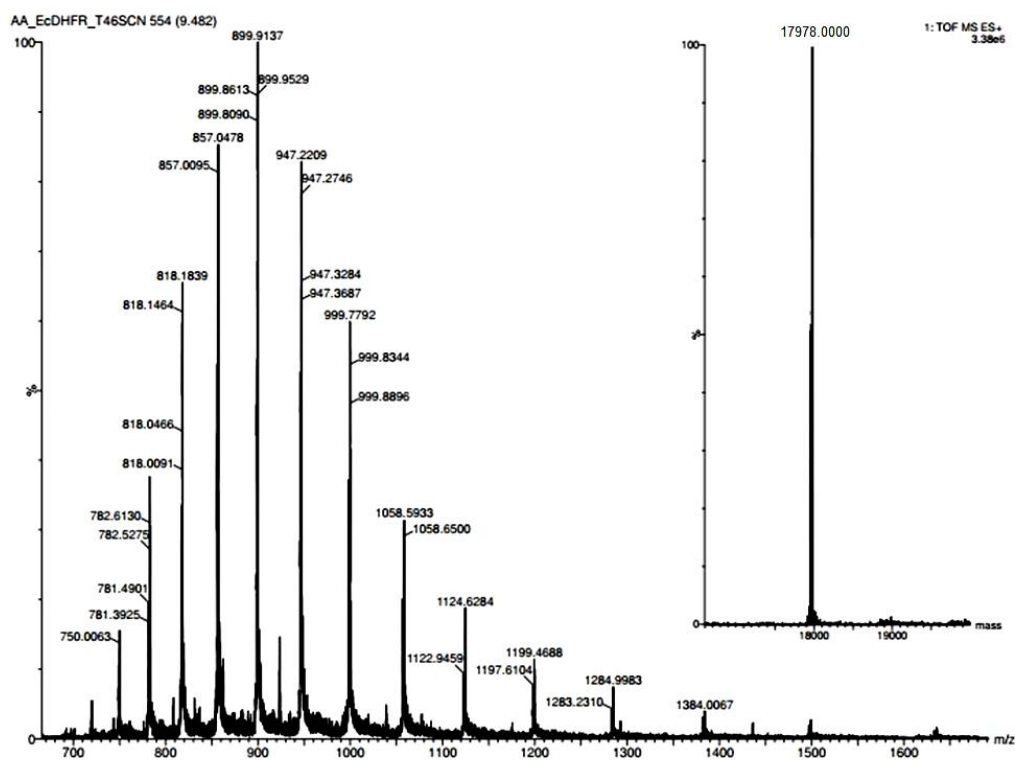


Figure A13: Charge envelope and deconvoluted mass spectra of EcDHFR_{cf} T46C-CN showing a mass of 26 Da (i.e. 17978.0 Da).

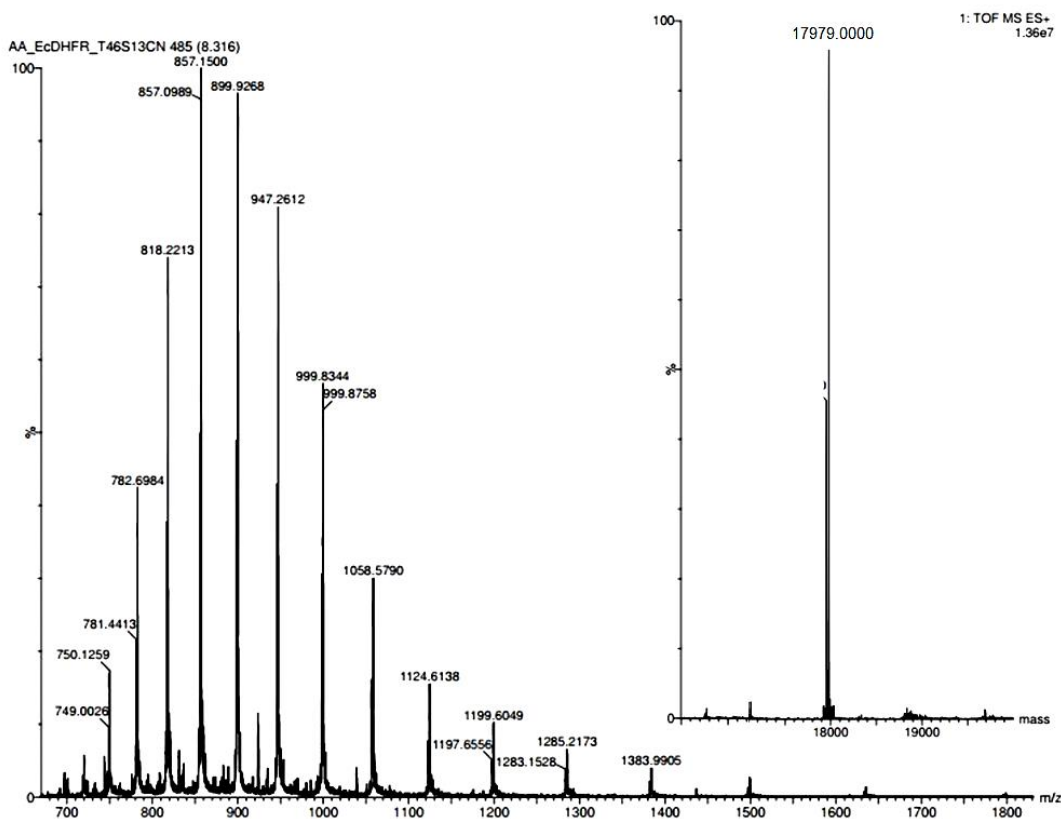


Figure A14: Charge envelope and deconvoluted mass spectra of $\text{EcDHFR}_{\text{cf}} \text{T46C-}^{13}\text{CN}$ showing a mass of 27 Da (i.e. 17979.0 Da).

Conformationally impaired EcDHFR variant

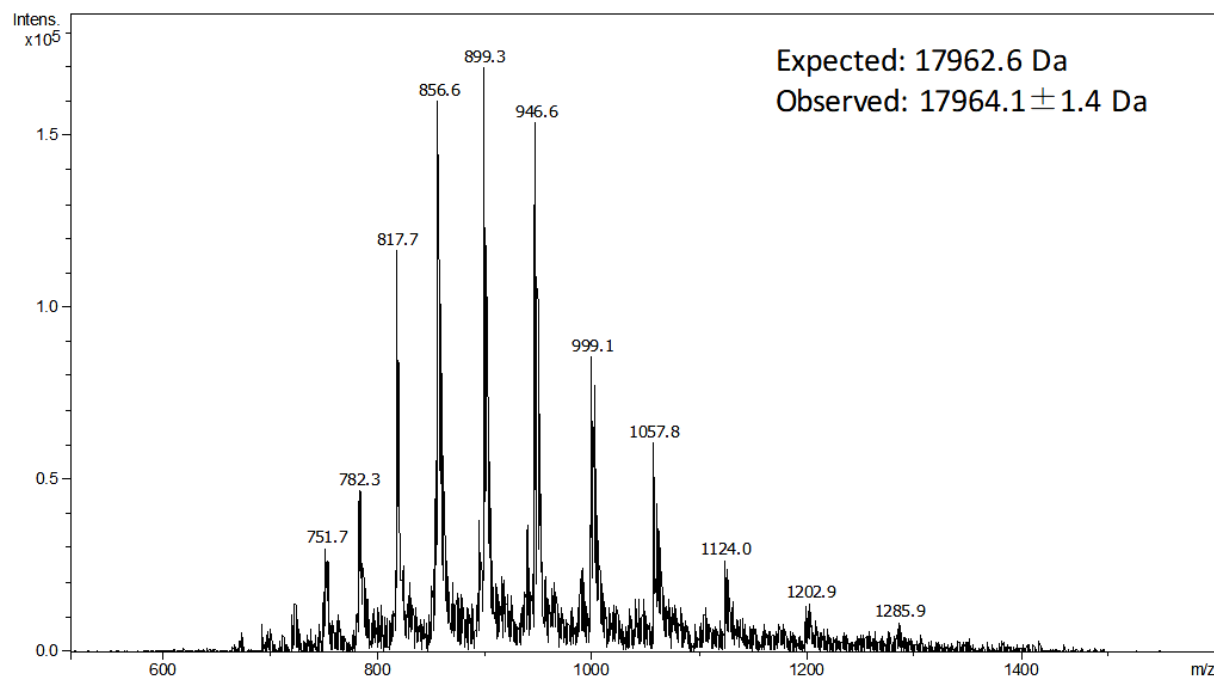


Figure A15: Charge envelope of $\text{EcDHFR}_{\text{cf}} \text{S148P/T46C}$ with a mass of 17964.0 Da.

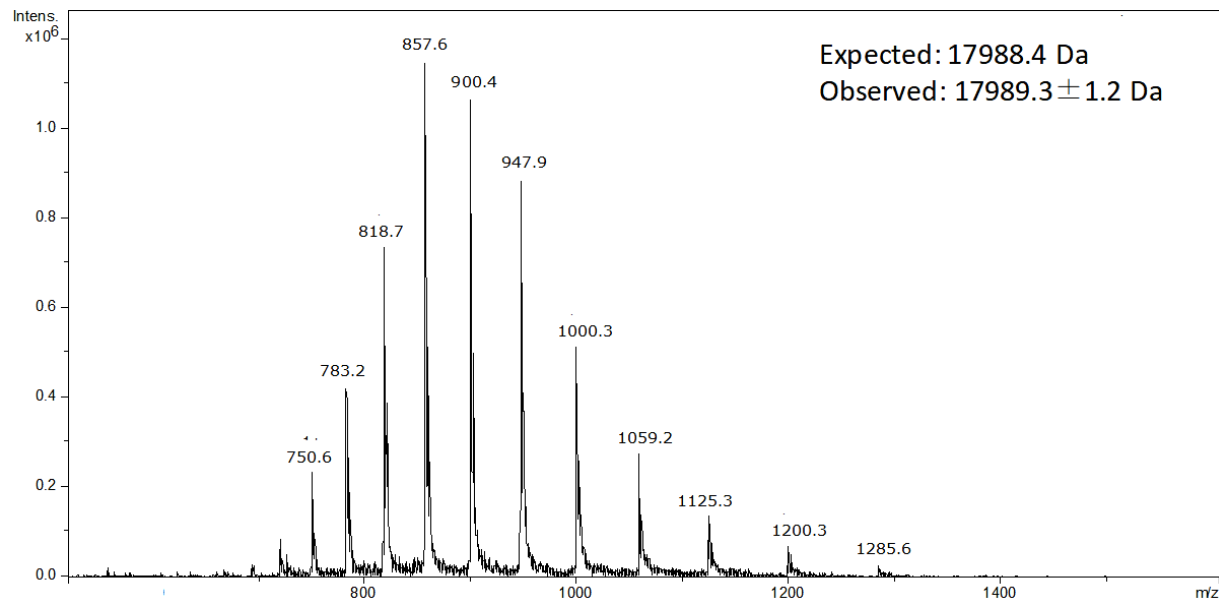


Figure A16: Charge envelope of $\text{EcDHFR}_{\text{cf}} \text{S148P/T46C-CN}$ showing a mass increase of ~26 Da (i.e. 17989.3 Da).

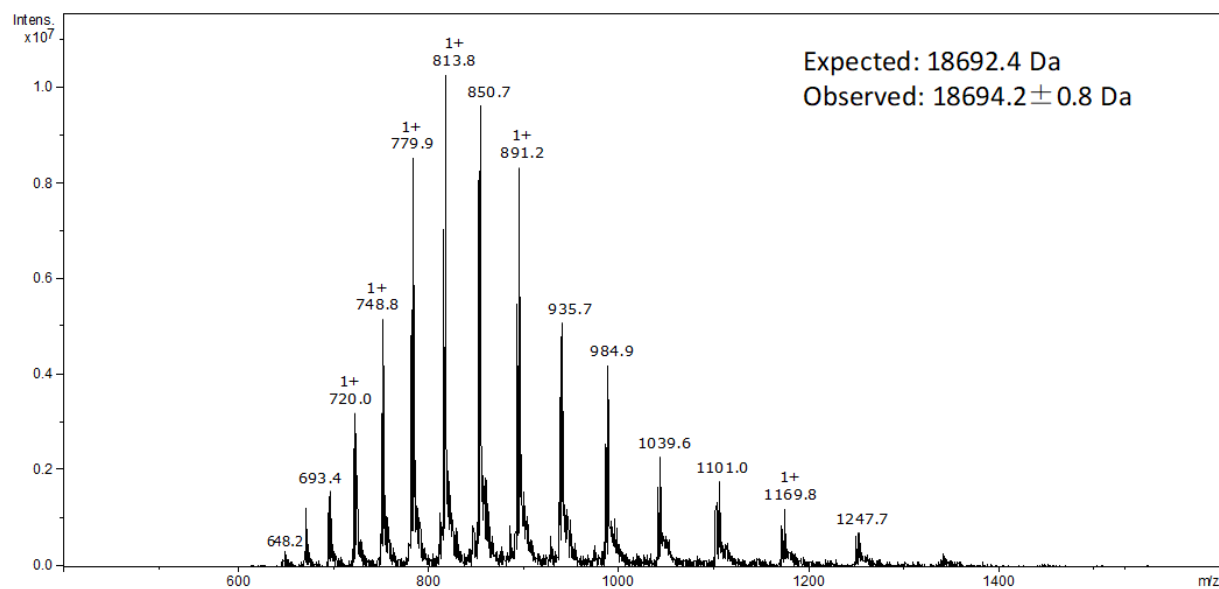
BsDHFR

Figure A17: Charge envelope of $BsDHFR_{cf}$ T46C showing a mass of 18694.2 Da.

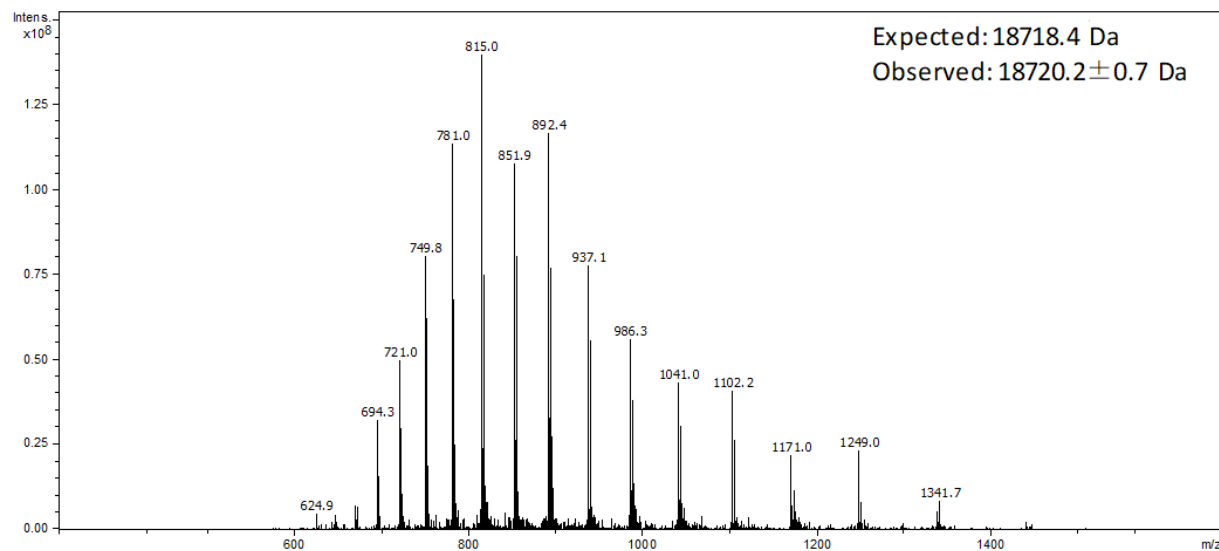


Figure A18: Charge envelope of $BsDHFR_{cf}$ T46C-CN showing a mass increase of ~26 Da (i.e. 18720.2 Da).

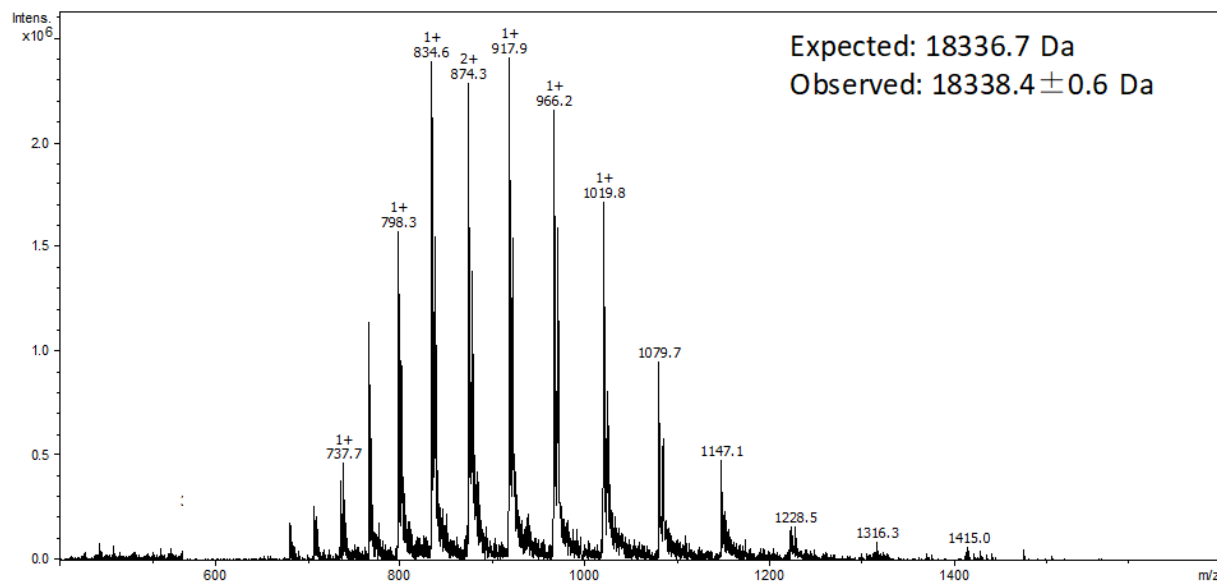
MpDHFR

Figure A19: Charge envelope of MpDHFR_{cf} T47C showing a mass of 18338.4 Da.

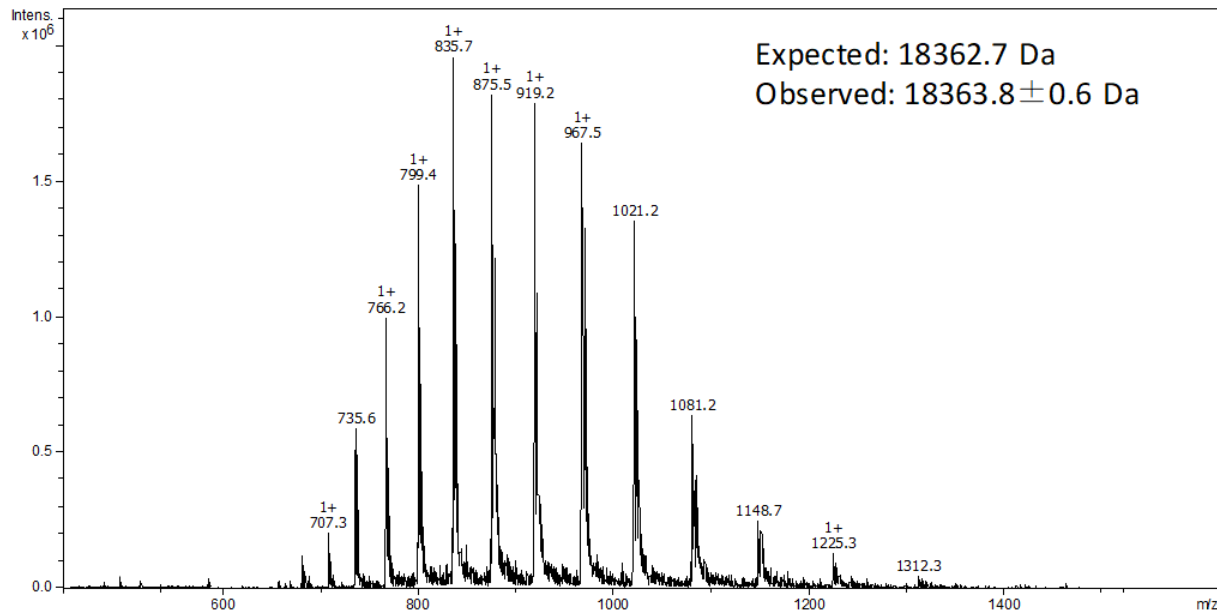


Figure A20: Charge envelope of MpDHFR_{cf} T47C-CN showing a mass increase of ~26 Da (i.e. 18363.8 Da).

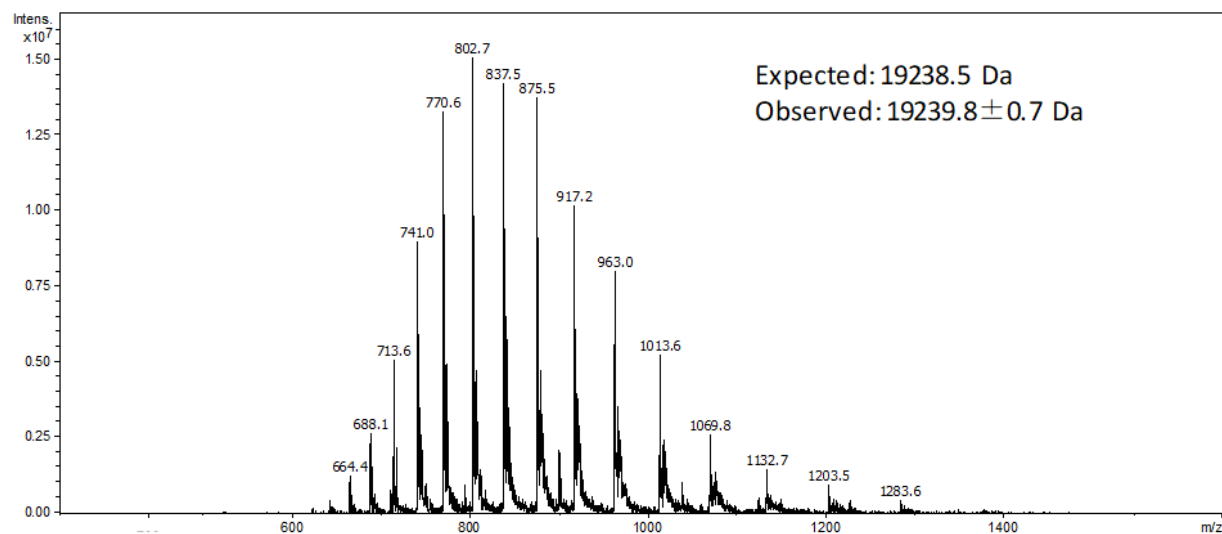
TmDHFR

Figure A21: Charge envelope of TmDHFR T47C showing a mass of 19239.8 Da.

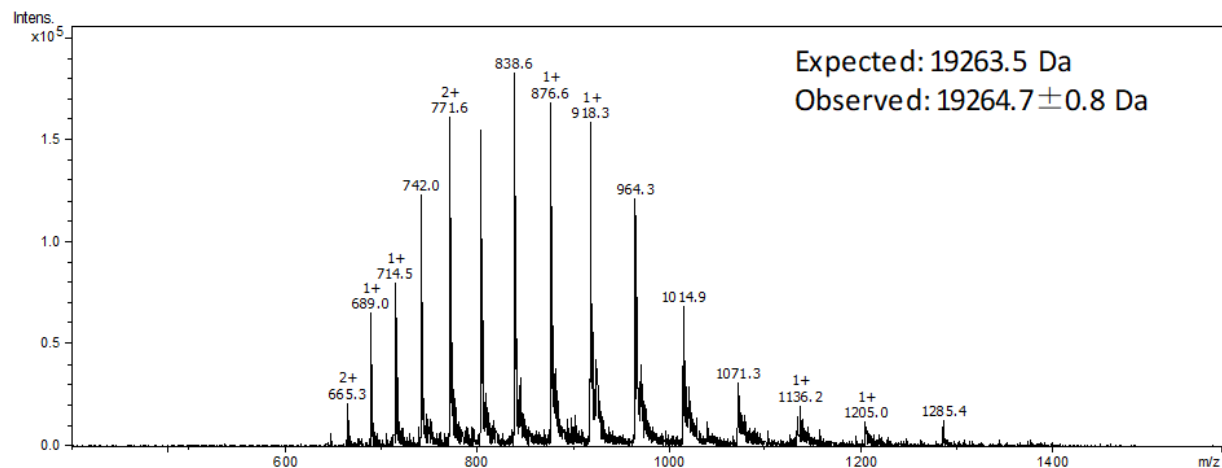


Figure A22: Charge envelope of TmDHFR T47C-CN showing a mass increase of ~26 Da (i.e. 19264.7 Da).

Data analysis

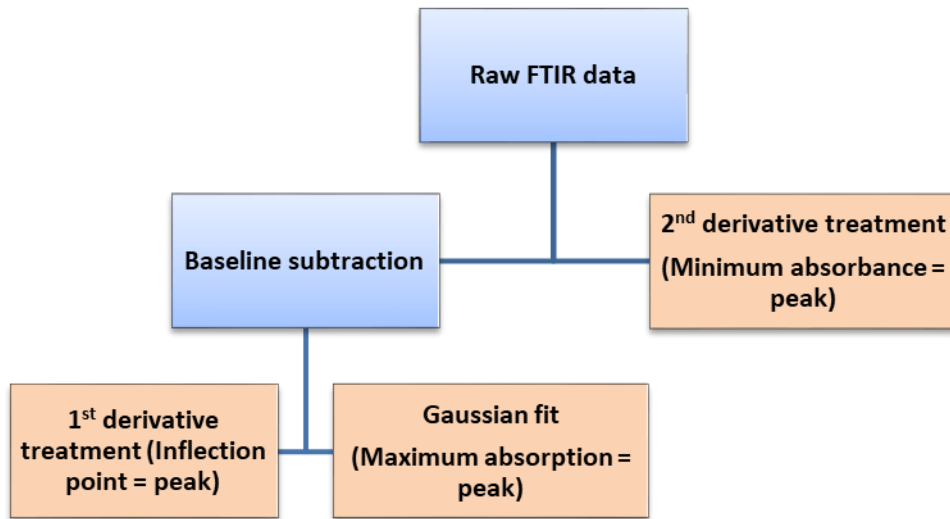


Figure A23: Scheme employed to determine the point of maximum absorbance of labelled DHFRs. Average of peaks obtained from data treatment (light brown boxes) are reported as peak of maximum absorption.

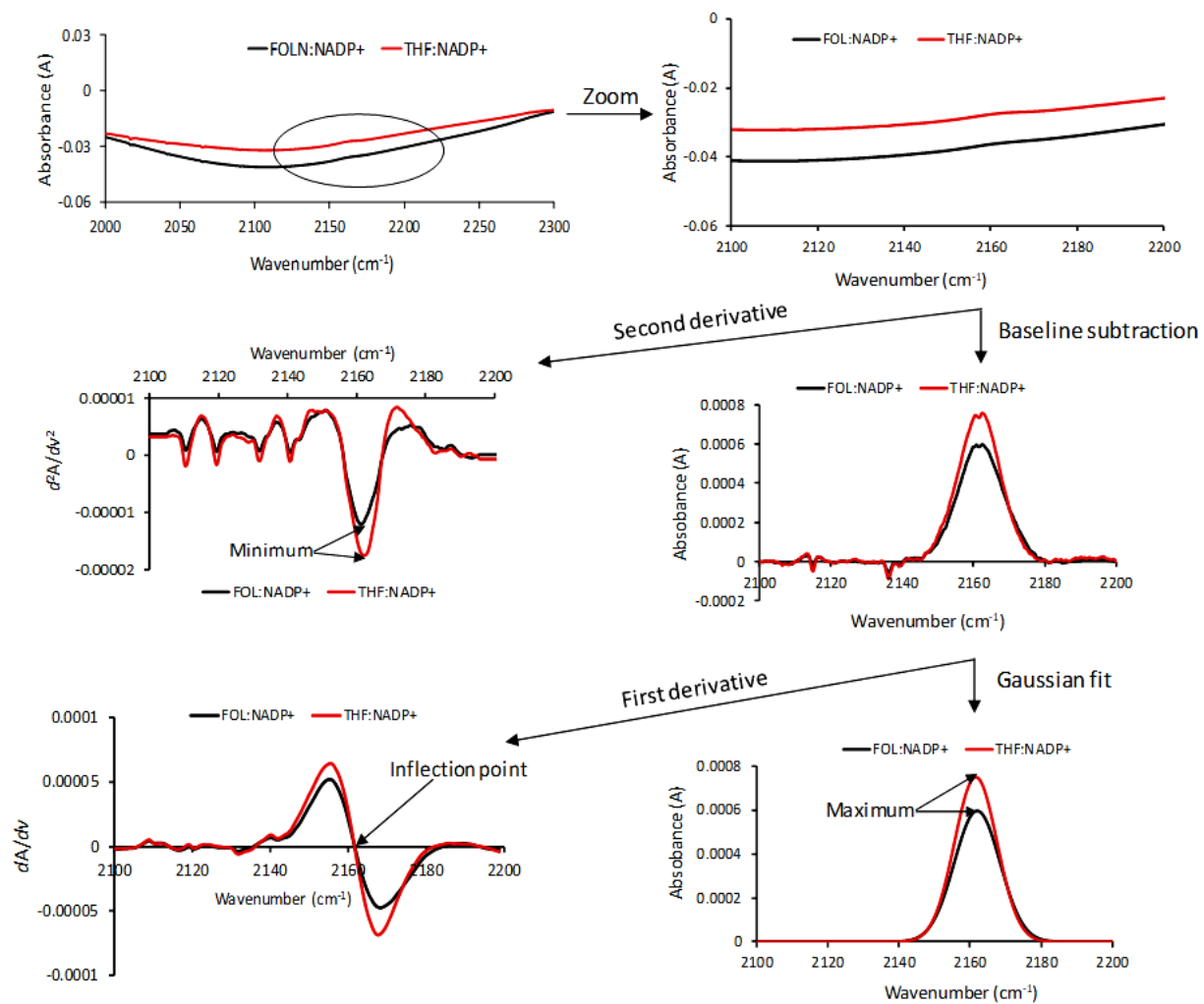


Figure A24: Graphical steps of spectra treatment employed for extracting the maximum vibrational frequency of labelled DHFRs. Reported peaks were averages of the minimum (2^{nd} derivative), maximum (Gaussian fit) and inflection point (1^{st} derivative) from at least two independent measurements. Error is reported as standard deviation of the treatments.

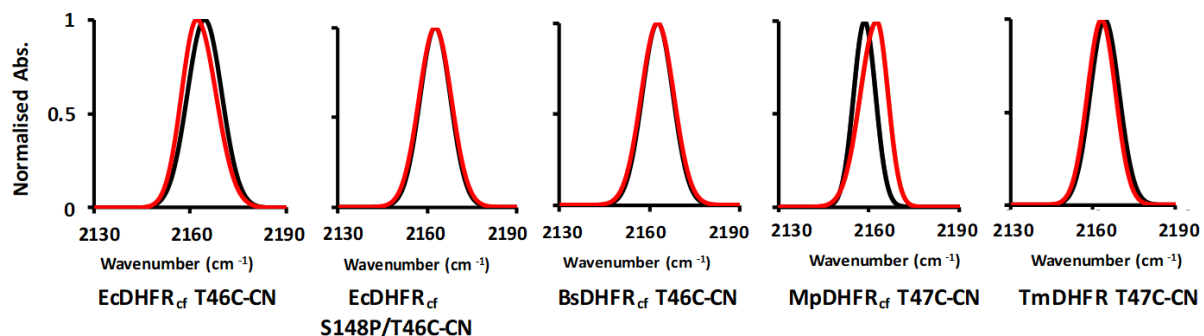


Figure A25: Gaussian fits of spectra measured for the Michaelis (FOL:NADP⁺, black) and product ternary (THF:NADP⁺, red) complexes of DHFRs at 20 °C.